UNIVERSIDADE ESTADUAL PAULISTA
"JÚLIO DE MESQUITA FILHO"
Câmpus de São José do Rio Preto

Airton Germano Bispo Junior

Light-emitting diodes based on Eu^{3+}, Eu^{2+} or Tb^{3+}-doped silicates for lighting and Circadian rhythm regulation

São José do Rio Preto
2019

Airton Germano Bispo Junior

Light-emitting diodes based on Eu^{3+}, Eu^{2+} or Tb^{3+}-doped silicates for lighting and Circadian rhythm regulation

Tese apresentada como parte dos requisitos para obtenção do título de Doutor em química, junto ao Programa de Pós-Graduação em Química, do Instituto de Biociências, Letras e Ciências Exatas da Universidade Estadual Paulista "Júlio de Mesquita Filho", Câmpus de São José do Rio Preto.

Financiadora: FAPESP – Proc.. 2016/20421-9

CAPES

Orientadora: Profª. Drª. Ana Maria Pires

Coorientador: Prof. Dr. Sergio Antonio Marques de Lima

São José do Rio Preto

2019

B622l

Bispo Junior, Airton Germano

Light-emitting diodes based on Eu3+, Eu2+ or Tb3+-doped silicates for lighting and circadian rhythm regulation / Airton Germano Bispo Junior. -- São José do Rio Preto, 2019

178 f. : il., tabs.

Tese (doutorado) - Universidade Estadual Paulista (Unesp), Instituto de Biociências Letras e Ciências Exatas, São José do Rio Preto

Orientadora: Ana Maria Pires

Coorientador: Sergio Antonio Marques Lima

1. LEDs. 2. Iluminação de estado sólido. 3. Terras raras. 4. Sol-gel. 5. Luminescência. I. Título.

Sistema de geração automática de fichas catalográficas da Unesp. Biblioteca do Instituto de Biociências Letras e Ciências Exatas, São José do Rio Preto. Dados fornecidos pelo autor(a).

Essa ficha não pode ser modificada.

Airton Germano Bispo Junior

Light-emitting diodes based on Eu^{3+}, Eu^{2+} or Tb^{3+}-doped silicates for lighting and Circadian rhythm regulation

Tese apresentada como parte dos requisitos para obtenção do título de Doutor em química, junto ao Programa de Pós-Graduação em Química, do Instituto de Biociências, Letras e Ciências Exatas da Universidade Estadual Paulista "Júlio de Mesquita Filho", Câmpus de São José do Rio Preto.

Financiadora: FAPESP – Proc.. 2016/20421-9

CAPES

Comissão Examinadora

Profª. Drª. Ana Maria Pires
UNESP – Campus de Presidente Prudente
Orientadora

Profª. Drª. Marian Rosaly Davolos
UNESP – Campus de Araraquara

Prof. Dr. Fernando Aparecido Sigoli
UNICAMP

Prof. Dr. Carlos José Leopoldo Constantino
UNESP - Campus de Presidente Prudente

Prof. Dr. Paulo Cesar de Sousa Filho
UNICAMP

Presidente Prudente
30 de agosto de 2019

To my parents Maria José Santander Bispo and Airton Germano Bispo

ACKNOWLEDGEMENTS

My parents Maria José Santander Bispo and Airton Germano Bispo for sure are the real responsible for this study because they always encouraged me to study and highlighted me how education can change someone's life. Fortunately, I got the opportunity to be born into a family with the opportunity of enabling my education and I am very proud of that. For giving me the inspiration to be a good person. Everything is for you!

I thank my sister Michele Santander Bispo and my niece Julia Maria Bispo Reis for the companionship. It is worth pointing out the importance of my aunts Maria Antonia Santander dos Anjos, Ivone Santander Tardim, Nair Santander, my uncle Roberto Santander and my cousins Carla Santander dos Anjos, Carlos Romão Santander dos Anjos Souza and Andrea Santander dos Anjos in my life and in my education. My grandfather Romão Santander (*in memoriam*) and grandmother Alice Santander Centeio (*in memoriam*) for being with me all the time, taking care of me.

Professor Ana M. Pires opened the doors of her lab and introduced me to the luminescence subject, something that now I am fascinated with. She is also an inspiration of the kind of person and professional I want to be: smart, hardworking, kind, polite, and ethical. Professor Sergio A. M. de Lima, co-head of LLuMes group, is acknowledged for my scientific education during the graduation and Ph.D., for the help in writing papers, data interpretation, and discussion. I also thank both for their friendship.

All my university classmates: Fernanda, Monica, Jéssica, Ariane and André for sharing with me hard study moments and friendship. A memorable acknowledge to my buddy André for all the friendship and help, my housemate Edy for the friendship, and Nagyla and Rebeca for sharing happy moments with me. All my friends of LLuMes for the companionship and the scientific discussions: André, Alessandra, Alessandro, Bianca, Bruno, Camila, Edy, Felipe, Filipe, João, Leonardo, Luis, Nagyla, Rebeca, Renan, Rodolpho and Vytor.

Professors Luis D. Carlos and Rute A. S. Ferreira for opening the doors of their lab in Aveiro and giving me the opportunity to finish my study. A special thanks to Professor Rute Ferreira for all the patience in teaching me some fundamentals on rare-earth spectroscopy and helping me in writing papers, data interpretation, and discussion. All my fellows from Aveiro: Caixeta, Fernanda, Fernando, Gosia, Joana Costa, João

Ramalho, Justyna, Rita Bastos, Rita Frias, Luis, Rodolfo, Sofia, and Talita for making easier my stay in Portugal.

All the collaborators of this study:

Professor Celso X. Cardoso for the synthesis with PVDF and BO.

LAB-MEV and MSc Glenda G. Souza for MEV measurements.

Sol-gel research group from UNIFRAN coordinated by Professors Eduardo J. Nassar and Professor Lucas A. Rocha for the photoluminescence measurements.

Laboratório Multiusuário de análises químicas of IQ-UNESP and Alberto C. Alécio and Naira C. Pesquero for the diffuse reflectance measurements.

Laboratório de difração de raios X coordinated by Professor Silvio R. Teixeira and MSc Wagner D. Macedo Júnior for the XRD measurements.

Núcleo de inovação tecnológica em borracha natural coordinated by Professor Aldo E. Job for the thermal analysis measurements.

Laboratório de compósitos e cerâmica funcional coordinated by Professor Silvania Lanfredi Nobre and MSc Fabiano R. Prachedes, Leonardo P. de M. Simões, MSc Gisele S. Silveira and MSc Eliane A. Namikuchi for the XRD measurements.

Laboratório de filmes nanoestruturados e espectroscopia coordinated by Professor Carlos J. L. Constantino, and Dr. Sabrina A. Camacho, MSc José D. Fernandes, MSc Rafael J. G. Rubira and Dr. Cibely da S. Martin for Raman measurements.

University of Aveiro, Professors Luís D. Carlos and Rute A. S. Ferreira for receiving me in phantom-g.

Dr. Carlos D. S. Brites from phantom-g for the quantum yield measurements.

Dr. Alexandre M. P. Botas and Dr. Sandra F. H. Correia from phantom-g for helping me with the photoluminescence measurements.

MSc Marita A. Cardoso for the help with the fabrication of PMMA films.

Dr. Andrei Kovalevsky from CICECO for the help in the heat treatments.

Dr. Rosário T. Soares from Chemistry department of University of Aveiro for XRD measurements and Rietveld Refinement.

I thank IBILCE and the post-graduation in chemistry.

This work was carried out with the support of the Coordination of Superior Level Staff Improvement - Brazil (CAPES) - Financing Code 001, to which I thank.

I thank FAPESP for granting the research grant under process no. 2016/20421-9 São Paulo Research Foundation - FAPESP (FAPESP).

“[…] Hey you, don't tell me there's no hope at all,

Together we stand, divided we fall”

Gilmour, D.; Manson, N.; Waters, R.; Wright, R.
The wall, Harvest Records, 4 vinyl, track 1 (Vinyl 2).

RESUMO

Diodos emissores de luz branca (WLEDs) são as principais fontes de luz branca para iluminação e fundo de tela de displays devido ao alto brilho (800 lm) e eficácia luminosa (150 $lm \cdot W^{-1}$), alto tempo de vida útil (50.000 horas), baixo consumo energético (8,5 W), baixo preço (60 dólares em 20 anos de uso) e baixa toxicidade comparados a lâmpadas incandescentes e fluorescentes. Além dos WLEDs, LEDs monocromáticos têm ganhado atenção nos últimos anos devido ao comum consenso e entendimento da influência da luz na regulação do ritmo circadiano Humano e de plantas. Entretanto, os principais desafios são obter WLEDs com parâmetros ópticos de temperatura de cor correlata (4.500 K) e índice de renderização de cor (> 90) desejáveis e contornar o "*green gap*" na fabricação de LEDs emissores de luz verde. Desta forma, o objetivo desta tese de doutorado foi fabricar LEDs emissores de luz branca ou monocromática para iluminação, luz de tráfico e controle do ritmo circadiano. Para esta proposta, luminóforos emissores de luz verde ($Ba_2SiO_4:Eu^{2+}$ e $Ba_2SiO_4:Tb^{3+}$), amarela ($Sr_2SiO_4:Eu^{2+}$) e vermelha ($Ba_2SiO_4:Eu^{3+}$) foram sintetizados pela metodologia sol-gel, caracterizados e dispersos em filmes poliméricos (PVDF ou PMMA), aos quais foram utilizados para recobrir LEDs emissores na região espectral do UV. As condições de síntese dos luminóforos foram variadas a fim de otimizar a composição das fases e a emissão dos dopantes. A dispersão dos luminóforos em PMMA potencializa a emissão dos ativadores luminescentes, sendo que os luminóforos baseados em $Ba_2SiO_4:Eu^{3+}$ e $Ba_2SiO_4:Tb^{3+}$ mostram potencial para serem combinados a LEDs UV (250 nm), fazendo um dispositivo multifuncional que emite luz e também radiação UV, importante para o controle do ritmo circadiano de plantas e desinfecção em agricultura (cultivo *indoor*). Já os LEDs emissores de luz verde construídos combinando LEDs UV (365 nm) e filmes de $Ba_2SiO_4:Eu^{2+}$/PMMA apresentaram eficácia luminosa e estabilidade radiante entre as melhores reportadas, sendo uma alternativa para suprir a ausência de LEDs emissores de luz verde com alta eficácia luminosa. Finalmente, WLEDs construídos combinando LEDs UV (395 nm) e filmes de $Sr_2SiO_4:Eu^{2+}$/BAM:Eu^{2+}/PMMA apresentaram valores de eficácia luminosa e estabilidade radiante entre os melhores reportados e temperatura de cor dependente da proporção dos luminóforos, podendo ser ajustada para aplicações em iluminação diurna (CCT = 6.000 K) e noturna (CCT = 4.500 K), além de usos em fototerapia.

Palavras-chaves: LEDs. Iluminação de estado sólido. Terras raras. Sol-gel. Luminescência.

ABSTRACT

White-light-emitting diodes (WLEDs) are the main light sources for indoor and outdoor lightings as well as for backlighting of displays due to their high brightness (800 lm) and luminous efficacy (150 $lm \cdot W^{-1}$), long lifespan (50,000 hours), low power consumption (8.5 W), low cost (60 dollars over 20 years of use) and environmentally friendly properties compared to the traditional incandescent and fluorescent bulbs. Beyond WLEDs, attention has currently been paid to monochromatic LEDs due to the common consensus on the light impact on human and plant circadian rhythm regulation. Nonetheless, the main challenges are to come up with WLEDs featuring desirable correlated color temperature (4,500 K) and color rendering index (> 90) and work around the "green gap" drawback in the fabrication of green-emitting LEDs. Therefore, the goal of this Ph.D. thesis is to report on the fabrication of white or monochromatic-emitting LEDs, and for this propose, UV-to-green ($Ba_2SiO_4:Eu^{2+}$ e $Ba_2SiO_4:Tb^{3+}$), yellow ($Sr_2SiO_4:Eu^{2+}$) and red ($Ba_2SiO_4:Eu^{3+}$) downshifting converter phosphors were synthesized by the sol-gel route, fully characterized and dispersed as polymeric films (PVDF or PMMA), to which were used to coat commercial UV LEDs. The synthesis conditions of the phosphors were changed aiming to optimize phase composition and emission intensity of the dopants. PMMA plays the role of enhancing the luminescent activator emission, and both $Ba_2SiO_4:Eu^{3+}$ and $Ba_2SiO_4:Tb^{3+}$ phosphors feature the required characteristics to be used as coatings of UV LEDs (250 nm), making multifunctional prototypes emitting UV and red light for simultaneous application in indoor farms by regulating the plant circadian rhythm and as a disinfection agent. On the other hand, the green-emitting LEDs built by coating UV LEDs (365 nm) with $Ba_2SiO_4:Eu^{2+}$/PMMA films match high luminous efficacy and radiant stability, among the best values reported so far, being a practicable alternative to supply the absence of commercially-available high-efficient green-emitting LEDs. Finally, WLED prototypes built by combining UV LEDs (395 nm) and $Sr_2SiO_4:Eu^{2+}$/BAM:Eu^{2+}/PMMA films display luminous efficacy and radiant stability among the best reported, and correlated color temperature depending on the phosphor mixture proportion, that may be tuned for daylight (6,000 K) and night light (3,500 K) applications, as well as phototherapy and backlighting of displays.

Keywords: LEDs. Solid-state lighting. Rare earth. Sol-gel. Luminescence.

LIST OF FIGURES

LIST OF TABLES

LIST OF ABBREVIATIONS

365-B LED	Green-emitting LED prototype
B2S	$Ba_2SiO_4:Eu^{2+}$
Ba_9	Barium site in Ba_2SiO_4 with CN = 9
Ba_{10}	Barium site in Ba_2SiO_4 with CN = 10
BO	Buriti oil
BSXEu	Eu-doped Ba_2SiO_4 (X %) calcinated for 2 hours
BSXEuYTb	Eu and Tb-doped Ba_2SiO_4
BSXTb	Tb-doped Ba_2SiO_4 (X %)
CD	Carbon dot
CCT	Correlated color temperature
CFL	Compact fluorescent lamp
CIE	1,931 *Commission internationale de l'éclairage*
CRI	Color rendering index
CM-LED	Color-mixed LED
CN	Coordination number
CR	Cross-relaxation
CTB1	Charge transfer band from Eu^{3+} in Ba local sites
CTB2	Charge transfer band from Eu^{3+} -O^{2-} associates
D	Donator specie
D*	Excited donator specie
D-D	Dipole-dipole
D_{ED}	Electric dipole strength
D_{MD}	Magnetic dipole strength
DSC	Differential scanning calorimetry
D-Q	Dipole-quadrupole
DR	Diffuse reflectance spectroscopy
DTG	Differential thermal analysis
DRX	X-ray diffraction
ED	Electric dipole oscillator
EDS	Energy-dispersive X-ray spectroscopy
EHT	Electron high tension
EM	Magnetic dipole oscillator
E_{photon}	Energy of a photon
EQ	Electric quadrupole oscillator
EQE	External quantum efficiency
ET	Energy transfer
Eu_{1-3}	Eu local sites in Ba_2SiO_4 or $BaSiO_3$ lattice
$Eu_{A1,2}$	Eu local sites related to Eu^{3+}-O^{2-} associates
Eu_{D1-3}	Defect-related Eu local sites
FTIR	Fourier transform infrared spectroscopy
FWHM	Full-width-at-half-maximum
HID	High-intensity discharge lamp
ICDD	International Centre for Diffraction Data
ipRGCs	Intrinsically photosensitive retinal ganglion cells
IR	Infrared radiation
LE	Luminous efficacy
LED	Light-emitting diodes

Ln-X	Ba_2SiO_4: Ln (Ln = Eu or Gd) and X = 2 h and 10 h (calcination time)
MW	Molar weight
Near-UV LED	Near-UV-emitting LED chip
OLED	Organic light-emitting diode
PC-LED	Phosphor-converted LED
PL	Photoluminescence
PLE	Excitation spectrum
PLED	Polymer light-emitting diode
PMMA	Poly(methyl methacrylate)
PMMA:MEu-X	PMMA films with different amount of BSEu
PVDF	Polyvinylidene fluoride
PVDF:XBO	PVDF films with X mL of BO
PVDF:yBSEu	PVDF films with 400 mL of BO and different amount of BS4Eu
$\boldsymbol{P_{eletric}}$	Electric power
$\boldsymbol{P_{optical}}$	Optical power
QD	Quantum dots
Q-Q	Quadrupole-quadrupole
RE	Rare Earth
RGB	Red, blue and green
S2S	$Sr_2SiO_4:Eu^{2+}$
S2S(X)BAM(Y)	PMMA films doped with X % of S2S and Y % of BAM
SAD	Seasonal Affective Disorder
SD	Starting delay
SEM	Scattering electron microscope
SI	International System of Units
SMD	Surface mounted LED
Sr_9	Strontium site in Sr_2SiO_4 with CN = 9
Sr_{10}	Strontium site in Sr_2SiO_4 with CN = 10
SSL	Solid-state lighting
$T_{calc.}$	Calcination temperature
Td	Fluorescent bulb with 15.9 mm of diameter
TEM	Transmission electron microscopy
TEOS	Tetraethyl orthosilicate
TG	Thermogravimetric analysis
TWh	Terawatt-hour
UV	UV radiation
WPE	Wall-plug efficiency
WLED	White-emitting LED
XRD	X ray diffraction
YAG	Yttrium Aluminium Garnet
ZPL	Zero-phonon line

LIST OF SYMBOLS

10Dq	Strength of the ligand field
$^{2S+1}L_J$	Russell-Saunders term
(x,y)	1,931 CIE color coordinates
$\langle f^N \psi J \vert U^{(\lambda)} \vert f^N \psi' J' \rangle^2$	Reduced matrix elements
°C	Degree Celsius
η	Quantum efficiency of an emitting state
η_{CR}	Cross-relaxation efficiency
η_{ext}	Extraction efficiency
$\eta_{PC\text{-}LED}$	LED efficiency
η_{SA}	Self-absorption efficiency
η_{stokes}	Ratio between the energy of the excitation and emission photons
η_{yield}	Phosphor quantum yield
λ	Wavelength
λ_{em}	Emission wavelength
λ_{ex}	Excitation wavelength
τ^{rad}	Radiative lifetime
χ	Lorentzian field correction
χ^2	"Chi squared"
ϕ_V	Luminous flux
μm	Micrometer
ΔE	Thermal activation energy
ΔE_1	Energy barrier for the energy transfer from the Eu_{10} to the Eu_9 site in the Ba_2SiO_4
ΔE_2	Energy barrier for the energy transfer from the Eu9 to the Eu10 site in the Ba_2SiO_4
ΔH_m	Heat of fusion
ΔS_m	Entropy variation in the melting process
Ω_2 **e** Ω_4	Judd-Ofelt intensity parameters
A_{01}	Einstein's coefficient for spontaneous emission
Å	ångström
A	amper
A	Acceptor specie
A*	Excited acceptor specie
A_{nrad}	Non-radiative decay rate
A_{tp}	Crystal field parameters
A_{rad}	Radiative decay rate
cm	Centimeter
e	Electron charge
E_a	Electron affinity of the ligand atoms
eV	Electronvolt
g	Gram
$g \cdot cm^{-3}$	Gram per centimeter
$g \cdot mol^{-1}$	Gram per mol
h	Plank's constant
Hz	Hertz
I	Electric current
J	Total angular quantum number

$J \cdot g^{-1}$	Joule per gram
$J\ g^{-1}K^{-1}$	Joule per gram Kelvin
k	Boltzmann constant
K	Kelvin
L	Total orbital angular momentum quantum number
Lm	Lumen
Ln^{3+}	Lanthanide(III)
$lm \cdot W^{-1}$	Lumen per watts
m_e	Mass of the electron
mJ·pulse	MiliJaule per pulse
mL	Milliliter
ms	Millisecond
Mol	Mol
n	Refractive index
nm	Nanometer
P	Oscillator strength
pm	Picometer
q	Emission quantum yield
R_0	Förster distance
R_{exp}	Expected R factor
R_i	Munsell code
R_c	Critical distance
R_{WP}	weighted profile R-factor
s	Second
S	Total spin quantum number
$T_{1/2}$	Temperature at which the emission intensity is half of that at 14 K
I_T/I_{300K}	Ratio between the intensities at a given temperature T and at 300 K
T8	Fluorescent bulb with 25.5 mm of diameter
T12	Fluorescent bulb with 38.1 mm of diameter
T_g	Glass transition temperature
T_m	Melting temperature
TWh	Terawatt-hour
V	Volts
W	Watts
W_{CR}	Cross-relaxation rate

TABLE OF CONTENTS

CHAPTER 1 – INTRODUCTION

1.1 State-of-the-art

Have you ever thought how would be human life without lighting? Or better, how would society evolve in the dark? Thanks to Thomas Edison that manufactured the first electric bulb based on incandescence at the end of the XIX century, we do not ask ourselves those questions.[1] The lighting evolution has not stopped with Edison's invention since, in 1926, Edmund Germer patented the modern fluorescent lamp, opening up new opportunities of lighting by using bulbs with better efficiency and color qualities compared to incandescent sources.[2]

However, the most exciting lighting technology came up in 1996 with Shuji Nakamura at Nichia labs, who invented the first efficient white-emitting LED (WLED) based on a blue-emitting LED coated by a yellow-emitting phosphor, starting the LED boom.[2] Over the past 23 years, the luminous efficacy (LE) of WLEDs have improved from 25 lm/W to almost 200 lm/W, and this huge increase is correlated with the fabrication of high-efficient blue-light-emitting diodes by Hiroshi Amano, Shuji Nakamura, and Isamu Akasaki, who were laureates with the Nobel prize of Physics in 2014.[2]

Nowadays, WLEDs are estimated to achieve at about 60 % of penetration in 2020 in various market segments as indoor (offices, homes, shops) and outdoor (streets, traffic signals) lighting, displays (backlighting for displays, digital cameras, security equipment, mobile phone, etc.), automotive lighting and medical applications.[3,4] This huge and outstanding expansion of WLED commercialization compared to the traditional incandescent and fluorescent lamps is due to their relative low cost-benefit (60 dollars over 20 years of use), high brightness (800 lm), long lifespan (50.000 hours), compact size and shape, environmentally-friendly properties, low power consumption (8.5 W) and high LE (150 $lm.W^{-1}$), as represented in Figure 1.1 and Table 1.1.[5]

Table 1.1 Comparison of typical market prices for various lighting sources. CFL = Compact fluorescent lamp.

Lighting Source	Price ($/klm)
Halogen Lamp (A19 43W; 750 lumens)	$2.5
CFL (13W; 800 lumens)	$2
Fluorescent Lamp and Ballast System (F32T8)	$4
LED Lamp (A19 12W; 800 lumens, dimmable)	$16
LED 6" Downlight (11.5W; 625 lumens)	$43
OLED Luminaire	$1,400

Source: Adapted from Bardsley *et al.*[6]

Figure 1.1 Temporal development of the luminous efficacy of different kinds of lamps.

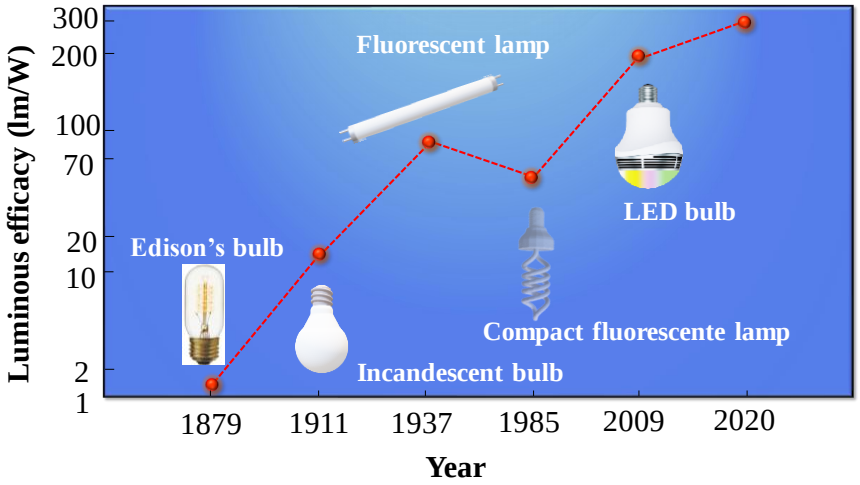

Source: Adapted from Mitch.[4]

A recent report from the US Department of energy[6] points out that the traditional bulb replacement by WLEDs is expected to reduce the lighting sector consumption by 15 % in 2020 and by 40 % in 2030, saving 261 TWh (equivalent to the total energy consumption of at about 24,000,000 homes in the US). A recent example from the commercial lighting sector is also shown in Figure 1.2, highlighting the energy saves due to the replacement of traditional bulbs by LED lamps in the US.

Figure 1.2 (a) Global commercial lighting revenue forecast, (b) Forecast of shipments of commercial lamps and luminaires. (c) Lighting inventory, electricity consumption, and lumen production. Abbreviations: HID (High-intensity discharge lamp), CFL (Compact fluorescent lamp), T12 (fluorescent bulb with 38.1 mm of diameter), T8 (fluorescent bulb with 25.5 mm of diameter), T5 (fluorescent bulb with 15.9 mm of diameter).

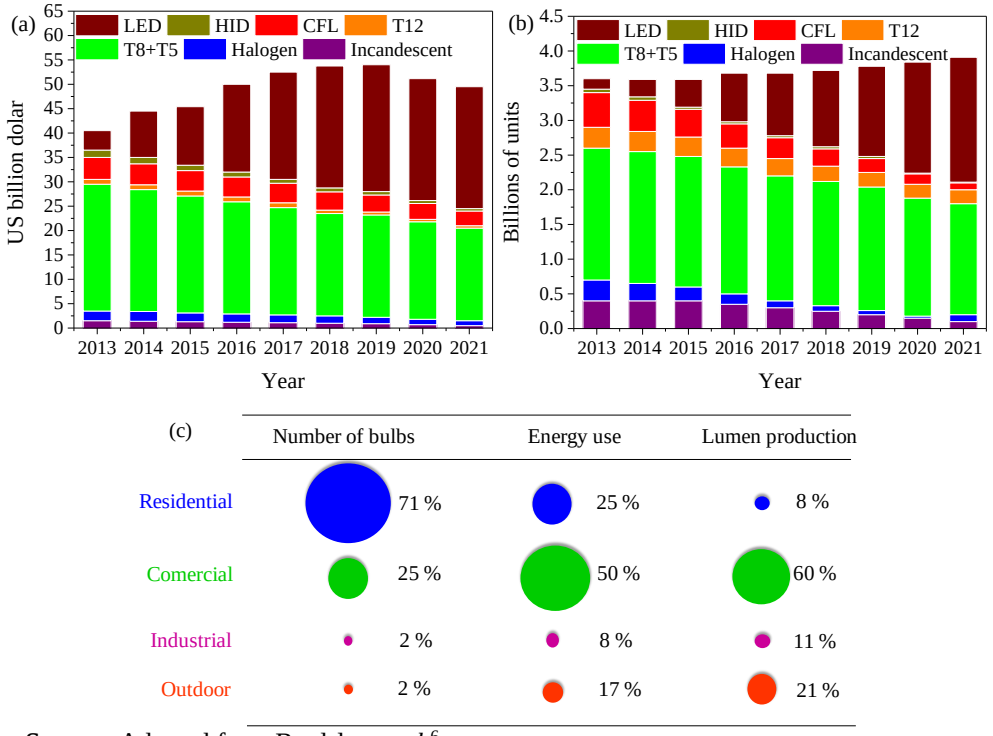

Source: Adapted from Bardsley *et al.*[6]

However, although most of the governments are providing financial support for solid-state lighting (SSL), many countries have still experienced less than 10 % of LED bulbs in the lighting market.[6] Therefore, the basic research on SSL has an enormous impact on energy savings in the world and a vast field of opportunities taking into account the improvement of WLED properties, namely the luminous efficacy and the color qualities as correlated color temperature (CCT) and color rendering index (CRI).[4]

The main commercially-available WLED is based on the combination of the GaN blue-emitting LED chip and the blue-to-yellow downshifting converter $Y_3Al_5O_{12}$: Ce^{3+} (YAG:Ce^{3+} - Yttrium Aluminium Garnet) phosphor.[7] The combination of the yellow with the remaining blue light generates a bluish-white light sensation to the human eye. Yet, although this approach displays high LE, it also features high CCT dependent on the operating voltage and time of use, and poor CRI due to the absence of red-emitting components.[8] It is important to point out that much attention has currently been paid to the color qualities of WLEDs since, in the last few years, many studies have shown that light has a huge impact on the human circadian rhythm.[9] Those disadvantages, combined to the higher price compared to the traditional lighting bulbs, create a barrier between the customer and the WLED market, even that its lifespan is immensely higher.[5]

In order to overcome those issues, the SSL engineering is now focused on three different research fields: (1) the fabrication of high-efficient and stable blue-to-red downshifting-converter phosphors to improve the CRI and decrease the CCT of the YAG-based WLED, (2) the fabrication of high-efficient near-UV-to-visible downshifting converter phosphors to be used as coatings of near-UV-emitting LEDs because the human eye does not see UV radiation, solving the CCT stability problem or (3) the fabrication of high-efficient and stable green or red-emitting semiconductor LED chips to be combined to the blue-emitting chip.[6]

However, for the best of our knowledge, all the compositions with red-emitting phosphors for the issue (1) decrease the luminous efficacy of the YAG-based LED, as shown in the figure of merit of LE, CCT and CRI, Table 1.2. Furthermore, the human eye does not have good sensitivity in the red spectral region, requiring high amounts of red-emitting phosphor in the LED composition to be detected by the retina.[10] For issue (2), there is a lack of high-efficient and stable near-UV-to-visible downshifting converter phosphors. Considering issue (3), there is a lack of green-emitting semiconductor materials that is known as “green-gap”, minutely discussed as follow.[11]

Table 1.2 State-of-the-art of WLEDs comparing luminous efficacy (LE), correlated color temperature (CCT) and color rendering index (CRI) as figures of merit. The values reported for incandescent and fluorescent lamps are also reported.

Composition	LED chip / nm	LE / $lm.W^{-1}$	CCT / K	CRI	[ref]
Incandescent [1]	-	26	2,812	43	12
Fluorescent [2]	-	60	3,753	100	12
YAG	460	164	5,468	78	12
YAG and $K_2GeF_6:Mn^{4+}$	460	125	3,882	90.4	13
YAG and $K_2SiF_6:Mn^{4+}$	460	116	3,900	89.9	14
YAG and $K_2(Si,Ge)F_6:Mn^{4+}$	460	145.33	6,110	70.5	15
YAG and $CsNaGeF_6:Mn^{4+}$	460	176.3	3,783	92.5	16
YAG and $Rb_3AlF_6:Mn^{4+}$	460	167.11	4,053	88.6	17
YAG and CdS:Cu/ZnS	460	37	3,357	89	18
YAG and CdSe/CdS/ZnS	460	32	3,865	88	19
YAG and $K_2TiF_6:Mn^{4+}$	455	116	3,556	81	20
YAG and $Li_3Mg_2SbO_6:Mn^{4+}$	454	87	3,254	81	21
YAG and $Ba_{0.8}Sr_{0.2}Mg_3SiN_4:Eu^{2+}$	450	120	4,000	96	22
YAG and $Cs_2GeF_6:Mn^{4+}$	450	141.5	3,673	84.9	23
$Lu_3(Al/Ga)_5O_{12}:Ce^{3+}$ and $Ca_{1-x}Li_xAl_{1-x}Si_{1+x}N_3:Eu^{2+}$	450	101	3,036	95	24
$Lu_3(Al/Ga)_5O_{12}:Ce^{3+}$ YAG and $Sr[Li_2Al_2O_2N_2]:Eu^{2+}$	449	-	2,700	91	25
$RbNa_2K(Li_3SiO_4)_4:Eu^{2+}$, $(Sr,Ba)_2SiO_4:Eu^{2+}$ and $CaAlSiN_3:Eu^{2+}$	395	10.37	3,707	70.9	26
$CsNa_2K(Li_3SiO_4)_4:Eu^{2+}$, $(Sr,Ba)_2SiO_4:Eu^{2+}$ and $CaAlSiN_3:Eu^{2+}$	395	5.19	3,331	71.5	26
CdZnSeS/ZnS	390	222.7	6,029	95.1	27
Phosphor-in-glass [3]	385	27.19	2,984	84.2	28
Multi-color phosphor-in-glass	385	27.8	4,245	92.6	29
$(Ba,Sr,Ca)BP_2O_8:Eu^{2+}$ and $CaAlSiN_3:Eu^{2+}$	380	-	5,995	91	30
$Cs_{(1x)}Rb_xVO_3$	365	94.8	5,178	82	31
BAM, YAG	310	-	4,437	93.8	32
BAM and S2S	390	120	4,390	72	This study

[1] Tungsten filament, [2] Mercury-vapor and phosphors (λ_{exc} = 250 nm), [3] $CaAlSiN_3:Eu^{2+}$, $Ba_2MgSi_2O_7:Eu^{2+}$, and $(Sr,Ba)_3MgSi_2O_8:Eu^{2+}$.

Source: Own authorship.

The US Department of energy has brought up a multi-year program plan to overcome all the barriers that are currently found in SSL, Table 1.3.[6] In all those projections, the CRI value is expected to be greater than 85 and the CCT, lower than 4,500 K. It is important to decrease the CCT value of the commercial WLED because the human circadian system is exquisitely sensitive to blue-rich light, especially at night, leading to many diseases such as diabetes, insomnia, and depression.[33] Yet, although light may have undesirable consequences to human health depending on the wavelength and CCT, it may be useful in medical applications and indoor farms, in the last case, by increasing the biomass production rate of plants, opening up new and exciting frontiers in SSL engineering to fabricate high-brightness monochromatic LEDs for several applications, Table 1.4.[4]

Table 1.3 Target LE for different kind of WLED approach. λ_{em} represents the emission wavelength, FWHM is the full-width at half maximum of the emission band, RGB is the red, green and blue emission, RGBA is the red, green, blue and Amber emission, R_9 is the Munsell code for the red emission quantification, LE is the luminous efficacy, CM-LEDs are the color-mixed LEDs, and PC-LEDs are the phosphor-converted LEDs.

RGB CM-LED with CCT of 3,000 K and CRI of 85 (R9 > 0)				
Emissions	Blue LED	Green LED	Red LED	Representation
λ_{em} (nm)	464	546	612	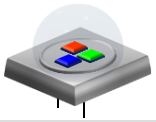
FWHM (nm)	20	20	20	
LE (lm/W)	Current		Target	
	133		191	
PC-LED with CCT of 3,000 K and CRI of 85 (R9 > 0)				
Emissions	Blue LED	Green phosphor	Red phosphor	Representation
λ_{em} (nm)	464	536	612	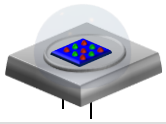
FWHM (nm)	20	100	100	
LE (lm/W)	Current		Target	
	123		189	
Hybrid-LED with CCT of 3,000 K and CRI of 85 (R9 > 0)				
Emissions	Blue LED	Green phosphor	Red LED	Representation
λ_{em} (nm)	459	539	612	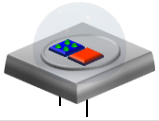
FWHM (nm)	20	100	20	
LE (lm/W)	Current		Target	
	165		231	
RGBA CM-LED with CCT of 3,000K and CRI of 85 (R9>0)				
Emissions	Blue LED	Green LED	Amber LED	Red LED	Representation
λ_{em} (nm)	460	539	590	615	
FWHM (nm)	20	20	20	20	
LE (lm/W)	Current		Target		
	85		153		

Source: Own authorship.

Table 1.4 Monochromatic LEDs for human phototherapy and plant and food technology.

LED emission spectral range	Application for human healthy	Application for plant and food technology
Red (630 nm)	Rhinitis treatment, wound healing and anti-inflammatory[34]	Algae growth, microalgae cultivation, plant tissue culture[34]
Green (550 nm)	Correct hyperpigmentation, eliminate skin spots[35]	Algae growth, bacteria and microalgae cultivation[34]
Blue (480 nm)	Seasonal Affective Disorder (SAD), non-seasonal depression and bipolar disorder therapies[9]	Algae growth, astaxanthin production[34]
UV (250 nm)	Disinfection, water treatment[34]	Disinfection, water treatment [34]

Source: Own authorship.

The main commercially-available monochromatic LEDs are based on AlInGaN or AlGaInP (Indium aluminum gallium nitrite or Aluminum gallium indium phosphide) semiconductor and their bandgap may be tuned from 0.7 eV to 3.4 eV by changing the composition, within the 365 – 1,900 nm spectral range.[36] Nonetheless, the main challenge on the fabrication of monochromatic LEDs lies on the previously mentioned “green gap”, i.e., the absence of high-efficient semiconductors in the green spectral region. This issue

arises from the abrupt decrease of the external quantum efficiency (EQE) of the InGaN-based LEDs in the green-yellowish spectral range. On the other hand, the EQE of the AlGaInP-based LEDs increases only from 600 nm, as represented in Figure 1.3.[36]

Figure 1.3 External quantum efficiency of conventional monochromatic LEDs emitting in the visible spectral region.

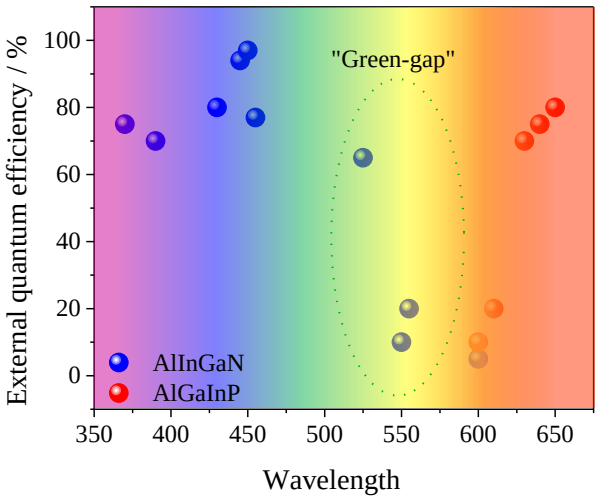

Source: Adapted from Seong *et al.*[37]

To address the "green gap" drawback, a feasible alternative is combining a near-UV-emitting LED chip (near-UV LED) with near-UV-to-green downshifting converter phosphors thanks to the huge improvement of the WPE of near-UV LEDs achieved in the last few years.[38] Therefore, the main challenge on the fabrication of high-efficient white or monochromatic LEDs lies on the improvement of the phosphor properties as the emission quantum yield and the thermal and structural stabilities.

In this study, we have chosen silicate-based phosphors, well-known as coatings of PC-LEDs. The state-of-the-art of Ba_2SiO_4 and Sr_2SiO_4 based-phosphors comparing the emission quantum yield and the annealing temperature as figures of merits is shown in Table 1.5.

Table 1.5 Figure of merit of the emission quantum yield (q) of M_2SiO_4:RE (M = Sr or Ba and RE = Eu^{2+}, Eu^{3+} or Tb^{3+}) phosphors. The excitation wavelength (λ_{exc}), emission wavelength (λ_{em}) and the calcination temperature (T. calc.) to get the phase are also provided.

Sample	T. calc. / ºC	λ_{exc}/ nm	λ_{em}/ nm	q / %	[ref]
$Ba_2SiO_4:Eu^{2+}$	1,200	450	508	0.53	39
$Sr_2SiO_4:Eu^{2+}$	1,200	400	550	0.60	39
$Ba_2SiO_4:Eu^{3+}$	1,300	250	612	-	43
$Ba_2SiO_4:Tb^{3+}$	1,450	250	545	-	40
$Ba_2SiO_4:Eu^{3+}$, Tb^{3+}	-	-	-	-	-

Source: Own authorship.

In this study, attention was placed on the improvement of the synthesis of silicate-based phosphors, since, although there are several methods for the phosphor obtention,[41,42,43] some points as high calcination temperature (1,200 ºC-1,500 ºC) and low emission quantum yield (50 %) still need to be addressed.

To contextualize, the Ba_2SiO_4 matrix is a current subject of research in the LLuMeS research group. The study of this host for rare earth ions has started at about in 1995 [44] with Professor Ana Maria Pires under supervision of Professor Marian Rosaly Davolos. In this study, it was investigated the barium silicate matrix synthesis by the solid-state route and its use as host for Eu^{2+} and/or Eu^{3+} as precursor for $BaZnSiO_4:Eu^{3+},Mn^{2+}$ phosphor for application in fluorescent lamp.[45]

In 2010, Master Diego Ariça Ceccato started, in LLuMeS laboratory, the investigation of the Ba_2SiO_4 synthesis by the sol-gel route, and its use as an electrochemical sensor.[46] Finally, taking advantage of the sol-gel synthesis, we started in 2013 a scientific initiation scholarship to optimize the Eu^{3+} concentration in the Ba_2SiO_4 host. Then, in 2015, during the Ph.D., we have started to develop all the study showed in this thesis.

1.2 Motivation, challenges and justifications

We got involved in this study motived by three main points: (i) to apply deep-UV-to-visible downshifting converter phosphors as coatings of deep-UV-emitting LEDs, fabricating multifunctional UV and visible-emitting LED prototypes to be used in indoor farms, (ii) to work around the “green gap” issue by coating near-UV-emitting LEDs with $Ba_2SiO_4:Eu^{2+}$ green-emitting phosphors, making green-emitting LED prototypes and (iii) to improve the color qualities of WLEDs by combining near-UV-to-visible downshifting converter phosphors and commercial near-UV-emitting LED chips.

The reason behind point (i) lies on the potential application of a multifunctional UV and visible-emitting LED in indoor farms because of the UV radiation may be applied as an antibacterial agent, and the visible light is helpful to enhance the photosynthesis rate, by controlling the plant Circadian rhythm, as previously highlighted in Table 1.4.

Already about point (ii), the use of near-UV-emitting LEDs coated by green-emitting phosphors seems to be an alluring approach to overcome the “green gap” drawback.

Considering point (iii), there are many challenges to be overcome concerning the fabrication of high-efficient and stable WLEDs with desirable CCT and CRI values such as (a) the fabrication of thermally-stable phosphors with high emission quantum yield, (b) to elect an ideal phosphor mix to fill all the visible spectrum in order to get desirable color qualities, (c) to get photostable LED prototypes with no changes in the color emission over the time of use and (d) how to process the phosphor particles as coatings.

To cope with point (i), we chose to synthesize red-emitting phosphors based on $Ba_2SiO_4:Eu^{3+}$ and blue or green-emitting phosphors based on $Ba_2SiO_4:Tb^{3+}$, all processed as polymeric films. Already to fill points (ii) and (iii), we chose the $Ba_2SiO_4:Eu^{2+}$ and $Sr_2SiO_4:Eu^{2+}$ phosphors, respectively, dispersed in polymeric films.

The justifications on their selection lie on the thermal stability (1,000 ºC), relatively low phonon frequency of the matrices (800 cm^{-1}), transparency to UV radiation, desirable emission quantum yield, and the possibility of hosting divalent and trivalent dopant cations. The role of the phosphor processing as films lies on the decrease of the light scattering, and the improvement of the heat dissipation, to which are drawbacks currently found in the traditional protocol for the phosphor processing as coatings of LED chips (dispersion in silicone, epoxy resin or polyurethane).

1.3 Goals

The goal of this study is to fabricate light-emitting diodes by coating UV-emitting LED chips with UV-to-visible downshifting converter phosphors dispersed in polymeric matrices, in order to come up with prototypes featuring potential to be applied in lighting, devices, agriculture or phototherapy through the control of the Circadian rhythm of plants and humans, Figure 1.4.

The specific goals are:

1. To synthesize deep-UV-to-visible downshifting converter phosphors based on Eu^{3+} and/or Tb^{3+} doped Ba_2SiO_4 phosphor;
2. To use Eu^{3+} as spectroscopic probe aiming to understand the impacts of the doping on the Ba_2SiO_4 network;
3. To understand the energy transfer process between $Tb^{3+} – Tb^{3+}$ and $Eu^{3+} – Tb^{3+}$ in the Ba_2SiO_4 matrix;
4. To elect a suitable polymeric matrix to disperse the phosphors in order to make films with controlled thickness;

5. To use the $Ba_2SiO_4:Eu^{3+},Tb^{3+}$ phosphor as coatings of deep-UV-emitting LEDs;

6. To synthesize a green-emitting phosphor based on $Ba_2SiO_4:Eu^{2+}$ and use it as coating of near-UV emitting chips in order to fabricate green-emitting LED prototypes;

7. To synthesize a yellow-emitting phosphor based on $Sr_2SiO_4:Eu^{2+}$ and use it as coating of near-UV emitting chips combined to a blue-emitting phosphor ($BAM:Eu^{2+}$), aiming to fabricate a WLEDs featuring tunable CCT.

Figure 1.4. Goals of the thesis.

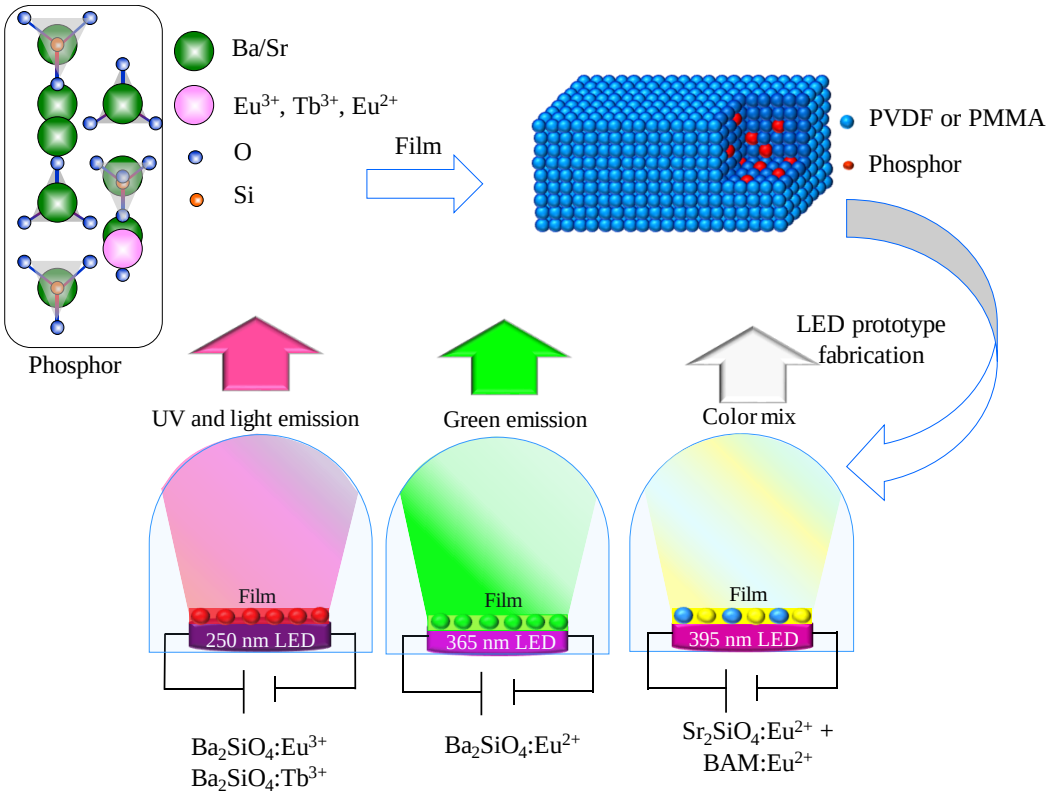

Source: Own authorship.

1.4 Thesis organization

Chapter 1 – Introduction: Discussion on the state-of-the-art of LEDs and silicate-based phosphors.

Chapter 2 - Background: Presentation of the main concepts used to discuss the results.

Chapter 3 – Tunable blue-green emission and energy transfer properties in $Ba_2SiO_4:Tb^{3+}$: Discussion on the synthesis of green/blue-emitting phosphors, impacts of the Tb^{3+}-doping on the Ba_2SiO_4 network, energy transfer properties and quantum efficiency of Tb^{3+}. This chapter was written based on a paper published in the Journal of Luminescence.[47]

Chapter 4 – Sol-gel synthesis of Eu^{3+}-doped Ba_2SiO_4: Synthesis of red-emitting phosphors, optimization of the synthesis and impacts of the doping on the defect-related structure of the Ba_2SiO_4 lattice. Part of this chapter was written based on a paper published in the RSC Advances.[48]

Chapter 5 – Energy transfer between Tb^{3+} and Eu^{3+} in barium orthosilicate phosphors. Discussion on the tunable red-blue light emission in $Ba_2SiO_4:Eu^{3+},Tb^{3+}$, energy transfer properties and use of Tb^{3+} as a sensitizer to Eu^{3+}. This chapter was written based on a paper published in the Journal of Luminescence.[49]

Chapter 6 – Red-light-emitting coatings for LEDs applied to plant circadian rhythm control: Fabrication of polymeric films containing $Ba_2SiO_4:Eu^{3+}$ and evaluation of these films as coatings of deep-UV-emitting LEDs. Part of this chapter was written based on a paper published in the Materials Chemistry and Physics.[50]

Chapter 7 - Green-emitting LEDs based on $Ba_2SiO_4:Eu^{2+}$ and near-UV-emitting LEDs: Synthesis of the $Ba_2SiO_4:Eu^{2+}$ phosphor in the powder form or dispersed in PMMA and fabrication of green-emitting LEDs.

Chapter 8 - White-emitting LEDs based on Eu^{2+}-doped silicate: Synthesis of the $Sr_2SiO_4:Eu^{2+}$ phosphor in the powder form or dispersed in PMMA and fabrication of white-emitting LEDs.

Chapter 9 – Final remarks: Presentation of the final remarks and some proposals for future studies in the research group.

1.5 References

[1] FRIEDEL, R. D.; ISRAEL, P.; FINN, B. S. Edison's electric light, Bibliography, 1987, Rutgers University Press.

[2] CHO, J. et al. White light-emitting diodes: History, progress, and future, Laser & Photonics Reviews, 2017, v. 11, n. 2, p. 1600147-17.

[3] JACOBY, M. Tuning phosphors for better white light Advances in the inorganic powders boost the efficiency and appeal of LED bulbs, Chemical and Engineering News, 2018, v. 96, n. 46, p. 28-33.

[4] PATTISON, P. M; HANSEN, M.; TSAO, J. Y. LED lighting efficacy: Status and directions, Comptes Rendus Physique, 2018, v. 19, n. 3, p. 134-145.

[5] MITCH JACOBY, Tuning phosphors for better white light, C&EN, 2018, v. 96, n. 46, p. 28-33.

[6] BARDSLEY, N. et al. Solid-State Lighting Research and Development Multi-YearProgram Plan, Building Technologies Office, Office of Energy Efficiency and Renewable Energy, U.S. Department of Energy, 2014 (DOE/EE-1089).

[7] CHEN, L. et al. Light Converting Inorganic Phosphors for White Light-Emitting Diodes, Materials, 2010, v. 3, n. 3, p. 2172-2195.

[8] BAI, X. et al. Efficient and tuneable photoluminescent boehmite hybrid nanoplates lacking metal activator centres for single-phase white LEDs, Nature Communications, 2014, v. 5, n. 0, p. 5702-8.

[9] LEGATES, T. A.; FERNANDEZ, D. C.; HATTAR, S. Light as a central modulator of circadian rhythms, sleep and affect, Nature Reviews, 2014, v. 15, n. 7, p. 443–454.

[10] OH, J. H.; YANG, S.J.; DO, Y. R. Healthy, natural, efficient and tunable lighting:four-package white LEDs for optimizing the circadian effect, color quality and vision performance, Light: Science & Applications, 2014, v. 3, n. 0, p. 141-9.

[11] ZHAO, M. et al. Next-Generation Narrow-Band Green-Emitting $RbLi(Li_3SiO_4)_2:Eu^{2+}$ Phosphor for Backlight Display Application, Advanced Materials, 2018, v. 30, n. 38, p. 1802489-7.

[12] PATTISON, P. M. et al. LEDs for photons, physiology and food, Nature, 2018, v. 543, n. 0, p. 493 – 500.

[13] HONG, F. et al. Room-temperature synthesis, optimized photoluminescence and warm-white LED application of a highly efficient non-rare-earth red Phosphor, Journal of Alloys and Compounds, 2019, v. 775, n. 0, p. 1365-1375.

[14] LV, L. et al. The formation mechanism, improved photoluminescence and LED applications of red phosphor $K_2SiF_6:Mn^{4+}$, Journal of Materials Chemistry C, 2014, v. 2, n. 20, p. 3879–3884.

[15] ZHENG, F. et.al, Reliability of fluoride phosphor $K_2XF_6:Mn^{4+}$ ($K_2SiF_6:Mn^{4+}$, $K_2(Si,Ge)F_6:Mn^{4+}$, $K_2TiF_6:Mn^{4+}$) for LED application, Journal of Materials Science: Materials in Electronics, 2018, v. 29, n. 24, p. 21061–21071.

[16] JIANG, C, et al. Mn^{4+}-Doped Heterodialkaline Fluorogermanate Red Phosphor with High Quantum Yield and Spectral Luminous Efficacy for Warm-White-Light-Emitting Device Application, Inorganic Chemistry 2018, v. 57, n. 23, p. 14705−14714.

[17] DENG, T. et al. Implementation of high color quality, high luminous warm WLEDusing efficient and thermally stable $Rb_3AlF_6:Mn^{4+}$ as red color converter, Journal of Alloys and Compounds, 2019, v. 795, n. 0, p. 453-461.

[18] WANG, X. et al. Doped Quantum Dots for White-Light-Emitting Diodes Without Reabsorption of Multiphase Phosphors, Advanced Materials, 2012, v. 24, n.20, p. 2742–2747.

[19] WANG, X. LI, W. SUN, K. STABLE efficient CdSe/CdS/ZnS core/multi-shell nanophosphors fabricated through a phosphine-free route for white light-emitting-diodes with high color rendering properties, Journal of Materials Chemistry, 2011, v. 21, n. 24, p. 8558-8565.

[20] ZHU, H. et al. Highly efficient non-rare-earth red emitting phosphor for warm white light-emitting diodes, Nature communications, 2014, v. 5, n. 0, p. 4312-10.

[21] WANG, S. et al. Mn^{4+}-activated $Li_3Mg_2SbO_6$ as an ultrabright fluoride-free red-emitting phosphor for warm white light-emitting diodes, RSC Advances, 2019, v. 9, n. 6, p. 3429- 3435.

[22] OSBORNE, R. A. et al. $Ba_{(1-x)}Sr_xMg_3SiN_4$:Eu narrow band red phosphor, Optical Materials, 2018, v. 84, n. 0, p. 130–136.

[23] WANG, Z. et al. Highly efficient red phosphor $Cs_2GeF_6:Mn^{4+}$ for warm white light-emitting diodes, RSC Advances, 2015, v. 5, n. 100, p. 82409-82414.

[24] WANG, L. et al. $Ca_{1-x}Li_xAl_{1-x}Si_{1+x}N_3:Eu^{2+}$ solid solutions as broadband, color-tunable and thermally robust red phosphors for superior color rendition white light-emitting diodes, Light: Science & Applications, 2016, v. 5, n. 0, p. 16155.

[25] HOERDER, G. J. et al. $Sr[Li_2Al_2O_2N_2]:Eu^{2+}$—A high performance red phosphor to brighten the future, Nature Communications, 2019, v. 10, n. 0, p. 1824-9.

[26] ZHAO, M. et al. Discovery of New Narrow-Band Phosphors with the UCr4C4-Related Type Structure by Alkali Cation Effect, Advanced Optical Materials, 2018, v. 1801631, n. 6, p. 1-9.

[27] LE, T. et al. Highly Luminescent Quantum Dots in Remote-Type Liquid-Phase Color Converters for White Light-Emitting Diodes, Advanced Materials Technology, 2018, v. 3, n. 3, p. 1800235-9.

[28] PENG, Y. et al. Luminous efficacy enhancement of ultraviolet-excited white light-emitting diodes through multilayered phosphor-in-glass, Applied Optics, 2016, v. 55, n. 18, p. 4933- 4938.

[29] JIANG, P. Thermally stable multi-color phosphor-in-glass bonded on flip-chip UV-LEDs for chromaticity tunable WLEDs, Applied Optics, 2017, v. 56, n. 28, p. 7921- 7926.

[30] SU, S. et al. Near UV-pumped bluish-white emitting K(Ba,Sr,Ca)BP_2O_8:Eu^{2+} phosphors, Journal of Alloys and Compounds Volume. 2013, v. 575, n. 0, p. 309-313.

[31] PAVITRA, E. et al. Evolution of highly efficient rare-earth free $Cs_{(1x)}Rb_xVO_3$ phosphors as a single emitting component for NUV-based white LEDs, Journal of Materials Chemistry C, 2018, v. 6, n. 46, p. 12746- 12757.

[32] Li, H. et al. Synthesis and Luminescence Properties of Bi^{3+}-Activated K_2MgGeO_4: A Promising High-Brightness Orange-Emitting Phosphor for WLEDs Conversion, Inorganic Chemistry, 2018, v. 57, n. 19, p. 12303−12311

[33] FIGUEIRO, M. G. An Overview of the Effects of Light on Human Circadian Rhythms: Implications for New Light Sources and Lighting Systems Design, Journal of Light & Visual Environment, 2013, v. 37, n. 2, p. 51-61.

[34] YEH, N. et al. Applications of light-emitting diodes in researches conducted in aquatic environment, Renewable and Sustainable Energy Reviews, 2014, v. 32, n.0, p. 611–618.

[35] KLEIN, R. M. Effects of green light on biological systems, Biological reviews of the Cambridge Philosophical Society, 1992, v. 67, n. 2, p.199-284.

[36] JEONG, H. et al. Indium gallium nitride-based ultraviolet, blue, and green light emitting diodes functionalized with shallow periodic hole patterns, Scientific Reports, 2017, v. 7, n. 0, p. 45726-9.

[37] SEONG, T. et al. III-Nitride Based Light Emitting Diodes and Applications, Topics in Applied Physics, 2013, springer.

[38] MATAFONOVA, G. BATOEV, V. Recent advances in application of UV light-emitting diodes for degrading organic pollutants in water through advanced oxidation processes: A review, Water Research, 2018, v. 132, n. 1, p. 177-189.

[39] SATO, Y. et al. Large redshifts in emission and excitation from Eu^{2+} activated Sr_2SiO_4 and Ba_2SiO_4 phosphors induced by controlling Eu^{2+} occupancy on the basis on crystal-site engineering, Optics and Photonics Journal, 2015, v. 5, n. 11, p. 326-333.

[40] DA-WEI, H. et al. VUV Luminescent Properties of M_2SiO_4:Re (M =Mg, Ca, Ba) (Re= Ce^{3+}, Tb^{3+}), Chinese Journal of Luminescence, 2007. v. 28, n.1, p. 53-57.

[41] AWATE, V. et al. Synthesis, characterization and luminescence studies of rare earth activated Sr_2SiO_4 phosphor: a review, Journal of Materials Science: Materials in Electronics, 2018, v. 29, n.6, p. 4391–4401.

[42] SZCZODROWSKI, K. et al. The role of compensation defects in Eu^{3+} stabilization under reductive atmosphere in Sr_2SiO_4 matrix, Journal of Alloys and Compounds, 2018, v. 748, n.5, p. 44-50.

[43] WANG, Z. et al. Luminescent properties of Ba_2SiO_4:Eu^{3+} for white light emitting diodes, Physica B, 2013, v. 411, n.15, p. 110–113.

[44] PIRES, A. M.; DAVOLOS, M. R.; MALTA, O.L. Eu^{3+}-O^{2-}associates luminescence in Ba_2SiO_4, Journal of Luminescence, 1997, v. 72-74, n. 0, p. 244-246.

[45] PIRES, A. M.; DAVOLOS, M. R. Luminescence of Europium(III) and Manganese(II) in Barium and Zinc Orthosilicate, Chemistry of Materials, 2001, v. 13, n. 1, p. 21-27.

[46] RAYMUNDO-PEREIRA, et al. Study on the structural and electrocatalytic properties of Ba^{2+}- and Eu^{3+}-doped silica xerogels as sensory platforms. RSC Advances, 2016, v. 6, n. 106, p. 104529-104536.

[47] BISPO-JR, A.G. et al. Tunable blue-green emission and energy transfer properties in Ba_2SiO_4:Tb^{3+} obtained from sol-gel method, Journal of luminescence, 2019, v. 214, n. 0, p. 116604-8.

[48] BISPO-JR, A. G. et al. Red phosphor based on Eu^{3+}-isoelectronically doped Ba_2SiO_4 obtained via sol–gel route for solid state lightning, RSC Advances, 2017, v. 7, n. 85, p. 53752–53762.

[49] BISPO-JR, A. G. et al. Energy transfer between terbium and europium ions in barium orthosilicate phosphors obtained from sol-gel route, Journal of Luminescence, 2018, v. 199, n. 0, p. 372–378.

[50] BISPO-JR, A. G. et al. Red-light-emitting polymer composite based on PVDF membranes and Europium phosphor using Buriti Oil as plasticizer, Materials Chemistry and Physics, 2018, V 217, n. 0, p. 160-167.

CHAPTER 2- BACKGROUND

2.1 Phenomenon of luminescence

2.1.1 Fundaments of luminescence

The phenomenon of luminescence is a process in which non-thermal radiation is produced as the return of a portion of energy absorbed from an independent source.[1] The phenomenon of luminescence may occur in all kind of materials, condensed or not, organic or inorganic, crystalline or not, and it may be classified according to the excitation source.[1]

In this study, emphasis will be placed on photoluminescence and electroluminescence. Electroluminescence is a process in which a material (usually a semiconductor) emits light as response to an electric field or an electric current, resulting in radiative recombination of holes and electrons.[2] Already in the photoluminescence, a material is excited by photons in the UV, visible or IR spectral range.[1]

Specifically, in the case of crystalline systems, the photoluminescence may be classified according to the nature of the emission: (i) intrinsic luminescence, a process correlated with network emission and (ii) emission coming from impurities, named as dopant or luminescent activator.[3]

In the emission arising from the luminescent activator, the excitation process occurs simultaneously by two different pathways, (i) the activator is indirectly excited by an intramolecular energy transfer coming from the matrix to the dopant and/or (ii) the activator is directly excited through transitions associated to its ground and excited states, as represented in Figure 2.1.[4]

Figure 2.1 Photoluminescence mechanism in a crystalline matrix doped with an activator ion (A) excited (a) indirectly by the matrix and (b) directly.

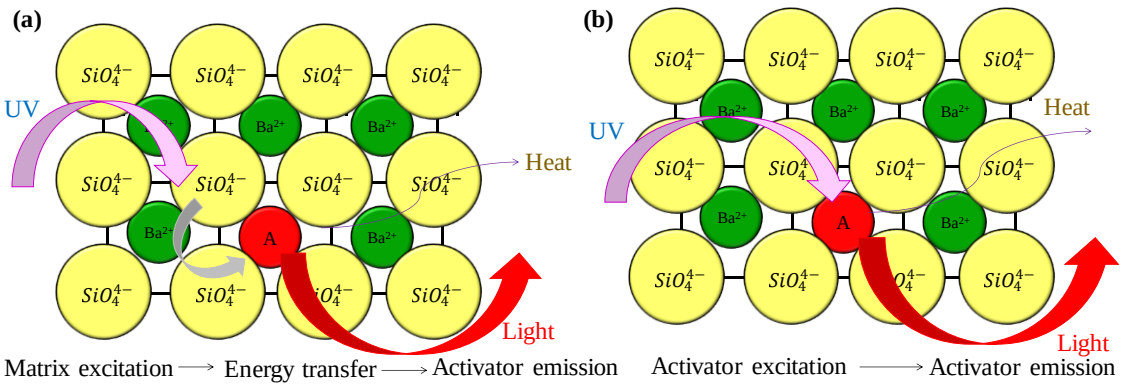

Source: Own authorship.

In both mechanisms represented in Figure 2.1, non-radiative processes as heat dissipation, vibrational relaxation and/or phonon release are competitively associated with the emission.[4] Among the main hosts for luminescent activators are oxides, sulfides, silicates, and oxysulfides, and as activators, transition metal and rare earth ions (RE^{3+} or RE^{2+}).[5]

Finally, the photoluminescence phenomenon may be also classified according to the energy of the excitation photons as Stokes process (or downshifting) and anti-Stokes process.[1] In the Stokes emission, the emitted photons feature lower energy than the excitation photons and in the anti-Stokes process, the opposite occurs. For the sake of clarity, some figures of merit used for photoluminescence quantification and qualitative aspects of energy transfer are pointed out as follow.

2.1.2 Characteristics of photoluminescence

Lifetime of an emitting state (τ)

A greatness extremely important to the photophysics of photoluminescent processes is the lifetime of the emitting state. The lifetime is the needed time to the initial population of a state to decrease to 1/e, and it may also be expressed as the inverse of the velocity constant (K) related to an electronic relaxation.[6] The lifetime is also dependent on the radiative (A_{rad}) and non-radiative (A_{nrad}) transition probabilities, as represented in Equation 2.1.[6]

$$\tau = \frac{1}{A_{rad} + A_{nrad}} \quad (2.1)$$

Quantum efficiency of an emitting state (η)

The quantum efficiency (η) of an emitting state is the ratio of the radiative (A_{rad}) and total (A_{total}) transition probabilities involved in the deactivation of the emitting state, as represented by Equation 2.2.[7]

$$\eta = \frac{A_{rad}}{A_{total}} = \frac{A_{rad}}{A_{rad} + A_{nrad}} \quad (2.2)$$

Theoretically, for downshifting converter phosphors, the quantum efficiency is expected to be 100 % in a process without any non-radiative pathways. Yet, there are several non-radiative processes that may deactivate an excited state including multiphoton relaxation, cross-relaxation processes, heat release, electronic defect levels among others.[8]

Absolute emission quantum yield (*q*)

The absolute emission quantum yield (*q*) of a radiation-induced process is defined by the number of emitted photons by a sample divided by the number of the absorbed ones.[8]

Qualitative aspects of energy transfer processes

In this study, energy transfer (ET) processes among RE^{3+} was investigated. The ET between two luminescent centers takes place by two different pathways: radiatively or non-radiatively.[9]

For the radiative process, the transfer occurs by two steps: First, the donator emits radiation and then, the acceptor absorbs this radiation, as highlighted in Equation 2.3 and 2.4, where D represents the donator and A, the acceptor species. In this case, the energy transfer efficiency depends on the superposition of the emission spectra: higher efficiencies are achieved as the Stokes shift decreases.*

$$D^* \rightarrow D + h\nu \quad (2.3), \qquad A + h\nu \rightarrow A^* \quad (2.4)$$

The non-radiative energy transfer occurs by just one step and does not involve radiation absorption or emission, as represented in Equation 2.5. In this case, the energy transfer is not directional and occurs directly by the interaction of both donator and acceptor. The two main models for non-radiative processes were first introduced by Förster and Dexter.[9]

$$D^* + A \rightarrow D + A^* \quad (2.5)$$

The Förster model is associated with dipole-dipole interactions among donator and acceptor.[10] For this, it is necessary that the oscillations coming from the electric field of the excited states of donator and the ground state of acceptor are resonant, plus overlap between the emission of donator and the excitation of acceptor and correct spatial orientation between the electric dipole of both states involved in the process.

In the dipole-dipole mechanism, Figure 2.2 (a), the interactions among donator and acceptor occur by the overlap between their dipolar electric field, operating by an electric filed oscillator arising from the donator and do not require a Van Der Waals contact, or orbital overlap.[11]

* Stokes shift is the energy difference of the absorption and emission bands that arise from the same electronic transition.

To examine the electric field oscillator of the donator, it is necessary to consider the electron as a harmonic oscillator that may experience oscillations (like electronic vibrations) into the direction of some cartesian axis in the crystalline network. In the classic mechanical model, an electron in the ground state of harmonic oscillation does not oscillate, but the donator has an excited electron, to which, according to this classic theory, correspond to an excited state of harmonic oscillator. This electron experience periodic harmonic oscillations with a natural frequency (ν_0) and some of these oscillators randomly dispersed in the network create an oscillating electric dipole close to the electric dipole oscillator of the electromagnetic radiation. Thus, the donator (but not the acceptor) is idealized as having an electric dipole oscillator that creates an oscillating electric field around the donator.[11]

Figure 2.2 Scheme of energy transfer mechanisms by (a) dipole-dipole and (b) exchange interactions. (c) Diagrams for electropole radiators.

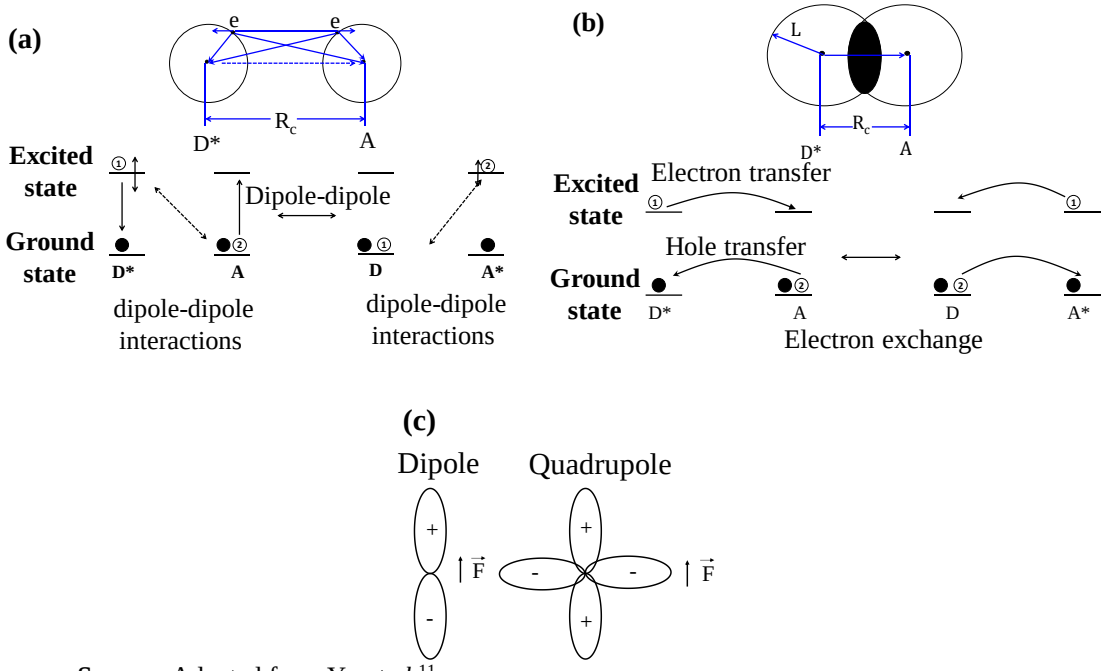

Source: Adapted from Ye *et al*.[11]

Förster reported the energy transfer by interactions of electric dipoles from both donator and acceptor, but some phenomena have not been foreseen, and Dexter expanded the Förster model considering the electron exchange or multipolar interactions between donator and acceptor. Thus, the Dexter theory is observed almost exclusively in quite short distances or in cases that the Förster mechanism is forbidden. This mechanism is also known as electron exchange or overlap mechanism, and it is limited by distances of 4 Angstroms, since it requires an orbital overlap, Figure 2.2 (b).[12]

In the Dexter model, exchange interactions and multipole dipole-quadrupole and quadrupole-quadrupole interactions are introduced, and the energy transfer probabilities depend on R^{-8} and R^{-10}, respectively, being R the distance between donator and acceptor. This theory may be correlated with the electron transfer in oxy-reduction reactions in transition metal complexes, mostly those ones that involve the inner-sphere mechanism.[9]

I. G. Van Uitert (1967)[13] came up with a model that it is possible to determine the mechanism of energy transfer between donator and acceptor by measuring the emission intensity (or lifetime) of the acceptor in different concentrations by applying Equation 2.6, where *x* represents the acceptor concentration, I the emission intensity (or lifetime), β is a constant, and θ = 6, 8 or 10, and represents electric dipole–dipole, dipole–quadrupole or quadrupole–quadrupole interactions, respectively. This model is applied for ET processes between RE^{3+} as $Tb^{3+} \rightarrow Tb^{3+}$, $Eu^{3+} \rightarrow Eu^{3+}$ or $Eu^{3+} \rightarrow Tb^{3+}$ and the selection rules of those processes are highlighted in Table 2.1.

$$\frac{I}{x} = \left[1 + \beta(x)^{\theta/3}\right]^{-1} \quad (2.6)$$

Table 2.1 Selection rules for ET processes of RE ions (RE = RE^{2+}, RE^{3+}). EQ is the electric quadropole-quadrupode ET, 2^{λ} represents multipolar interactions.

Mechanism	Selection rule	Exemple
(i) RE–RE ET ED	$\Delta J = 0, 1$	Ce^{3+} and Eu^{2+}: $5d$ - $4f$
Forced ED	$6 \geq \Delta J \geq 0$	Eu^{3+}: $^5D_0$ - $^7F_{2,4,6}$
EQ	$\Delta J \leq 2$	Yb^{3+}: $^2F_{5/2}$–$^2F_{7/2}$
Exchange	$\lvert J - J' \rvert = 0, 1$	Eu^{3+}: $^5D_1$ - $^5D_0$
(ii) Ligand–Ln ET Dipole-2^{λ} pole and D-D	$\lvert J - J' \rvert < \lambda \leq J + J'$	Eu^{3+} transfer from $^7F_0$ to $^5D_2$, $^5L_6$, $^5G_6$, $^5D_4$. $^7F_0$ to $^5D_{0,1}$ forbidden.
Exchange	$\lvert J - J' \rvert = 0, 1$	ET involving Eu^{3+} $^7F_0$–$^5D_0$ forbidden, but relaxed by J-mixing; Eu^{3+} $^7F_0$–$^5D_1$

Source: Reproduced from Tanner at al.[14]

2.2 Solid-state lighting

2.2.1 Light-emitting diodes

The solid-state lighting (SSL) is a field of lighting engineering that studies all kinds of lightings that use semiconductor light-emitting diodes (LEDs), organic light-emitting diodes (OLED), or polymer light-emitting diodes (PLED). In this study, we will focus on LEDs, and the spontaneous emission of them occurs by radiative recombination of electron-holes due to an electric field (electroluminescence phenomenon). Theoretically, this process may occur infinitely, increasing the device lifespan and cost-benefit compared to the traditional lightings.[15]

The fundamental on the LED architecture is a *p*-*n* junction, Figure 2.3 (a), and in this approach, the *n* layer is composed by electrons as majority load conductors and the *p* layer uses holes for the same purpose. The cathode is connected to the negative terminal and the anode to the positive one, making that the electrons from the *n* terminal be repelled to the depletion region of the "*p*-*n*" junction and tunnel to the *p* terminal. The same occurs for the holes in the *p* terminal and this charge movement generates the emission by the electron-hole recombination.[16]

Figure 2.3 (a) Schematic of a *p*-*n* junction in LEDs. (b) Architecture of CM-LEDs, PC-LEDs and hybrid-LEDs. CB = conduction band, VB = valence band.

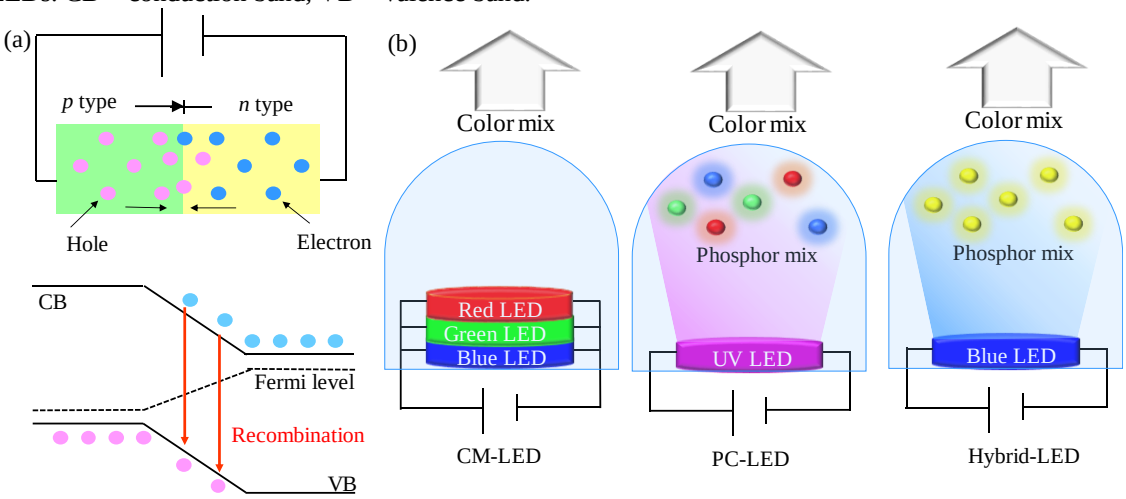

Source: Adapted from Held.[16]

There are several methods to get white light from WLEDs, and the main ones are highlighted in Figure 2.3 (b). All those approaches are based on color-mixed LEDs (CM-LEDs), phosphor-converted LEDs (PC-LEDs), or hybrid-LEDs. In CM-LEDs, the color mix is achieved from the intrinsic electroluminescence of LED chips (semiconductor material emission). Already the PC-LED architecture is predicated on the use of near-UV-emitting LED chips coated by a phosphor mixture. In this case, the LED chip emits radiation by electroluminescence within the near-UV spectral window and this radiation is used to excite the phosphor mixture on the LED chip through photoluminescence. Finally, in Hybrid-LEDs, the LED chip emits light by electroluminescence, a portion of this energy is used to excite a mixture of phosphors, and the combination of both LED chip and phosphor emissions generates the white light sensation.[17]

Among these three approaches to fabricate WLEDs, there are different color combinations to get white light, as highlighted in Figure 2.4, pointing out LE, CCT and CRI of the devices.

Figure 2.4 Different architectures of WLEDs. The terms R (red), G (green), B (blue) and A (Amber) corresponds to the different combinations of color emissions to get white light.

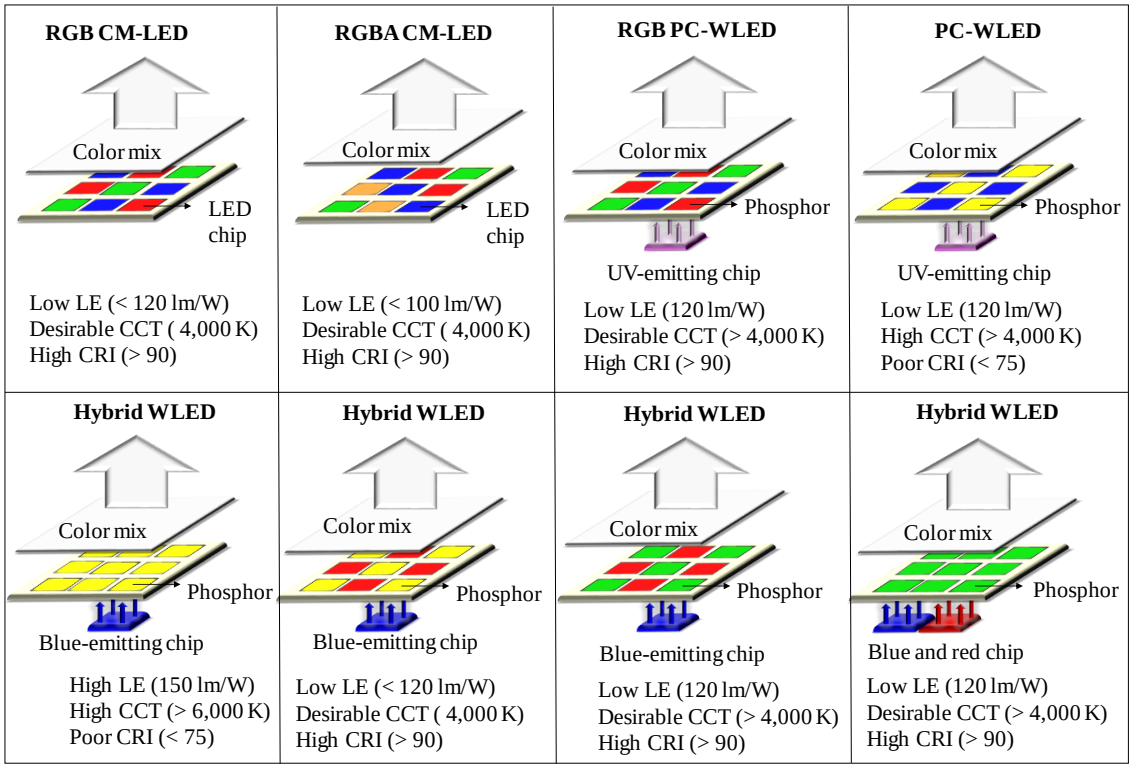

Source: Own authorship.

In this study, particular attention is placed on PC-LEDs due to the relatively-high wall-plug efficiency (WPE) and external quantum efficiency (EQE) achieved in the last years for near-UV emitting LEDs, and the non-dependence of the white light emitted by the WLED on the excitation source (near-UV LED chip), to which guarantee the stability of the correlated color temperature (CCT) over the time of use.[18] Moreover, other advantages of near-UV-emitting LEDs compared, for instance, to blue-emitting LEDs are less current drooping and significantly less binning, producing greater photon density at higher currents.[18]

The total efficiency ($n_{PC\text{-}LED}$) of PC-LEDs depends on several factors represented in Equation 2.7, being η_{yield} the phosphor quantum efficiency, η_{stokes} the ratio between the energy of the excitation and emission photons, η_{SA} the self-absorption efficiency and η_{ext} the extraction efficiency and it is expected to be 1 due to the high refractive index of both phosphor and the near-UV-emitting LED chip. All those parameters must be optimized to get the highest efficiency in the WLED.

$$\eta_{PC-LED} = \eta_{yield} x \eta_{ex} x \eta_{stoke} x \eta_{SA} \quad (2.7)$$

It is worth pointing out the effect of the phosphor composition and packaging structure on the efficiency of the PC-LED. Traditionally, the LED packaging uses a

dispersing method, based on the phosphor particles blended in silicone or organic resins (polyurethane, epoxy) that are directly dropped onto the LED chip surface, Figure 2.5 (a).[19] Although those methods are the mainstream for commercially-available PC-LEDs, they feature several disadvantages such as: (i) at about 60 % of the LED light is backscattered by the phosphor and reabsorbed by the LED chip since the phosphor blend is tightly close to the LED chip, Figure 2.5 (a); (ii) poor heat dissipation due to the silicone or organic resin, resulting in thermal quenching of the phosphor luminescence and (iii) the silicone resin may crack over the time of use.[20]

Figure 2.5 Schematic diagram of LED packaging. (a) Phosphors dispersed in silicone or organic resins, (b) phosphors processed as films.

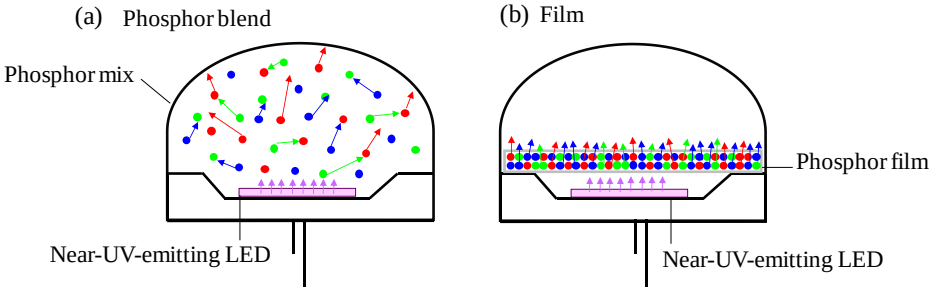

Source: Own authorship.

To cope with all those limitations, our strategy in this study is to process the phosphors as films, Figure 2.5 (b), by dispersing the particles of the phosphors in polymeric matrices as Polyvinylidene fluoride (PVDF) or Poly(methyl methacrylate) (PMMA), making films with tunable thickness, decreasing the light scattering.[21,22,23]

2.2.2 Photometric quantities

1,931 *Commission Internationale de L'éclairage* (CIE) color coordinates

The (x,y) color coordinates were defined by the *Commission Internationale de L'éclairage* (CIE) in 1931 adopting a standard colorimeter that represents the color attributes in a tridimensional diagram. The cartesian coordinates are represented as following in Equations 2.8, being *X*, *Y* and *Z*, representations of the integrals in all visible spectral range, Equations 2.9.[24] The $\bar{X}(\lambda), \bar{Y}(\lambda)\ and\ \bar{Z}(\lambda)$ spectral stimulus represent the human eye sensibility to the electromagnetic radiation corresponding to the red, green and blue primary colors, respectively.[24]

$$x = \frac{X}{X+Y+Z}, y = \frac{Y}{X+Y+Z}, z = \frac{Z}{X+Y+Z} \quad (2.8)$$

$$X = \int_0^\infty I(\lambda)\bar{X}(\lambda)d\lambda, \quad Y = \int_0^\infty I(\lambda)\bar{Y}(\lambda)d\lambda, Z = \int_0^\infty I(\lambda)\bar{Z}(\lambda)d\lambda \quad (2.9)$$

Correlated color temperature (CCT)

The CCT of a bulb is the temperature in Kelvin of an ideal heated black-body radiator that radiates the same color of the light source. Strictly speaking, this is a greatness that measures the appearance of the white light as cool (> 5,000 K) or warm (2,000 – 3,800 K). It is important to highlight that the CCT must be calculated only for colors that are represented by a black-body, i.e., orange, yellow or blue-white and not for pure colors as red or green.[25]

The CCT is derived from the CIE color coordinates by using Equation 2.10 developed by McCamy,[26] where $n = (x - 0.3320)/(0.1858 - y)$ and x and y are the CIE color coordinates.

$$CCT = 449\,n^3 + 3524n^2 + 6823.3n + 5520.33 \quad (2.10)$$

The CCT is the main greatness regarding the impact of white light on human circadian rhythm regulation. The ideal white color for lighting must follow the CCT changes of sunlight during the day, as represented in Figure 2.6 (a), in order to avoid disturbs in human health.

Figure 2.6 (a) Sunlight CCT dependence over the day. (b) CCT of white-emitting bulbs compared to the sunlight CCT. (c) CCT dependence on the (*x*,*y*) 1,931 CIE color coordinates.

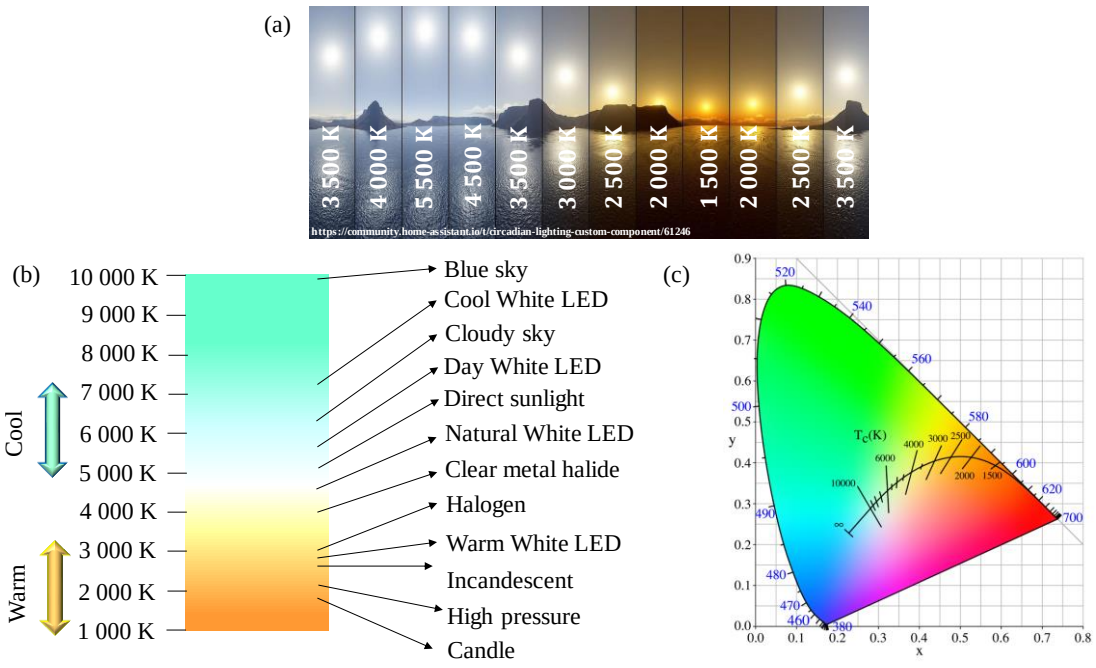

Source: Own authorship.

Therefore, bluish-white light (cool white light) is desirable during the day but must be avoided at night. A detailed description of the color quality impacts on the human health will be provided in section 2.2.4 and an overview on CCT values of some WLEDs compared to traditional lightings is shown in Figure 2.6 (b). The dependence of CCT on the CIE color coordinates are represented in Figure 2.6 (c).

Color rendering index (CRI)

The CRI is the greatness that measures the capability of a bulb to reproduce the color of an object faithfully compared to a natural light source (sunlight). By way of explanation, the color of an object will be closer to the real color of it seen by sunlight at higher CRI values, Figure 2.7 (a).[25]

Figure 2.7 (a) Representation of the image projection by the human eye of an object illuminated by lighting sources with different CRI values. (b) Correlation between the R_i value and different colors set up by the Munsell code.

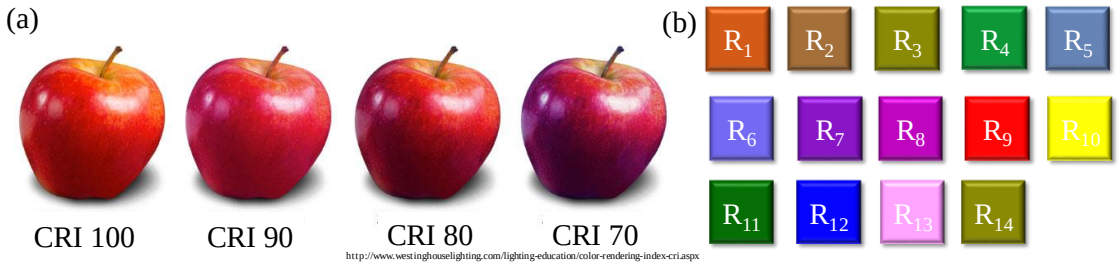

Source: Own authorship.

The CRI is calculated as an average value of R_1-R_9, being R_i calculated by Equation 2.11, to which R_i is the indication of CRI for each particular color, Figure 2.7 (b), and E_i is the color difference between those color samples and fourteen color reference set up by Munsell.[27]

$$R_i = 100 - 4.6\Delta E_i \quad (2.11)$$

Luminous flux (ϕ_V)

The luminous flux (ϕ_V) of a light source is the greatness that measures the perceived power of light by the human eye and its unity in the SI is lumen (lm). The human eye sensitivity as a function of the wavelength in the visible spectral range is shown in Figure 2.8, and it may be noticed that the human eye features the best perception in the green spectral region.[25]

Figure 2.8 Response of the human eye sensibility to light as a function of the wavelength.

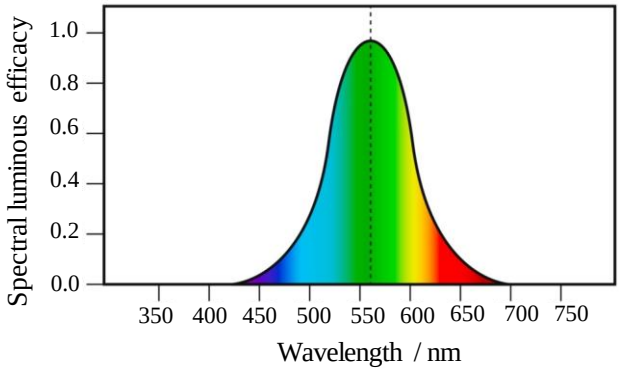

Source: Adapted from Pust *et al.*[25]

As the human eye features low sensibility in the red spectral range, it is important to get white light in WLEDs without red-emitting phosphors, since large amounts of phosphor are desirable to be distinguished by the human eye, leading to the decrease of the luminous flux because there are not many commercially-available high-efficient red-emitting phosphors. Moreover, the red-emitting phosphors tend to decrease the luminous flux of WLEDs due to the large Stokes shift, as previously represented in Equation 2.7.[25]

Luminous efficacy (LE)

The LE of a light source is a quantitative measurement of how efficient a light source produces radiation in the visible spectral range, being the ratio of the luminous flux (ϕ_V) divided to the electric power ($P_{electric}$), with unity in the SI of lm/W.

Wall-plug efficiency (WPE)

The WPE or radiant efficiency is the greatness that measures the energy efficiency of a light source. In other words, it quantifies how a light source converts electric power ($P_{electric}$) in optical power ($P_{optical}$), and the value is expressed as percentage (%).

External quantum efficiency (EQE)

The EQE of a light source is the ratio of the number of photons emitted from a light source to the number of electrons injected in the device. In other words, it is how efficiently a bulb converts electrons in photons. The EQE is calculated according to Equation 2.12, being $P_{optical}$ the optical power, E_{photon} the photon energy and I the input current.

$$EQE = \frac{P_{optical}}{E_{photon} x I} \quad (2.12)$$

2.2.3 Requirement of ideal phosphors for PC-WLEDs

There are several requirements that the ideal phosphor must simultaneously possess to optimize the PC-LED efficiency:[28]

1) Emission quantum yield and absorptivity as high as possible;
2) Emission spectrum that combined with the emission of the other components leads to a pure white emission with desirable color qualities;
3) An excitation spectrum that overlaps the LED chip emission;
4) Emission quantum yield and excitation and emission spectrum independent on the temperature;
5) Chemical and thermal stabilities;
6) Absence of emission saturation at high photon fluxes;
7) The radiative lifetime of the phosphor must be short enough to avoid saturation effects due to depletion of the ground state and excited state interactions;
8) Low-cost and non-toxic;
9) The particle size is required to be as uniform as possible, and the distribution as narrow as possible

The main phosphors applied in WLEDs are based on Eu^{2+}, Mn^{2+}, Mn^{4+} and/or Ce^{3+} activators, because of their emissions are based on *f-d* transitions allowed by Laporte's rule, being possible to achieve emission quantum yield values as high as 90 %. In Table 2.2, it is pointed out the state-of-the-art of phosphors for PC-WLED applications.

Table 2.2 State-of-the-art of phosphors applied in PC-WLEDs, representing excitation range, emission maximum, emission quantum yield (*q*) and luminescence thermal quenching at 150 ºC compared to 25 ºC.

Phosphor	Excitation / nm	Emission / nm	*q*	Thermal quenching / %
$BaMgAl_{10}O_{17}:Eu^{2+}$	300 - 400	450	0.9	5
$Ba_2SiO_4:Eu^{2+}$	300 - 400	508	0.6	23
$Lu_3Al_5O_{12}:Ce^{3+}$	460	540	0.8	3
$(Y_{2.93}Ce_{0.07})Al_5O_{12}:Ce^{3+}$	460	570	> 0.9	6
$(Sr,Ba)SiO_4:Eu^{2+}$	300 - 400	570	0.6	51
$Rb_2GeF_6:Mn^{4+}$	460	630	0.6	5
$(Sr,Ba)_2Si_5N_8:Eu^{2+}$	400 - 500	632	0.8	12
$Ba_2Si_5N_8:Eu^{2+}$	400 - 500	570	0.8	10
$K_2TiF_6:Mn^{4+}$	460	630	> 0.9	0

Source: Reproduced from Smet, Parmentier and Poelman.[28]

Although all phosphors shown in Table 2.2 display high emission quantum yield, some problems as thermally-quenched luminescence at relatively high temperatures (150 ºC), reabsorption of the emission by the phosphor mix, broad emission band, especially in the red-near-IV spectral region, price, and hard synthesis condition still need to be addressed.[28]

To overcome those issues, attention has been currently paid for the use of dyes, complexes or quantum dots as coatings of near-UV or blue-emitting LEDs. In the case of dyes and organic complexes, the broad absorption band in the near-UV and blue spectral range and high emission quantum yield are the main advantages, and for the quantum dots, sharp emission bands (FWHM < 50 nm) that may be tuned from the blue toward the red spectral region by changing the particle size. However, the main limitation for their application is the low thermal stability, that decreases the LED lifespan, and for quantum dots, they are not environmentally-friendly.[29,30] Therefore, phosphors stand out since they are thermally-stable and do not have a large amount of toxic metals in their composition.

2.2.4 Light and Circadian rhythm control

As Earth rotates on its axis, there is a regular 24-hour pattern of darkness and daylight almost in all its surface. Following this pattern, living beings have adapted to this regular movement by evolving the biological rhythms, repeating it at approximately 24-hour intervals, Figure 2.9.[31]

Figure 2.9 Human circadian clock.

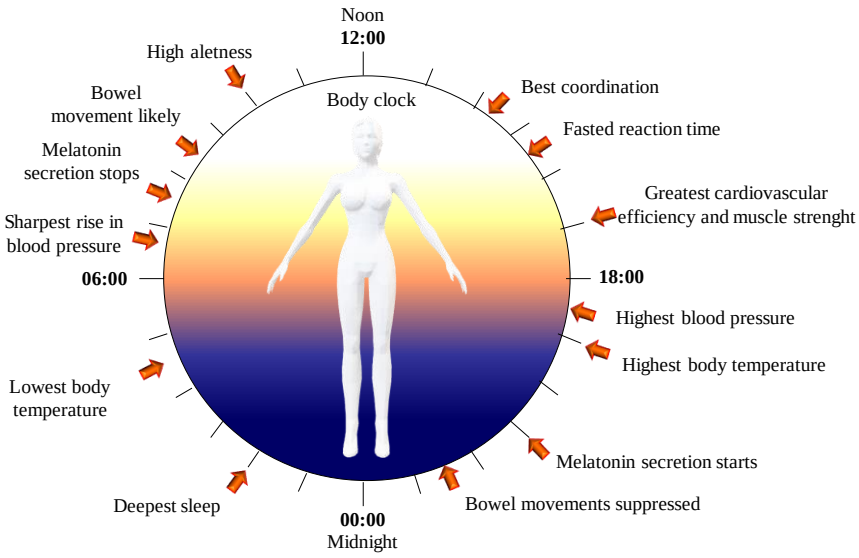

Source: Adapted from Figureiredo.[31]

These rhythms are known as Circadian rhythms and it governs several biological cycles as hormone production, cell division, and behavior according to the natural dark/light cycle, enabling organisms to entrain these cycles to their photic niche, and to the location on Earth.[31]

There are several external influences that regulate the living being's Circadian rhythm, and three of them must be highlighted: (1) temperature, (2) sound and (3) light. In this study, we are focused on the light impacts on the human and plant Circadian rhythm regulation. In the human case, illumination enables humans to see objects via their primary optical track and by the retinohypothalamic track, that has the primary role of supporting the light regulation of human circadian rhythm, neurobehavioural and neuroendocrine responses.[32]

At the front end of the retinohypothalamic track, there is a population of ipRGCs (intrinsically photosensitive retinal ganglion cells) that are responsive to light via the photopigment known as melanopsin that project images through the retinohypothalamic tract to the paired hypothalamic suprachiasmatic nuclei. The suprachiasmatic nuclei are the main oscillators in the circadian rhythm, transmitting information on lighting and circadian clock to several loci in the nervous system. Finally, the systems of sleep- and arousal-promoting neurons in the central nervous system are synchronized to the daily rhythms of sleep, body temperature, as well as alertness, and psychomotor performance.[32]

Plants respond to light in more vast ways than in humans, utilizing more than a dozen of photoreceptors. As plants live in communities, they also respond to the light reflected by neighboring plants, being the light that reaches lower leaves filtered by the upper ones. Thus, plants use light both as energy for photosynthesis and as a signal that directly controls the plant shape, leaf color, leaf expansion as well as radiation capture.[32]

Recently, many medical-related studies have reported that the spectral features of light emitted by white-emitting source impacts human circadian physiology, alertness, and cognitive performance levels.[33] For instance, bluish-white light is desirable during the day since it follows the same profile of daylight CCT, as previously reported in Figure 2.6. However, blue light enhances the concentration of melanopsin, responsible for alertness, attention, and emotional processes, thus, it must be avoided at night, when the melanopsin concentration must go down.

On the other hand, yellowish-white light is desirable at night, to avoid the melanopsin production. Consequently, exposure to cool white light late from bulbs, cellphones and computers in the evening and at night is detrimental to Human health,

leading to diseases as depression, diabetes, obesity and sleep disorder.[33] Table 2.3 points out the main impacts of cool or warm white light in human health and some ideal application surroundings of WLEDs according to the CCT.

Table 2.3 Human circadian rhythm dependence on the white-LED CCT values and application in phototherapy and lighting.

CCT / K	Circadian rhythm control	Applications in phototherapy	Disadvantages	Indoor and outdoor lighting
2,700 – 4,000 (warm)	It induces melatonin production, (the human circadian system photopigment), important at bedtime[34]	Rhinitis treatment, wound healing and anti-inflammatory, jet leg[35]	Induces depression and anxiety-like behaviors. [31]	Dining areas, hotel lobbies, bedroom. restaurants, general retail
4,500 – 6,500 (Cool)	The most effective in suppressing melatonin. It activates melanopsin, responsible for alertness, attention, and emotional processes. Desirable during the day but not at night.[36]	It reduces symptoms of seasonal affective disorder (SAD), non-seasonal depression and bipolar disorder therapies [36]	Insomnia, disease, metabolic syndromes: diabetes, obesity and gastrointestinal disorders.[36]	Classrooms, hospitals, office space, jewelry display, parking garages, security lighting

Source: Own authorship.

Although light may have detrimental impacts on human health, it may be also used as phototherapy since correct light amounts regulate melanopsin production, being useful to treat diseases and disturbances as problems related to shift work, intercontinental jet travel, space flight, depression, seasonal affective disorder, bipolar disorder therapies, rhinitis, wound healing, etc, as represented in Table 2.4, next page.

In the past, the color emission of white-emitting sources was limited by the color of incandescent and fluorescent bulbs. However, with the WLED advent, it is possible to tune it from cool toward warm white, fitting the ideal bulb to the ambient necessity. Thus far, WLEDs have been optimized by characterizing some figures of merit as CCT, CRI and LE for good color quality and high vision performance. The benefits of WLEDs lie not only on the energy saves but on improving human health and productivity, including a potential decrease in some forms of cancer and other clinical disorders.[32]

It is worth pointing out that LEDs are also useful for plant development and food technology since monochromatic LEDs enhance the biomass production rate, photosynthesis, and control morphology, as reported in Table 2.4. Therefore, the tangible benefit of LEDs applied to food technology and plant production lies on the production of indoor farms that health-promote fresh food, an alternative to supply the world food demand, becoming more accessible in all regions of the world in all months of the year.[32]

Table 2.4 LED emission features for human and plant circadian rhythm control.

LED emission spectral range	Human circadian rhythm control	Application for human healthy	Plant circadian rhythm control	Application for plant and food technology
Red (630 nm)	It induces melatonin production, human circadian system photopigment, important at bedtime[37]	Rhinitis treatment, wound healing and anti-inflammatory[38]	It efficiently drives photosynthesis and photomorphogene-sis[39]	Algae growth, microalgae cultivation, plant tissue culture[34]
Green (550 nm)	It is the second most effective in suppressing melatonin, helpful to reset body clock[40]	Correct hyperpigmenta-tion, eliminate skin spots[40]	Photosynthesis (less than blue and red colors) [39]	Algae growth, bacteria and microalgae cultivation[34]
Blue (480 nm)	The most effective in suppressing melatonin. It activates melanopsin, responsible for alertness, attention, and emotional processes. Desirable during the day but not at night.[36]	Seasonal Affective Disorder (SAD), non-seasonal depression and bipolar disorder therapies [36]	It improves growth (dry mass gain) and minimize excessively elongated stems[39]	Algae growth, astaxanthin production [34]
UV (250 nm)	It is not well-understood, since just 2% of UV radiation survives after filtration through the eye lens.[41]	Disinfection, water treatment[34]	Carotenoids and polyamines induction, damage to photosynthetic apparatus[42]	Disinfection, water treatment and purification[34]

Source: Own authorship.

2.3 Rare-earth ions

2.3.1 Spectroscopic properties

The rare-earths are the set of 17 elements of the periodic table including the 15 lanthanides, scandium and yttrium.[43] One of their most alluring property is that, with exception of Sc, Y, La and Lu, the others have an incomplete 4*f* shell that is shielded from the outer environment by the most external shells, making that they experience lower influence of the ligand field. In this context, this fact causes that the *f-f* transitions are barely affected by the environment. Due to the weak absorptivity of the RE^{3+}, the absorption by the ion is compromised, thus, energy transfer from the matrix to the activator is almost the main process for the emission.[44]

In addition to transitions within the 4*f* configuration, 4*f*-5*d* transitions may also be noticed in some rare-earth ions such as Eu^{2+}, Ce^{3+}, Yb^{2+}, Sm^{2+} or Tm^{2+}, generating broader emission bands than that of the *f-f* transitions, but they suffer higher influence of the crystalline field. Depending on the characteristics of the chemical environment (crystalline or amorphous) and the temperature, *f-f* transitions feature full-width at half maximum (FWHM) lying within the 10 - 100 cm^{-1} range while 4*f*-5*d* transitions have FWHM close to 1,000 cm^{-1}.[45] The 4*f*-5*d* transitions are further described in section 2.3.3.

In the case of the photoluminescence phenomena, the emission of the RE ions comes from the absorption of photons. The light absorption by an electron moving around a nucleus occurs due to operators linked to the nature of the light: the odd-parity electric dipole (ED) operator, the even-parity magnetic dipole (MD) and the electric quadrupole (EQ) operator. Not all the electronic transitions are allowed, and they follow some selection rules. The first one is the so-called Laporte's rule (or parity rule) and it requires that for ED transitions, the angular moment sum of electrons in the initial and final states must change by an odd integer.

The other selection rules according to the S (total spin quantum number), J (total angular quantum number) and L (total orbital angular momentum quantum number) are pointed out according to the operator nature in Table 2.5.[44]

Table 2.5 Selection rules for *f–f* transitions between two spectroscopic levels.

Operator	Parity	ΔS	ΔL	ΔJ [a]
Forced ED	Opposite	0	≤ 6	≤ 6 (2, 4, 6 if J or J' = 0)
EM	Same	0, ±1	0, ±1	0, ±1
EQ	Same	0	0, ±1, ±2	0, ±1, ±2

[a] J = 0 to J' = 0 transitions are always forbidden.

Source: Adapted from Eliseeva and Bunzli.[44]

The *f-f* transitions are usually dominated by the electric dipole mechanism and the dynamic coupling, followed by the magnetic dipole that is relevant just for a few numbers of transitions and finally by the vibrionic mechanism, that normally is quite irrelevant. These last two mechanisms are important in the cases that the surrounding around the RE ion have inversion center. In this situation, there is no contribution of electric dipole and dynamic coupling mechanisms.[44]

The vibrionic mechanism is the coupling between two vibrational states, to which a molecular vibration temporarily changes the geometrical arrangement around the RE ion, in other words, its symmetry. In the dynamic coupling model, the dipoles are induced by the charge distribution caused by the radiation. The *f* electrons polarize the ligands around the RE ion, perturbating their wavefunction. Thus, the induced dipoles combine themselves to a dipole moment that did not disappear, interacting with the radiation field.[46]

The intensity of *f-f* transitions are explained by the Judd-Ofelt theory.[47] In this model, the forbidden electric-dipole transitions gain intensity by the first order mixing of the opposite-parity metal-ion configurations into the $4f^N$ configuration.[48] The radiative

transition probability of an emitting state in a RE^{3+} may be determined by using the Einstein's rates of spontaneous emission (*A*) from an initial |ψ> state with a quantum number *J* to a final |ψ'> state with a quantum number *J*' by aplying Equation 2.13, where $\bar{\nu}$ is the mean energy of the transition, *h* is the Planck's constant, *n* is the refractive index; D_{ED} is given by Equation 2.14 and D_{MD} by Equation 2.15, in which $\left\langle f^N \psi J \middle| U^{(\lambda)} \middle| f^N \psi' J' \right\rangle^2$ are reduced matrix elements of the tensor operator $U^{(\lambda)}$, m_e is the mass of the electron, *e* is the electron charge, h is the Plank's constant, and *c* the velocity of light in vacuo.

$$A(\Psi_J, \Psi'_J) = K^{rad} = \frac{1}{\tau^{rad}} = \frac{64\pi^4 \nu^3}{3h(2J+1)}\left[\frac{n(n^2+2)^2}{9} D_{ED} + \eta^3 D_{MD}\right] \quad (2.13)$$

$$D_{ED} = e^2 \sum_{\lambda=2,4,6} \Omega_\lambda \left|\langle \Psi \| U^\lambda \| \Psi' \rangle\right| \quad (2.14), \qquad D_{MD} = \left(\frac{eh}{4\pi m_c c}\right)^2 |\langle \Psi \| L + 2S \| \Psi' \rangle|^2 \quad (2.15)$$

The theory of the 4*f*–4*f* intensities also gives the integrated coefficient (A) of spontaneous radiative emission of a transition between two states and from that, it is possible to get the intensity parameters (Ω_2, Ω_4 and Ω_6), also known as Judd-Ofelt Parameters.[47] The Ω_λ experimental intensity parameters for *J*-*J*' transitions represent the contributions from the dynamic coupling and forced electric dipole mechanisms.[49] Some results in the literature previously shown that Ω_2 is more sensitive to angular changes of the RE^{3+}-ligand bonds while Ω_4 and Ω_6 are better probes for the covalency degree in the RE^{3+}-ligand bounds.[50]

2.3.2 Eu^{3+} ion

The electronic configuration of Eu^{3+} is [Xe]$4f^6$, and the six electrons in the seven 4*f* orbitals may combine in 3,003 microstates.[51,52] The $4f^6$ configuration degeneracy is affected by several perturbations as electronic repulsion, spin-orbital coupling, crystalline field effect, and Zeeman effect.[53]

The electronic repulsion comes from the electrostatic interactions between the electrons in the 4*f* shell. Already the spin-orbital coupling is a result of interactions between the spin-magnetic moment of the 4*f* electrons and the magnetic field that arises from the electronic movement around the nucleus. On the other hand, the crystalline field effect is caused by interactions between the 4*f* electrons and the ligand electrons and it destroys the spherical symmetry of the free ion. Finally, the Zeeman effect is the split of the 4*f* levels due to the interaction with the external magnetic field. The representations of those effects in the $4f^6$ configuration of Eu^{3+} are highlighted in Figure 2.10.[53]

Figure 2.10 Partial energy diagram of Eu^{3+} $4f^6$ configuration representing the interelectronic repulsion (terms), spin–orbital coupling (levels) and crystal-field effects (sublevels).

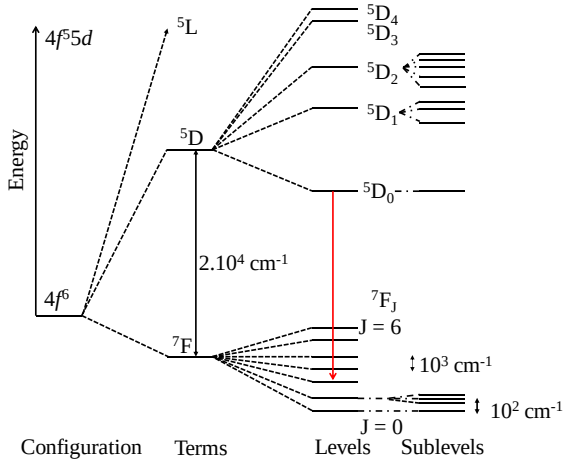

Source: Adapted from Binnemans.[53]

After the introduction of all the effects of electronic repulsion, the [Xe]$4f^6$ configuration is characterized by 295 $^{2S+1}L_J$ spectroscopic terms (Russell-Saunders term). The possible values for J are L+S, L+S–1, L+S–2, …, [L-S] and the maximum degeneracy of each term is 2J+1 (J split rule).[54]

The main Eu^{3+} transitions noticed in the emission spectrum, namely $^5D_0 \rightarrow {}^7F_{0,2,4}$, occur by an induced electric dipole oscillator. These transitions are forbidden by Laport's selection rule; yet, they are relaxed in the cases that Eu^{3+} is inserted in a local site without inversion center since the transitions are partially allowed by vibrionic coupling or 4*f* wavelength mix by the crystalline field effect. This occurs because the distortion of the spherical symmetry around the free ion leads to a mix of electronic configurations with opposite parities.

The $^5D_0 \rightarrow {}^7F_0$ transition occurs by an electric dipole mechanism and it is forbidden according to the selection rules. The explanation to why this transition is observed is the mix of J or mix of charge-transfer states with high energy in the $4f^6$ configuration wavefunctions. In this case, the wavefunction of the $^7F_0$ state contains contributions from states with J = 2, 4 and 6, relaxing the selection rules.[55]

Already the $^5D_0 \rightarrow {}^7F_1$ magnetic dipole transition, allowed by Laporte's selection rule, features intensity usually weaker than transitions that occur by the induced electric dipole mechanism. Yet, the radiative decay probability of the $^5D_0 \rightarrow {}^7F_1$ transition is normally taken as constant, being used to calibrate the intensity of the other transitions in the emission spectrum.[56]

Among the RE^{3+}, Eu^{3+} is a special case in what concerns its use as structural probe since the main emitting state ($^5D_0$) has J = 0, enabling to count the number of $^5D_0 \rightarrow {}^7F_J$ transition components to determine different Eu^{3+} local sites in a system according to the J split rule (2J+1). For example, as only one component for each Eu^{3+} non-equivalent local site is expected according to the J split rule, the number of $^5D_0 \rightarrow {}^7F_0$ transition components indicates the number of Eu^{3+} local sites without inversion center in a system (C_{nv}, C_n or C_s point group).[57]

2.3.3 Eu^{2+} ion

Eu^{2+} has [Xe]4*f*^{7} electronic configuration and its main electronic transitions arise from *f-d* interactions. For Eu^{3+}, the states coming from the 4*f*^{6} configuration are almost isolated and the next excited configuration 4*f*^{5}5*d* lies in the range of energies between 50,000 cm^{-1} and 100,000 cm^{-1} above the 4*f*^{6} state. On the other hand, for Eu^{2+}, the energy gap between the 4*f*^{7} and 4*f*^{6}5*d* configurations is shorter and transitions between them may be observed. As the parity of the initial and final states changes, the transitions are allowed by Laporte's rule, being 10^6 times stronger than the 4*f*-4*f* transitions.[58]

The electronic transitions in Eu^{2+} are notably different from those in Eu^{3+}, being mainly composed of two types of processes: weak 4*f*-4*f* transitions at lower energy and strong 4*f*-5*d* transitions at higher energies. The Eu^{2+} absorption spectrum is usually constituted by two broadbands situated in the UV spectral range and the sensitivity of those bands to the crystal structure confirms that they arise from electronic transitions from the ground state to the 4*f*^{6}5*d* configuration.[59]

Already the emission spectrum of Eu^{2+} consists of only one broadband whose peak maximum depends on the host crystal nature, and it may be tuned from the near-UV toward the red spectral region.[59]

Figure 2.11 represents a partial energy diagram of Eu^{2+} in a crystalline matrix. In the ground state of Eu^{2+}, there are seven 4*f* electrons that give rise to the $^8S_{7/2}$ spectroscopic term. The lowest excited states are formed by $^6P_{7/2}$ and $^6P_{5/2}$ states with 4*f*^{6} configuration or from states with 4*f*^{6}5*d* configuration. In the last case, there are 6 4*f* electrons that give rise to seven labels ($^7F_0 - {}^7F_6$) with energy close to Eu^{3+}. On the other side, the 5*d* electron in the 4*f*^{6}5*d* configuration gives rise in a cubic configuration to two E_g ($d_{x^2-y^2}$ and d_{Z^2}) and three T_{2g} (d_{xy}, d_{xz}, d_{yz}) levels, ignoring the interactions with the 4*f* electrons. The energetic separation between them is well-known as 10Dq. However, if

interactions between $4f^6$ and $5d$ electrons are strong enough, the states are mixed and many transitions in the excitation spectrum are noticed. In the opposite way, the $4f^6 5d$ configuration retains much of the nature of the uncoupled $4f^6$ and $5d$ levels.[59] This type of absorption is pointed out in Figure 2.11 (a).

Figure 2.11 (a) Schematic energy level diagram of Eu^{2+} into a crystalline solid. (b) Representation of crystalline field effect acting on the $4f^6 5d$ energy level of Eu^{2+}.

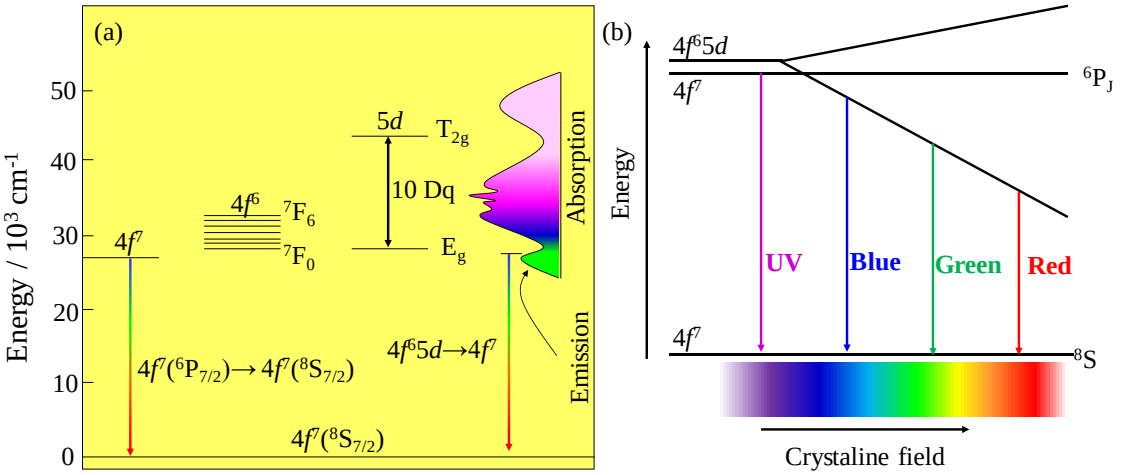

Source: Adapted from Rubio et al.[59] and Blasse and Grabmaier.[60]

The energy position of E_g and T_{2g} levels depends on the CN of the Eu^{2+} local site as well as the point group. For CN = 8 or 12 in a O_h point group, the T_{2g} level is situated at lower energy compared to the T_{2g}, while for CN 6, the situation is the opposite. The 10Dq may be evaluated by Equation 2.16, in which Z is the charge of the anion, e is the electron charge, r is the d wavefunction radius and R is the distance among Eu^{2+} and the ligand.[61] Therefore, as R increases, 10Dq decreases.

$$Dq = \frac{Ze^2r^4}{6R^5} \quad (Equation\ 2.16)$$

In the case of low interaction between $4f^6$ and $5d$ electrons, seven narrow bands that evidence the character of the $4f^6$ levels have been observed in the absorption spectrum, for instance for Eu^{2+} in CaF_2, EuF_2, EuO, and EuSe. If the Stokes shift is short enough, zero-phonon lines (ZPLs) and some sharp phonon-related bands might also be observable in the emission spectrum. This is only possible if the crystal field acting at the Eu^{2+} local sites is weak and the center of gravity of the crystal field split into the $4f^6 5d$ configuration levels are situated at higher energy than the ^6P_J excited states, as pointing out in Figure 2.11 (b), also representing the emission color dependence on the crystal field.[59]

Van Uitert brought up a theory used to determine the emission band energy of Eu^{2+} by using Equation 2.17,[62] being Q the energy of the lower d-band of Eu^{2+} in vacuum (34,000 cm^{-1}), V is the valence of the ion (2), $\Phi = (nE_ar)/80$, n is the CN of the ion, E_a is the electron affinity of the ligand atoms (2.2 eV for the SiO_4^{4-} ligands) and r is the ionic radius of Eu^{2+}.[63] There are also other parameters that influence the Eu^{2+} energy levels as oxidation state of the crystal, arrangement of the ligands around the crystal, nature of the ligands as well as Eu^{2+} concentration. Yet, from Equation 2.17, it is feasible to conclude that as the energy of the emission band is proportional to the CN of Eu^{2+}.

$$E = Q\left[1 - (V/4)^{1/V}.10^{-\Phi}\right] \quad (2.17)$$

2.3.4 Tb^{3+} ion

Tb^{3+} has [Xe]$4f^8$ electronic configuration, with energy levels like those ones of Eu^{3+}, but inverted, Figure 2.12. Tb^{3+} features electronic transitions with energy in the visible spectral range that arise from the $^5D_4$ emitting state to the ^7F_J states (J = 0 – 6) and the $^5D_4 \rightarrow {}^7F_5$ transition is usually the most intense one, lying within the green spectral region.[64]

Figure 2.12 Partial energy diagram of Tb^{3+}. CR is the cross-relaxation process between two Tb^{3+} neighbors.

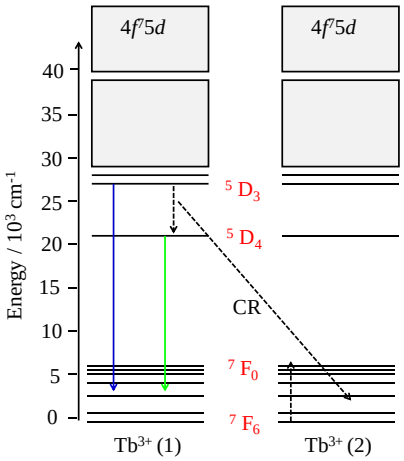

Source: Adapted from Hao *et al.*[65]

Tb^{3+} may also display electronic transitions from the $^5D_3$ excited state in the near-UV and blue spectral range, Figure 2.12. Usually, the Tb^{3+} blue emission is noticed for matrices with low phonon frequency (<1,000 cm^{-1}) and low Tb^{3+} concentration due to an energy transfer ($^5D_3 \rightarrow {}^5D_4$) by a cross-relaxation (CR) mechanism between Tb^{3+} neighbors that are favored at low Tb-Tb distances (high doping concentrations) and quenches the emission from the $^5D_3$ level, Figure 2.12.[65] The CR process is also favored

because the $^5D_3$-$^5D_4$ and $^7F_0$-$^7F_6$ levels are close enough in energy to allow resonance between them.[65]

2.4 Silicate-based phosphors

Orthosilicates are silicon oxides that are constituted by $[SiO_4]^{4-}$ tetrahedral oxyanions in which each Si-O bond have a strong covalent contribution. The silicates are usually classified as non-ionic compounds since there is a significant covalence degree in the interatomic Si-O bonds, being strong and directional. Yet, there is a negative charge on the $[SiO_4]^{4-}$ tetrahedra, being responsible to give an ionic character to this structure.[66]

Ba_2SiO_4 has orthorhombic crystalline structure and P_{nam} space group, Figure 2.13. In this structure, Ba^{2+} occupies two local sites, one with CN 9 and other with CN 10. The 10-coordinated site forms chains along the *c*-axis in the Ba_2SiO_4 lattice with one side of Si^{4+} and the other side of barium sites. The other site with CN 9 forms chains along the *b*-axis.[67]

Figure 2.13 (a) Ba_2SiO_4 unit cell representation. (b) Representation of the Ba_9, Ba_{10} and SiO_4 polyhedra. (The Ba_9 and Ba_{10} are the notation of sites with CN 9 and 10, respectively).

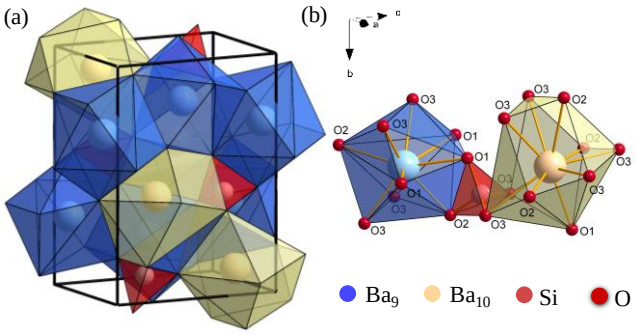

Source: Own authorship.

Conversely, Sr_2SiO_4 may coexist in two different phases at 300 K. The first one is the orthorhombic α'-form that crystallizes in the P_{mnb} space group, while the second one is the monoclinic β-form, with $P12_1/n_1$ space group.[68] Orthorhombic α-Sr_2SiO_4 phase is isostructural to Ba_2SiO_4, Figure 2.14 (a).[67] Already in the monoclinic β-Sr_2SiO_4 phase, Sr also occupies two sites with CN 9 and 10, Figure 2.14 (b), but the $[SiO_4]^{4-}$ tetrahedron is bigger compared to the α-phase and the Sr-O bond lengths are scattered over wide range values, but their average Sr-O bond lengths are almost the same to the α-phase.[69] The Sr_{10} site is underbonded in the α-phase with respect to the β one, leading to a lower bond-valence contribution of the oxygen atoms in the surroundings of the Sr_{10} site.[69]

Figure 2.14 (a) α and (b) β-Sr_2SiO_4 unit cell representations and SrO_9, SrO_{10} and SiO_4 polyhedra.

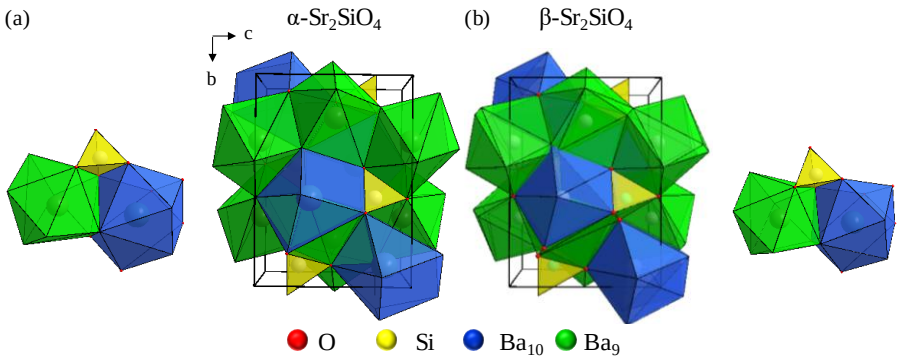

Source: Own authorship.

It must be recalled that all papers found before we have started this study (2015) report only the solid-state synthesis of the Tb^{3+} or Eu^{3+}-doped Ba_2SiO_4 phosphor without any mention of the sol-gel synthesis, as highlighted in Table 2.6. However, in the case of Eu^{2+}-doped Ba_2SiO_4 or Sr_2SiO_4, some papers are found where the sol-gel synthesis is used, Table 2.6, but applying high annealing temperatures, that is a disadvantage considering energy saves.

Table 2.6 Main Ba_2SiO_4 and Sr_2SiO_4-based phosphor synthesis. $T_{calc.}$ is the calcination temperature.

Material	Synthesis	$T_{calc.}$ / ºC	Calcination atmosphere	[ref]
$Ba_2SiO_4:Eu^{2+}$	Solid-state	1,300	5 % H_2 and 95 % N_2	70
$Ba_2SiO_4:Eu^{2+}$	Sol-gel	1,100	5 % H_2 and 95 % N_2	67
$Ba_2SiO_4:Eu^{2+}$	Sol-gel and microwave	1,200	CO	71
$Ba_2SiO_4:Eu^{2+}$	Co-precipitation	1,150	5 % H_2 and 95 % N_2	72
$Ba_2SiO_4:Eu^{2+}$	Hydrothermal	900	5 % H_2 and 95 % N_2	73
$Ba_2SiO_4:Eu^{3+}$	Solid-state	1,300	Air	74
$Ba_2SiO_4:Tb^{3+}$	Solid-state	1,450	CO	75
$Sr_2SiO_4:Eu^{2+}$	Sol-gel	900	H_2 and N_2	76
$Sr_2SiO_4:Eu^{2+}$	Solid-state	1,300	5 % H_2 and 95 % N_2	77
$Sr_2SiO_4:Eu^{2+}$	Sol-gel	1,300	5 % H_2 and 95 % N_2	78
$Ba_2SiO_4:Eu^{3+},Tb^{3+}$	*	*	*	*

* No study so far was found.

Source: Own authorship.

In this regard, for the synthesis of the phosphors, the sol-gel route was chosen due to the relatively low synthesis temperature of the gel (70 ºC), relatively low precursor annealing temperature (1,100 ºC), particle shape control, and the possibility of getting materials with improved optical properties.[79]

The chemistry of this process is based on inorganic polymerization reactions. First, a solution with the molecular precursor (sol) is converted by hydrolyzes and condensation reactions in a gel, that after drying, results in a solid material with an amorphous tridimensional network (xerogel).[80] The precursors are usually aqueous

solutions with inorganic salts or alkoxides such as Tetraethyl orthosilicate (TEOS) dissolved in organic solvents.[81] The hydrolysis and condensation reactions of the precursor used in this study (TEOS) are shown as following in Equations 2.18 and 2.19:

1) Alkoxide hydrolysis getting silanol (Si-OH) groups:

$$Si - OR + H_2O \rightarrow \equiv Si - OH + ROH \quad (2.18)$$

2) Condensation between toe Si-OH groups, leading to water formation:

$$\equiv Si - OH + HO - Si \equiv \rightarrow \equiv Si - O - Si \equiv + H - OH \quad (2.19)$$

2.5 On the polymeric matrices applied in this study.

As previously mentioned in section 2.2.1, in this study, we have applied the strategy of fabricating films by dispersing the phosphor in polymeric matrices. For that, poly(methyl methacrylate) (PMMA) and Polyvinylidene fluoride (PVDF) were chosen, Figure 2.15. The justifications behind their selection lie on the low-cost, waveguide property, relatively high thermal stability (200 ºC), and transparence to near-UV radiation.[21,22,23]

Figure 2.15 Structure of (a) PVDF and (b) PMMA polymers.

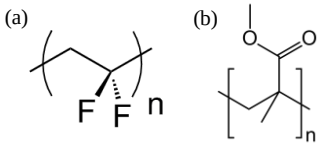

Source: Own authorship.

PVDF is a semicrystalline polymer and it may crystallize in 4 well-known phases: α (type II), β (type I), γ (type III) and δ (type IV).[82] In the α phase, chains adopt a trans-cis conformational structure (TCTC), and the fluorine atoms are as far as possible, thus, this is the most thermodynamically stable arrangement. On the other hand, in the β phase, PVDF chains have a zig-zag structure and the fluorine atoms are on the same side of the chain. Already in the γ phase, to every three trans conformation, there is a cis conformation (T3C – T3C). Finally, in the δ phase, the chains have the α phase conformation, but with different packing.[83]

PMMA, on the other hand, is one of the amorphous polymers that belongs to the acrylate family. PMMA is among the polymers that have high resistance to sunshine exposure because it has low structural variation under the effect of UV-radiation.[21]

Aiming to improve the polymer properties as processing and flexibility, we have chosen Buriti oil (BO), a Brazilian natural oil, as a plasticizer. The rationales on its

selection lie on the low cost, environmentally-friendly properties, and easy processing.[84] BO is an Amazonia oil featuring orange-reddish color, being composed by fatty acids, tocopherols, and carotenes.[85]

2.6 References

[1] KIRA, M. Semiconductor Quantum Optics, 2011, Cambridge University Press.

[2] XUA, H. et al. Electroluminescence from Europium(III) complexes, Coordination Chemistry Reviews, 2015, v. 293–294, n. 15, p. 228–249.

[3] KALT, HEINZ, HETTERICH, MICHAE, Optics of Semiconductors and Their Nanostructures, 2004, Springer Series in Solid-State Sciences.

[4] MAESTRO, P., DOUGIER, P. Les Terres rares dans les applications de la luminescence, 1982, L'actualité chimique - Juin - Juillet, p. 15-26.

[5]SINGH, V. Combustion synthesized $MgAl_2O_4$:Cr phosphors — an EPR and optical study, Journal of Luminescence, 2009, v. 129, n. 2, p. 130–134.

[6] CROSBY, G. A.; WHAN, R. E.; ALIRE, R. M. Intramolecular energy transfer in rare earth chelates. Role of the triplet state. The Journal of Chemical Physics, 1961, v. 34, n. 3, p. 743-748.

[7] MALTA, O. L. et al. Theoretical Intensities of 4f-4f Transitions Between Stark Levels of the Eu^{3+} Ion in Crystal, Journal of Physics and Chemistry of Solids, 1991, v. 52, n. 6, p. 777-778.

[8] VALEU, B. Molecular Fluorescence Principles and Applications, 2001 Wiley-VCH Verlag GmbH

[9] SOUZA, E.R., SIGOLI, F.A. Princípios fundamentais e modelos de transferência de energia inter e intramolecular, Química Nova, 2012, v. 35, n. 9, p. 1841-1847.

[10] FÖRSTER, T.; Zwischenmolekulare Energiewanderung und Fluoreszenz, Annalen der physic, 1948, v. 2, n. 1-2, p. 55-75.

[11] YE, S. et al. Phosphors in phosphor-converted white light-emitting diodes: Recent advances in materials, techniques and properties, Materials Science and Engineering R, 2010, v. 71, n. 1, p 1–34.

[12] NETO, A. N. C, MOURA JR, R. T.; MALTA, O. L.; On the mechanisms of non-radiative energy transfer between lanthanide ions: centrosymmetric systems, Journal of Luminescence, 2019, v. 210, n. 0, p. 342–347.

[13] VAN UITER, L.G. Characterization of Energy Transfer Interactions between Rare Earth Ions, Journal of The Electrochemical Society, 1967, v.14, n. 10, p. 1048-1053.

[14] TANNER, P. A. et al. Misconceptions in electronic energy transfer: bridging the gap between chemistry and physics, Chemical Society Reviews, 2018, v. 47, n. 0, p. 5234-5265.

[15] SCHUBERT, E. F.; KIM, J. K. Solid-state light sources getting smart, Science, 2005, v. 308, n. 5726, p. 1274−11278.

[16] G. HELD, ―Introduction to Light Emitting Diode Technology and Applications, 2008, Taylor & Francis Ltd, Hoboken.

[17] PATTISON, P. M.; HANSEN, M.; TSAO, J. Y. LED lighting efficacy: Status and directions, Comptes Rendus Physique, 2018, v. 19, n. 3, p. 134-145.

[18] MATAFONOVA, G.; BATOEV, V. Recent advances in application of UV light-emitting diodes for degrading organic pollutants in water through advanced oxidation processes: A review, Water Research, 2018, v. 132, n. 1, p. 177-189.

[19] LIU, Y. et al. Effect of phosphor composition and packaging structure of flexible phosphor films on performance of white LEDs, Journal of Materials Science: Materials in Electronics, 2018, v. 29, n. 5, p. 18476–18485.

[20] JIA, J. et al. Preparation and properties of theflexible remote phosphorfilm for bluechip-based white LED, Materials and Design, 2016. v. 102, n. 0, p. 8–13.

[21] ALI, U. et al. A Review of the Properties and Applications of Poly(Methyl Methacrylate) (PMMA), Polymer Reviews, 2015, v. 55, n. 4, p. 678–705.

[22] ZHOU, F. et al. Transparent and luminescent ionogels composed of Eu^{3+} coordinated ionic liquids and poly(methyl methacrylate), Luminescence, 2015, v. 30, n. 8, p. 1303–1307.

[23] ZETTL, M. et al. Investigation of Host Polymers for Luminescent Solar Concentrators, 2017, v. 5, n. 7, p. 1037-1044.

[24] RACK, P.D., et al., Materials used in electroluminescent Displays. Materials Research Bulletin, 1996, v. 21, n. 3, p. 49.

[25] PUST, P.; SCHMIDT, P. J., SCHNICK, W. A revolution in lighting, Nature materials, 2015, v. 14, n. 0, p. 454-458.

[26] MCCAMY, C. S. Correlated color temperature as an explicit function of chromaticity coordinates, Color Research & Application, 1992, v. 17, n. 2, p. 142-144.

[27] MUNSELL, A. H. Atlas of the Munsell Color System‖, 1915, Wadsorth -Howland & Company, Malden.

[28] SMET, P. F.; PARMENTIER, A. B.; POELMAN, D. Selecting Conversion Phosphors for White Light-Emitting Diodes, Journal of The Electrochemical Society, 2011, v. 158, n. 6, p. R37-R54.

[29] LI, L. et al. A facile method to prepare polymer functionalized carbon dots inspired by the mussel chemistry for LED application, Dyes and Pigments, 2019, v. 162, n. 0, p. 845–854.

[30] PIDLUZHNA, A. Et al. Multi-channel electroluminescence of CdTe/CdS core-shell quantum dots implemented into a QLED device, Dyes and Pigments, 2019, v. 162, n. 0, p. 647–653.

[31] FIGUEIRO, M. G. An Overview of the Effects of Light on Human Circadian Rhythms: Implications for New Light Sources and Lighting Systems Design, Journal of Light & Visual Environment, 2013, v. 37, n. 2-3, 51-61.

[32] PATTISON, P. M. et al. LEDs for photons, physiology and food, Nature, 2018, v. 563, n.0, p. 493–500.

[33] OH, J. H., YANG. S. J., DO, Y. R. Healthy, natural, efficient and tunable lighting: four-package white LEDs for optimizing the circadian effect, color quality and vision performance, Light: Science & Applications, 2014, v. 3, n. 0, p. 141-9.

[34] WUNSCH, A., MATUSCHKA, K. A Controlled Trial to Determine the Efficacy of Red and Near-Infrared Light Treatment in Patient Satisfaction, Reduction of Fine Lines, Wrinkles, Skin Roughness, and Intradermal Collagen Density Increase. Photomedicine and Laser Surgery, 2014, v. 32, n. 2, p. 93-100.

[35] YEH, N. ET al. Applications of light-emitting diodes in researches conducted in aquatic environment, Renewable and Sustainable Energy Reviews, 2014, v. 32, n. 0, p. 611–618.

[36] LeGATES, T. A.; FERNANDEZ, D. C.; HATTAR. S. Light as a central modulator of circadian rhythms, sleep and affect, Nature Reviews Neuroscience, 2014, v. 15, n. 0, p. 443–454.

[37] WUNSCH, A. MATUSCHKA, K. A. Controlled Trial to Determine the Efficacy of Red and Near-Infrared Light Treatment in Patient Satisfaction, Reduction of Fine Lines, Wrinkles, Skin Roughness, and Intradermal Collagen Density Increase, Photomedicine and Laser Surgery, 2014, v. 32, n. 2, p. 93-100.

[38] YEH, N. et al. Applications of light-emitting diodes in researches conducted in aquatic environment, Renewable and Sustainable Energy Reviews, 2014, v. 32, n. 0, p. 611–618.

[39] SNOWDEN, M. C.; COPE, K. R.; BUGBEE, B. Sensitivity of Seven Diverse Species to Blue and Green Light: Interactions with Photon Flux, Plos, 2016, v. 11, n. 10, p. 1-32.

[40] KLEIN R. M. Effects of green light on biological systems, Biological reviews of the Cambridge Philosophical Society, 1992, v. 67, n. 2, p. 199-284.

[41] NEGELSPACH, D. C.; KALADCHIBACHI, S. FERNANDEZ, F. The circadian activity rhythm is reset by nanowatt pulses of ultraviolet light, Proceedings of the Royal Society B: Biological Sciences, 2018, v. 285, n. 1884, p. 1288-7.

[42] STAPLETON, A. E. Ultraviolet Radiation and Plants: Burning Questions, The Plant Cell, 1992, v.4, n. 11, p. 1353-1358.

[43] CONNELLY, N.G., DAMHUS, T. Nomenclature of Inorganic Chemistry: IUPAC Recommendations 2005. Cambridge: RSC Publ.

[44] ELISEEVA, S.V., BUNZLI, J.G. Lanthanide luminescence for functional materials and bio-sciences, Chemical Society Reviews, 2010, v. 39, n. 1, p. 189–227.

[45] XIE, R.J., HIROSAKI, N. Silicon-based oxynitride and nitride phosphors for white LEDs a review, Science and Technology of Advanced Materials, 2007, v. 8, n. 7-8, p. 588-600.

[46] BÜNZLI, J. G., ELISEEVA, S.V. Basics of Lanthanide Photophysics, 2011, Springer Series on Fluorescence, v. 7.

[47] OFELT, G. S. Intensities of Crystal Spectra of Rare-Earth Ions, The Journal of Chemical Physics, 1962, v. 37, n. 3, p. 511-520.

[48] MASON; S. F., PEACOCK, R. D.; STEWART, B. Dynamic coupling contributions to the intensity of hipersensitive lanthanide transitions, Chemical physics letters, 1974, v. 29, n., p. 49-153.

[49] KODAIRAA, C.A. et al. Luminescence and energy transfer of the europium (III) tungstate obtained via the Pechini method, Journal of Luminescence, 2003, v. 101, n. 1-2, p. 11–21.

[50] MOURA JR., R. T. et al. On the calculation and interpretation of covalency in the intensity parameters of 4f–4f transitions in Eu^{3+} complexes based on the chemical bond overlap polarizability, Journal of Luminescence, 2016, v. 170, n. 2, p. 420–430.

[51] RONDA, C.R., JUSTEL, T., NIKOL, H., J. Rare earth phosphors: fundamentals and applications, Journal of Alloys and Compounds, 1998, v. 275-277, n. 0, p. 669–676.

[52] HOPPE, H.A. Recent developments in the field of inorganic phosphors, Angewandte Chemie International Edition, 2009, v. 48, n. 20, p. 3572- 3582.

[53] BINNEMANS, K. Interpretation of europium(III) spectra, Coordination Chemistry Reviews, 2015, v. 295, n. 0, p. 1-45.

[54] NIELSON, C.W., KOSTER, G.F. Spectroscopic Coefficients for the p^n, d^n, and f^n Configurations, 1963, MIT Press, Cambridge.

[55] GÖRLLER-WALRAND, C., BINNEMANS, K. Handbook on the Physics and Chemistry of Rare Earths, 1998, Elsevier, v. 25.

[56]CARLOS, L. D.; MALTA, O. L. Intensities of 4f-4f transitions in glass materials, Qu mica nova, 2003, v. 26, n. 6, p. 889-895.

[57] HUANG, Y. et al. Laser site-selective excitation and emission spectroscopy of Eu^{3+} -doped $Ba_3BP_3O_{12}$, Journal of Alloys and Compounds, 2008, v. 465, n. 1-2, p 474–478.

[58] JIA, Y. et al. First-principles study of the luminescence of Eu^{2+}-doped phosphors, Physical Review B, 2017, v. 96, n. 0, p. 125132.

[59] RUBIO, J. Doubly-valent rare-earth ions in halide crystals, Journal of Physics and Chemistry of Solids, 1991, v. 52, n. 1, p. 101-174.

[60] BLASSE, G.; GRABMAIER, B.C.Luminescent materials, 1994, Springer-Verlag.

[61] DORENBOS, P. Energy of the first $4f^7 \rightarrow 4f^6 5d$ transition of Eu^{2+} in inorganic compounds Journal of Luminescence, 2003, v. 104, n. 4, p. 239–260.

[62] L.G. VAN UITERT, An empirical relation fitfing the position in energy of the lower d-band edge for Eu^{2+} or Ce^{3+} in various compounds, Journal of Luminescence, 1984, v. 29, n. 1, p. 1-9.

[63] BIRKEL, A. et al. Eu^{2+}-doped M_2SiO_4 (M = Ca, Ba) phosphors prepared by a rapid microwave-assisted sol-gel method: Phase formation and optical properties, Solid State Sciences, 2013, v. 19, n. 0, p. 51-57.

[64] REISFELD, R., et al. Intensification of rare earths luminescence in glasses, Journal of Luminescence, 2003, v. 102, n. 0, p. 243-247.

[65]HAO, Z. et al. Blue-Green-Emitting Phosphor $CaSc_2O_4$:Tb^{3+} Tunable Luminescence Manipulated by Cross-Relaxation, Journal of The Electrochemical Society, 2009, v. 156, n. 3, p. 193-196.

[66] WILLIAN, D.; CALLISTER, JR. Materials Science and Engineering: An Introduction, 1994, 3. ed. New York: John Wiley & Sons.

[67] HAN, J. K., et al. Europium-Activated $KSrPO_4$–$(Ba,Sr)_2SiO_4$ Solid Solutions as Color-Tunable Phosphors for Near-UV Light-Emitting Diode Applications, Journal of the American Ceramic Society, 2013, v. 96, n. 5, p. 1526–1532.

[68] MADEJ, A.; ZYCH, E. Controlled synthesis of the monoclinic and orthorhombicpolymorphs of Sr_2SiO_4 activated with Ce^{3+} or Eu^{2+}, RSC Advances, 2015, v. 5, n. 0, p. 104441-104450.

[69] CATTI, M.; GAZZONI, G.; IVALDI, G. Structures of Twinned β-Sr_2SiO_4 and of (α'-$Sr_{1.9}Ba_{0.1}SiO_4$, Acta Crystallographica Section C, 1983, v. 39, n.1, p. 29-34.

[70] ZHANG, M. Optical properties of Ba_2SiO_4:Eu^{2+} phosphor for green light-emitting diode (LED), Materials Research Bulletin, 2007, v. 42, n. 1, p. 33-39.

[71] BIRKEL, A. et al. Eu^{2+}-doped M_2SiO_4 (M = Ca, Ba) phosphors prepared by a rapid microwave-assisted sol-gel method: Phase formation and optical properties, Solid State Sciences, 2013, v. 19, n. 29, p. 51-57.

[72] HAN, J. K. et al. Nano- and Submicron Sized Europium Activated Silicate Phosphors Prepared by a Modified Co-Precipitation Method, ECS Journal of Solid State Science and Technology, 2012, v. 1, n. 3, p. 98-102.

[73] HAN, J. K. et al. Particle morphology and luminescence properties of green emitting Ba_2SiO_4:Eu^{2+} through a hydrothermal reaction route. Journal of Luminescence, 2015, v. 161, n. 0, p. 20-24.

[74] WANG, Z. Luminescent properties of Ba_2SiO_4:Eu^{3+} for white light emitting diodes, Physica B, 2013, v, 411, n. 0, p. 110–113.

[75] DA-WEI, H. et al. VUV Luminescent Properties of M_2SiO_4 Re (M = Mg, Ca, Ba) (Re= Ce^{3+}, Tb^{3+}), Chinese journal of luminescence, 2007, v. 28, n. 5, p. 53-56.

[76] NASIR, S. S. B. et al. Luminescence properties of Li_2SrSiO_4:Eu^{2+} silicate yellow phosphors withhigh thermal stability for high-power efficiency white LED application, Journal of Luminescence, 2019, v. 207, n. 0, p. 22–28.

[77] LEE, J. H.; KIM, Y. J. Photoluminescent properties of Sr_2SiO_4:Eu^{2+} phosphors prepared by solid-state reaction method, Materials Science and Engineering B, 2008, v. 146, n.1-3, p. 99–102.

[78] PARK, J. H.; AHN, W.; KIM, Y. J. Phase formation and luminescence of Sr_2SiO_4:Eu^{2+} nanopowders prepared by a hybrid process, Ceramics International, 2015, v. 41, n. 1, p. S734–S739.

[79] HIRATSUKA, R. S., SANTILLI, C. V., PULCINELLI, S. H. O processo Sol-gel: Uma visão físico-química, Química nova, 1995, v. 18, n. 2, p. 171-180.

[80]LIVAGE, J. The Sol-Gel Route to Advanced Materials, Material Science Forum, 1994, v. 43, n. 0, p. 152-153.

[81] JAFELICCI, M. J., SOUZA, D. F., ZANOTTO, E. D. Sol-gel science and technology, 1989, World. Scientific.

[82] LOVINGER, A. J. Ferroelectric Polymers, Science, 1983, v. 220, n. 4602, p. 1115-1121.

[83] SALIMI, A.; YOUSEFI, A. A. Conformational Changes and Phase Transformation Mechanisms in PVDF Solution-Cast Films, Journal of Polymer Science: Part B: Polymer Physics, 2004, v.42, n. 0, p. 3487–3495.

[84] GU, M. H.; et al. Formation of poly (vinylidene fluoride) (PVDF) membranes via thermally induced phase separation, Desalination, 2006, v. 192, n. 1-3, p. 160-167.

[85] ALBUQUERQUE, M. L. S. et al. Characterization of Buriti (Mauritia flexuosa L.) Oil by Absorption and Emission Spectroscopies, Journal of Brazilian Chemistry Society, 2005, v. 16, n. 6, p. 1113-1117.

CHAPTER 3 – TUNABLE BLUE-GREEN EMISSION AND ENERGY TRANSFER PROPERTIES IN $Ba_2SiO_4:Tb^{3+}$

3.1 Introduction

Tb^{3+} is a well-known green-emitting luminescent activator due to its radiative decay from the $^5D_4$ excited level.[1] Besides the green emission, the blue emission from the higher energy $^5D_3$ excited level may also be noticed depending on the matrix phonon frequency (> 1,000 cm^{-1}), doping concentration (typically > 0.1 at.%) and crystal structure.[2] Some reports have mentioned the unusual Tb^{3+} blue emission in different hosts such as in $Na_3YSi_3O_9$,[3] $SrWO_4$,[4] and $ZnMoO_4$,[5] however, in all those cases, the blue emission is weak, limiting the phosphor application in photonic devices. In our case, the Tb^{3+}-doped Ba_2SiO_4 phosphor exhibits a quite-remarkable intense blue emission, opening up new and exciting opportunities of applications in solid-state lighting as coatings of UV-emitting LEDs.

Concerning the use of $Ba_2SiO_4:Tb^{3+}$ phosphor in optical devices, two main points need to be overcome: (i) the improvement of this phosphor manufacturing, since just one paper[6] so far reports the $Ba_2SiO_4:Tb^{3+}$ synthesis under high annealing temperature (1,450 ºC) by using the conventional solid-state methodology; (ii) the elucidation of its luminescent properties considering the doping concentration effect and the fundamentals on the unexpected Tb^{3+}-blue emission. Therefore, in this chapter, regarding point (i), we present the sol-gel synthesis of $Ba_2SiO_4:Tb^{3+}$(0.1-5 %) phosphors. Concerning point (ii), based on a spectroscopic study on the Tb–Tb energy transfer (ET), we introduce a new approach to calculate the $^5D_3$ state quantum efficiency and to tune the emission from the blue towards the green spectral region by changing the Tb^{3+} concentration.

3.2 Experimental procedure

3.2.1 $Ba_2SiO_4:Tb^{3+}$ synthesis

Barium acetate ($Ba(CH_3COO)_2$, VETEC, 99.9%), terbium oxide (Tb_4O_7, Aldrich, 99.99%), TEOS ($C_8H_{20}O_4Si$, Fluka, 99.9%), isopropyl alcohol (C_3H_8O, VETEC, 99.7 %), hydrochloric acid (HCl, ALDRICH, 36 %), hydrogen peroxide (H_2O_2, SYTNH, 34-46 %) and acetic acid (CH_3COOH, VETEC, 97%) were used as reactants without any further purification.

Pure Ba_2SiO_4 and Tb^{3+}-doped Ba_2SiO_4 were synthesized via an adapted sol-gel route reported by us.[7] Terbium chloride solution was prepared by dissolving the Tb_4O_7 in

hot hydrochloric acid according to Equation 3.1. For the complete dissolution of the Tb_4O_7, it was necessary the addition of some drops of H_2O_2. The $TbCl_3$ solution was titrated by the well-known EDTA method.

$$Tb_4O_{7(s)} + 12HCl_{(aq)} + H_2O_{2(aq)} \rightarrow 4TbCl_{3(aq)} + 7H_2O_{(l)} + O_{2(g)} \quad (3.1)$$

For the gel synthesis, a stoichiometric amount of barium acetate and terbium chloride were dissolved in 10 mL of acetic acid (See Table 3.1). Then, a stoichiometric amount of TEOS dissolved in 10 mL of isopropyl alcohol was added. Finally, 0.4 mL of deionized water was introduced to initiate hydrolysis reactions. Acetic acid was used as both solvent and catalyst. The mixture was kept under stirring for 4 h at 25 ºC until the gel formation; the gel was thermally treated at 100 ºC in a static air atmosphere for 2 hours to enable the solvent evaporation, resulting in the SiO_2:Ba^{2+},Tb^{3+} xerogel phase. Finally, xerogel precursors were calcined at 1,100 °C with a heating ramp of 10 °C/min for 2 hours in an EDG muffle furnace.

Table 3.1 Doping proportions and amounts of reagents added, assuming 1.0000 g of the product.

Name	**Tb^{3+} % [a]**	**Tb^{3+} at% [b]**	**Tb^{3+} ch% [c]**	**Structural formula**	**MW / mol·L^{-1}**	**$Ba(Ac)_2$ / ± 0.0002 g**	**$Tb(Cl)_3$ / mL***	**TEOS / ±0.1 mL ******
BS5Tb	5.0	5.1	7.5	$Ba_{1.85}Tb_{0.1}SiO_4$	362.032(6)	1.3047	7.3±0.1	5.0
BS4Tb	4.0	4.1	6.0	$Ba_{1.88}Tb_{0.08}SiO_4$	362.973(9)	1.3224	5.8±0.1	5.0
BS3Tb	3.0	3.0	4.5	$Ba_{1.91}Tb_{0.06}SiO_4$	363.915(2)	1.3400	4.3±0.1	4.9
BS2Tb	2.0	2.0	3.0	$Ba_{1.94}Tb_{0.04}SiO_4$	364.856(5)	1.3572	2.9±0.1	4.9
BS1Tb	1.0	1.0	1.5	$Ba_{1.97}Tb_{0.02}SiO_4$	365.798(0)	1.3751	1.4±0.1	4.9
BS0.5Tb	0.50	0.50	0.75	$Ba_{1.985}Tb_{0.01}SiO_4$	366.268(4)	1.3837	0.72±0.01	4.9
BS0.1Tb	0.10	0.10	0.15	$Ba_{1.997}Tb_{0.002}SiO_4$	366.644(9)	1.3907	0.14±0.01	4.9
BS0Tb	0	-	-	Ba_2SiO_4	366.822(0)	1.3927	-	4.9

[a] Tb-doping percentage in relation to 2 mols of Ba in the undoped Ba_2SiO_4. [b] Tb-doping percentage in relation to the total cation mol number for each sample; [c] Tb-doping percentage in relation to the total charge in each sample. * 0.038 mol·L^{-1} in acetic acid solution. ** 0.55 mol·L^{-1} in isopropyl alcohol solution. **Source:** Own authorship.

The samples were calcined under CO reducing atmosphere (Figure 3.1) in order to avoid the Tb^{4+} formation.

Figure 3.1 Scheme of the SiO_2:Ba^{2+},Tb^{3+} xerogel calcination by using charcoal as an in situ source for CO.

Source: Own authorship.

The Tb^{3+}concentration was isoelectronically varied, i.e., keeping the same overall charge in the Ba_2SiO_4 matrix in relation to Ba^{2+}, according to Ba^{2+}, Tb^{3+} and SiO_4^{4-} charges ($3n_{Tb^{3+}} + 2n_{Ba^{2+}} = +4$, where $n_{Ba^{2+}}$ and $n_{RE^{3+}}$are the mol number of Ba^{2+} and RE^{3+}, respectively). The calculated amounts of reagents and the detailed description of this calculus are found in Table 3.1. The samples will be hereafter designated as BSXTb, where X is the Tb doping percentage.

3.2.2 Characterization

Powder X-ray diffraction (XRD)

X-ray diffractograms for the BSYTb were obtained in a Shimadzu diffractometer model *XRD-6000,* Cu(Kα) radiation (1.5418 Å), T = 20 ºC, with a graphite monochromator available in LaCCeF under supervision of Professor Silvania Lanfredi. Measurements were carried out over an angular range of $5^o \leq 2\theta \leq 80^o$ with a scanning step of 0.02^o and integration time of 1.20 s. Divergence, scattered and receiving radiation slits were 1^o, 1^o and 0.2 mm, respectively. The crystalline structures were refined for the BSXTb sample according to the Rietveld method using the Fullprof program[8] and the refinement conditions are shown in Table 3.2.

Table 3.2 Refinement conditions obtained by using a polynomial – 5 order function for background level, and a Pseudo-Voight function for peak shape ($H^2 = U\,tan^2\theta + V\,tan\theta + W$).

	BS0.1Tb	**BS0.5Tb**	**BS1Tb**	**BS2Tb**	**BS3Tb**	**BS4Tb**	**BS5Tb**
U	0.2669	0.2668	0.0905	0.1025	0.2397	0.2617	0.2633
V	-0.2000	-0.2000	-0.0728	-0.0758	-0.2000	-0.2000	-0.2000
W	0.0473	0.0483	0.0285	0.0253	0.0510	0.0480	0.0501
R_{Bragg} (%)	12.6	18.5	6,90	10.4	8.02	13.6	11.0
R_f-Factor (%)	8.65	14.0	4.43	7.62	5.86	10.0	7.79
cR_p (%)	28.2	41.6	17.8	23.6	19.9	28.1	25.1
cR_{wp} (%)	27.9	37.5	21.7	25.3	23.5	28.9	27.1
cR_{exp} (%)	18.01	23.89	15.04	17.0	14.38	19.01	18.66
χ	2.682	2.744	2.280	2.479	2.856	2.534	2.302

Source: Own authorship.

The crystallite size (D) was determinate according to Equation 3.2,[9] where β_p is the FWHM in radians of a given *h k l* reflection peak and *c* is a constant that depends on the reflection symmetry which is usually given as 0.9. To calculate the crystallite size,

the four most intense peaks observed in the diffraction pattern related to the (1 2 1), (2 1 2), (0 3 1) and (0 0 2) planes were considered.

$$\beta_p = \frac{c\lambda}{Dcos\theta} \quad (3.2)$$

Fourier-transform infrared spectroscopy (FTIR)

The samples were investigated by FTIR using a Shimadzu Spectrometer IRAffinity-1model available in *Central de Laboratórios* (FCT/UNESP), increment of 4 cm^{-1}, 128 scans. The samples were prepared in KBr pellets.

Raman spectroscopy

Raman spectroscopy was carried out at 25 ºC by using a Micro-Raman spectrograph Renishaw, in-Via model, increment of 1 cm^{-1}, with a 514 nm laser available in *Laboratório de Materiais Nanoestruturados para Análises Ambientais e Biológicas* under supervision of Professor Carlos José Leopoldo Constantino.

Scanning electron microscopy (SEM)

The measurements were performed by using a Carls Zeiss model EVO LS15 microscope with a detector of secondary electrons (SE) in a high vacuum and constant temperature. The samples were prepared by depositing the powder phosphors in carbon tape and then, a thin layer of gold was deposited by using a sputtering from Quorum model Q 150R ES. The equipment is available in *Laboratório Multiusuário de Microscopia Eletrônica de Varredura* of FCT-UNESP.

Diffuse reflectance spectroscopy (DR)

Samples were characterized by UV-Vis diffuse reflectance in a PERKIN ELMER LAMBDA 1050 spectrophotometer in order to evaluate the band gap of the phosphors through a graphic of $(\alpha h\nu)^n$ versus the energy of the incident photon (h), where *n* has a value equal to 2 for direct transition and 0.5 for indirect transition.[10] The α value is the ratio of the scattering and absorption coefficients according to the Kubelka-Munk's approximation,[11] Equation 3.3, where R is the reflectance observed for the different incident energies. The equipment is available in IQ-UNESP-Araraquara.

$$\alpha = \frac{K}{S} = \frac{(1-R)^2}{4R} \quad (3.3)$$

Photoluminescence (PL)

Photoluminescence measurements at 300 K for the BSXEuYTb samples were carried out in a Horiba JobinYvon spectrometer Fluorolog-3 with a Xe lamp (450 W) source and double excitation monochromators available in Sol-gel Group of University of Franca under supervision of Professor Eduardo José Nassar. The slits were placed at 1 and 0.2 mm for excitation and emission, respectively. Emission lifetime was evaluated using a phosphorimeter equipped with a Xe (5 J/pulse) lamp.

3.3 Results

3.3.1 Structural characterization

The X-ray diffraction pattern data of all BSYTb samples obtained after the heat treatment is summarized in Figure 3.2 (a) and they exhibit a set of diffraction peaks associated to the single-phase crystalline Ba_2SiO_4, identified from the JCPDS-70-2113 card, with orthorhombic symmetry and space group P_{mcn} (number 62). However, the undoped sample exhibits a secondary phase identified from the JCPDS-45-1471 card, associated to the witherite ($BaCO_3$) with orthorhombic symmetry, suggesting that the $TbCl_3$ precursor somehow assists the crystallization process of the Ba_2SiO_4 phase.

Figure 3.2 (a) Powder X-ray diffractograms and (b) FTIR spectra of BSXTb samples.

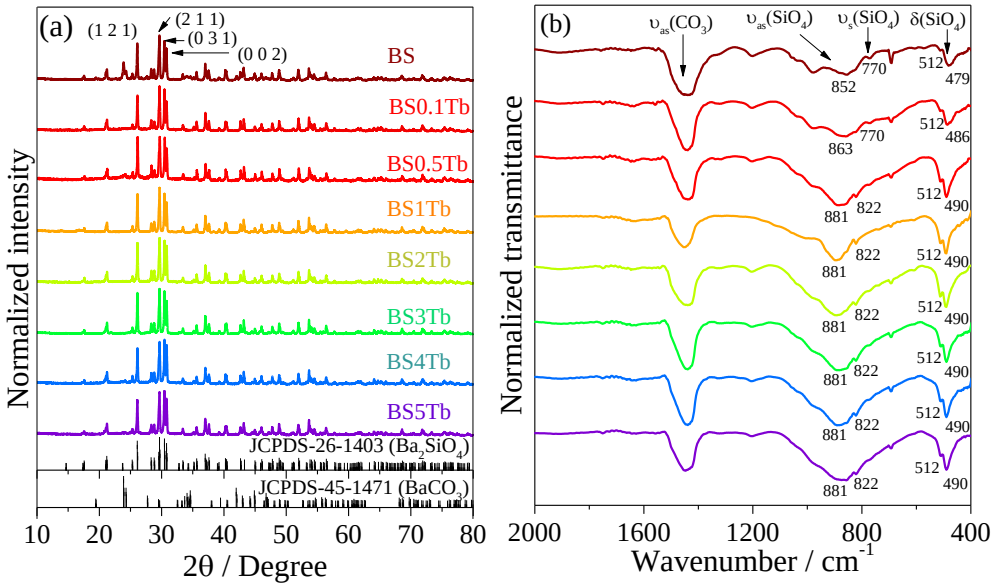

Source: Own authorship.

As the temperature to get the xerogel precursor (100 ºC) is not enough to release Cl^- coming from the $TbCl_3$ solution,[12] it is feasible to assume that low amounts of $TbCl_3$

(melting point = 558 ºC) are formed during the thermal annealing, and as this salt has melting point lower than the calcination temperature (1,100 ºC), it can act as a molten salt, enhancing the reaction rate and reducing the reaction temperature to get the Ba_2SiO_4 phase.[13] It is well-known that Cl^--based compounds act as molten salts in the synthesis of ceramics by shortening the diffusion distance and increasing the precursor mobility.[14] This presumption is supported by the fact that the only report on the Ba_2SiO_4:Tb^{3+} synthesis by using Tb_4O_7 as precursor,[6] features some $BaCO_3$ traces in the XRD profile.

No diffraction peaks associated with terbium, barium, silicon oxide or chloride phases are observed, regarding the limit of detection of this technique, and for this reason, we assume that Tb^{3+} is inserted into the Ba_2SiO_4 structure and the remaining Cl^- is probably inserted in interstice local sites. Thus, as a preliminary and important finding, the Tb^{3+}-doped Ba_2SiO_4 phosphors were successfully obtained from the sol-gel synthesis, decreasing the calcination temperature (1,100 °C) compared to the solid-state route (1,450 °C).[6]

The structural parameters set, calculated only for the doped powders, were derived using the Rietveld method considering the space group P_{mcn} (62) compatible with the orthorhombic symmetry. Figure 3.3 (a) shows, as an example, the Rietveld plot of the BS1Tb sample with the observed and derived X-ray diffraction and their differences. Figure 3.3 (b) shows the graphic representation of the unit cell obtained for BS1Tb.

Figure 3.3 (a) Rietveld plot of the BS1Tb sample. (b) Unit cell obtained for Ba_2SiO_4 representing Ba1 (CN = 10), Ba2 (CN = 9), Si and O atoms.

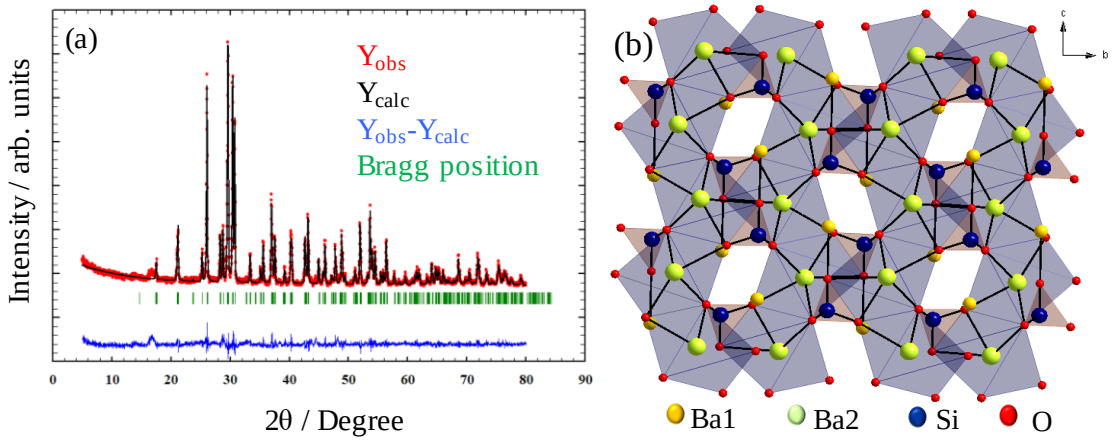

Source: Reproduced from Bispo-Jr et al.[7]

The lattice parameters evaluated from the Rietveld refinement are shown in Table 3.3. The calculated values are statistically the same to those reported by L. Lin et al[15] for the undoped Ba_2SiO_4.

Table 3.3 Average bond length (Ba-O), polyhedral distortion index (D), lattice parameters (a, b and c) and cell volume (V) determined for the phosphors.

Sample	Ba1		Ba2		a / Å	b / Å	c / Å	V / Å^3
	Ba-O / Å	D	Ba-O / Å	D				
BS5Tb	2.96(3)	0.0485(4)	2.87(2)	0.0589(9)	5.80(7)	10.2(1)	7.50(2)	445.(0)
BS4Tb	2.96(7)	0.0532(2)	2.87(1)	0.0546(4)	5.80(6)	10.2(1)	7.50(3)	444.(9)
BS3Tb	2.98(0)	0.0409(8)	2.86(3)	0.0608(5)	5.80(8)	10.2(1)	7.50(5)	445.(3)
BS2Tb	2.98(0)	0.0498(8)	2.98(0)	0.0610(0)	5.80(7)	10.2(1)	7.50(2)	444.(9)
BS1Tb	2.99(3)	0.0367(1)	2.99(3)	0.0670(6)	5.80(7)	10.2(0)	7.50(1)	444.(7)
BS0.5Tb	2.99(2)	0.0533(9)	2.89(7)	0.0544(6)	5.81(1)	10.2(1)	7.50(5)	445.(5)
BS0.1Tb	2.98(9)	0.0462(3)	2.84(8)	0.0670(9)	5.80(8)	10.2(0)	7.50(1)	444.(8)
Ba_2SiO_4[15]	2.98(4)	0.0440(5)	2.82(8)	0.0460(6)	5.807	10.21	7.504	445.6

Source: Reproduced from Bispo-Jr et al.[7]

The Ba-O bond length values are shown in Table 3.4, and the average bond length and polyhedral distortion index values are also shown in Table 3.3. The polyhedral distortion index was calculated from Equation 3.4, where l_i is the Ba-O bond length and l_{av} is the average bond length. The average Ba-O bond length for both Ba local sites are close to the values reported by L. Lin et al[15] for the undoped Ba_2SiO_4 even that there is a tendency to increase the value for the Ba1-O bond and decrease for the Ba2-O bond as the Tb amount increases in the samples. However, the polyhedral distortion index values are higher than those reported by L. Lin et al[15] for the undoped matrix. The increase of the Ba site polyhedral distortion is directly correlated with the impacts of the Ba^{2+} replacement by Tb^{3+} in the matrix network.

Table 3.4 Ba-O bond length for Ba1 (CN 10) and Ba2 (CN 9) sites of BSTb.

Tb %	BS0.1Tb	BS0.5Tb	BS1Tb	BS2Tb	BS3Tb	BS4Tb	BS5Tb
Ba1 / Å	3.23(8)	3.29(2)	3.12(6)	2.84(2)	2.94(0)	2.93(1)	2.94(2)
	3.23(8)	2.97(6)	3.12(6)	2.94(1)	2.90(0)	2.82(8)	2.83(0)
	2.92(4)	3.29(2)	2.64(3)	3.25(5)	3.19(2)	3.28(1)	3.28(7)
	2.70(2)	2.59(8)	2.92(8)	2.58(1)	2.60(3)	2.55(4)	2.64(6)
	2.85(0)	2.97(6)	2.94(9)	3.25(5)	3.19(2)	3.28(1)	3.28(7)
	2.85(0)	2.80(6)	2.94(9)	2.84(2)	2.90(0)	2.82(8)	2.83(0)
	2.92(4)	2.80(6)	3.09(6)	3.01(6)	3.04(2)	2.97(3)	2.94(8)
	3.08(5)	3.13(8)	3.09(7)	3.11(4)	3.05(8)	3.09(1)	2.97(1)
	3.04(0)	3.01(8)	3.09(7)	3.01(6)	3.04(2)	2.97(3)	2.94(8)
	3.04(0)	3.01(8)	2.92(7)	2.94(1)	2.94(0)	2.93(1)	2.94(2)
Average	2.98(9)	2.99(2)	2.99(3)	2.98(0)	2.98(0)	2.96(7)	2.96(3)
Ba2 / Å	2.76(4)	2.79(7)	2.84(5)	3.09(5)	2.78(5)	2.78(1)	2.71(5)
	2.76(4)	2.64(5)	2.67(7)	2.78(1)	2.94(6)	3.09(4)	2.78(9)
	2.81(9)	3.03(5)	3.10(7)	2.93(9)	2.75(8)	2.82(7)	2.71(5)
	2.77(1)	3.09(9)	2.77(2)	2.78(1)	3.10(8)	2.88(0)	3.11(5)
	2.77(1)	2.78(0)	2.71(6)	3.09(5)	2.73(8)	2.82(7)	2.84(2)
	3.12(3)	2.78(0)	2.85(7)	2.74(1)	2.71(1)	3.09(0)	2.85(5)
	3.12(3)	3.03(5)	2.77(2)	2.63(4)	2.73(8)	2.78(0)	2.84(2)
	2.82(5)	3.10(6)	2.71(6)	2.87(7)	3.10(8)	2.90(0)	2.83(0)
	2.67(2)	2.79(7)	3.10(7)	2.74(1)	2.84(8)	2.66(4)	3.11(5)
Average	2.84(8)	2.89(7)	2.84(1)	2.85(4)	2.86(3)	2.87(1)	2.87(2)

Source: Reproduced from Bispo-Jr et al.[7]

$$D = \frac{1}{n}\sum_{i=1}^{n}\frac{|l_i - l_{av}|}{l_{av}} \quad (3.4)$$

As Tb^{3+} replaces Ba^{2+} in the lattice, Tb^{3+} may occupy both sites with CN 9 and 10. Due to the charge compensation mechanism considered in the present study, it is feasible to say that Tb^{3+} non-equivalently replaces Ba^{2+}, in other words, two mols of Tb^{3+} are needed to substitute three mols of Ba^{2+} and, as consequence, one mol of vacancy defect of V_{Ba}" with two negative charges is formed, and two mols of positive defects of $Tb_{Ba}^{\bullet}\cdot$are created, as shown in Equation 3.5.[16]

$$3Ba^{2+} + 2Tb^{3+} \rightarrow V_{Ba}^{"} + 2Tb_{Ba}^{\bullet} \quad (3.5)$$

The V_{Ba}" vacancies cause a local expansion in the Ba_2SiO_4 lattice due to the repulsion of the oxi negative charges, and the $Tb_{Ba}^{\bullet}$ defects cause a local compression in the lattice due to the increase of the positive charge in that site. This compression also occurs because Tb^{3+} is smaller than Ba^{2+}, as shown in Table 3.5. However, even that Tb^{3+} is smaller than Ba^{2+}, the substitution is favored since the difference (D_r) between both ion radii is lower than 30 %. Due to the large difference between the ionic radii of Tb^{3+} and Si^{4+}, the substitution of Si^{4+} by Tb^{3+} is unlikely.

Table 3.5 Ionic Radii, bond distance and difference of ionic radii (Dr) between Tb^{3+} and Ba^{2+}.

Cation	Radii / pm (CN)	D_r / %	Bond (CN)	Bond distance /pm
Ba	166 (10)		Ba-O (10)	298.3
Ba	161 (09)		Ba-O (09)	282.4
Si	40 (04)		Si-O	163.2
Tb	109 (09)	30 %		
Tb	114 (10)	30 %		

Source: Reproduced from HUHEEY, KEITER, KEITER, R. L. [17]

The crystallite size values for the planes in each sample are different, Table 3.6, indicating that the particle growth is not isotropic. There is a tendency of crystallite size increases for all planes from the undoped sample up to the BS3Tb, then the crystallite size decreases again, although the (2 1 1) plan has the lowest values in all phosphors.

Table 3.6 Crystallite size (D, nm) for the four most intense plans of the samples.

Plan	BS5Tb	BS4Tb	BS3Tb	BS2Tb	BS1Tb	BS0.5Tb	BS0.1Tb	BS
(1 2 1)	49.(2)	51.(0)	51.(1)	54.(0)	53.(3)	50.(0)	49.(2)	50.(1)
(2 1 1)	35.(6)	34.(6)	38.(8)	35.(7)	40.(9)	30.(3)	39.(2)	36.(4)
(0 3 1)	45.(3)	49.(4)	48.(6)	46.(5)	49.(0)	42.(7)	48.(2)	46.(5)
(0 0 2)	45.(6)	48.(1)	46.(4)	52.(8)	46.(0)	43.(8)	46.(2)	46.(5)

Source: Reproduced from Bispo-Jr et al.[7]

Undoped and doped samples were also investigated under the molecular structure point of view by using FTIR spectroscopy, Figure 3.2 (b). All spectra exhibit bands assigned to genuine vibrational modes characteristic of the [SiO_4^{4-}] tetrahedra inserted in the Ba_2SiO_4 orthorhombic structure. In the orthosilicate structures, the SiO_4^{4-} anions are not linked but surrounded by Ba^{2+} and the chemical bond distance between Si and O is shorter than the distance between the metal and oxygen. Therefore, the internal vibrational modes for the [SiO_4^{4-}] are almost independent of external vibrations.

In the orthosilicate structures, the [SiO_4^{4-}] internal modes are split because of their site symmetry (crystal field splitting) and unit-cell space symmetry (Davydov's splitting), to which depends on the mixed anion-cation vibrations whereas the crystal field splitting depends on the anion internal force field change.[18] Three vibrational modes are noticed in the FTIR spectra, Figure 3.2 (b), the (ν_3) antisymmetric stretching (~916 cm^{-1}), the (ν_4) deformation (~497 cm^{-1}), and the (ν_1) symmetric stretching (~822 cm^{-1}).

In addition, vibrational modes of the carbonate group are also observed in all the FTIR spectra, Figure 3.2 (b), and they are assigned to carbonate ions on the surface of the particles since no carbonate phase is observed in the XRD data, considering the technique detection limit of 1 wt%. Considering that the particles exhibit an active surface during the cooling step after the calcination process, the particles may react with atmospheric CO_2 to form carbonate ionically bonded to Ba^{2+} on the particle surface. Besides that, this carbonate should not be an amorphous phase formed during the synthesis because the baselines in the XRD are well-defined, indicating the absence of any cluster of amorphous material in the final product.

Still considering the FTIR spectra in Figure 3.2 (b), the undoped silicate exhibits shifted ν_{as} (~916 cm^{-1}), ν_s (~826 cm^{-1}) and δ (~509 and ~ 497 cm^{-1}) bands compared to the doped samples. These shifts suggest the existence of uniform stresses in the network, that are generally associated with defects in the material, confirming the proposition of defects that arise from the doping.

These defects may lead to a shortening of the Si-O bond around Ba^{2+} vacancies and an enlargement around Tb^{3+} local sites, that is responsible for the observed vibrational modes displacements in relation to the undoped sample.[19] However, as the amount of terbium is much lower than the amount of Ba^{2+} and SiO_4, these defects are local and do not cause extended deformations in the Ba_2SiO_4 lattice, since the same number of vibrational modes was observed after the doping. Furthermore, the rigid second

coordination sphere of Tb^{3+} counteracts expansions or compressions in the Tb^{3+} local sites.

Raman spectra of the samples are shown in Figure 3.4. The bands observed at 910, 886, 851, 821, 519, 597, 370, and 350 cm^{-1} are assigned to the vibrational modes of the silicate tetrahedron, as represented in Figure 3.4.[18] Also, the absence of vibration mode with energy at 450 cm^{-1} characteristics of terbium oxide confirms the absence of any terbium oxide spurious phase and the formation of a solid solution of Tb^{3+} with the host lattice.

Figure 3.4 Raman spectra (300 K) of BSXTb. Laser 514 nm.

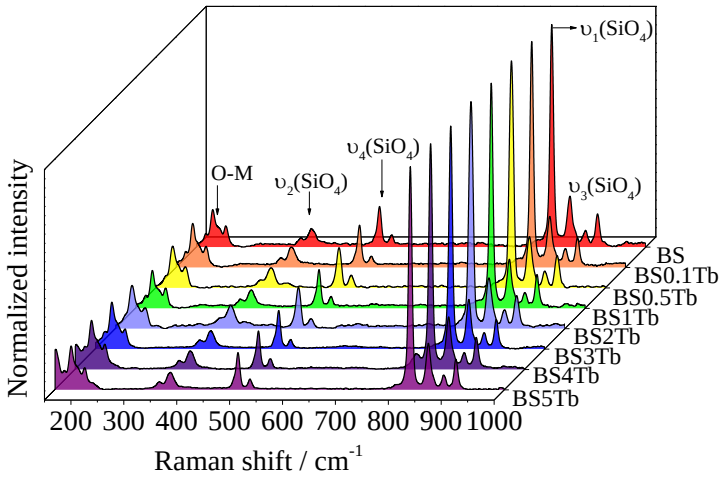

Source: Reproduced from Bispo-Jr et al.[7]

3.3.2 Morphology

SEM images of the BSTb samples are shown in Figure 3.5, in the next page. All samples, independently on the presence, or amount of doping ion, exhibit the formation of aggregate particles featuring an irregular shape. Many authors have attributed the degree of agglomeration and the irregular morphology to the sol-gel method catalyzed by acid and to the high annealing temperature.[20,21,22] The doping does not lead to appreciable modifications in the particle shape or size, but for the doped samples, nanowires on the particle surface are noted, Figure 4.5 (b). These nanowires increase the particle surface area and the surface defect concentration since more superficial sites with incomplete coordination sphere are formed, causing considerable influence on the spectroscopic properties of the material, as will be presented in the next section.

Figure 3.5 SEM images of the BSTb phosphors. (a) Magnification = 5.000 times under electron high tension (EHT) of 30 kV. (b) Magnification of 25.000 times.

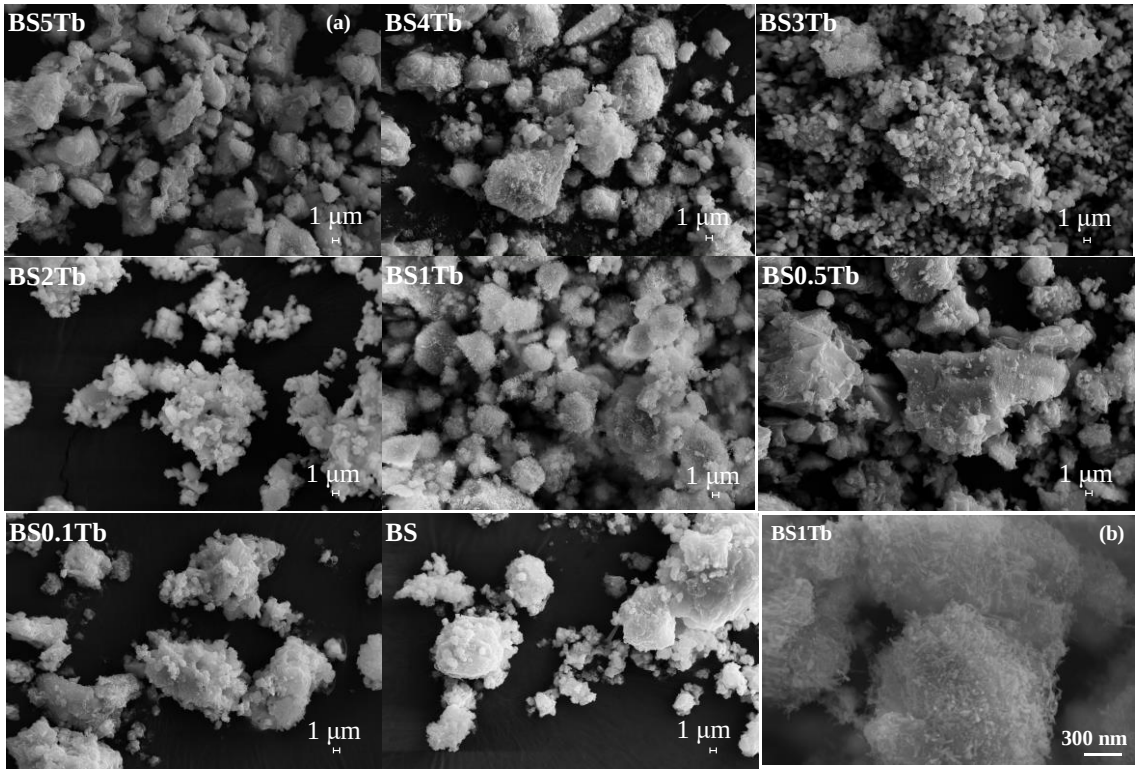

Source: Reproduced from Bispo-Jr et al.[7]

3.3.3 Band gap evaluation

Figure 3.6 shows the DR spectra of the samples and three bands are noticed.

Figure 3.6 (a) UV-Vis diffuse reflectance spectra of BSTb. (b) Magnification of the region between 270-520 nm.

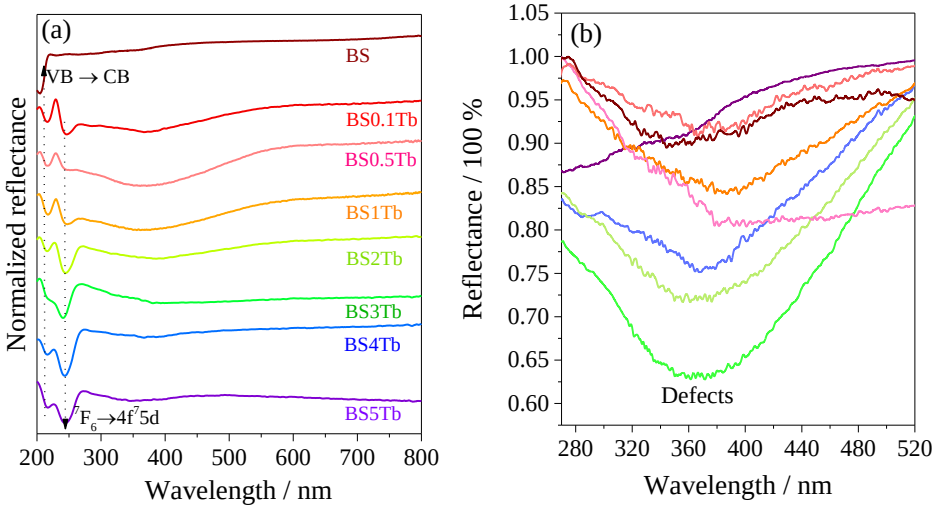

Source: Reproduced from Bispo-Jr et al.[7]

The first band at 364 nm, Figure 3.6 (a), is ascribed to the defect-related matrix absorption, the second at 240 nm is assigned to the $4f^8 \rightarrow 4f^7 5d$ absorption of Tb^{3+} and the

third at about 200–220 nm is attributed to the transition from the valence band (VB) to the conduction band (CB) of the matrix. When the dopant is inserted in the Ba_2SiO_4 structure, the matrix absorption enhances, Figure 3.6 (b), confirming that Tb^{3+} increases the structural/superficial defect concentration.

The optical bandgap values were estimated from the Kubelka-Munk's approximation, and the values are summarized in Figure 3.7. The curves are best fitted considering direct transitions, as also shown in Figure 3.7. The bandgap values lie within the 5.7–6.0 eV range and they decrease for the Tb-doped samples due to changes in the surface area of the particles that directly influence the concentration of the defect-related electronic levels that lie between the VB and CB. As the Tb amount increases in the samples, the relative absorption of the Tb^{3+} $4f^8 \rightarrow 4f^7 5d$ transition at 5.1 eV increases compared to the matrix absorption at 3.4 eV.

Figure 3.7 Bandgap calculation considering direct transition for BSTb.

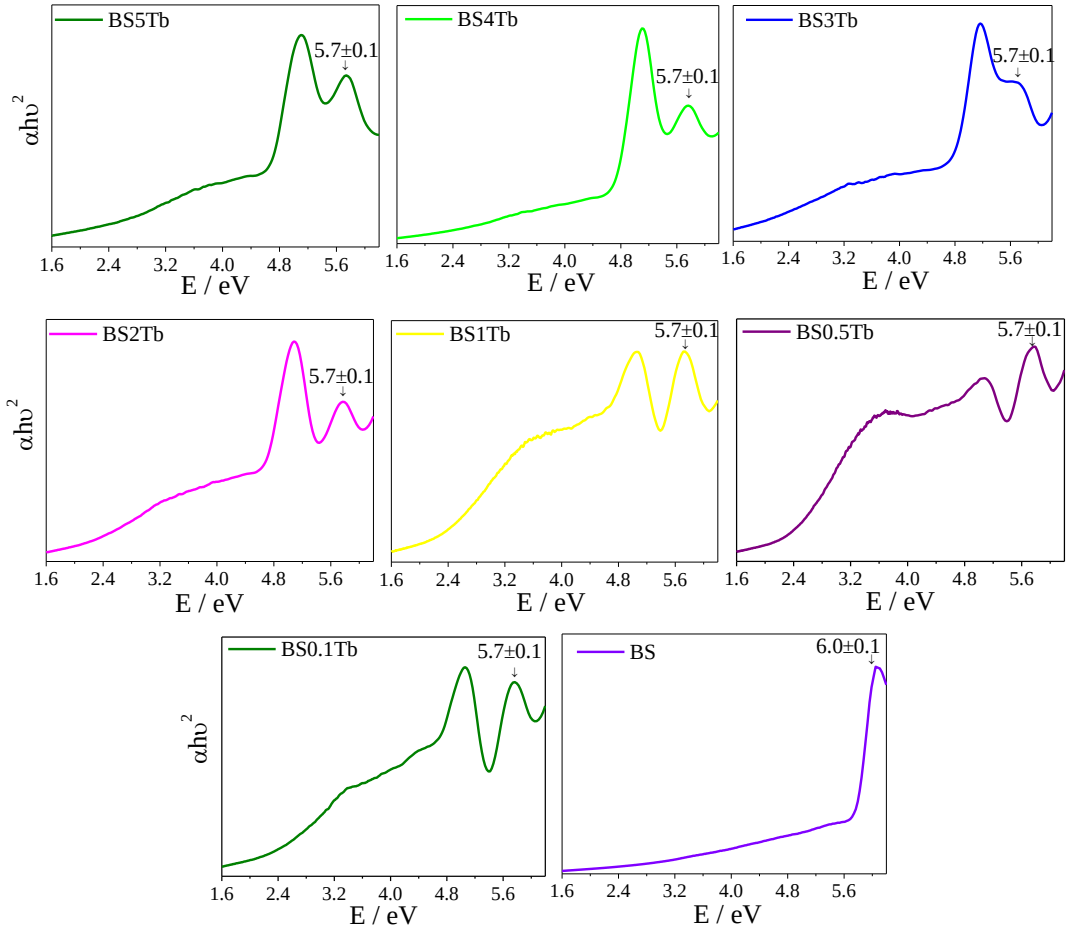

Source: Reproduced from Bispo-Jr et al.[7]

3.3.4 Photoluminescence

Considering now the photophysical features of the BSTb samples, their excitation spectra, Figure 3.8 (a), are dominated by an intense broadband near to 250 nm assigned to the Tb^{3+} $4f^8 \rightarrow 4f^7 5d$ transition; the narrow bands with lower intensity at 338, 350, 368, 377, and 481 nm ascribed to Tb^{3+} *f-f* transitions that are forbidden by Laporte's rule, on the other hand, are only seen through the magnification of the 300–500 nm interval, Figure 3.9. Therefore, these phosphors may be used as coatings of deep-UV LEDs emitting at 250 nm.

Figure 3.8 (a) Excitation (300 K, 542 nm) and (b) emission (300 K, 250 nm) spectra of BSTb.

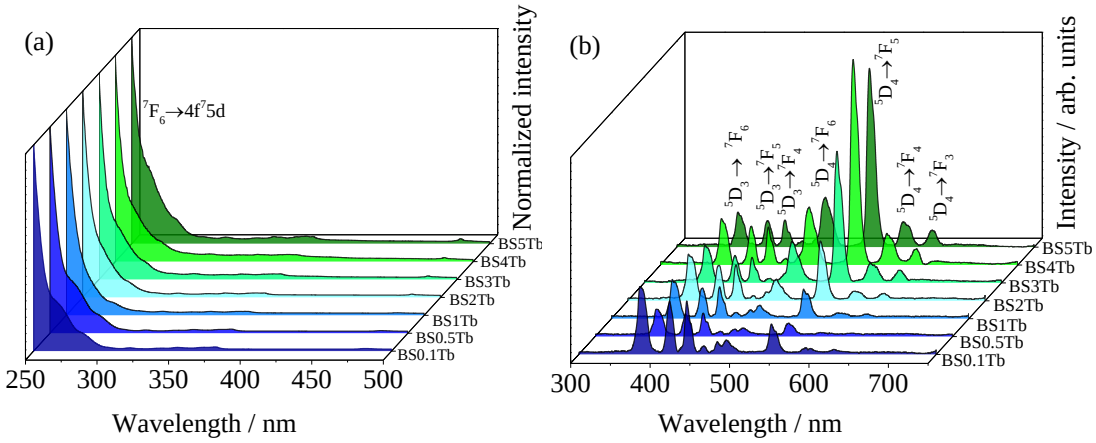

Source: Reproduced from Bispo-Jr et al.[7]

Figure 3.9. Magnification in the 300 – 500 nm range of the excitation spectra of BSTb. The electronic transitions come from the $^7F_6$ ground state to excited states assigned in the figure.

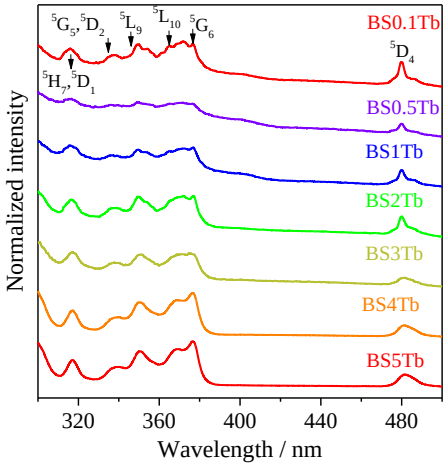

Source: Reproduced from Bispo-Jr et al.[7]

The emission spectra, Figure 3.8 (b), reveal two sets of transitions; the first at 378, 414, 436, 457 and 476 nm is assigned to the Tb^{3+} $^5D_3 \rightarrow {}^7F_J$ transitions in the blue spectral region, and the second at 486, 542 and 585 nm are ascribed to the Tb^{3+} $^5D_4 \rightarrow {}^7F_J$

transitions in the green spectral region. Among all the phosphors, the BS4YTb sample displays the highest emission intensity at 542 nm, showing that above this concentration, a quenching mechanism by concentration takes place. This process occurs due to nonradiative channels that arise from the enhancement of the energy transfer probability between the dopant ions because of the shortening of the Tb – Tb distance as the dopant amount increases.

The relative emission intensity of the transitions coming from the $^5D_4$ state enhances as the Tb^{3+} content increases while the relative intensity of the transitions arising from the $^5D_3$ state does not follow a regular pattern, yet, it shows an overall tendency of decreasing as the Tb^{3+} amount increases, Figure 3.10 (a).

Figure 3.10 (a) Area under the transitions coming from the $^5D_3$ and $^5D_4$ states as a function of the Terbium concentration. (b) Ratio of the integrated areas of the transitions coming from the $^5D_3$ and $^5D_4$ states as a function of the Terbium content. (c) 1931 CIE chromaticity diagram of the phosphors (λ_{exc} = 250 nm). The inset in Figure (c) is a photograph of the BS4Tb sample under UV radiation (270 nm).

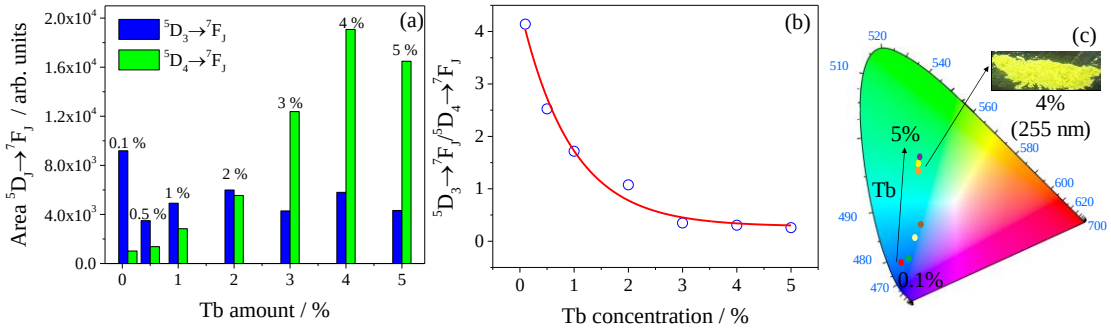

Source: Reproduced from Bispo-Jr et al.[7]

The changes over the tendency of the $^5D_3$ state relative emission are correlated to two opposite effects: 1) As the Tb^{3+} concentration diminish, the relative emission intensity tends to decrease due to the reduction of the emitting center number. 2) On the other hand, the $^5D_3$ state relative emission intensity enhances as the Tb^{3+} concentration decreases since the cross-relaxation (CR) effect that quenches the $^5D_3$ state is shut off at lower doping concentration,[23] as further discussed below. Therefore, these two effects occurring in opposite directions make that the relative emission intensity of the $^5D_3$ state does not follow a regular tendency as the $^5D_4$ state emission intensity. Yet, there is an exponential tendency between the ratio of the integrated areas of the transitions coming from the $^5D_3$ and $^5D_4$ states as a function of Terbium content, Figure 3.10 (b).

The blue emission quenching is a function of the Terbium amount. As the Terbium concentration increases, the CR process quenches the emission from the higher-

energy $^5D_3$ excited level of a Tb^{3+}, and the energy is transferred to the $^7F_6$ level of a close enough Tb^{3+} neighbor, as represented in Equation 3.6.[23] This mechanism is favored at high doping concentrations because of the Tb–Tb distance is short enough to allow the energy transfer process.

$$Tb^{3+}(^5D_3) + Tb^{3+}(^7F_6) \rightarrow Tb^{3+}(^5D_4) + Tb^{3+}(^7F_0) \quad (3.6)$$

On the other hand, at low doping percentages, the distance between Terbium neighbors is long enough to inhibit the energy transfer, shutting off this nonradiative decay process from the $^5D_3$ state.[24] Thus, the Tb^{3+} emission may be tuned from the blue at low doping concentration towards the green spectral region by increasing the Tb amount, as represented in the CIE color coordinate diagram, Figure 3.10 (c).

Besides the CR process, the multi-phonon relaxation related to the matrix phonon frequency may contribute to the $^5D_3$ state deactivation.[25] It is well-known that in a multi-phonon deactivation, for a four to five-phonon process, radiative and nonradiative decays have comparable probabilities to occur.[25] However, if the phonon frequency of the matrix is too low and requires six or more phonons, the nonradiative relaxation is unlikely to take place.[25] In our case, from the FTIR and Raman spectra, Figures 3.2 (b) and 3.4, respectively, the Ba_2SiO_4 phonon frequency is at about 900 cm^{-1} and as the energy difference between the $^5D_3$ and $^5D_4$ level is near to 6,500 cm^{-1}, the combination to allow a multi-phonon deactivation requires more than 5 phonons, indicating that this process may be neglected in the $^5D_3$ state deactivation. It is important to highlight the effect of the carbonate on the $^5D_3$ state deactivation since its phonon energy (at about 1,750 cm^{-1}) is higher than the silicate matrix. However, as the carbonate is only on the particle surface, its contribution might be low because of the particles are micro-sized.

Usually, multipolar interactions, exchange coupling, or radiative processes dominate the CR energy transfer mechanism between RE ions.[26] In the present situation, the radiative process is unlikely to take place because it requires a wide overlap between the emission and excitation spectra of the donor and the acceptor species (Figure 3.8), respectively, that is not the case.

To evaluate the exchange coupling possibility, it is necessary to determine the critical distance (R_c) between the Tb atoms in the lattice since this energy transfer mechanism is limited by a distance of at about 4 Å,[27] as discussed in section 2.1.2. The critical distance was estimated by applying Equation 3.7, where $n_A = (x.n)/V$, being V the unit cell volume, x is the Terbium concentration (Tb mol number/Ba mol number), and n is the Ba mol number per unit cell (n = 8 for the orthorhombic Ba_2SiO_4).[28] The R_c values

represented in Table 3.7 are higher than 4 Å for all phosphors and the exchange coupling contribution must be low. Therefore, multipolar interactions are the main mechanism that contributes to the CR process.

$$R_c = \left[\frac{3}{4\pi n_A}\right]^{1/3} \quad (3.7)$$

Table 3.7 Tb-Tb critical distance (R_c), $^5D_3$ and $^5D_4$ lifetime values (τ), cross-relaxation probability (W_{CR}) and cross relaxation efficiency (η_{CR}) of BSTb.

	R_c / Å	**τ ($^5D_3$) / ms**	**τ ($^5D_4$) / ms**	**W_{CR} / s^{-1}**	**η_{CR} / %**
BS5Tb	6.(3)	1.48±0.02	1.31±0.02	375±29	55.5±0.1
BS4Tb	6.(8)	1.10±0.03	1.25±0.02	608±50	66.9±0.2
BS3Tb	7.(5)	1.33±0.01	1.33±0.02	451±18	60.0±0.2
BS2Tb	8.(6)	1.92±0.02	1.41±0.03	220±25	42.3±0.1
BS1Tb	10.(9)	2.21±0.04	1.37±0.01	152±13	33.6±0.1
BS0.5Tb	13.(8)	2.71±0.04	1.32±0.02	68±14	18.6±0.1
BS0.1Tb	23.(7)	3.33±0.06	1.31±0.02	0	0

Source: Reproduced from Bispo-Jr et al.[7]

The multipolar interaction that dominates the cross-relaxation was pointed out by using the theoretical model developed by Van Uitert that was previously represented in Equation 2.6.[29] Figure 3.11 (a) shows the plot of the log(x) versus log(I/x), where the θ value deduced from a linear fitting approximation is closer to 6, suggesting that the electric dipole-dipole interaction is the main contribution for the nonradiative cross-relaxation between Tb^{3+} ions in the Ba_2SiO_4 matrix.

Figure 3.11 (a) Plot of log(x) versus log(I/x). (b) Cross-relaxation rate (W_{CR}) as a function of the Tb amount. (c) $^5D_3$ lifetime as a function of the Terbium amount. (d) Dependence of the $R_{G/B}/R_0$ on W_{CR}.

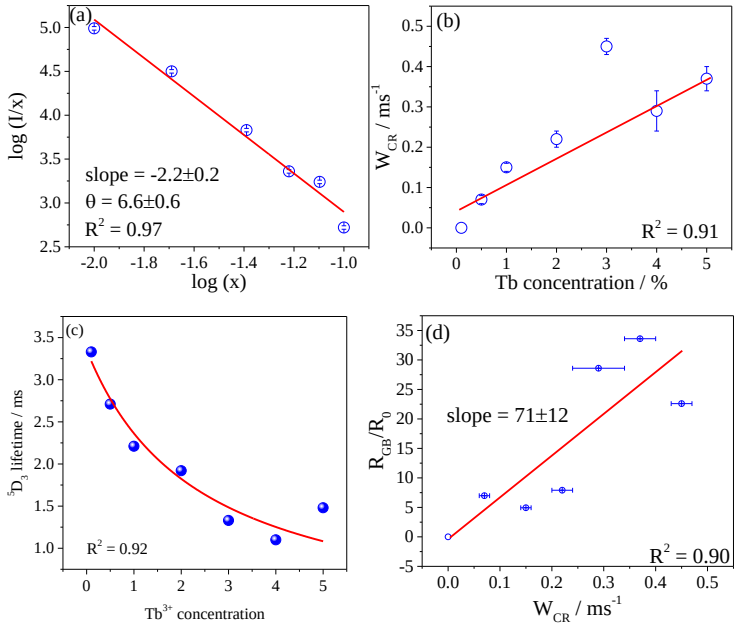

Source: Reproduced from Bispo-Jr et al.[7]

Emission decay-curves (300 K) were performed monitoring the $^5D_3 \rightarrow {}^7F_5$ and $^5D_4 \rightarrow {}^7F_5$ transitions of Tb^{3+} aiming to determine the lifetime of the $^5D_3$ and $^5D_4$ states. The exponential decay curves, Figure 3.12, were fitted through the Inokuti–Hirayama model described in Equation 3.8 and the values are listed in Table 3.7.

$$\tau = \frac{\int_0^\infty I(t)tdt}{\int_0^\infty I(t)dt} \quad (3.8)$$

Figure 3.12 Luminescence decay curves fixing excitation wavelength at 250 nm and emission wavelength at (a) 414 nm (Tb^{3+} $^5D_3 \rightarrow {}^7F_5$ transition) and (b) 542 nm (Tb^{3+} $^5D_4 \rightarrow {}^7F_5$ transition).

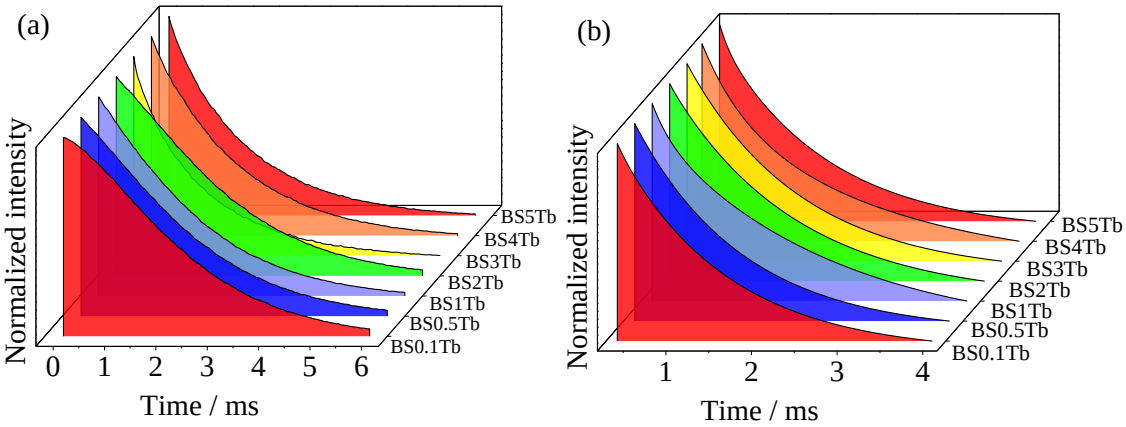

Source: Reproduced from Bispo-Jr et al.[7]

The $^5D_4$ state lifetime values are close for all phosphors, Table 3.7, but the $^5D_3$ state lifetime decreases as the Terbium amount increases since the already mentioned nonradiative CR channel becomes relevant.[30] In addition, the similar $^5D_4$ state lifetime values for all phosphors indicate that the other nonradiative contributions for all samples are identical. Yet, the radiative decay rate of the $^5D_4$ state shall increase because of the green emission enhances as the Terbium amount increases. Thus, the $^5D_4$ state quantum efficiency increases up to the BS4Tb sample.

The CR probability (W_{CR}) and the CR efficiency (η_{CR}) may be directly obtained from the $^5D_3$ state lifetime values by applying Equations 3.9 and 3.10, respectively, where τ_1 is the $^5D_3$ state lifetime and τ_{10} is the $^5D_3$ state lifetime for the BS0.1Tb, to which the CR may be negligible. As expected, the W_{CR} and η_{CR} increase as the Terbium concentration increases, Table 3.7, due to the shortening of the distance between Tb^{3+} neighbors. Moreover, there is a linear dependence of W_{CR} and Terbium percentage (x), Figure 3.11 (b), as represented in Equation 3.11, where A is a proportionality constant.

$$W_{CR} = \frac{1}{\tau_1} - \frac{1}{\tau_{10}} \quad (3.9); \qquad \eta_{CR} = 1 - \frac{\tau_1}{\tau_{10}} \quad (3.10); \qquad W_{CR} = Ax \quad (3.11)$$

For the BS0.1Tb sample, since the cross-relaxation is negligible, the only processes that contribute for the $^5D_3$ deactivation are the multi-phonon deactivation (nonradiative) and the emission (radiative), as shown in Equation 3.12, where W_0 is the multi-phonon decay probability and γ_1 is the radiative contribution.

$$\tau_{10} = \frac{1}{W_0 + \gamma_1} \quad (3.12)$$

As the concentration of Tb is too low in comparison to the rest of the matrix, it is feasible to assume that the multi-phonon rate is independent on the Terbium concentration. Therefore, by replacing Equations 3.11 and 3.12 in Equation 3.9, we can find a representation that correlates τ_1 and Terbium concentration, as stated in Equation 3.13, where $B = \gamma_1 + W_0$. In this context, a graphic of τ_1 as a function of x presented in Figure 3.11 (c) may be fitted using Equation 3.14 to determine the B value.

$$\tau_1 = \frac{1}{Ax + B} \quad (3.13)$$

Z. Zhang et al[31] established that Equation 3.14 could correlate the intensity of blue and green emissions of Tb^{3+}, in which $R_{G/B}$ is the ratio between the green and blue emissions, and R_0 is the ratio between the green and blue emissions for the BS0.1Tb sample. In this context, in Figure 3.11 (d), the graphic of $R_{G/B}/R_0$ versus W_{CR} is plotted and it was used to determine the W_0 value and, as consequence, to evaluate the γ_1 value for the BS0.1Tb sample using Equation 3.13. The W_0 and γ_1 values are equal to 0.014±0.002 ms^{-1} and 0.29±0.04 ms^{-1}, respectively, proofing that the multi-phonon deactivation does not effectively contribute to the deactivation of the $^5D_3$ level, as expected since the $^5D_3$ level is 6,500 cm^{-1} above the $^5D_4$ level.

$$\frac{R_{G/B}}{R_0} = 1 + \frac{W_{CR}}{W_0} \quad (3.14)$$

From the W_{CR}, W_0 and τ_1 values, it is possible to figure out the quantum efficiency (η) of the $^5D_3$ excited level by applying the Equations 2.2, and 3.15. These values are summarized in Table 3.8. The $^5D_3$ state quantum efficiency values are relatively high, especially those for the samples with low Tb percentages, and as expected, the quantum efficiency decreases as the Terbium concentration increases due to the CR process favored by the shortening of the Tb-Tb distance.

$$A_{nrad} = W_{CR} + W_0 \quad (3.15)$$

Table 3.8 Radiative decay probability (A_{rad}), non-radiative decay probability (A_{nrad}), total decay probability ($A_{rad+nrad}$) and $^5D_3$ state quantum efficiency (η) of BSYTb.

	$A_{rad+nrad}$ / 10^2 s^{-1}	A_{rad} / x10^2 s^{-1}	A_{nrad} / 10^2 s^{-1}	η($^5D_3$) / %
BS5Tb	6.76±0.09	2.9±0.3	3.9±0.3	42±1
BS4Tb	9.1±0.2	2.9±0.7	6.2±0.5	32±1
BS3Tb	7.5±0.5	2.9±0.3	4.6±0.2	38±1
BS2Tb	5.2±0.5	2.9±0.2	2.3±0.2	55±1
BS1Tb	4.5±0.8	2.9±0.1	1.7±0.1	63±1
BS0.5Tb	3.7±0.5	2.8±0.1	0.8±0.1	78±1
BS0.1Tb	3.0±0.5	2.85±0.05	0.12±0.02	95±1

Source: Reproduced from Bispo-Jr et al.[7]

In this context, considering the three main nonradiative pathways for the deactivation of the $^5D_3$ level in Tb-doped Ba_2SiO_4, the CR, multi-phonon relaxation, and electronic defects, we conclude that the first strongly influences at higher Terbium concentrations, but not at lower concentration, while the second barely influences due to its high energy position, and it is Terbium concentration independent; the last one is apparently constant for all samples.

3.4 Conclusions

The tunable blue-green emission of Tb^{3+}-doped Ba_2SiO_4 phosphors obtained as a monophasic material from the sol-gel route by changing the doping amount and the energy transfer properties were introduced in this chapter. Tb^{3+} replaces Ba^{2+} local sites with CN 9 and 10 in the matrix and the doping leads to distortions in the matrix network. The phosphors under excitation at 250 nm emit light in the blue spectral region from the $^5D_3$ level of Tb^{3+} at low doping concentrations, but the emitted color dislocates towards the green spectral region as the Tb amount increases. This effect is assigned to a dipole-dipole energy transfer between Tb neighbors that is favored at high-doping concentration. A new approach to calculate the Tb^{3+} $^5D_3$ quantum efficiency was proposed, and these values increase as the Terbium concentration decreases in the matrix. In this context, the color tunability from the green towards the blue spectral region and the high quantum efficiency qualify the phosphors for future application as coatings of UV-emitting LEDs.

3.5 References

This chapter was written according to the paper published by the authors in Journal of Luminescence (2019).[7]

[1] RATNAM, B. et al. Synthesis and luminescent features of $NaCaPO_4:Tb^{3+}$ green phosphor for near UV-based LEDs, Journal of Alloys and Compounds, 2013, v. 564, n.0, p.100–104.

[2] GANJI, S. R. R. et al. UV-A and UV-B excitation region broadened novel green color-emitting $CaGd_2ZnO_5:Tb^{3+}$ nanophosphors, RSC Advances, 2017, v. 5, n. 28, p. 22217–22223.

[3] ZHANG, Z.; WANG, Y.; ZHANG, J. A novel green-emitting VUV phosphor $Na_3YSi_3O_9:Tb^{3+}$, Materials Letters, 2008, v. 62, n. 6-7, p. 846–848.

[4] LIAO, J. et al. Hydrothermal synthesis and photoluminescence of $SrWO_4:Tb^{3+}$ novel green phosphor, Materials Research Bulletins, 2009, v. 44, n. 9, p. 1863–1866.

[5] JU, X. et al. Luminescence properties of $ZnMoO_4:Tb^{3+}$ green phosphor prepared via co-precipitation, Materials Letter, 2011, v. 65, n. 17-18, p. 2642–2644.

[6] DA-WEI, H. et al. VUV Luminescent Properties of M_2SiO_4 Re (M = Mg, Ca, Ba) (Re= Ce^{3+}, Tb^{3+}), Chinese Journal of Luminescence, 2007, v. 28, n. 0, p. 53-56.

[7] BISPO-JR, A.G. et al. Tunable blue-green emission and energy transfer properties in $Ba_2SiO_4:Tb^{3+}$ obtained from sol-gel method, Journal of luminescence, 2019, v. 214, n. 0, p. 116604-8.

[8] CARVAJAL, J. R. An Introduction to the Program FullProff 2000, 2008, CEA/Saclay, France.

[9] PATTERSON, A. L. The Scherrer Formula for X-Ray Particle Size Determination, Physical Review, 1939, v. 56, n. 10, p. 978-982.

[10] MURPHY, A. B. Band-gap determination from diffuse reflectance measurements of semiconductor films, and application to photo electrochemical water-splitting, Solar Energy Materials and Solar Cells, 2001, v. 91, n. 14, p. 1326–1337.

[11] KUBELKA, P.; MUNK, F. Ein Beitrag zur Optik der Farbanstriche, Zeitschrift für Technische Physik, 1931, v. 15, n. 0, p. 593–601.

[12] WENDLANDT, W. W. The thermal decomposition of the heavier rare earth metal chloride hydrates, Journal of Inorganic and Nuclear Chemistry, 1959, v. 9, n. 2, p. 136-139.

[13] KIMURA, T. Molten Salt Synthesis of Ceramic Powders, Advances in Ceramics - Synthesis and Characterization, Processing and Specific Applications, 2011, IntechOpen.

[14] Xue, P. et al. Recent progress in molten salt synthesis of low-dimensional perovskite oxide nanostructures, structural characterization, properties, and functional applications: A review, Journal of Materials Science & Technology, 2018, v. 34, n. 6, p. 914–930.

[15] LIN, L. et al. Luminescence properties and site occupancy of Ce^{3+} in Ba_2SiO_4: a combined experimental and ab, initio study, RSC Advances, 2017, v. 7, n. 41, p. 25685–25693.

[16] YAO, S.; XUE, L.; YAN, Y. Properties of Eu^{3+} luminescence in the monoclinic $Ba_2MgSi_2O_7$, Ceramics-Silikáty, 2011, v. 55, n. 3, p. 251-255.

[17] HUHEEY, J. B.; KEITER, E. A.; KEITER, R. L. Inorganic Chemistry: Principles of Structure and Reactivity: 4th ed.; Harper and Row Publishers: New York, 1993.

[18] HANDKE, M.; URBAN, M. IR and Raman spectra of alkaline earth metals orthosilicates, Journal of Molecular Structure, 1982, v. 79, n. 0, p. 353-356.

[19] SILVA, A. C. S. et al. Synthesis and structural characterization of Eu(III)-doped $Zn_7Sb_2O_{12}$, Journal of Materials Science, 2010, v. 45, n. 15, p. 4216-4223.

[20] CHEN, S. et al. Sol–gel synthesis and luminescent properties of M′-type $LuTaO_4:Eu^{3+}$ phosphors, Journal of Luminescence, 2013, v. 140, n. 0, 1-6.

[21] THEYVARAJU, D.; MUTHUKUMARAN, S.; ASHOKKUMAR, M. pH-induced modification on the structural, optical and morphological properties of $Zn_{0.94}Ni_{0.04}Mn_{0.02}O$ nanopowders, Journal of Materials Science: Materials in Electronics, 2013, v. 24, n. 12, 5189-5198.

[22] OLIVEIRA, H. F. N.; TRINCA, R. B.; GUSHIKEM, Y. Síntese e estudo de ortossilicatos de zinco luminescentes com aplicação da técnica sol-gel, Química nova, 2009, v. 32, n. 5, p. 1346-1349.

[23] KIM, G. C.; PARKA, H. L.; KIM, T. W. Emission color tuning from blue to green through cross-relaxation in heavily Tb^{3+}-doped $YAlO_3$, Materials Research Bulletin, 2001, v. 36, n. 9, p. 1603–1608.

[24] KIM, G. C. et al. Tuning Emission Colors Through Cross-Relaxation in Heavily Tb^{3+}-Doped $CaYAlO_4$, Journal of the Korean Physical Society, 1999, v. 34, n. 1, p. 97-99.

[25] ZHANG, J. et al. Interionic cross relaxation and tunable color luminescence in $KY_3F_{10}:Tb^{3+}$ nano/microcrystals synthesized by hydrothermal approach, Journal of Fluorine Chemistry, 2012, v. 144, n. 0, p. 1–6.

[26] GUO, N. et al. Color Tuning and Energy Transfer in Eu^{2+}/Mn^{2+}-Doped $Ba_3Y(PO_4)_3$Eulytite-Type Orthophosphate Phosphors, RSC Advances, 2015, v. 5, n. 58, 46517-46524.

[27] MALTA, O. L. Mechanisms of non-radiative energy transfer involving lanthanide ions revisited, Journal of Non-Crystalline Solids, 2008, 354, n. 42-44, p. 4770–4776.

[28] DEXTER, D. L.; SCHULMAN, J. H. Theory of Concentration Quenching in Inorganic Phosphors, The Journal of Chemical Physics, 1954, v. 22, n. 6, p. 1063– 1070.

[29] UITERT, L. G. Characterization of Energy Transfer Interactions between Rare Earth Ions, Journal of the Electrochemical Society, 1967, v. 14, n. 10, p. 1048-1053.

[30] BORUCA, Z. et al. Temperature and concentration quenching of Tb^{3+} emissions in $Y_4Al_2O_9$ crystals, Journal of Alloys and Compounds, 2012, v. 532, n. 0, p. 92-97.

[31] ZHANG, Z. H. et al. Blue-Green-Emitting Phosphor $CaSc_2O_4:Tb^{3+}$: Tunable Luminescence Manipulated by Cross-Relaxation, Journal of the Electrochemical Society, 2009, v. 156, n. 3, p. 193-196.

CHAPTER 4 – SOL-GEL SYNTHESIS OF Eu^{3+}-DOPED Ba_2SiO_4

4.1 Introduction

Eu^{3+}-doped orthosilicate phosphors, such as Ba_2SiO_4 and $BaZnSiO_4$, synthesized by the conventional solid-state reaction had already been investigated and showed interesting optical properties for applications in lighting.[1] However, reports on the use of Eu^{3+} in such systems are uncommon since Eu^{2+} is more suitable to substitute the divalent barium in silicate lattices. In addition, all reports on the Ba_2SiO_4:Eu^{3+} synthesis previously highlighted in Table 2.6, section 2.4, involve the solid-state route instead of the sol-gel methodology, that is considered a versatile and convenient low-temperature process to produce luminescent materials.[2]

Considering the sol-gel synthesis of Ba_2SiO_4:Eu^{3+}, one of the challenges to be overcome is the synthesis adjustment to yield single-phased Ba_2SiO_4, avoiding undesirable spurious phases, such as $BaCO_3$ and $BaSiO_3$. Therefore, we report in this chapter the synthesis of Ba_2SiO_4:Eu^{3+} via the sol-gel route, and its morphological, structural and spectroscopic characterization, aiming the improvement of its properties for applications as coatings of UV-emitting LEDs.

4.2 Experimental procedure

4.2.1 Ba_2SiO_4:Eu^{3+} synthesis.

Barium acetate ($Ba(CH_3COO)_2$, VETEC, 99.9%), europium oxide (Eu_3O_4, Aldrich, 99.99%), TEOS ($C_8H_{20}O_4Si$, Fluka, 99.9%), isopropyl alcohol (C_3H_8O, VETEC, 99.7 %), and acetic acid (CH_3COOH, VETEC, 97%) were used as reactants without any further purification.

Pure Ba_2SiO_4 and Eu^{3+}-doped Ba_2SiO_4 were synthesized via an adapted sol-gel route reported by us.[3,4] The experimental procedure for the synthesis of the SiO_2:Ba,Eu xerogel is the same previously reported for the SiO_2:Ba,Tb in section 3.2.1. The xerogel precursor samples were pre-calcined at 450 ºC with a heating ramp of 10 °C/min for 2 hours, and then, calcined at 1,100 °C with a heating ramp of 10 °C/min for 2 hours in an EDG muffle furnace in circulating air atmosphere.

The Eu^{3+} concentration was isoelectronic varied for the Eu^{3+}-doped Ba_2SiO_4 series and the stoichiometric amounts of each composition are pointed out in Table 4.1. The samples will be hereafter designated as BSXEu where X is the Eu doping percentage.

Table 4.1 Doping proportions and amounts of reagents added, assuming 2.0000 g of the product.

Name	Eu^{3+} doping			Structural formula	MW / g·mol^{-1}	$Ba(Ac)_2$ / ± 0.0002 g	Volume / ± 0.1 mL	
	%[a]	at%[b]	ch%[c]				$Eu(Ac)_3$*	TEOS**
BS5Eu	5	5.13	7.5	$Ba_{1.85}Eu_{0.1}SiO_4$	361.412(5)	2.6149	11.1	10.1
BS4Eu	4	4.08	6	$Ba_{1.88}Eu_{0.08}SiO_4$	362.494(4)	2.6494	8.8	10.0
BS3Eu	3	3.05	4.5	$Ba_{1.91}Eu_{0.06}SiO_4$	363.576(3)	2.6836	4.6	10.0
BS2Eu	2	2.02	3	$Ba_{1.94}Eu_{0.04}SiO_4$	364.658(2)	2.7175	4.3	9.9
BS1Eu	1	1.00	1.5	$Ba_{1.97}Eu_{0.02}SiO_4$	365.740(1)	2.7517	2.2	9.9
BS0Eu	0	-	-	Ba_2SiO_4	366.822(0)	2.7852	-	9.9

[a] Eu^{3+}-doping percentage in relation to 2 mols of Ba^{2+} in the undoped Ba_2SiO_4. [b] Eu^{3+}-doping percentage in relation to the total cation mol amount for each sample; [c] Eu^{3+}-doping percentage in relation to the total cation charge in each sample.

*0.05 mol·L^{-1}in acetic acid solution

**0.55 mol·L^{-1}in isopropyl alcohol solution.

Source: Reproduced from Bispo-Jr et al.[4]

The BS4Eu sample was also calcinated at 1,100 ºC for 10 hours in order to understand the impacts of the doping in the Ba_2SiO_4 network and to optimize the phase composition. Isostructural Ba_2SiO_4:Gd^{3+}(4%) calcined for 2 hours was also synthesized. These samples will be hereafter designated as Ln-X, where Ln = Eu or Gd and X = 2 h and 10 h indicates the duration of the thermal treatment at 1,100 ºC.

4.2.2 Characterization

Powder X-ray diffraction (XRD)

X-ray diffractograms of the BSXEu were obtained in the same equipment described in section 3.2.2.

For the Eu-2h and Eu-10h samples, the diffractograms were acquired in a PANalytical Empyrean diffractometer at 293 K, from 9.0000 º to 99.9000 º, step size of 0.0260 º, scan step time of 67.0650 s using CuKα radiation (1.54060 Å) in the Chemistry Department of University of Aveiro. The Refinement conditions are in Table 4.2.

Table 4.2 Refinement conditions obtained by using a polynomial – 5 order function for background level, and a Pseudo-Voight function for peak shape ($H^2 = U\,tan^2\theta + V\,tan\theta + W$).

	Eu-2h	Eu-10h		Eu-2h	Eu-10h
U	0.0000	0.0000	**cR_p (%)**	6.89	3.46
V	0.0000	0.0000	**cR_{wp} (%)**	9.79	4.57
W	0.0100	0.0100	**cR_{exp} (%)**	5.53	3.00
χ	1.768	1.519			

Source: Own authorship.

Fourier-transform infrared spectroscopy (FTIR)

FTIR analyses were carried out in the same equipment described in section 3.2.2.

Raman spectroscopy

Raman spectroscopy was carried out at in the same equipment described in section 3.2.2.

Scanning electron microscopy (SEM)

The measurements were performed in the same equipment described in section 3.2.2.

Diffuse reflectance spectroscopy (DR)

BSXEu samples were characterized in the same equipment described in section 3.2.2. For Eu-2h and Gd-2h samples, the RD spectra were carried out in a UV/visible absorption spectra Lambda 950 dual-beam spectrometer (Perkin-Elmer). The equipment is available in phantom-G group of the University of Aveiro under supervision of Professor Luis D. Carlos.

Photoluminescence (PL)

Photoluminescence measurements at 25 ºC for the BSXEu samples were carried out in in the same equipment described in section 3.2.2.

For the Eu-2h and Eu-10 h samples, high-resolution spectra were recorded from 14–300 K with a modular double-grating excitation spectrofluorimeter with a TRIAX 320 emission monochromator (Fluorolog-3, Horiba Scientific) coupled to a R928 Hamamatsu photomultiplier. The reciprocal Linear Dispersion is 2.66 $nm.mm^{-1}$, the excitation and emission slits were placed at 2 and 0.03 mm, respectively, resulting in bandpass of $\Delta\lambda = 0.079$ nm. Lifetime measurements for the Eu-doped samples were carried out by using a pulsed Xe arc lamp (6 mJ/pulse) coupled to a Kratos GM-252 monochromator and a Spex 1934 C phosphorimeter. The excitation and emission slits were placed at 2 and 0.1 mm, respectively, resulting in a bandpass of $\Delta\lambda =$ 0.27 nm. The equipment is available in phantom-G group of University of Aveiro under supervision of Professor Luis D. Carlos.

Absolute Emission Quantum Yield (*q*)

The absolute emission quantum yields of Eu-2h and Eu-10h samples were measured at 300 K using a system Quantaurus-QY Plus C13534 (Hamamatsu) with a 150 W xenon lamp coupled to a monochromator for wavelength discrimination, an integrating sphere as the sample chamber, and a multichannel analyzer for signal detection. The method is accurate to within 10%. The emission quantum yield is given by Equation 4.1, where N_{Em} and N_{Abs} are the number of photons emitted and absorbed by the sample, respectively; $\boldsymbol{I_{em}^{sample}}$ and $\boldsymbol{I_{em}^{reference}}$ are the emission intensities with and without a sample, respectively, in a wavelength interval (λ_1,λ_2); and $\boldsymbol{I_{ex}^{sample}}$ and $\boldsymbol{I_{ex}^{reference}}$ are the integrated intensities of the excitation radiation measured with and without a sample, respectively, in an excitation wavelength interval (λ_3,λ_4).

$$q = \frac{N_{Emi}}{N_{Abs}} = \frac{\int_{\lambda_1}^{\lambda_2} \frac{\lambda}{hc}\left(I_{Em}^{sample}(\lambda) - I_{Em}^{Reference}(\lambda)\right) d\lambda}{\int_{\lambda_3}^{\lambda_4} \frac{\lambda}{hc}\left(I_{Ex}^{sample}(\lambda) - I_{Ex}^{Reference}(\lambda)\right) d\lambda} \quad (4.1)$$

4.3 Optimization of Eu^{3+} concentration in $Ba_2SiO_4:Eu^{3+}$

4.3.1 Structural characterization

The X-ray patterns of the BSEu samples calcined at 1,100 °C for two hours, Figure 4.1 (a), correspond to the orthorhombic Ba_2SiO_4 (P_{nam}) (JCPDS 26-1403, number 62) crystalline phase.

Figure 4.1 (a) Powder X-ray diffractograms and (b) FTIR spectra of BSXEu samples.

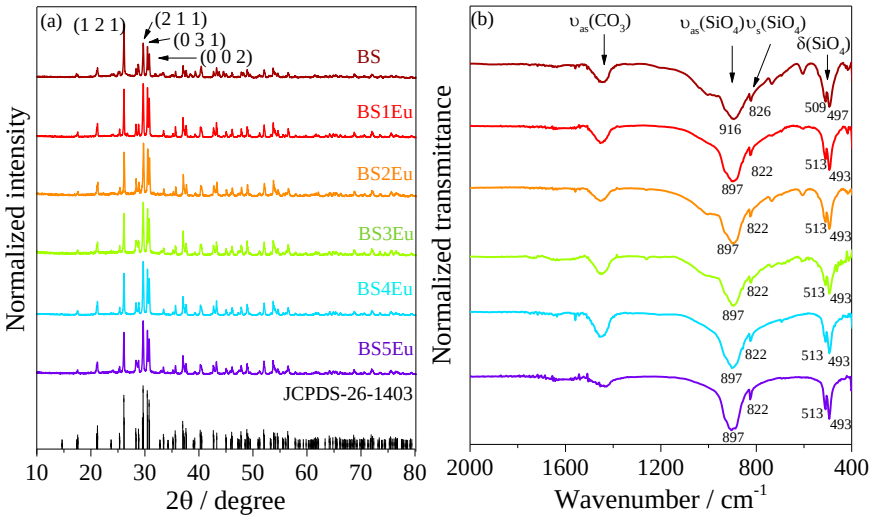

Source: Reproduced from Bispo-Jr et al.[4]

Regarding the limit of detection of the XRD technique, no diffraction peak characteristic of europium, barium, or silicon oxides is detected, corroborating to the fact that Eu^{3+} is inserted into the Ba_2SiO_4 lattice. Since no significant shifts for the interplanar distances are observed in the XRD, Figure 4.1 (a), Eu^{3+} probably occupies Ba^{2+} sites into the Ba_2SiO_4 lattice. Moreover, the well-defined diffraction peaks, Figure 4.1 (a), confirm that the sol-gel method was efficient to the synthesis of well-crystallized Ba_2SiO_4:Eu^{3+} under lower calcination temperature than other routes such as solid-state reactions reported by A. M. Pires et al. (1,200 °C for 12 hours),[1] or Z. Wang et al. (1,300°C for 3 hours).[5]

The crystallite size values shown in Table 4.3 are comparable to those ones reported for other oxide compounds prepared by the sol-gel method by applying high annealing temperatures (>1,000 ºC).[6,7] For some samples, it is observed a preferential growth of certain crystallographic planes, indicating that the crystallites are not spherical. The crystallite size does not vary for the (1 2 1) plane, yet, it increases for the (2 1 1) plane as the Eu^{3+} concentration increases and for the (0 3 1) plane, it increases for the BS1Eu, BS4Eu and BS5Eu samples. These modifications may be correlated to the defects generated in the Ba_2SiO_4 lattice minutely discussed for the BSTb series, section 3.3.1.

Table 4.3 Crystallite size (D, nm) for the three most intense planes of BSEu.

Plane	BS5Eu	BS4Eu	BS3Eu	BS2Eu	BS1Eu	BS
(1 2 1)	4(9)	4(9)	4(9)	4(9)	4(9)	4(9)
(2 1 1)	4(1)	4(0)	3(9)	3(7)	3(9)	3(7)
(0 3 1)	5(5)	4(5)	4(2)	4(1)	4(6)	4(4)

Source: Reproduced from Bispo-Jr et al.[4]

FTIR spectra of BSEu are shown in Figure 4.1 (b) and they exhibit bands assigned to vibrational modes related to the silicate tetrahedron. In addition, carbonate group vibrational modes are also observed in all IR spectra and they are assigned to the presence of carbonate ions on the surface of particles. It is also observed that the undoped silicate exhibits shifted ν_{as} (~916 cm^{-1}), ν_s (~826 cm^{-1}) and δ (~509 and ~ 497 cm^{-1}) bands compared to the doped samples, confirming that Eu^{3+} leads to structural defects in the Ba_2SiO_4 lattice.

In the Raman spectra shown in Figure 4.2, the bands observed at 910, 886, 851, 821, 519, 597, 370, and 350 cm^{-1} are assigned to the vibrational modes related to the silicate tetrahedron and the absence of bands at 559, 425, 385, 339, or 289 cm^{-1}

characteristics of Eu_2O_3 confirms the doping and the formation of a solid solution between Ba_2SiO_4 and Eu^{3+}.[8]

Figure 4.2 Raman spectra (300 K) of the BSEu samples. Laser 514 nm.

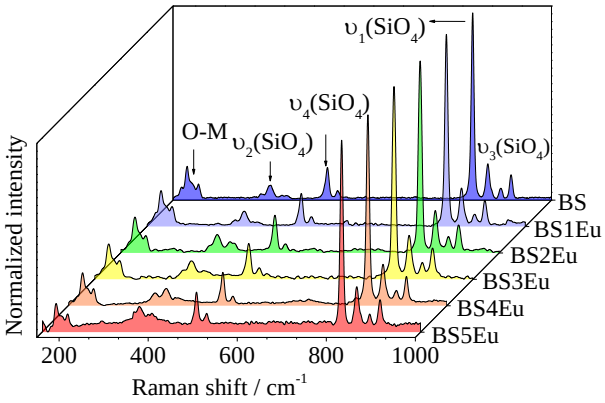

Source: Reproduced from Bispo-Jr et al.[4]

4.3.2 Morphology

A representative SEM image of the BS5Eu phosphor is shown in Figure 4.3 (a).

Figure 4.3 (a) SEM images of BS5Eu. Magnification of 5.000 x, EHT = 30 kV. (b) EDS spectrum of the BS5Eu sample. (c) Chemical mapping by EDS of BS5Eu sample monitoring Ba, Eu and Si atoms. (d) Superposition of the Ba (in red), Eu (in blue), and Si (in green) distribution on the BS5Eu sample surface.

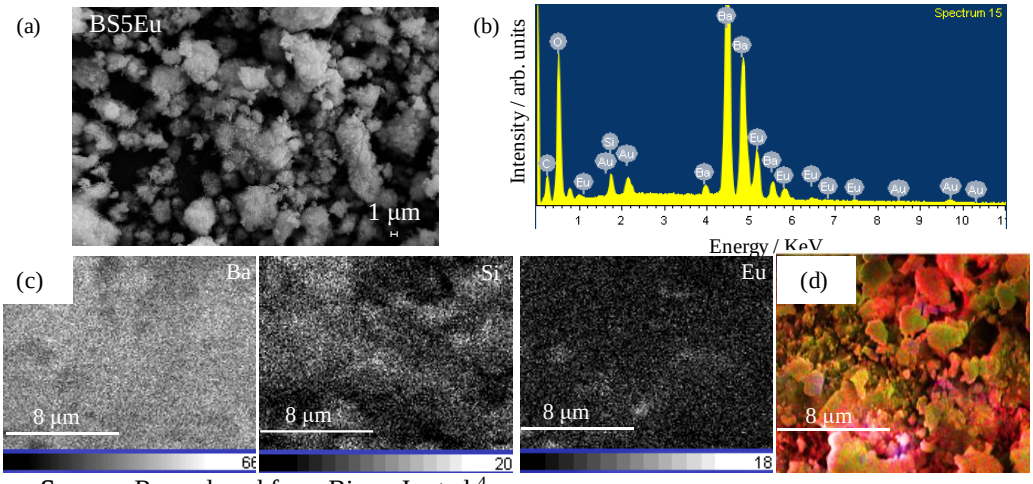

Source: Reproduced from Bispo-Jr et al.[4]

The BSEu phosphors exhibit irregularly shaped aggregate particles with nanowires on the surface, in accordance with the BSTb series, Figure 3.5, section 3.3.2. Also, Energy-dispersive X-ray spectroscopy (EDS), Figure 4.3 (b), confirms the presence of the elements Ba, Eu and Si on the particle surface and the chemical mapping performed

by EDS, Figures 4.3 (c) and (d), shows their homogeneous distribution in an agglomerate of particles

4.3.3 Band gap evaluation

UV-Vis diffuse reflectance (DR) spectra of the samples are viewed in Figure 4.4 (a), and a magnification from 310 to 500 nm range is provided in Figure 4.4 (b). Zhang et al. [9] reported diffuse reflectance measurements for Ba_2SiO_4 synthesized via the solid-state route. The DR spectrum profile recorded by them matches with those shown here for the samples obtained via the sol-gel route, except for slight differences that arise from the discrete morphology related to each synthetic methodology that directly affects the sample reflection profile.[9]

Figure 4.4 (a) UV-Vis diffuse reflectance spectra of BSEu. (b) Magnification of the region between 310-500 nm.

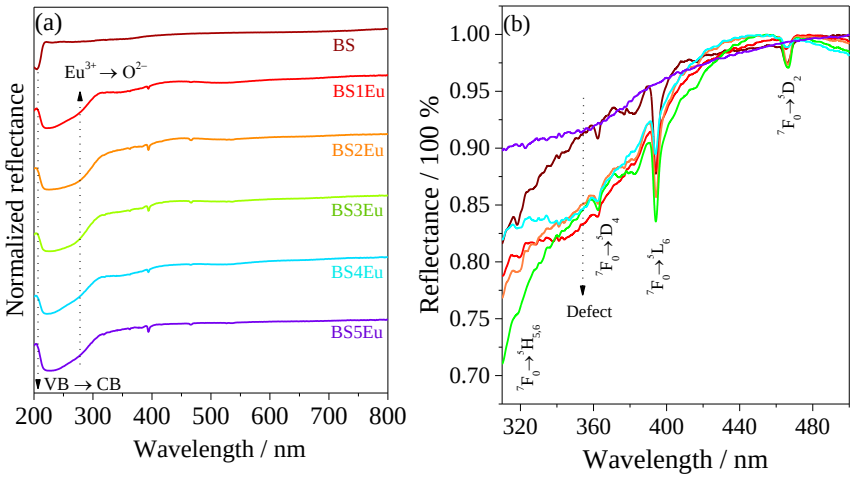

Source: Reproduced from Bispo-Jr et al.[4]

The BSXEu samples display the characteristic absorption lines of Eu^{3+} at 320, 362, 395 and 467 nm assigned to transitions from the $^7F_0$ ground state to the ^5H_J, $^5D_4$, $^5L_6$ and $^5D_2$ excited states, respectively. In addition, a smooth broadband observed at 360 nm is assigned to the Ba_2SiO_4 absorption,[9] and it is related to the presence of traps or intrinsic defects in the matrix. These defects may be generated, among other causes, by the thermal decomposition of organic material or by products of the sol-gel synthesis during the Ba_2SiO_4 lattice formation or through the calcination of samples.[10]

For the doped samples, the region corresponding to the matrix band, that is better viewed in Figure 4.4 (b), has its reflectance decreased, meaning a greater absorption

in relation to the undoped sample, except for the BS5Eu. This behavior indicates that Eu^{3+} contributes to the formation of defects in the Ba_2SiO_4 lattice, corroborating with FTIR data. Another effect that may contribute to formation of structural defects is the surface defects, as evidenced by SEM images, Figure 4.3, to which could justify the anomalous behavior of the BS5Eu sample among the others.

The DR spectra also exhibit a strong absorption in the higher-energy region with a maximum near to 225 nm related to transitions from the valence band (VB) to the conduction band (CB) that corresponds to the optical bandgap of the material. Thus, the bandgap values were evaluated according to the Kubelka-Munk's approximation previously shown in section 3.2.2, and the plots for the bandgap calculations are represented in Figure 4.5.

Figure 4.5 Bandgap calculation considering direct transition of the BSXEu samples.

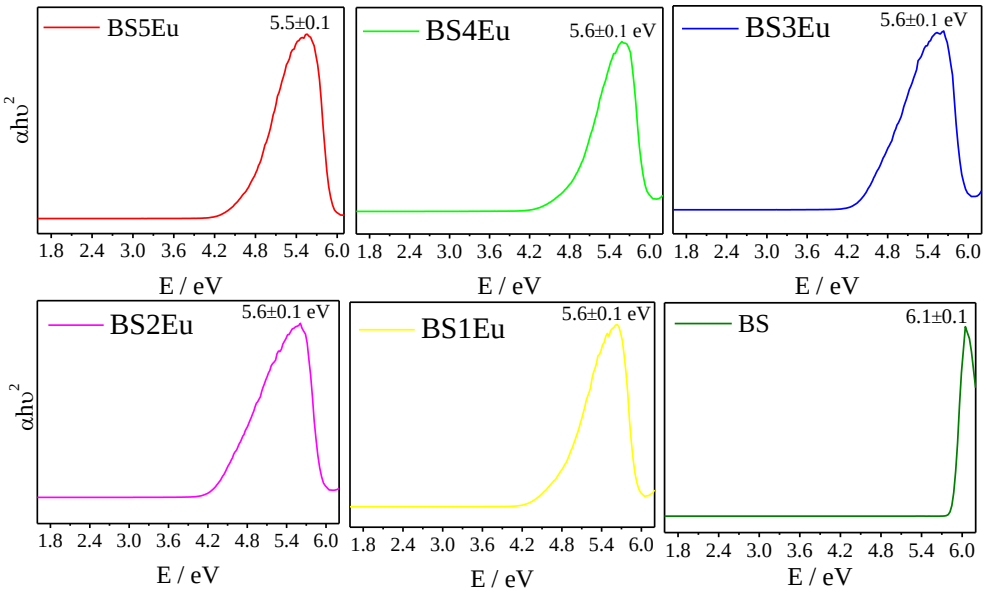

Source: Reproduced from Bispo-Jr et al.[4]

The bandgap value reported for the BS sample is relatively high and it is in accordance with the study previously reported by S. Z. Karazhanov et al.[11] for Zn_2SiO_4. The doping decreases the bandgap and it may be associated to the increase of the surface defect concentration for the doped samples, increasing the concentration of defect-related energy levels lying within the VB and CB. The slight modifications of the bandgap in the doped samples are also correlated to changes on the particle surface to which, in this case, is difficult to quantify due to the high agglomeration degree of the particles.

4.3.4 Photoluminescence

The excitation and emission spectra of the samples are viewed in Figure 4.6 (a) and 4.6 (b), respectively. A broad Eu^{3+}-O^{2-} charge transfer band (CTB) is observed below 300 nm in all excitation spectra, Figure 4.6 (a), as well as the expected narrow lines with lower relative intensity related to the *f-f* transitions of Eu^{3+}.

Figure 4.6 (a) Excitation spectra (300K, 612 nm), (b) emission spectra (300 K, 393 nm) and (c) 1931 *Commission Internationale d´Eclairage* (CIE) chromaticity diagram of the phosphors.[12]

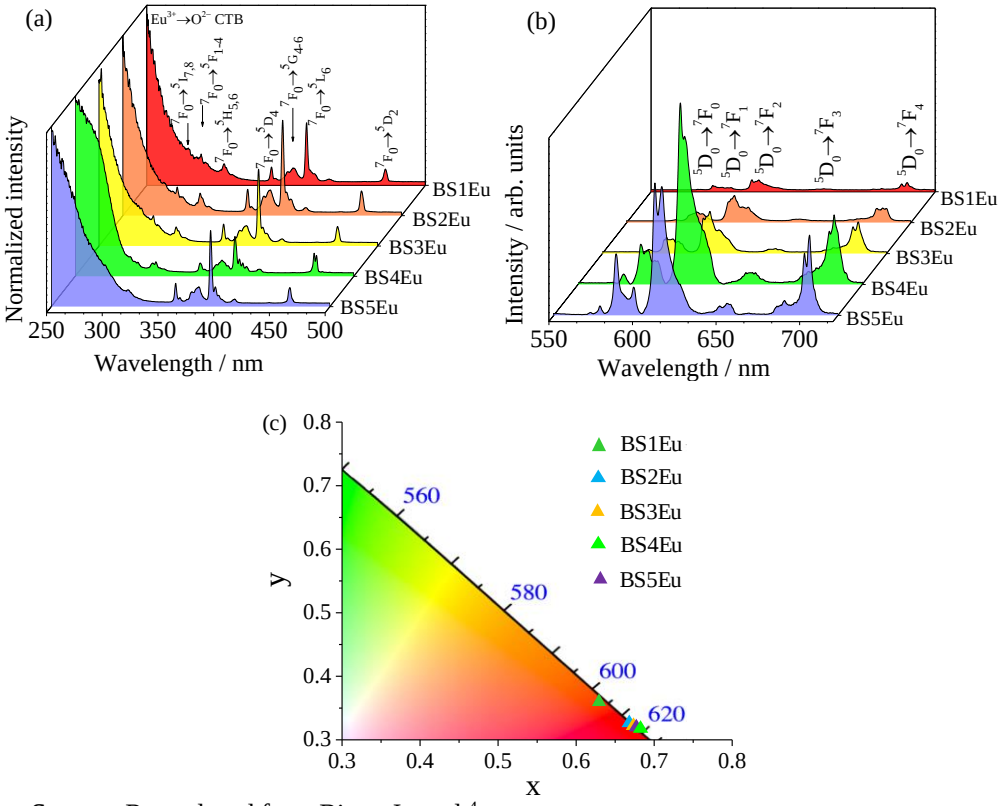

Source: Reproduced from Bispo-Jr et al.[4]

The emission spectra excited at 393 nm, Figure 4.6 (b), that corresponds to the $^7F_0 \rightarrow {}^5L_6$ transition of Eu^{3+}, exhibit the set of $^5D_0 \rightarrow {}^7F_{0,1,2,3,4}$ transitions in the red spectral region attributed to Eu^{3+} in low-symmetry local sites.[13] The BS4Eu sample displays the highest relative emission intensity, indicating that above this nominal doping percentage, luminescence quenching by concentration takes place. It is important to highlight that the 1,931 CIE chromaticity diagrams built for all produced phosphors, Figure 4.6 (c), guarantee high red color purity.

Therefore, as the BS4Eu sample displayed the best emission intensity, it was chosen to be fully characterized by selective excitation and emission spectra to understand

the impacts of the doping on the Ba_2SiO_4 network, and these results are discussed in the following sections.

4.4 Optimization of the calcination time

Powder XRD measurements were performed for the Eu-10h and Eu-2h samples (BS4Eu calcinated for 2 our 10 hours), Figure 4.7.

Figure 4.7 (a) Powder XRD of the Eu^{3+}-based phosphors calcined for 2 or 10 hours compared to the JCPDS-26-1403 Ba_2SiO_4 pattern (the asterisks represent the peaks assigned to the $BaSiO_3$ spurious phase). (b) Ba_2SiO_4 unit cell representation based on the CIF file available on Inorganic Crystal Structure Database (ICSD); Ba1 and Ba2 are the notation for sites with CN 9 and 10, respectively.

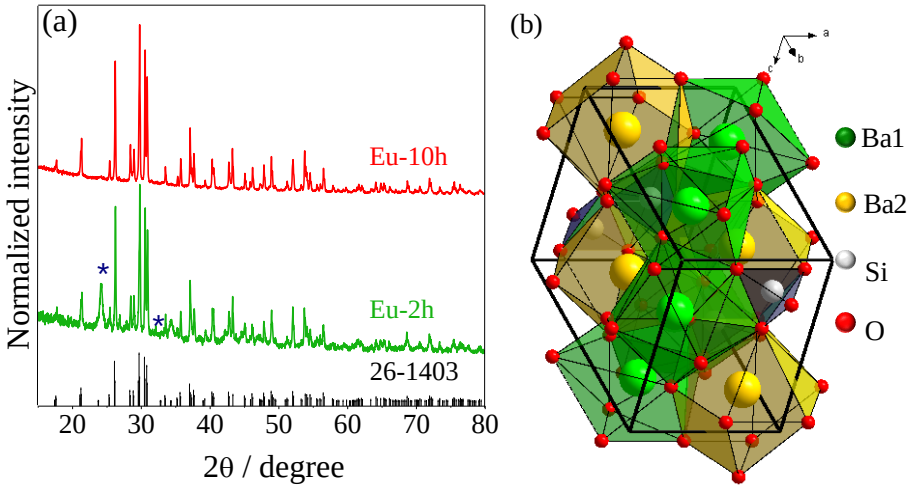

Source: Own authorship.

The diffraction profile related to the Eu-2h is indexed to the orthorhombic Ba_2SiO_4 phase (JCPDS 26-1403, number 62, P_{nma} space group) as the major phase (82.9 wt.%) and two other secondary phases were identified as β-$BaSiO_3$ (JCPDS 26-1402, number 19, $P2_12_12_1$ space group) (16.8 wt.%) and SiO_2 (quartz, JCPDS 46-1045, number 152, $P3_121$ space group) (0.3 wt.%). On the other hand, for the Eu-10h, only the orthorhombic Ba_2SiO_4 phase (JCPDS 26-1403) is noticed in the XRD pattern, regarding the concentration limit of detection of the XRD technique, proving that the increase of the calcination time is crucial to decrease the amount of spurious phases.

The $BaSiO_3$ formation observed in the case of Eu-2h is related to the Eu^{3+} doping since the stoichiometry of the material is different from the undoped system. According to the phase diagram of the BaO-SiO_2 binary mixture reported by M. E. Huntelaar *et al.*,[14] the suitable mol proportion of Si in relation to Ba to get the Ba_2SiO_4 without any spurious phases is 33.3 %, under 1,100 ºC. However, due to the doping with the activator ion, to

compensate the charge difference between Eu^{3+} and Ba^{2+}, the silicon mol number proportion becomes 35 %, allowing the formation of some $BaSiO_3$ phase. Because of this non-stoichiometry, it will be always possible to find some $BaSiO_3$ fraction in the phosphor composition regardless of the calcination condition, even below the limit detection of the XRD technique.

The standardized crystallographic data for the Eu-based samples are represented in Table 4.4 and they are in accordance with the data found in the literature for Ba_2SiO_4 [15] and $BaSiO_3$.[16] There are two crystallographic positions occurring in equal amounts for barium ions in the Ba_2SiO_4 structure with CN 10 or 9. In the $BaSiO_3$ lattice, barium ions occupy a single site with CN 8 and ionic radius of 142 pm.

Table 4.4 Refinement parameters obtained from the XRD measurement. The refinement factors converge to R_p = 6.89 %, R_{wp} = 9.79 %, and χ^2 =1.76 (Eu-2h) and R_p = 3.46 %, R_{wp} = 4.57 %, and χ^2 =1.51 (Eu-10h).

Sample	**Eu-2h**			**Eu-10h**
Phase	**Ba_2SiO_4**	**$BaSiO_3$**	**SiO_2**	**Ba_2SiO_4**
ICDD database code	04-011-2153	04-002-6752	04-015-7194	04-011-2153
Density / g·cm^{-3}	5.47	4.41	2.68	5.49
Mass absorption coefficient / cm^2	266.3	233.7	34.83	266.3
Weight fraction / %	82.8	16.8	0.3	100 %
Space group (No.)	*P*$_{nma}$ (62)	$P2_12_12_1$ (19)	$P3_121$ (152)	*P*$_{nma}$ (62)
Lattice parameters / Å	a = 7.5036 b = 5.8086 c = 10.217	a = 4.5964 b = 5.6079 c = 12.452	a = 4.8910 b = 4.8910 c = 5.3880	7.4931 5.80823 10.1874
Angle / °	α = β = γ = 90	α = β = γ = 90	α = β = 90, γ = 120	α = β = γ = 90
V/ 10^6 pm^3	445.09	320.97	111.60	443.37

Source: Own authorship.

Due to the charge compensation mechanism considered in the phosphor synthesis, structural defects may arise in the lattice since two Eu^{3+} replace three Ba^{2+}, as previously discussed in section 3.3.1. Due to the non-stoichiometry of the synthesis, it could be formed distorted Eu^{3+} or Ba^{2+} sites (local sites hereafter named as $Eu_{D1\text{-}D3}$) according to Avram et al.,[17] leading to the appearance of Eu^{3+} sites different from that of the usual replacement of Ba^{2+} in the Ba_2SiO_4 and $BaSiO_3$ structures (local sites hereafter named as $Eu_{1\text{-}3}$, Table 4.5). In this context, by considering the XRD data, we expect that Eu^{3+} occupies six non-equivalent sites ($Eu_{1\text{-}3}$ and $Eu_{D1\text{-}D3}$, Table 4.5) in the Eu-2h sample and four non-equivalent sites ($Eu_{1\text{-}2}$ and $Eu_{D1\text{-}D2}$) in the Eu-10h sample.

Table 4.5 Polyhedral information of the potential sites for Eu^{3+} substitution including coordination number (CN), site symmetry (Wyckoff) and notation in the text for the Eu^{3+} coordination sites.

Phase	Atom	CN	Notation for Eu ions	Defect-related site
Ba_2SiO_4	Ba_9	9	**Eu_1**	**Eu_{D1}**
	Ba_{10}	10	**Eu_2**	**Eu_{D2}**
$BaSiO_3$	Ba_8	8	**Eu_3**	**Eu_{D3}**

Source: Own authorship.

To infer the excitation optical paths, excitation spectra were monitored at 610.4 nm ($^5D_0 \rightarrow {}^7F_2$ transition) for Eu-2h and Eu-10h (Figure 4.8) exhibiting a broad excitation band in the deep-UV region assigned to the $Eu^{3+} \rightarrow O^{2-}$ charge transfer band (CTB) and narrow excitation lines attributed to the Laporte's forbidden Eu^{3+} *f-f* transitions.

Figure 4.8 Excitation spectra (300 K) monitored at 610.14 nm of Eu^{3+}-based phosphors.

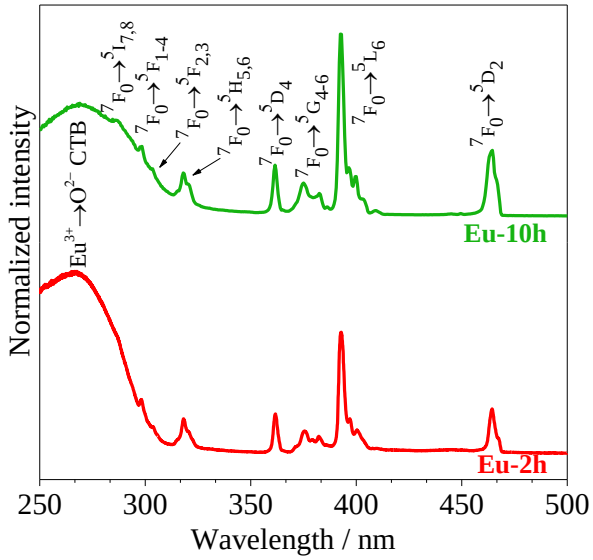

Source: Own authorship.

Under UV irradiation, the samples display an intense red emission color, as illustrated in Figure 4.9 (a) for Eu-10h. The phosphor emission spectra under 255 nm excitation reveal a series of Eu^{3+} transitions from the $^5D_0$ excited level to the ^7F_J (J = 0-4) levels, Figure 4.9 (c). The high number of components for each Eu^{3+} transition, that is, more than one component for the non-degenerated $^5D_0 \rightarrow {}^7F_0$ transition, readily indicates that Eu^{3+} is inserted in more than one non-equivalent local coordination site, as detailed below.

Figure 4.9 (a) Photo of the Eu-10 h sample under UV radiation exposition (255 nm). (b) Absolute emission quantum yield (*q*) compared to the excitation spectra of the Eu-10h sample. (c) Emission spectra (300 K, 255 nm). (d) 1,931 CIE chromaticity diagram of Eu-2h and Eu-10h.[12]

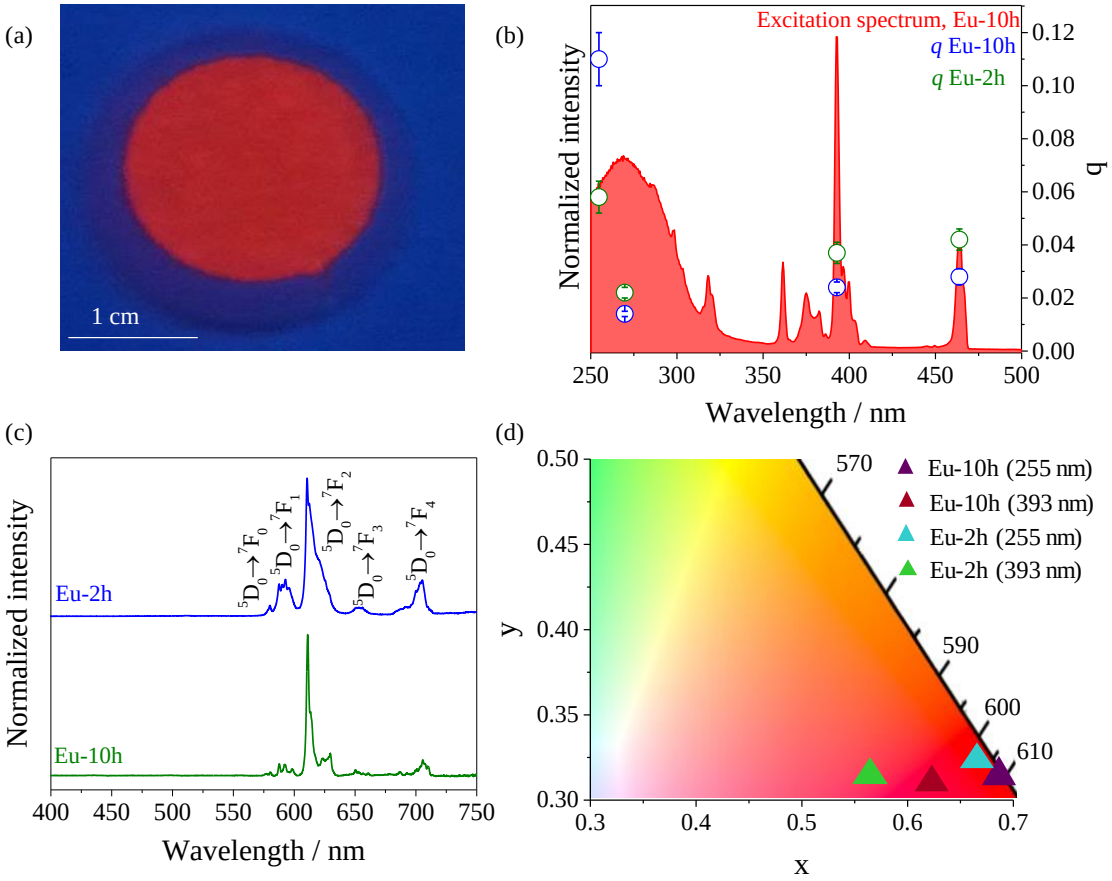

Source: Own authorship.

The red emission was quantified by the calculation of the *Commission Internationale d´Eclairage* (CIE) color coordinates for Eu-2h/Eu-10h as (0.659;0.324)/(0.686;0.315) and (0.569;0.316)/(0.622;0.310) under excitation at 255 nm and 393 nm, respectively, Figure 4.9 (d).

The absolute emission quantum yield (*q*) was measured as a function of the excitation wavelength, namely around 250 nm and within the *f-f* levels at 393 nm ($^5L_6$) and at 464 nm ($^5D_2$), Figure 4.9 (b). The maximum *q* values are found at 255 nm excitation and they increase from 0.058±0.006 to 0.11±0.01 as the calcination time increases from 2 hours to 10 hours, respectively. The achieved *q* values resemble those of other silicate-based Eu^{3+}-phosphors,[18] but are lower compared to classic Eu^{3+}-based phosphors, such as Y_2O_3:Eu^{3+} and YOF:Eu^{3+}, Table 4.6.[19]

Table 4.6 Emission quantum yield (*q*) for the Eu^{3+}-based phosphors. The excitation wavelength (λ_{exc}) is also indicated.

Sample	λ_{exc} / nm	*q**	Reference	Sample	λ_{exc} / nm	*q**	Reference
Eu-2h	255	0.058	-	$Y_2(MoO_4)_3:Eu^{3+}$	275	0.10	[20]
Eu-2h	393	0.037	-	$Bi_4Si_3O_{12}:Eu^{3+}$	271	0.145	[19]
Eu-2h	464	0.042	-	$Bi_4Si_3O_{12}:Eu^{3+}$	394	0.016	[19]
Eu-10h	255	0.11	-	$YOF:Eu^{3+}$	254	0.20-0.50	[19]
Eu-10h	393	0.024	-	$MgYBO_4:Eu^{3+}$	254	0.25-0.30	[19]
Eu-10h	464	0.028	-	$Y_2O_3:Eu^{3+}$	254	0.90	[19]
$YVO_4:Eu^{3+}$	310	0.07	[21]				

* The error is 10% of the absolute value.

Source: Own authorship.

4.5 High-resolution photoluminescence

To further discuss the Eu^{3+} local environments as function of the heat treatment, low-temperature (14 K) high-resolution emission spectra under 255 nm and 393 nm excitation were collected in the $^5D_0 \rightarrow {}^7F_0$ transition range, Figure 4.10.

Figure 4.10 (a) High-resolution emission spectra (14 K) monitoring different excitation wavelength in the $^5D_0 \rightarrow {}^7F_0$ transition region. (b) Representation of Eu^{3+} local sites (Eu_{1-3}, Eu_{D1-3} and $Eu_{A1,2}$).

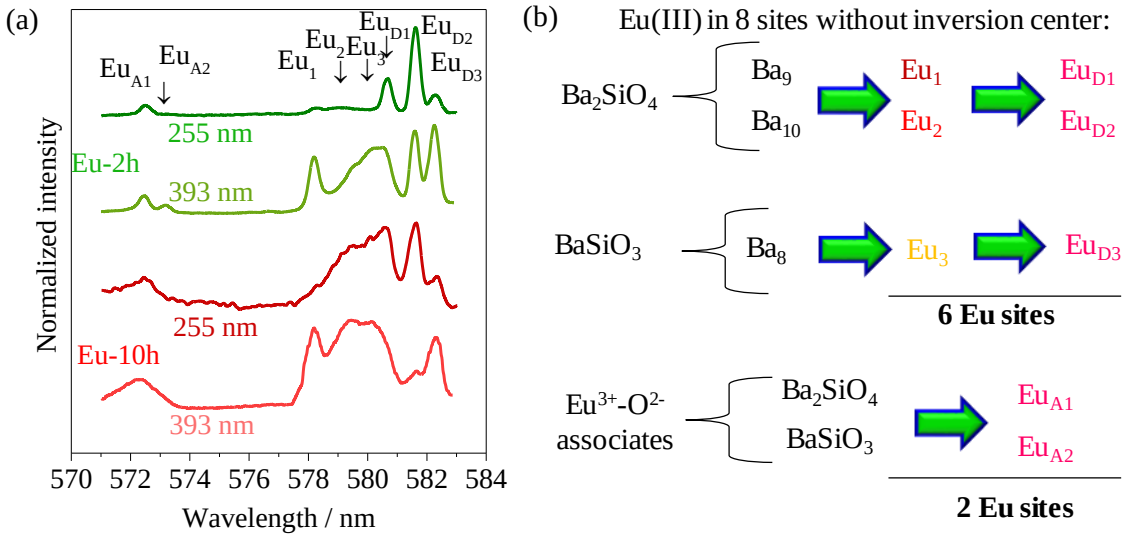

Source: Own authorship.

The $^5D_0 \rightarrow {}^7F_0$ transition exhibits at least five and eight components under excitation at 255 and 393 nm respectively, suggesting that Eu^{3+} is, at least, inserted in 8 non-equivalent local sites without inversion center.

In accordance, we note that the $^5D_0 \rightarrow {}^7F_1$ transition displays at least eight and eleven components at 255 and 393 nm excitation, respectively, Figure 4.11 (a). Likewise,

the $^5D_0 \rightarrow {}^7F_2$ transition in both Eu-2h and Eu-10h displays at least ten components in the emission spectra, Figure 4.11 (b).

Figure 4.11 High-resolution emission spectra (14 K) excited at 255 nm and 393 nm in the (a) $^5D_0 \rightarrow {}^7F_1$ and (b) $^5D_0 \rightarrow {}^7F_2$ transition region.

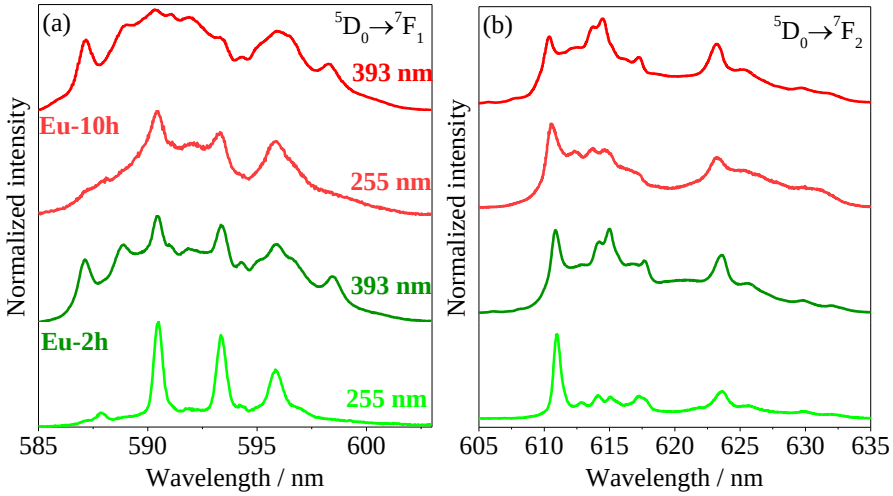

Source: Own authorship.

Focusing our attention into the eight components found for the $^5D_0 \rightarrow {}^7F_0$ transition, the components at 580.1 and 508.6 nm are tentatively assigned to the Eu_1 and Eu_2 local sites, respectively, Table 4.7 and Figure 4.10 (b), based on the changes in their intensities as the calcination time increases.

Table 4.7 Energy of the components for the $^5D_0 \rightarrow {}^7F_0$ transitions and $^5D_0$ lifetime (τ) values of each component excited at 393 nm (14 K) for the Eu-2h and Eu-10h.

Notation for Eu ions	Wavelength / ±0.08 nm	Energy / ±3 cm^{-1}	τ Eu-2h / ms	τ Eu-10h / ms
Eu_1	578.22	17,295	1.60±0.03	1.73±0.03
Eu_2	579.56	17,256	1.19±0.04	1.50±0.02
Eu_3	580.12	17,238	1.36±0.03	0.79±0.02
Eu_{D1}	580.62	17,223	1.22±0.03	1.13±0.01
Eu_{D2}	581.54	17,196	0.60±0.02	0.66±0.03
Eu_{D3}	582.35	17,173	0.28±0.02	0.11±0.02
Eu_{A1}	572.64	17,464	0.77±0.02	0.68±0.01
Eu_{A2}	573.13	17,448	0.69±0.01	-

Source: Own authorship.

By the XRD data, we would expect six and four non-equivalent $^5D_0 \rightarrow {}^7F_0$ components for the Eu-2h and Eu-10h samples, respectively. However, both samples show the same number of $^5D_0 \rightarrow {}^7F_0$ transitions with the same energy, Table 4.7, whose relative intensity variation indicates that there are some $BaSiO_3$ traces in the sample

composition, even for Eu-10h, evidencing the greater sensitivity of the spectroscopic technique in detriment of X-ray diffraction.

As the calcination time increases from 2 h to 10 h, the $^5D_0 \rightarrow {}^7F_0$ components at 580.1 (Eu_3), 580.6 (Eu_{D1}), 581.5 (Eu_{D2}) and 582.3 nm (Eu_{D3}) have their relative intensity decreased compared to the other components, Figure 4.10 (a). Besides that, the relative intensity of the components at 578.2 nm (Eu_1) and 579.5 nm (Eu_2) increases. These observations suggest that the components at 580.1 (Eu_3), 580.6 (Eu_{D1}), 581.5 (Eu_{D2}) and 582.3 nm (Eu_{D3}) correspond to the $BaSiO_3$ spurious phase or defect sites, and for the other 2 components, they arise from the Ba_2SiO_4 phase because the fraction of the $BaSiO_3$ phase decreases as the calcination time increases, according to the XRD data.

In order to further assign the other $^5D_0 \rightarrow {}^7F_0$ transition components, site-selective excitation spectra were monitored around each $^5D_0 \rightarrow {}^7F_0$ position, Figure 4.12.

Figure 4.12 Excitation spectra (14 K) of the (a) Eu-2h and (b) Eu-10h samples monitored at distinct wavelengths around the $^5D_0 \rightarrow {}^7F_0$ transitions. CTB1 arises from Eu in Ba sites, CTB2 comes from Eu^{3+}-O^{2-} associates and the black arrows represent the two components for the CTB1.

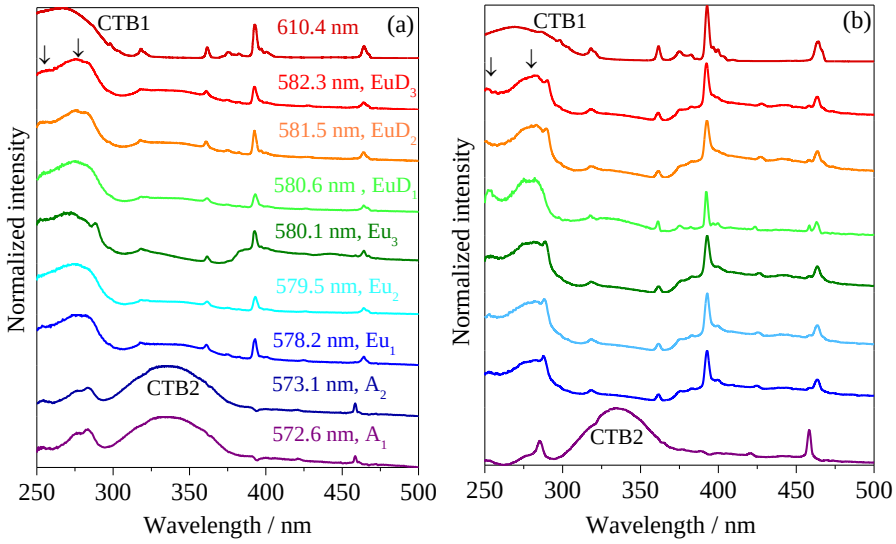

Source: Own authorship.

For monitoring wavelengths around 578.2 nm (Eu_1), 579.6 nm (Eu_2), 580.1 nm (Eu_3), 580.6 nm (Eu_{D1}), 581.5 nm (Eu_{D2}), and 582.3 nm (Eu_{D3}), the excitation spectra are similar, Figure 4.12, indicating analogous $^5D_0$ population paths being tentatively ascribed to Eu^{3+} located within the Ba_2SiO_4 or $BaSiO_3$ matrices. For these components, it is also possible to distinguish two different bands in the excitation spectra at 255 nm and 275 nm assigned to the CTB arising from the Eu replacing Ba sites in the Ba_2SiO_4 or $BaSiO_3$ matrices (CTB1).

It is feasible to assign the CTB1 band at 275 nm in Figure 4.12 to the Eu_{D1-3} sites, since the CN of the defect-related sites are lower than the Eu_{1-3} ones according to Voort Dirksen, and Blasé,[22] and it is well-known that a decrease in the number of ligands around Eu^{3+} leads to a decrease in the CTB energy.[23] This premise confirms that the sites at 578.2 (Eu_1), 579.5 (Eu_2) and 580.1 (Eu_3) nm come from the Ba_2SiO_4 or $BaSiO_3$ structures since they are not in the emission spectra under 255 nm excitation for the Eu-2h, Figure 4.10, but they are noticed for the Eu-10h, where the concentration of Eu_{1-3} local sites is larger than for the Eu-2h.

Regarding the $^5D_0 \rightarrow {}^7F_0$ components at 572.6 (Eu_{A1}) and 573.1 nm (Eu_{A2}), their excitation spectra, Figure 4.12, display a broadband peaking around 330 nm (hereafter designated as CTB2) quite different from that found in the excitation spectra monitored within the other $^5D_0 \rightarrow {}^7F_0$ components. This red-shifted CTB2 resembles the CTB already observed in the excitation spectra of Eu^{3+}-O^{2-} associates,[24] suggesting that in the Eu_{A1} and Eu_{A2} sites, Eu^{3+} is bonded to oxygen ions that do not belong to the silicate network.

The formation of Eu^{3+}-O^{2-} associates is usually related to a charge compensation mechanism but they still may be formed in cases that the matrix is rather loosely packed or contain chains formed by M-O polyhedral with unfilled spaces that may locate oxygen ions in their interstices.[25] In the present case, whereas the Ba_2SiO_4 and $BaSiO_3$ matrices in fact contain Ba-O polyhedral chains with unfilled spaces, it is feasible to assign the arising of the Eu^{3+}-O^{2-} associates to this explanation, i.e., both components at 572.6 (Eu_{A1}) and 573.1 nm (Eu_{A2}).

Selective emission-spectra were carried out monitoring the CTB2, Figure 4.13.

Figure 4.13 High-resolution emission spectra (14 K) monitoring different excitation wavelengths. The * represents the $^5D_0 \rightarrow {}^7F_2$ transition components that come from the Eu_{A1} and Eu_{A2} local sites.

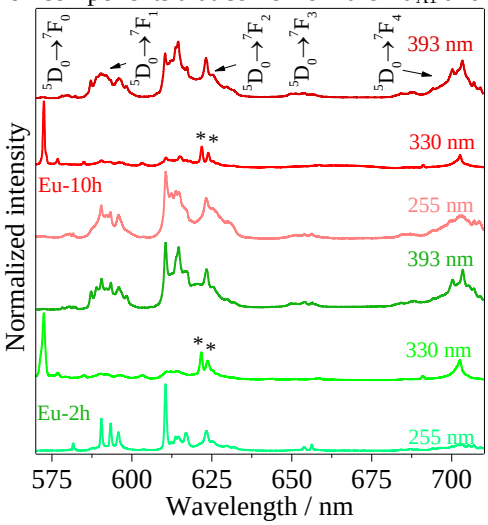

Source: Own authorship.

Under excitation at 330 nm (CTB2), the anomalous $^5D_0 \rightarrow {}^7F_0$ transition at 572.6 nm (Eu_{A1}) dominates the emission profile, Figure 4.13. This behavior is characteristic of the Eu^{3+}-O^{2-} associate emission according to the literature.[22,24,25] There are also two components of the $^5D_0 \rightarrow {}^7F_2$ transition at 621.8 and 623.9 nm that cannot be seen in the emission spectra under 255 nm excitation, Figure 4.13, but they are noticed under 330 nm excitation, suggesting that they come from the Eu^{3+}-O^{2-} associate sites.

To further discuss the nature of the CT bands at 255 nm, 275 nm and 330 nm in the excitation spectra (Figure 4.12), the diffuse reflectance spectra of the isostructural Gd-2h sample was carried out, Figure 4.14. The energy of the Gd^{3+} excited levels is much higher than the typical energy of defects-related bands, inhibiting any energy transfer process, and therefore the spectrum of Gd-2h is free from any CTB contribution.[26]

Figure 4.14. (a) Diffuse reflectance spectra of Eu-2h and Gd-2h samples. (b) Arithmetic difference between the Eu-2h and Gd-2h-related reflectance spectra within the range of 200-360 nm. CTB1 comes from Eu inserted in Ba sites and CTB 2 arises from Eu^{3+}-O^{2-} associates.

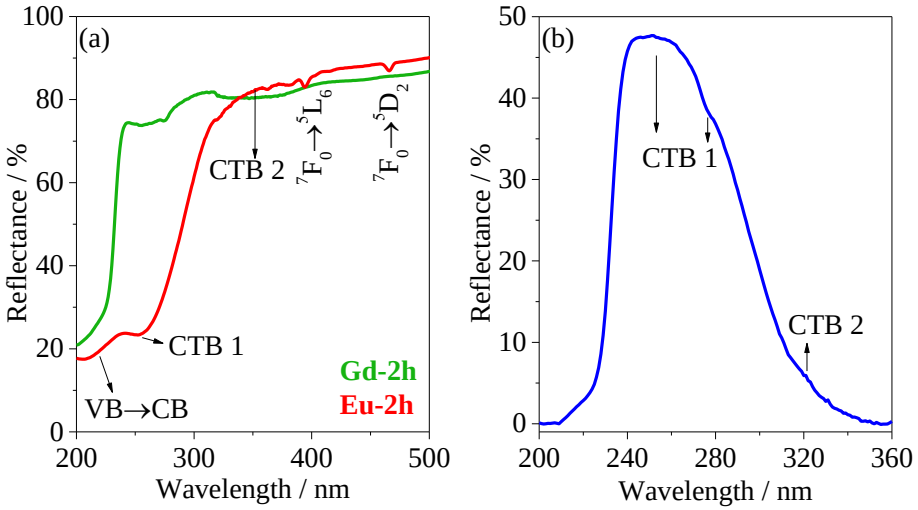

Source: Own authorship.

The diffuse reflectance spectrum of Eu-2h, Figure 4.14 (a), reproduces that one previously reported for the same sample, Figure 4.4. Regarding the two bands at about 250 nm and 320 nm, the spectrum of the Eu-2h is compared with that of the analogous Gd-2h. Interestingly, the arithmetical difference between them, Figure 4.14 (b), reveals two bands at 250 nm (CTB1) and 320 nm (CTB2) confirming that they arise from CT processes between the matrix and Eu^{3+}, supporting the assignments in the excitation spectra, Figure 4.12. The band at 250 nm (CTB1) also displays two components at 255 nm and 275 nm, in accordance with the previously shown excitation spectra, Figure 4.12.

To further examine the nature of each Eu^{3+} local site, selective emission decay curves (Figures 4.15, 4.16 and 4.17) were monitored around each of the eight $^5D_0 \rightarrow {}^7F_0$ components at 14 K, since at 300 K, it is not possible to distinguish all the eight $^5D_0 \rightarrow {}^7F_0$ components.

Figure 4.15 Emission decay curves (14 K) excited at 393 nm and monitored at distinct wavelengths around the $^5D_0 \rightarrow {}^7F_0$ transitions for the Eu-2h sample. The solid lines correspond to the data best fit (R^2>0.9), using a single exponential function. The insert in the figures represents residual plots.

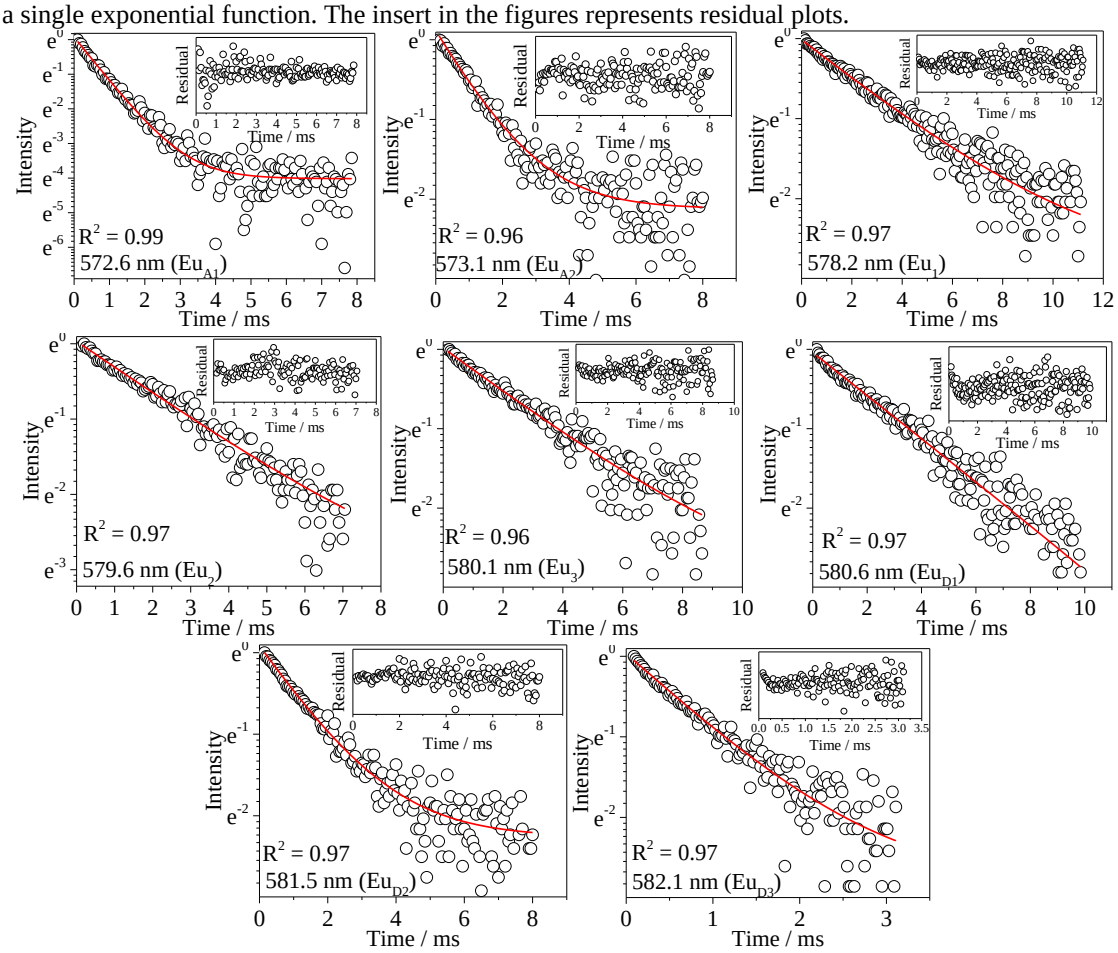

Source: Own authorship.

Figure 4.16 Emission decay curves (300 K) excited at 393 nm and monitored at 578.2 nm for the Eu-2h sample. The solid line corresponds to the data best fit (R^2>0.9), using a biexponential function. The insert in the figure represents residual plots.

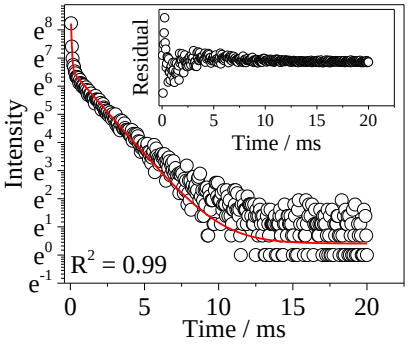

Source: Own authorship.

Figure 4.17 Emission decay curves (14 K) excited at 393 nm and monitored at distinct wavelengths around the $^5D_0 \rightarrow {}^7F_0$ transitions for the Eu-10h sample. The solid lines correspond to the data best fit (R^2>0.9), using a single exponential function. The insert in the figures represents residual plots.

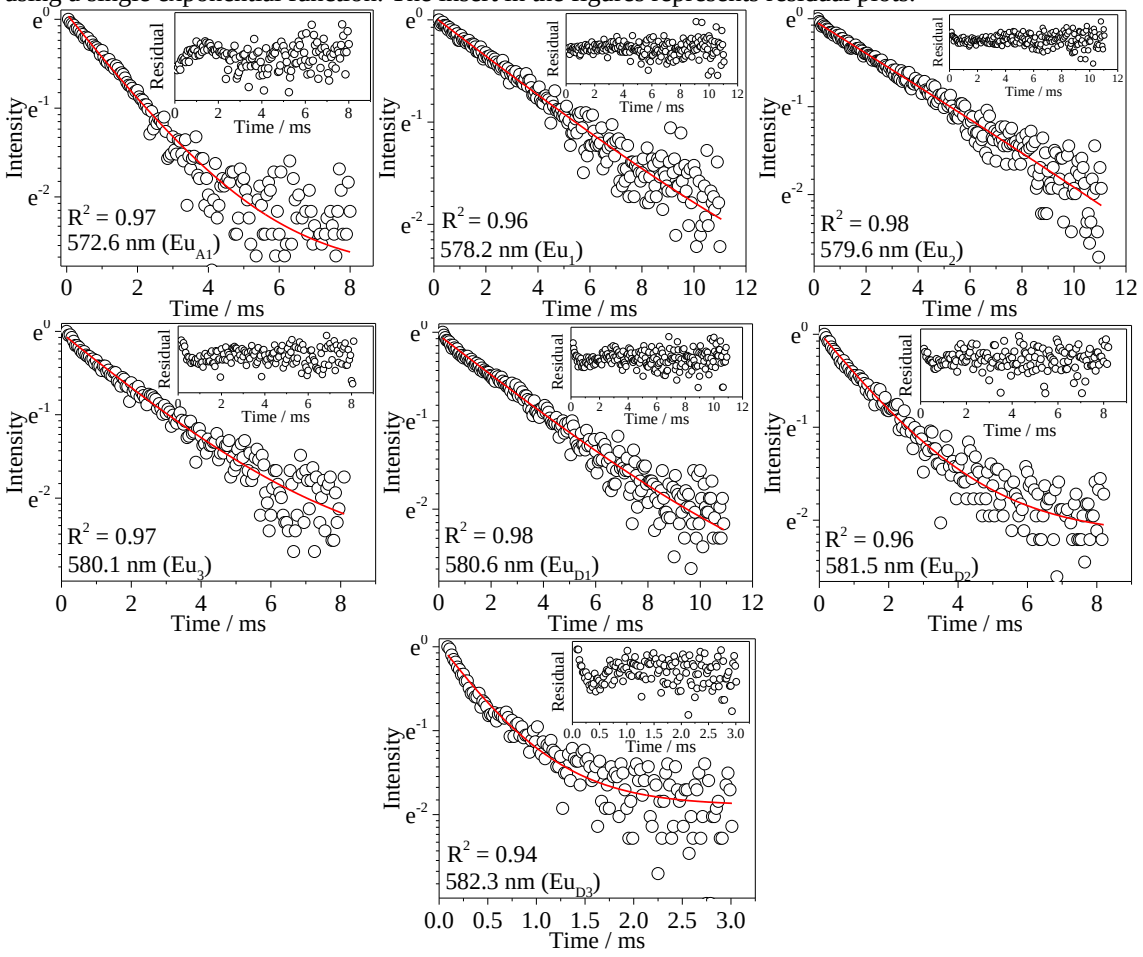

Source: Own authorship.

All the decay curves measured at 14 K, Figures 4.15 and 4.17, reveal a single exponential behavior in good agreement with experimental site-selective conditions. From the data best fit, the $^5D_0$ lifetime (τ) values were calculated for each Eu^{3+} local environment, Table 4.7. The $^5D_0$ lifetime values (14 K) for $Eu_{1\text{-}3}$ local sites are similar to those found in other silicate-based matrices,[27,28] and for the Eu_{A1} and Eu_{A2}**,** they are faster, in accordance with the Eu^{3+}-O^{2-} associate assignment.[24]

The distinct values found for the $^5D_0$ lifetime at 14 K (Eu-2h) compared to those ones at 300 K, Figure 4.16, give further evidence for the proposed assignment of the 8 Eu^{3+}-local sites. However, it was only possible to estimate the $^5D_0$ lifetime value (300 K) for the component at 578.2 nm (Eu_1) through a biexponential fit, Figure 4.16 due to the superposition of the Eu_1 and Eu_2 components at 300 K; therefore, the values obtained through the biexponential fit may be associated with the Eu_1 and Eu_2 local sites.

The $^5D_0$ lifetime values at 300 K of the Eu_1 and Eu_2 local sites (Eu-2h) are to be found as 1.55±0.04 ms and 0.0568±0.005 ms and they are shorter than the values found at 14 K, Table 4.7. Attending to the fact that the experimental transition probability may be expressed as $\tau^{-1}=\tau_{nr}^{-1}+\tau_r^{-1}$, where τ_{nr} and τ_r represent the non-radiative and radiative lifetimes, respectively, and that at 14 K, $\tau^{-1}\sim\tau_r^{-1}$, the increase in τ as the temperature decreases suggests the presence of competing thermally activated non-radiative mechanisms.

Eu^{3+} at defect-related local sites usually are characterized by longer τ_{nr} due to the semi-filled coordination sphere, as previously reported,[29,30,31] since the oxy vacancies lead to a higher network vibration degree around Eu^{3+}. Linked to this observation, by the previously introduced definition of lifetime in the last paragraph, a decrease of τ_{nr} value entails to a decrease in the lifetime value.

In this way, it is feasible to correlate the shortest lifetimes of the $^5D_0$ state monitored around the components at 580.6 (Eu_{D1}), 581.5 (Eu_{D2}) and 582.3 nm (Eu_{D3}) to Eu^{3+} sites associated to the structural defects. In fact, previously (Table 4.7), we concluded that the components at 578.2 nm (Eu_1) and 579.5 nm (Eu_2) come from Eu^{3+} in the usual sites of the Ba_2SiO_4 network and the lifetime values are in accordance with this assignment. In addition, by increasing calcination time to 10 h, the lifetime of the $^5D_0\rightarrow{}^7F_0$ components at 578.2 (Eu_1) and 579.5 nm (Eu_2) enhances.

As the temperature is a crucial parameter in what concerns the balance between the radiative and non-radiative lifetime values, high-resolution emission spectra were measured by changing the temperature from 14 K up to 300 K, Figure 4.18, in the next page. The $^5D_0\rightarrow{}^7F_0$ lines at 580.6 (Eu_{D1}), 581.5 (Eu_{D2}) and 582.3 nm (Eu_{D3}) are favored only at low temperatures, Figure 4.18 (a), when the non-radiative losses are minimized. This observation is in accordance with our previous assignment for the nature of the $^5D_0\rightarrow{}^7F_0$ transition components.

Already the components at 590.4 ($^5D_0\rightarrow{}^7F_1$ transition), 593.3 ($^5D_0\rightarrow{}^7F_1$ transition), 595.8 ($^5D_0\rightarrow{}^7F_1$ transition), 610.4 ($^5D_0\rightarrow{}^7F_2$ transition) and 623.9 nm ($^5D_0\rightarrow{}^7F_2$ transition) reveal analogous thermal dependence, Figures 4.18 (b) and (c), thus, being related to the Eu_{D1-2} local sites.

Figure 4.18 Temperature-dependent emission spectra monitored at 393 nm of the Eu-2h phosphor in the (a) $^5D_0 \rightarrow {}^7F_0$, (b) $^5D_0 \rightarrow {}^7F_1$ and (c) $^5D_0 \rightarrow {}^7F_2$ transition region. The black arrows represent the transition components that disappear as the temperature increases.

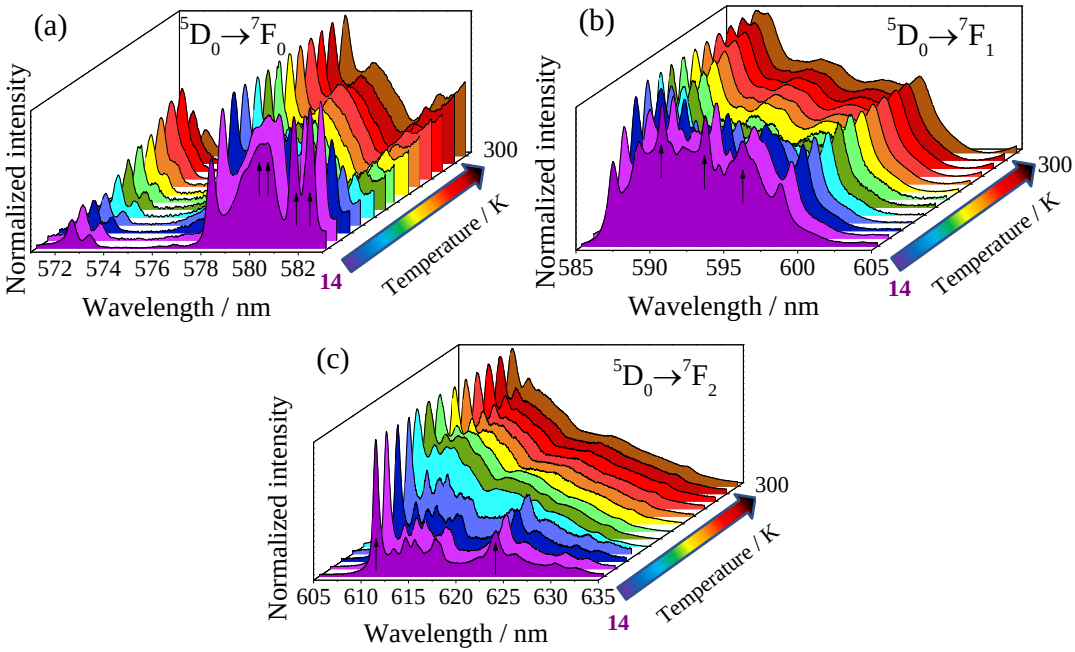

Source: Own authorship.

Finally, the finds reported in this chapter confirm that the best condition for the $Ba_2SiO_4:Eu^{3+}$ synthesis is the Eu^{3+} doping with 4 % and calcination temperature at 1,100 ºC for 10 hours, where the concentration of $BaSiO_3$ spurious phase and defect-related local sites decreases. Therefore, due to the absorption of the phosphors near to 250 nm, they may be used as coatings of deep-UV-emitting LEDs (250 nm), making prototypes that feature both red light and UV radiation emission desirable in indoor farms.

4.6 Conclusions

Herein, $Ba_2SiO_4:Eu^{3+}$ phosphors were synthesized by the sol-gel route using softer condition than the standard solid-state route that requires higher temperatures and longer synthesis time. Besides that, a detailed spectroscopic study not reported yet was provided for this system by using Eu^{3+} as spectroscopic probe, proving that Eu^{3+} is inserted in at least 8 non-equivalent local sites in this structure, 2 coming from the Ba_2SiO_4 matrix, 1 in the $BaSiO_3$ spurious phase, 3 defect-related local sites due to the charge compensation and 2 sites arising from Eu^{3+}-O^{2-} associates, being that these oxy anions do not belong to the matrix. Under 250 nm excitation, the phosphors exhibit an intense red-light emission due to the Eu^{3+} *f-f* transitions, and the 4 %-doped sample shows the highest relative

emission intensity and emission quantum yield, making it the most suitable to be applied as coatings of deep-UV emitting LEDs.

4.7 References

This chapter was written within the scope of two papers published by the authors in RSC advances (2016)[3] and (2017)[4] and another paper submitted to ECS Journal of Solid State Science and Technology (2019)[32].

---

[1] PIRES, A. M.; DAVOLOS, M. R. Luminescence of Europium(III) and Manganese(II) in Barium and Zinc Orthosilicate, Chemistry of Materials, 2001, v. 13, n. 1, p. 21-27.

[2] RITTER, B. ET AL. Nanoscale CaF_2 doped with Eu^{3+} and Tb^{3+} through fluorolytic sol–gel synthesis, Journal of Material Chemistry C, 2014, v, 2, n. 40, p. 8607–8613.

[3] RAYMUNDO-PEREIRA, P. A. et al. Study on the structural and electrocatalytic properties of Ba^{2+}- and Eu^{3+}-doped silica xerogels as sensory platforms, RSC Advance, 2016, v. 6, n. 106, p. 104529–104536.

[4] BISPO-JR, A. G. et al. Red phosphor based on Eu^{3+}-isoelectronically doped Ba_2SiO_4 obtained via sol–gel route for solid state lightning, RSC Advances, 2017, v. 7, n. 85, p. 53752–53762

[5] WANG, Z. et al. Luminescent properties of Ba_2SiO_4:Eu^{3+} for white light emitting diodes, Physica B Condensed Matter, 2013, v. 411, n. 0, p. 10–113

[6] XIA, G. et al. Sol–gel combustion synthesis and luminescent properties of nanocrystalline YAG:Eu^{3+} phosphors, Journal of Crystal Growth, 2005, v. 283, n. 1-2, p. 257-262.

[7] PARK, C. H. et al. VUV excitation of $Y_3Al_5O_{12}$:Tb phosphor prepared by a sol-gel process, Journal of Materials Science Letters, 2000, v. 19, n. 4, 335-338,

[8] ABRASHEV, M. V.; TODOROW, N. D.; GESHEW J. Raman spectra of R_2O_3 (R—rare earth) sesquioxides with C-type bixbyite crystal structure: A comparative study, Journal of Applied Physics,2014, v. 116, n. 0, p. 103508-7.

[9] ZHANG, M. et al. Optical properties of Ba_2SiO_4:Eu^{2+} phosphor for green light-emitting diode (LED), Materials Research Bulletin, 2007, v. 42, n. 1, 33.

[10] BARTHOU, C. et al. Mn^{2+} Concentration Effect on the Optical Properties of Zn_2SiO_4:Mn Phosphors, Journal of The Electrochemical Society, 1994, v. 141, n. 2, p. 524-528.

[11] KARAZHANOV, S. Z. et al. Electronic structure and optical properties of $ZnSiO_3$ and Zn_2SiO_4, Journal of Applied Physics, 2009, v. 106, n. 0, p. 123701-7.

[12] SANTA-CRUZ, P. A.; TELES, F. S. Spectra Lux Software. Versão 1.0 RENAMI, 2003, U. Federal de Pernambuco.

[13] CARNALL, W. T. et al. A systematic analysis of the spectra of the lanthanides doped into single crystal LaF_3, The Journal of Chemical Physics, 1989, v. 90, n. 0, p. 3443-3457.

[14] ROMERO-SERRANO, A. et al. Thermodynamic Modeling of the BaO–SiO_2 and SrO–SiO_2 Binary Melts, Glass Physics and Chemistry, 2010, v. 36, n. 2, p. 171–178.

[15] DENAULT, K. A. et al. Average and Local Structure, Debye Temperature, and Structural Rigidity in Some Oxide Compounds Related to Phosphor Hosts, ACS Applied Materials and Interfaces, 2015, v. 7, n. 13, p. 7264−7272.

[16] JIA, Y. et al. Sunlight activated new long persistent luminescence phosphor $BaSiO_3$:Eu^{2+},Nd^{3+},Tm^{3+}: Optical properties and mechanism, Materials and Design, 2016, v. 90, n. 4, p. 218–224.

[17] AVRAM, D. et al. Toward a Unified Description of Luminescence−Local Structure Correlation in Ln Doped CeO_2 Nanoparticles: Roles of Ln Ionic Radius, Ln Concentration, and Oxygen Vacancies, Journal of Physics Chemistry C, 2015, v. 119, n.28, p. 16303−16313.

[18] ZHANG, Y. et al. Eu^{3+}-doped $Bi_4Si_3O_{12}$ red phosphor for solid state lighting: microwave synthesis, characterization, photoluminescence properties and thermal quenching mechanisms, Scientific Reports, 2017, v. 7, n. 0, p. 42464-12.

[19] YENAND, W. M.; WEBER, M. J. Inorganic phosphors compositions, preparation and optical properties, The CRC Press Laser and Optical Science and Technology Series, 2004.

[20] BISPO-JR, A. G. et al. Red phosphor based on Eu^{3+}-doped $Y_2(MoO_4)_3$ incorporated with Au NPs synthesized via Pechini's method, 2018, Optical Materials. 2018, v. 84, n. 0, p. 137–145.

[21] SINGH, N. S. et al. Luminescence, lifetime and quantum yield studies of $YVO_4:Ln^{3+}$ (Ln^{3+} = Dy^{3+}, Eu^{3+}) nanoparticles: Concentration and annealing effects, Chemical Physics Letters, 2009, v. 480, n. 4, p. 237–242.

[22] VOORT, D. V. D.; DIRKSEN, G. J.; G. BLASÉ, Luminescence study of Eu^{3+}-O^{2-} associates in fluorides: CaF_2, $RbCdF_3$, and $RbCaF_3$, Journal of Physics Chemistry of Solids, 1992, v. 53, n. 2, p. 219-225.

[23] CARLOS, L. D. et al. White light emission of Eu^{3+}-based hybrid xerogels, Physical review B, 1999, v. 60, n. 14, p. 10042-10053 ·.

[24] PIRES, A. M.; DAVOLOS, M. R.; MALTA, O. L. Eu^{3+}-O^{2-} associates luminescence in Ba_2SiO_4, Journal of Luminescence, 1997, v. 72–74, n. 0, p. 244–246.

[25] FIACZYK, K.; ZYCH, E. On Peculiarities of Eu^{3+} and Eu^{2+} Luminescence in Sr_2GeO_4 Host, **RSC Advances**, 2016, v. 6, n. 94, p. 91836-91845.

[26] LIU, C. B. et al. Highly emissive Zn–Ln metal–organic frameworks with an unusual 3D inorganic subnetwork, Chemistry Communication, 2012, v. 48, n. 64, p. 7964–7966.

[27] DACANIN, L. J. ; et al. Judd–Ofelt analysis of luminescence emission from $Zn_2SiO_4:Eu^{3+}$ nanoparticles obtained by a polymer-assisted sol–gel method, Physica B, 2011, v. 406, n. 11, p. 2319–2322.

[28] GUPTA, S. K. et al. Structure and site selective luminescence of sol–gel derived $Eu:Sr_2SiO_4$, Journal of Luminescence, 2012, v. 132, n. 6, p. 1329–1338.

[29] MAGYAR, A. et al. Synthesis of luminescent europium defects in Diamond, Nature Communications, 2013, v. 5, n. 0, p. 3523-6.

[30] KOLESNIKOV, I. E. et al. Photoluminescence Properties of Eu^{3+} Ions in Yttrium Oxide Nanoparticles: Defect vs Normal Sites, RSC Advances, 2016, v. 6, n. 80, p. 76533-76541.

[31] ELISEEVA, S. V.; BUNZLI, J. G. Lanthanide luminescence for functional materials and bio-sciences, Chemistry Society Review, 2010, v. 39, n. 1, p. 189–227.

[32] BISPO-JR, A. G.; et al. Red-emitting coatings for multifunctional UV/red emitting LEDs applied in plant circadian rhythm control, ECS Journal of Solid State Science and Technology, 2019. ID number: JSSP-19-2763.

CHAPTER 5 – ENERGY TRANSFER BETWEEN Tb^{3+} AND Eu^{3+} IN BARIUM ORTHOSILICATE PHOSPHORS

5.1 Introduction

Eu^{3+} and Tb^{3+}-codoped phosphors find many optical applications due to the red light emission of Eu^{3+} and the blue and green emissions coming from Tb^{3+}.[1,2,3,4,5] Many reports are found on the synthesis of Eu^{3+} and Tb^{3+}-codoped phosphors, aiming application, for instance, in WLEDs.[6,7,8,9,10] As example, M. A. Tshabalala et al[11] described the solid-state synthesis of Eu^{3+} and Tb^{3+}-doped strontium orthosilicate and its white emission under UV excitation.

However, one of the challenges concerning this phosphor is to understand the energy transfer (ET) mechanism between Eu^{3+} and Tb^{3+} to modulate the phosphor white light emission. Indeed, there is a lack of this kind of approach dealing with ET between these ions specifically in orthosilicate matrix.

Therefore, in this chapter, we report the synthesis of Ba_2SiO_4:Eu^{3+},Tb^{3+} from the sol-gel route, and we introduce a detailed interpretation of the ET process by varying the concentration of the two activator ions. Moreover, the color tunability from the blue towards the red spectral region through changing the activator concentrations, Figure 5.1, is envisaged to fabricate coatings for multifunctional LEDs emitting in the deep-UV and visible windows for applications in indoor farming.

Figure 5.1 Representation of the goals of chapter 5.

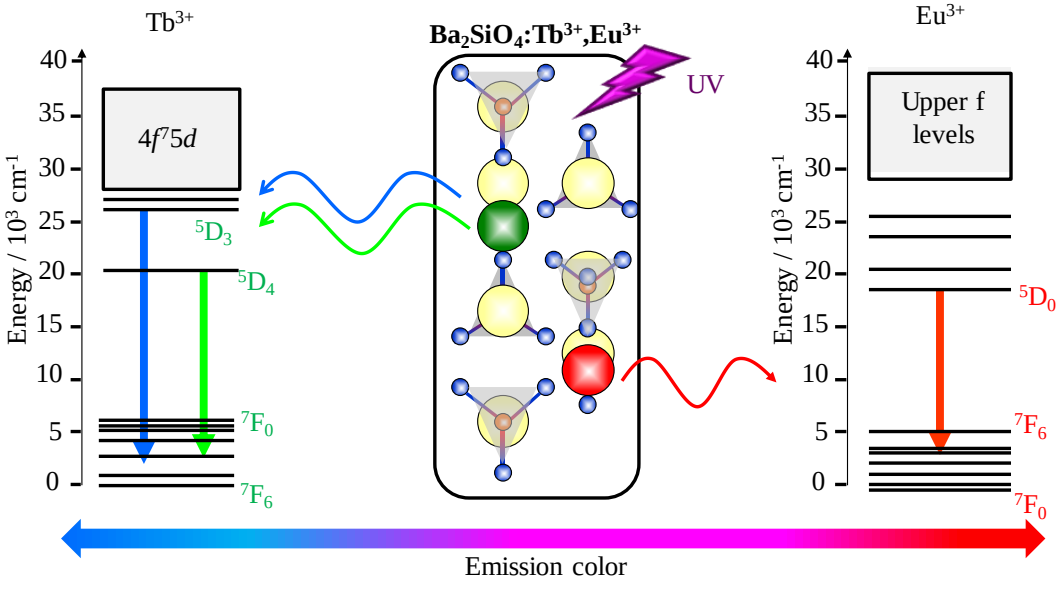

Source: Own authorship.

5.2 Experimental procedure

5.2.1 $Ba_2SiO_4:Eu^{3+},Tb^{3+}$ synthesis

The reactants applied for the phosphor synthesis are the same applied for the BSEu and BSTb series synthesis, sections 3.2.1 and 4.2.1. Eu^{3+} and Tb^{3+}-doped Ba_2SiO_4 was synthesized via an adapted sol-gel route reported by us.[12] The SiO_2:Ba^{2+},RE^{3+} xerogel phase was synthesized by the same methodology applied for the BSEu and BSTb synthesis, sections 3.2.1 and 4.2.1.

The-xerogel samples were pre-calcined at 450 ºC with a heating ramp of 10 °C/min for 2 hours, and then, calcined at 1,100 °C with a heating ramp of 10 °C/min for 2 hours in an EDG muffle furnace type under CO reducing atmosphere. The doping concentration was isoelectronically varied and the produced samples are shown in Table 5.1. The samples will be hereafter designated as BSXEuYTb, where X and Y are the Eu and Tb doping percentages, respectively. All the doped samples were obtained as monophasic Ba_2SiO_4 phase while the undoped Ba_2SiO_4 features some $BaCO_3$ traces.[12]

Table 5.1 Doping proportions.

Name	Tb^{3+} % [a]	Eu^{3+} %[a]	Tb^{3+} at %[b]	Eu^{3+} at% [b]	Tb^{3+} ch% [c]	Eu^{3+} ch% [c]	Structural formula	MW / g/mol
BS2Eu2Tb	2.0	2.0	2.01	2.0	3.0	3.0	$Ba_{1.88}Eu_{0.04}Tb_{0.04}SiO_4$	362.6820
BS2Eu0.1Tb	2.0	0.10	2.02	0.10	3.0	0.15	$Ba_{1.937}Eu_{0.002}Tb_{0.04}SiO_4$	364.7464
BS1Eu3Tb	1.0	3.0	1.02	3.1	1.5	4.5	$Ba_{1.88}Eu_{0.06}Tb_{0.02}SiO_4$	362.5426
BS1Eu2Tb	1.0	2.0	1.01	2.0	1.5	3.0	$Ba_{1.91}Eu_{0.04}Tb_{0.02}SiO_4$	363.6233
BS1Eu1Tb	1.0	1.0	1.01	1.0	1.5	1.5	$Ba_{1.94}Eu_{0.02}Tb_{0.02}SiO_4$	364.7156
BS1Eu0.05Tb	1.0	0.050	1.00	0.050	1.5	0.075	$Ba_{1.9685}Eu_{0.001}Tb_{0.02}SiO_4$	365.7417
BS1Eu0.01Tb	1.0	0.010	1.00	0.010	1.5	0.015	$Ba_{1.9697}Eu_{0.0002}Tb_{0.02}SiO_4$	365.7849
BS0.5Eu4Tb	0.50	4.0	0.510	4.1	0.75	6.0	$Ba_{1.865}Eu_{0.08}Tb_{0.01}SiO_4$	361.935
BS2Eu2Tb	0.50	1.0	0.503	1.0	0.75	1.5	$Ba_{1.955}Eu_{0.02}Tb_{0.01}SiO_4$	365.176
BS0.5Eu0.5Tb	0.50	0.50	0.502	0.50	0.75	0.75	$Ba_{1.97}Eu_{0.01}Tb_{0.01}SiO_4$	365.710
BS0.1Eu4Tb	0.10	4.0	0.102	4.1	0.15	6.0	$Ba_{1.877}Eu_{0.08}Tb_{0.002}SiO_4$	363.585

[a] doping percentage in relation to 2 mols of Ba^{2+} in the undoped Ba_2SiO_4. [b] Doping percentage in relation to the total cation mol amount for each sample; [c] Doping percentage in relation to the total cation charge in each sample.

Source: Reproduced from Bispo-Jr.[12]

5.2.2 Characterization

Photoluminescence (PL)

Photoluminescence measurements at 300 K for the BSXEuYTb samples were carried out in the same equipment described in section 3.2.2.

5.3 Results

Figure 5.2 exhibits the excitation spectra of the codoped phosphors monitored at 612 nm ($^5D_0 \rightarrow {}^7F_2$ transition of Eu^{3+}). The most intense band observed in the excitation spectra at higher energy is assigned to both Tb^{3+} $^7F_6 \rightarrow 4f^7 5d$ transition and $O^{2-} \rightarrow Eu^{3+}$ CTB, in accordance with the previously reported excitation spectra of the single-doped phosphors, Figures 3.8 (a) and 4.6 (a).

Figure 5.2 (a,c) Excitation spectra (300 K, 612 nm) of BSXEuYTb samples. (b,d) Magnification of the range between 325–500 nm, where Tb^{3+} transitions assignments are shown in green and Eu^{3+} ones in red**.**

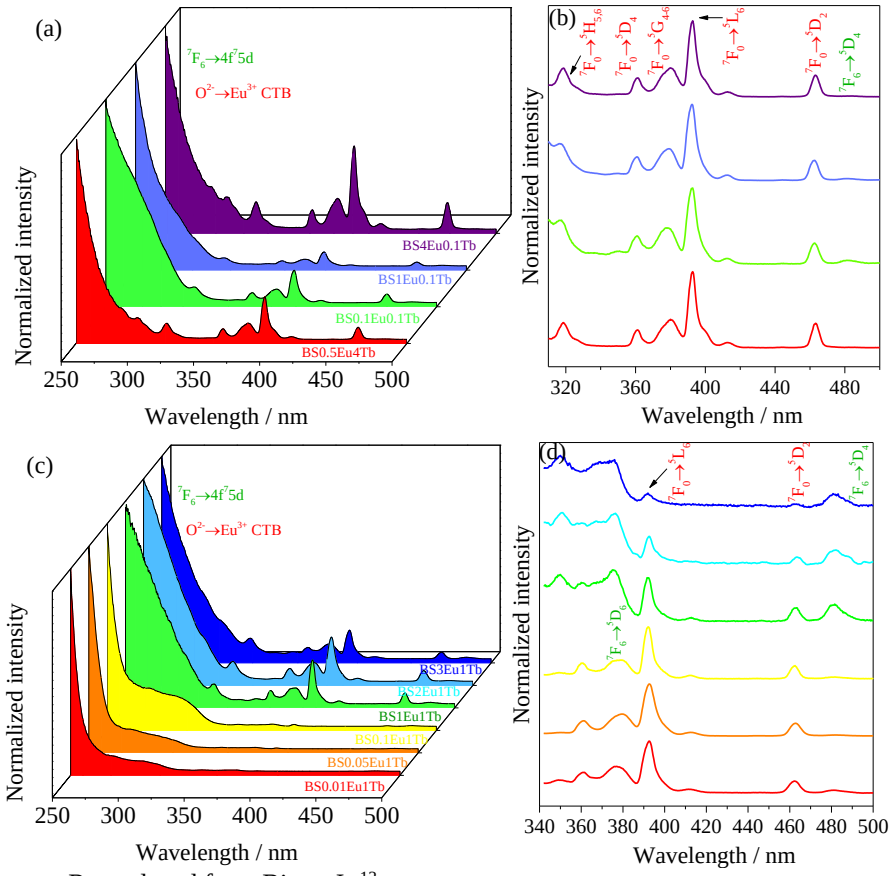

Source: Reproduced from Bispo-Jr.[12]

The magnification of the range within 325-500 nm shows the Eu^{3+} and the Tb^{3+} *f-f* transitions in all spectra, indicating that the Eu^{3+} emission arises from both RE^{3+} excitations. This observation leads us to conclude that the ET from Tb^{3+} to Eu^{3+} ($Tb^{3+} \rightarrow Eu^{3+}$) takes place in all phosphors. The ET between the two ions is favored since the energies of the $^5D_3$ (26,402 cm^{-1}) and $^5D_4$ (20,640 cm^{-1})[13] levels of Tb^{3+}, and the $^5D_0$ (17,280 cm^{-1}), $^5D_1$ (18,973 cm^{-1}), $^5D_2$ (21,445 cm^{-1}), and $^5D_3$ (24,335 cm^{-1}) levels of Eu^{3+} are close enough to allow the resonance between them.

In the emission spectra monitored at 250 nm (300 K), Figure 5.3, both ions are excited via Tb^{3+} $^7F_6 \rightarrow 4f^7 5d$ and $O^{2-} \rightarrow Eu^{3+}$ transitions, resulting in green and blue emission from Tb^{3+}, and red emission from Eu^{3+}. In the cases where the Eu^{3+} content is much higher than that of Tb^{3+}, the Tb^{3+} emission is neglected, just the matrix intrinsic emission is observed in the blue spectral region (see the matrix intrinsic luminescent profile in Figure 5.3 (c)).

Figure 5.3 (a,b) Emission spectra (300 K, 250 nm) of BSXEuYTb. Tb^{3+} transitions are shown in green and blue and Eu^{3+} ones in red. (c) Excitation spectrum (300 K, 441 nm) and emission spectrum (300 K, 340 nm) of the undoped Ba_2SiO_4 matrix.

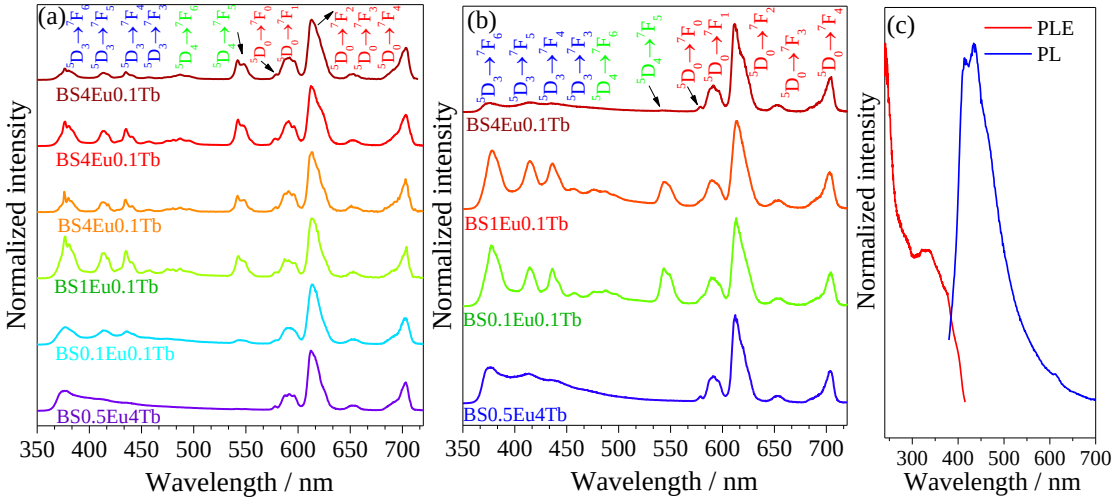

Source: Reproduced from Bispo-Jr.[12]

The ratio between the terbium and europium emission integrated areas for all phosphors is listed in Table 5.2.

Table 5.2 Tb/Eu emission rate, and critical distance (R_c) between Eu^{3+} and Tb^{3+}.

	Tb/Eu emission rate [a]	**R_c Eu-Eu /Å** [b]	**R_c Tb-Tb / Å** [b]	**R_c Eu-Tb / Å** [b]
BS3Eu1Tb	-	7.4(6)	10.(8)	6.7(8)
BS2Eu1Tb	0.58±0.01	8.5(8)	10.(8)	7.5(0)
BS1Eu1Tb	0.92±0.01	8.6(7)	10.(9)	8.6(3)
BS0.1Eu1Tb	0.48±0.01	23.(5)	10.(9)	10.(6)
BS0.05Eu1Tb	0.59±0.01	29.(7)	10.(9)	10.(7)
BS0.01Eu1Tb	0.34±0.01	50.(7)	10.(9)	10.(9)
BS4Eu0.5Tb	-	6.7(6)	13.(5)	6.5(0)
BS1Eu0.5Tb	1.13±0.01	10.(9)	13.(7)	9.5(2)
BS0.5Eu0.5Tb	0.96±0.01	13.(7)	13.(7)	10.(9)
BS4Eu0.1Tb	-	6.7(7)	23.(2)	10.(4)

[a] The Tb/Eu emission ratio parameter was determined by the ratio between the sum of the integrated area below the Terbium and Europium transitions in the emission spectra under excitation at 250 nm.
[b] The Ln-Ln distance was calculated considering the Ln^{3+} concentration in Equation 3.8.

Source: Reproduced from Bispo-Jr.[12]

For the BSXEu1Tb sample series, the increase of the Eu^{3+} concentration leads to an increment in the Tb^{3+} emission up to 1% of Eu^{3+}. Then, the Eu^{3+} emission overcomes the Tb^{3+} one. This behavior leads us to conclude that ET from Eu^{3+} to Tb^{3+} ($Eu^{3+}\rightarrow Tb^{3+}$) dominates the ET up to 1% of Eu^{3+}, and at higher Eu^{3+} concentrations, on the other side, the $Tb^{3+} \rightarrow Eu^{3+}$ ET is the main process. The same profile is observed for BSXEu0.5Tb series.

The $Eu^{3+}\rightarrow Tb^{3+}$ ET mechanism proposition is endorsed by analyzing the excitation spectra monitoring the Tb^{3+} $^5D_4\rightarrow{}^7F_5$ emission, Figure 5.4 (a), where the Eu^{3+} $^7F_0\rightarrow{}^5L_6$ transition is observed for the BS1Eu1Tb, indicating that Tb^{3+} emission is achieved via Eu^{3+} excitation. For the samples with low Eu^{3+} concentration, the Eu^{3+} excitation cannot be observed because the Ba_2SiO_4 intrinsic excitation overcomes the Tb^{3+} lines. An extrapolation of Eu^{3+}-doping in relation to the Tb^{3+} concentration (BS4Eu0.1Tb sample) shows that the Tb^{3+} emission is quenched in the cases where the Eu^{3+} content is too high, Figure 5.3 (b). In addition, when both Eu^{3+} and Tb^{3+} doping is the same, the Tb^{3+} and Eu^{3+} emission intensities are similar, Figure 5.3 (b), probably because the $Eu^{3+}\rightarrow Tb^{3+}$ and $Tb^{3+}\rightarrow Eu^{3+}$ ET probabilities are too close in these cases. Therefore, the Eu→Tb ET occurs just when both Eu^{3+} and Tb^{3+} contents are close.

Figure 5.4 (a) Excitation spectra (300 K, 545 nm) of BSXEu1Tb series. Tb^{3+} transitions are shown in green and Eu^{3+} in red. (b) Energy transfer mechanisms between Tb^{3+} and Eu^{3+} (dashed arrows: non-radiative transitions; solid line arrows: radiative transitions, curved lines: energy transfer).

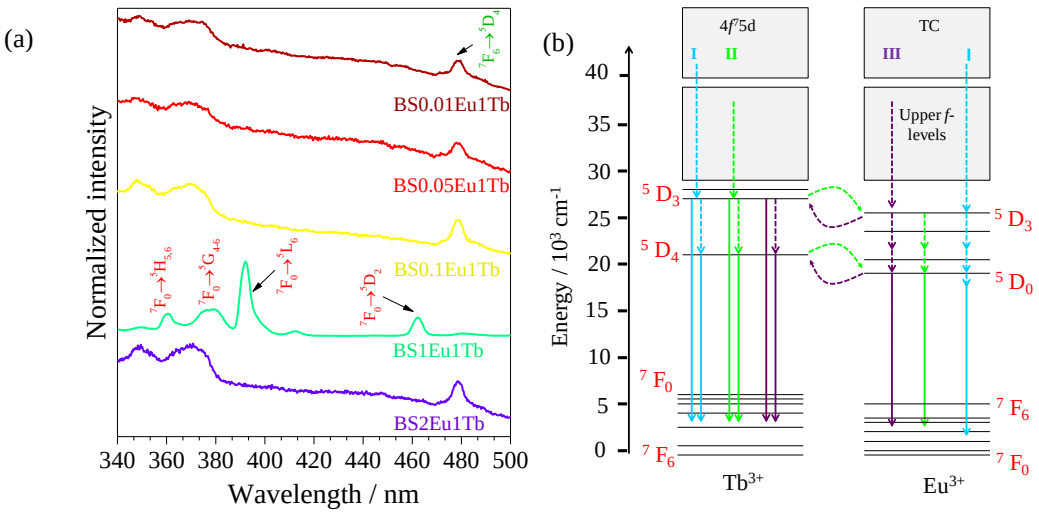

The mechanism I (blue lines) represent the emission from both RE^{3+} under excitation at 250 nm without any energy transfer. The mechanism II (green lines) represent the $Tb^{3+}\rightarrow Eu^{3+}$ ET and the emission from both RE^{3+}. The mechanism III (purple lines) represent the $Eu^{3+}\rightarrow Tb^{3+}$ ET and both RE emissions.

Source: Reproduced from Bispo-Jr.[12]

Figure 5.4 (b) shows some propositions of ET mechanisms between Tb^{3+} and Eu^{3+} in the Ba_2SiO_4 host. In the mechanism I, both Eu^{3+} and Tb^{3+} emit under 250 nm excitation. In the mechanism II, the ET from Tb^{3+} to Eu^{3+} is shown and occurs for all samples, dominating the ET profile at high Eu^{3+} concentration. In the case of mechanism III, the ET from Eu^{3+} to Tb^{3+} is represented and it dominates the ET between the RE^{3+} just for samples with low Eu^{3+} doping concentration.

The Eu-Tb ET mechanism was evaluated by the Van Uitert theory (Equation 2.6) as previously reported for the BSYTb samples, section 3.3.4. The calculated R_C (Table 5.2) indicates that the exchange interaction is unlikely to take place since the values are higher than 4 Å. Thus, multipolar interactions must be the main factor that contributes to the energy transfer mechanism. In Figure 5.5, it is plotted the log(*x*) versus log(*I*/*x*), where the intensity was fixed in both Tb^{3+} $^5D_4 \rightarrow {}^7F_5$ and Eu^{3+} $^5D_0 \rightarrow {}^7F_2$ transitions. The θ values deduced from the fitting plots monitoring the emission of both RE^{3+} are closer to 6, suggesting that the dipole-dipole interaction is the main contribution for the ET between Tb^{3+} and Eu^{3+}.

Figure 5.5 Linear fitting of log(*x*) versus log(*I*/*x*) for BSXEy1Tb series considering the emission intensity at (a) 612 nm and (b) 545 nm.

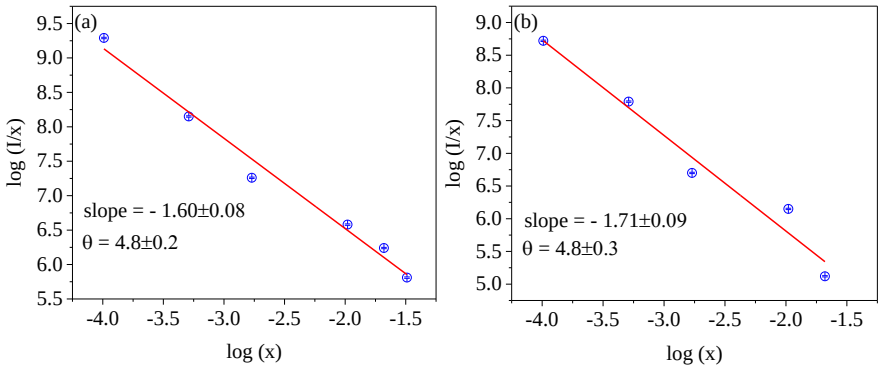

Source: Reproduced from Bispo-Jr.[12]

The CIE color coordinate diagram obtained for all phosphors is presented in Figure 5.6. For the BSXEu1Tb series, the emission moves to pink as the Eu^{3+} concentration increase from 0.01 up to 1%, then it goes back to red. This occurs because the Tb^{3+} emission is favored up to 1% of Eu^{3+}, and from then on, the Eu^{3+} emission overcomes the Tb^{3+} emission, Figure 5.3. Samples with equal RE concentration emit near to pink since both red and blue emissions of Eu^{3+} and Tb^{3+} respectively, have similar intensities, Figure 5.3. The phosphors with low Tb^{3+} concentration emit near to pink due

to the blue contribution of the matrix emission, Figure 5.3. Thus, the emission color is tunable by varying the dopant concentration.

Figure 5.6 CIE diagram of BSXEuYTb samples excited at 250 nm.

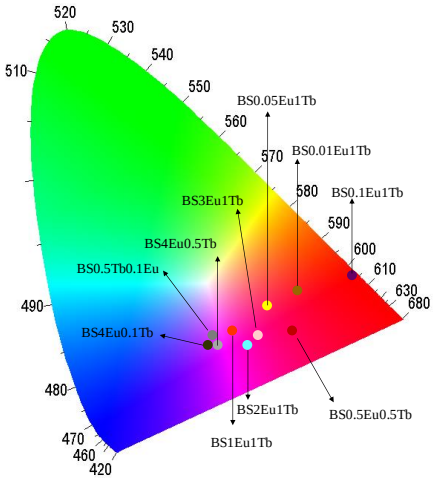

Source: Reproduced from Bispo-Jr.[12]

Luminescent-decay curves were measured by monitoring the Eu^{3+} $^5D_0$ level and Tb^{3+} $^5D_3$ and $^5D_4$ levels, and the curves were fitted thought a monoexponential (Equation 5.1) adjustment, Figure 5.7.

Figure 5.7 Emission decay curves excited at 250 nm and monitored at (a) 370 nm, (b) 545 nm and (c) 612 nm.

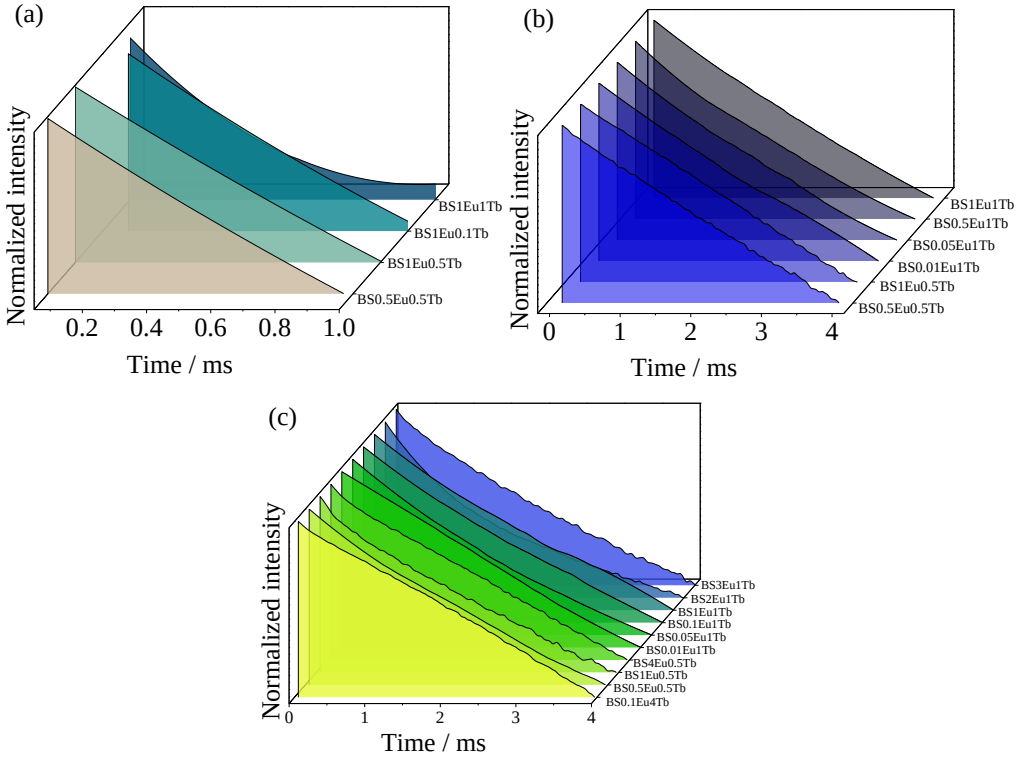

Source: Reproduced from Bispo-Jr.[12]

The Tb^{3+} lifetime values were used to estimate the Tb→Eu ET efficiency by applying Equation 5.2,[14] where τ_1 is the lifetime value for the codoped sample and τ_{10} is the lifetime value for the single doped samples. The ET efficiencies are shown in Table 5.3.

$$I = I_0 + Ae^{\left(-\frac{T}{\tau}\right)} \quad (5.1), \qquad \eta_{Tb\rightarrow Eu} = 1 - \frac{\tau_1}{\tau_{10}} \quad (5.2)$$

Table 5.3 Tb→Eu ET efficiency (the $\eta_{Tb\rightarrow Eu}$ ($^5D_3$) and the $\eta_{Tb\rightarrow Eu}$ ($^5D_4$) correspond to the ET from the Tb^{3+} $^5D_3$ and $^5D_4$ levels to the Eu^{3+} levels, respectively), Tb^{3+} $^5D_3$ ($\tau_{Tb}{}^5D_3$) and $^5D_4$ ($\tau_{Tb}{}^5D_4$) lifetime values and Eu^{3+} $^5D_0$ lifetime values (τ_{Eu}).

	$\tau_{Tb}{}^5D_3$ / ms	$\tau_{Tb}{}^5D_4$ /ms	τ_{Eu} / ms	$\eta_{Tb\rightarrow Eu}$ ($^5D_3$) / %	$\eta_{Tb\rightarrow Eu}$ ($^5D_4$) / %
BS3Eu1Tb	- [a]	- [a]	0.99±0.03	100 [b]	100 [b]
BS2Eu1Tb	- [a]	- [a]	0.57±0.03	100 [b]	100 [b]
BS1Eu1Tb	0.20±0.01	1.26±0.04	0.83±0.02	91±1	8±1
BS0.1Eu1Tb	0.20±0.01	1.14±0.02	1.28±0.04	91±1	17±1
BS0.05Eu1Tb	0.18±0.01	1.21±0.03	1.22±0.05	92±1	12±1
BS0.01Eu1Tb	- [a]	1.22±0.04	1.49±0.06	100 [b]	12±1
BS4Eu0.05Tb	- [a]	- [a]	1.67±0.06	100 [b]	100 [b]
BS1Eu0.5Tb	0.27±0.01	1.80±0.05	1.26±0.04	90±1	136±1
BS0.1Eu0.5Tb	- [a]	1.51±0.05	1.37±0.04	84±1	114±1
BS4Eu0.01Tb	- [a]	- [a]	1.97±0.05	100 [b]	100 [b]
BS4Eu	-	-	1.34±0.05	-	-

[a] Some samples do not showTb^{3+} emission and as consequence do not have lifetime values.
[b] For the samples that do not have $^5D_3$ and $^5D_4$ lifetime values, the Tb→Eu ET efficiency was considered as 100 %.
Source: Reproduced from Bispo-Jr.[12]

From Table 5.3, in the cases where Eu^{3+} and Tb^{3+} contents are similar (BS1Eu1Tb and BS0.5Eu0.5Tb), the Tb→Eu ET efficiency for the $^5D_3$ level is lower than that found for the others, and the ET efficiency from the $^5D_4$ level is higher than 100 % or very low. These results show that in the $^5D_3$ level, the Eu→Tb ET is more efficient for the $^5D_3$ level population in relation to the other samples, and as consequence, it decreases the Tb→Eu ET efficiency.

Considering the $^5D_4$ level, a Tb→Eu ET efficiency higher than 100 % indicates that the opposite process is the main ET process, contributing to the population of the $^5D_4$ level and its lifetime value increase. Also, in some cases, low $^5D_4$ Tb→Eu ET efficiency is an indicative that the opposite ET process is dominating. In this context, the Eu→Tb ET occurs mainly via the $^5D_4$ level.

The Tb→Eu ET efficiency increases in the samples that have Eu^{3+} content much lower or higher than that of Tb^{3+}, showing that the Tb→Eu ET prevails in relation to the opposite process. In these cases, the ET efficiency value from the Tb^{3+} $^5D_3$ level is higher

than that from the $^5D_4$ one, showing that the Tb→Eu ET occurs mainly via the Tb^{3+} $^5D_3$ level.

As expected from the emission spectra, when the Tb^{3+} content is much lower than that of Eu^{3+} (BS4Eu0.5Tb0 and BS4Eu0.1Tb), the ET efficiency from both $^5D_3$ and $^5D_4$ levels are 100 %, indicating that this is the best condition to improve the Eu^{3+} efficiency. This efficient Tb→Eu ET can also be evidenced by the increase of the Eu^{3+} $^5D_0$ lifetime values for these samples compared to the single doped Ba_2SiO_4:Eu^{3+}.

Therefore, the finds reported here confirm that Tb^{3+} acts as sensitizer for Eu^{3+}, enhancing the radiative decay probability from the $^5D_0$ emitting state. Moreover, by changing the doping concentration, the overall emitted color may be tuned from the blue towards the red spectral region, crossing the pink emission, enabling the fabrication of blue, pink or red-coatings for deep-UV LEDs.

5.4 Conclusions

In this chapter, an energy transfer approach between Eu^{3+} and Tb^{3+} in the Ba_2SiO_4 matrix was proposed. Both Eu^{3+} and Tb^{3+} emissions could be detected under 250 nm excitation, with an unexpected and intense Tb^{3+} blue emission arising from the $^5D_3$ level. However, at relatively high Eu^{3+} concentrations, the Tb^{3+} emission was quenched because of Tb^{3+} acts as sensitizer to the Eu^{3+} luminescence. It was possible to tune the phosphor emission from the blue towards the red spectral region by varying the doping content. Considering all the studied doping combinations, the energy transfer from Tb^{3+} to Eu^{3+} takes place in all samples, but the inverse process only dominates for samples with similar Tb^{3+} and Eu^{3+} contents. Therefore, the blue, red or pink-emitting phosphors may be used as coatings of deep-UV-emitting LEDs, making multifunctional devices for indoor farm application.

5.5 References

This chapter was written according to a paper published by the authors in Journal of Luminescence (2018).[12]

[1] SOMANI, M. et al. Structural, photoluminescent and thermoluminescent studies of rare earth ion (RE = Eu^{3+}) doped Sr_2SiO_4 phosphor, Optik, 2019, v. 182, n. 0, p. 839-847.

[2] ZHANG, J. et al. Optical temperature sensing using upconversion luminescence in rare-earth ions doped $Ca_2Gd_8(SiO_4)_6O_2$ phosphors, Journal of Alloys and Compounds, 2019, v. 771, n. 0, p. 838-846.

[3] VERMA, S. et al. Recent advances in rare earth doped alkali-alkaline earth borates for solid state lighting applications, Physica B, 2018, v. 535, n. 0, p. 106–113.

[4] WU, Y. et al. A high-performance non-rare-earth deep-red-emitting $Ca_{14-x}Sr_xZn_6Al_{10}O_{35}:Mn^{4+}$ phosphor for high-power plant growth LEDs, Journal of Alloys and Compounds, 2019, v. 781, n. 0, p.702-709.

[5] LIU, Q. et al. Multifunctional β-$NaGdF_4$: Ln^{3+} (Ln=Yb/Er/Eu) phosphors synthesized by L-arginine assisted hydrothermal method and their multicolor tunable luminescence, Materials Research Bulletin, 2019, v. 110, n. 0, p. 141-148.

[6] STEUDEL, F. et al. Quantum efficiency and energy transfer processes in rare-earth doped borate glass for solid-state lighting, Journal of Luminescence, 2016, v. 170, n. 3, p. 770–777.

[7] ZHOU, L.; YAN, B. Synthesis, microstructure and photoluminescence of Eu^{3+}/Tb^{3+} activated Y_2SiO_5 nanophosphors by new silicate sources, Applied Surface Science, 2008, v. 254, n. 6, p. 1847–1851.

[8] GUO, W. ET AL. Color tunable luminescence in novel $Li_3Ba_2Y_3(WO_4)_8:Tb^{3+}$, Eu^{3+} phosphor for white LEDs, Ceramics International, 2016, v. 42, n. 4, p. 5427–5432.

[9] SOM S.; SHARMA, S. K. Eu^{3+}/Tb^{3+}-codoped Y_2O_3 nanophosphors: Rietveld refinement, bandgap and photoluminescence optimization. Journal of Physics D: Applied Physics, 2012, v. 45, n. 41, p. 415102.

[10] FERNÁNDEZ-CARRIÓN, A. J. et al. New Single-Phase, White-Light-Emitting Phosphors Based on δ-$Gd_2Si_2O_7$ for Solid-State Lighting, Journal of Physics Chemistry C, 2014, v. 118, n. 31, p. 18035−18043.

[11] TSHABALALA, M. A.; SWART, H. C.; NTWAEABORWA, O. M. TOF SIMS analysis and generation of white photoluminescence from strontium silicate codoped with europium and terbium, Journal of Vacuum Science & Technology A, 2014, v. 32, n. 2, p. 021401-6.

[12] BISPO-JR, A. G. et al. Energy transfer between terbium and europium ions in barium orthosilicate phosphors obtained from sol-gel route, Journal of Luminescence, 2018, v. 199, n. 0, p. 372–378.

[13] COUWENBERG, I. et al. Spectroscopic properties of the trivalent terbium ion in the huntite matrix $TbAl_3(BO_3)_4$, Journal of Alloys and Compouds, 1998, v. 274, n. 1-2, p. 157 –163.

[14] GHOSH, P.; KAR, A.; PATRA, A. Energy transfer study between Ce^{3+} and Tb^{3+} ions in doped and core-shell sodium yttrium fluoride nanocrystals, Nanoscale, 2010, v. 2, n. 7, p. 1196–1202.

CHAPTER 6 – RED-LIGHT-EMITTING COATINGS FOR LEDs APPLIED TO PLANT CIRCADIAN RHYTHM CONTROL

6.1 Introduction

The commercial use of LEDs is not limited to lighting since the actual concern on improving life quality is catalyzing the solid-state lighting technology to come up with multifunctional LEDs that regulate human and plant circadian rhythm.[1] In what concerns plant growth, the regulation of the circadian rhythm by light exposition from LEDs appeals as an option to enhance the biomass production rate, especially in indoor farms, as an attractive alternative to supply the food world demand.[2] In this case, the quality of the produced biomass depends on the light source characteristics as wavelength and intensity applied to the process.[3]

Taking into account the impacts of the LED wavelength on the plant circadian rhythm, red light is the most suitable to regulate the photoreceptor phytochrome, that, in its turn, it is directly correlated with photosynthesis, germination, flowering as well as aerial architectural development.[4] Moreover, the use of blue and green light may be envisaged for plant circadian rhythm regulation, as previously highlighted in Table 2.4, section 2.2.4.

It is worth pointing out that extra UV radiation (210 – 250 nm) would also make a worthwhile contribution to food production since it is helpful to disinfection, water treatment, and purification.[5,6] However, it is essential to dose the UV radiation intensity, avoiding disturbs in the natural plant growth.[7] Therefore, the combination of a deep-UV emitting LED (250 nm) and a deep-UV-to-red downshifting converter phosphor allows fabricating a multifunctional prototype with decreased UV radiation emission compared to the bare-UV LED and getting red light suitable for indoor farming, Figure 6.1, in the next page.

To accomplish the multifunctional device fabrication, two main challenges need to be addressed: i) fabrication of compact and higher output power deep-UV LEDs and (ii) the choice of efficient monochromatic downshifting phosphors easily processed as coatings with tunable thickness. In what concerns issue (i), some progress has been achieved in the last 10 years,[8] despite low energy conversion efficiency (1 %),[9] being still a challenge. To address challenge (ii), we introduce the utilization of the $Ba_2SiO_4:Eu^{3+}$ phosphor. Moreover, in order to dose the UV radiation, we introduce the phosphor

dispersion in poly(methyl methacrylate) (PMMA) or polyvinylidene fluoride (PVDF) since they absorb deep-UV radiation, making a photo-selective film to UV radiation by controlling the film thickness. In order to improve the physical and chemical properties of polymeric matrices, usually chemical substances, such as Buriti oil (BO), may be also used as plasticizers.[10] For the record, this was the first time BO was used as plasticizer for PVDF.

Figure 6.1. Scheme of the UV and red-emitting multifunctional LED architecture for a potential application in indoor farming.

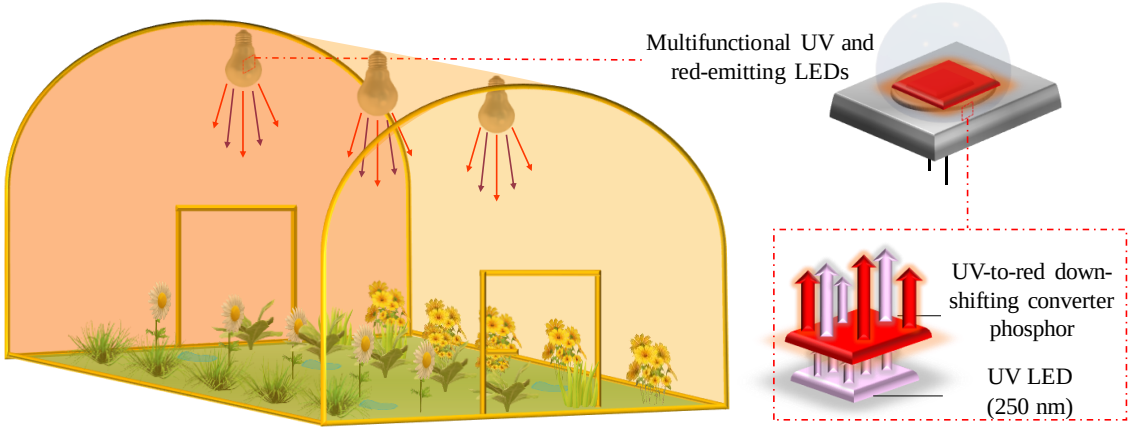

Source: Own authorship.

Therefore, inspired in the possibility of fabricating photo-selective films to be applied as coatings of multifunctional UV and red-emitting LEDs, in this study, we incorporated the $Ba_2SiO_4:Eu^{3+}$ phosphor in PMMA or PVDF films with deep-UV radiation filtering and emission in the red spectral region. As the BS4Eu sample showed the best luminescent properties (see chapter 4), it was chosen as a reference to fabricate the films. This sample was also chosen due to the spectroscopic probe properties of Eu^{3+}, enabling to evaluate the impacts of the phosphor dispersion in the polymeric matrices. In the future, the use of the $Ba_2SiO_4:Tb^{3+}$ and $Ba_2SiO_4:Eu^{3+},Tb^{3+}$ for the same purpose may be envisaged.

6.2 Experimental procedure

6.2.1 PVDF:BS4Eu film fabrication

The films were prepared by applying the drop casting method using BO as plasticizer according to a study reported by us.[11] For this, dimethylformamide (10.0±0.1 mL, C_3H_7NO, Cinética, 99.8 %) was mixed with PVDF (2.0000±0.0002 g,

CH_2F_2, Atochem, 99 %) and BO (400±1 μL, *Mundo dos óleos*). Then, the BS4Eu particles were introduced by varying the phosphor powder doping as 2, 5, 10, and 20 wt.% in relation to 2.000 g (PVDF and phosphor). The mixture was heated at 80 °C under stirring for two hours for the PVDF and oil dissolution, and after that, it was transferred to a Petri dish with a diameter of 9 cm and dried at 60 °C for 6 hours. These samples will be hereafter designated as PVDF:xBSEu, where x is the wt.% amount of BS4Eu.

6.2.2 PMMA:BS4Eu film fabrication

The PMMA matrix precursor was produced by mixing methyl methacrylate, (10.0000±0.0002 g, $CH_2=C(CH_3)COOCH_3$, Acros, 99 %) with benzoyl peroxide, (0.6000±0.0002 g, $C_{14}H_{10}O_4$, Alfa Aesar, 97 %) in a glass vial. The mixture was heated at 80-90 °C for 30 minutes and then placed in an oven at 40 °C until complete polymerization.[12]

PMMA:Eu films were deposited by the drop casting method. First, the fabricated PMMA polymer precursor (0.6069±0.0002 g) was dissolved in dichloromethane (10.0±0.1 mL, CH_2Cl_2, Sigma, 99.8 %), and 1.7±0.1 mL of this solution was transferred to a 2.2×2.2 cm^2 glass, in order to get a PMMA film with 0.1042 g. This PMMA weight was considered as the reference of 100 wt.%. The PMMA film syntheses were carried out without BO as plasticizer.

Then, stoichiometric amounts of Eu-2h (BS4Eu calcined for 2 hours) and PMMA/dichloromethane solution were mixed to get films with weight proportions of 1 PMMA:M Eu-2h, where M = 0.25, 1.00, 2.00, 3.00 and 4.00 (20, 50, 66, 75 and 80 wt.%, respectively). The PMMA/phosphor suspensions were deposited in a 2.2×2.2 cm^2 glass and they were dried at 25 ºC for 24 hours. Finally, the optimized deposition condition (1 PMMA:2 Eu-2h) was used to fabricate the film using the Eu-10h phosphor (BS4Eu calcined for 10 hours featuring the highest emission quantum yield, section 4.4). The films will be hereafter designated as PMMA:MEu-X, where M = 0.25, 1, 2, 3 and 4 and X = 2 h or 10 h.

6.2.3 Film characterization

Powder X-ray diffraction (XRD)

The PVDF:BSEu samples were characterized by XRD using a Shimadzu model 600 diffractometer in *Laboratório de Difração de Raios X* of FCT/UNESP under supervision of Professor Silvio R. Teixeira.

Scanning electron microscopy (SEM)

The PVDF:BSEu samples were characterized by SEM using the same equipment described previously in section 3.2.2.

Thermogravimetric analysis (TGA)

The PVDF:BSEu samples were characterized by TGA using a Netzsch equipment (model 204), approximate weight of 4 mg of each sample in alumina crucible under purified nitrogen gas flux (15 mL/min) and heating rate of 10 °C/min from 25 °C to 550 °C. The equipment is available in *Núcleo de Inovação Tecnológica em Borracha Natural* of FCT/UNESP under supervision of Professor Aldo E. Job.

Differential scanning calorimetry (DSC)

The PVDF:BSEu samples were characterized by DSC using a Netzsch equipment (model DSC 204), approximate weight of 2 mg of each sample in an alumina crucible, and a heating rate of 10 °C/min from -90 °C to 550 °C. The equipment is available in *Núcleo de Inovação Tecnológica em Borracha Natural* of FCT/UNESP under supervision of Professor Aldo E. Job.

Photoluminescence

For the PVDF:BSEu samples, the PL measurements were carried out in a Horiba Jobin Yvon Fluorolog-3 FL3-122 equipped with an excitation and emission double monochromator, continuous Xe lamp (450 W). Luminescent decay curves were evaluated by using a phosphorimeter Jobin Yvon, model FL-1040 equipped with a Xe lamp (25 Hz). The equipment is available in *Laboratório Multiusuário de Análises Químicas* of IQ/UNESP.

For the PMMA:Eu samples, PL measurements were carried out in the same equipment described in section 4.2.2.

Optical microscopy

The thickness of the PMMA:Eu films was estimated through optical microscopy using an Olympus BX51 bright field microscope (10× objective), in the reflection mode. The equipment is available in phantom-g of University of Aveiro under supervision of Professor Luis D. Carlos.

Ultraviolet (UV)/Visible Absorption spectroscopy

The UV/visible absorption spectra of the PMMA:Eu films were recorded using a Lambda 950 dual-beam spectrometer (Perkin-Elmer). The equipment is available in University of Aveiro under supervision of Professor Luis D. Carlos.

Luminous flux

For the PMMA:Eu films, the luminous flux was measured using an integrating sphere ISP 150L-131 from Instrument Systems ($BaSO_4$ coating) with an internal diameter of 150 mm and coupled to an array spectrometer MAS 40 from Instrument Systems. The measurements are accurate within 5%, accordingly to the manufacturer. A UV bulb (254 nm) and optical power of 3.2±0.1 mW was used as the excitation source.

Absolute Emission Quantum Yield

The absolute emission quantum yields of the PMMA:Eu films were carried out in the same equipment described in section 4.2.2.

6.3 Characterization of PVDF-based films

6.3.1 Structural characterization

The membranes are visually homogeneous, Figure 6.2, except for PVDF:20BSEu membrane, and for this reason, all the other membranes had their thickness measured, and the values are summarized in Table 6.1. A tendency of thickness decreasing was observed with the addition of BSEu probably because the PVDF amount decreases.

Figure 6.2 Images of the PVDF membranes: (a) PVDF:2BSEu, (b) PVDF:5BSEu, (c) PVDF:10BSEu, (d) PVDF:20BSEu.

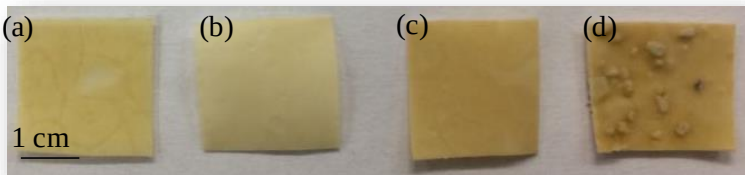

Source: Own authorship.

Table 6.1 2θ Bragg angle for the α-PVDF phase planes and thickness of the membranes.

Film	2θ Bragg angle / ±0.02 degree					Thickness / mm [a]
	(1 0 0)	(0 2 0)	(1 1 0)	(0 2 1)	(0 0 2)	
PVDF	16.98	18.53	20.43	25.55	39.40	0.10±0.02
PVDF:BO	17.09	18.74	20.61	25.49	39.49	0.39±0.04
PVDF:2BSEu	-	18.27	19.69	-	-	0.31±0.04
PVDF:5BSEu	-	18.25	19.80	-	-	0.26±0.04
PVDF:10BSEu	-	19.30	20.70	-	-	0.22±0.01

[a] Mean thickness obtained from the measure at 20 different points of the membrane using a Mitutoyo micrometer with an accuracy of 0.01 mm.

Source: Own authorship.

The X-ray diffraction profiles of the PVDF membranes are shown in Figure 6.3, and they exhibit five peaks around 17 º, 18 º, 20 º, 26 º and 40 º corresponding to the planes (1 1 0), (0 2 0), (1 0 0), (0 2 1) and (0 0 2) respectively, characteristic of the α-PVDF phase (JCPDS-38-1638).[13]

Figure 6.3 X-ray diffractograms of PVDF:BSEu films.

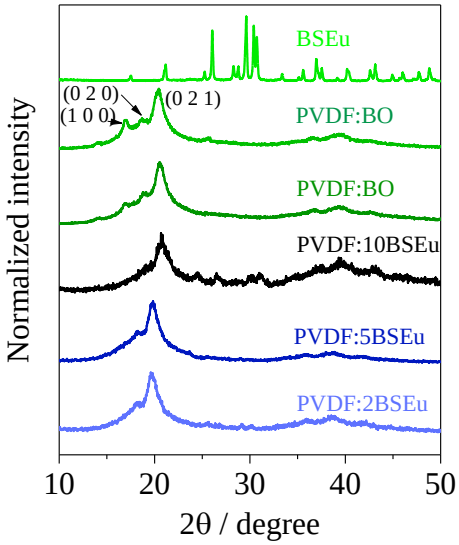

Source: Reproduced from Bispo-Jr.[11]

All 2θ Bragg angles for the indexed α-PVDF phase are also listed in Table 6.1, and the large FWHM values indicate the low crystallinity of the membranes and the PVDF semicrystalline nature.

Changes in the peak position indicate that the BS4Eu concentration influences the PVDF semicrystalline structure. These modifications are related to variations in the PVDF chain organization, in the degree of crystallinity, crystallite size, and changes in the molecular strengths that keep the chains together.[14] Finally, the X-ray patterns do not show other PVDF phases.

As the BS4Eu content increases, the PVDF (1 0 0) plane disappears and the (1 1 0) peak shifts to lower Bragg angles, indicating that the PVDF crystallization is inhibited by the BSEu particles. J. Song et al. obtained similar results for La_2O_3-doped α-PVDF membranes.[14]

6.3.2 Morphology

SEM images of the PVDF films are shown in Figure 6.4, revealing agglomerated spherical microstructures connected by necks on the membrane surface. These microstructures are probably composed by spherulites according to literature.[15,16]

Figure 6.4 SEM images of PVDF:BSEu films. The histogram was done by counting 200 particles.

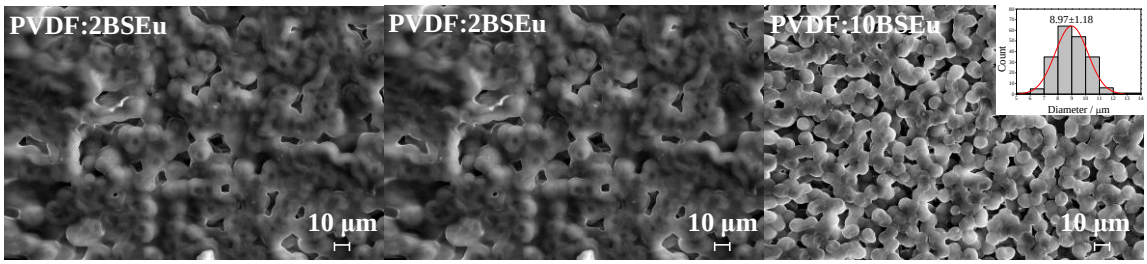

Source: Reproduced from Bispo-Jr.[11]

Some cavities are observed in the PVDF micro spherulites. A similar profile was also related by J. A. Dures et al. in PMMA membranes containing BO.[17] These cavities exhibit an oval shape and they arise because during the preparation of the membranes with BO, the solvent is evaporated and consequently, the oil coagulates into the polymer matrix. Then, phase separation is established after the total solvent evaporation thus, resulting in materials showing distinct microdomains of BO. In another study, J. A. Duraes et al. showed that the oval-shaped cavities may be correlated to the intermolecular interactions between the polymer and the oil.[18] Although these interactions experience low energy, they are present in a vast quantity, leading to good dispersion of BO.

The chemical mapping images of the PVDF:10BSEu film is viewed in Figure 6.5, and just C, F and O elements are detected in the PVDF particle surface regarding the penetrability of the EDS technique (1 µm). Carbon comes from PVDF chains and BO, F comes from PVDF chains, O comes from fatty acids in BO and all the three atoms have homogeneous distribution on the film surface. Yet, no signal related to Ba, Eu or Si atoms are observed in the chemical mapping, leading us to conclude that the phosphor particles are inside the membrane and not on its surface.

Figure 6.5 Chemical mapping of the PVDF:10BSEu film. In (a), atoms of carbon, fluorine and oxygen are shown together, in (b) only carbon, in (c) only fluorine, and in (d) only oxygen atom.

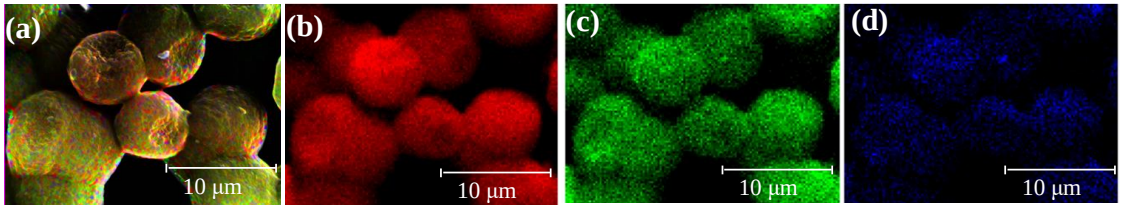

Source: Reproduced from Bispo-Jr.[11]

6.3.3 Thermal behavior of PVDF-films

Thermogravimetric analysis and DTG curves of the films are shown in Figure 6.6.

Figure 6.6 (a) TG thermograms and (b) DTG of PVDF:BSEu films.

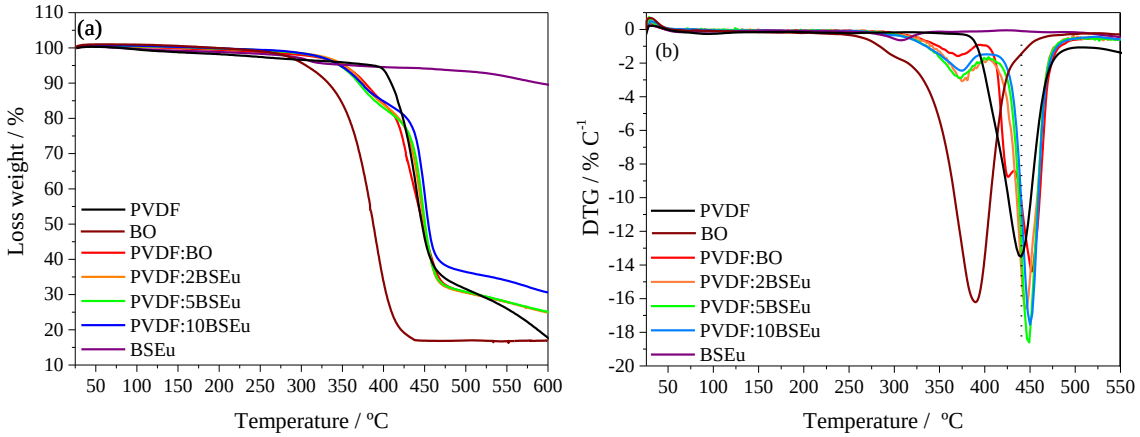

Source: Reproduced from Bispo-Jr.[11]

The PVDF films present good thermal stability, up to at least 350 ºC, to which it is correlated to the high electronegativity of the fluorine atoms composing the polymer chain and their high C–F bond dissociation energy. Above 350 °C, the PVDF begins to degrade releasing hydrogen fluoride, monomers and few amounts of $C_4H_3F_3$ according to the literature.[11,19,20]

The thermal decomposition of BO takes place in two steps, see Figure 6.6; the first one near to 260 °C is due to the release of volatile components and the second one around 425 °C indicates that the fatty acids break down completely.

BS4Eu itself exhibits a loss weight of 10.51 % between 25 °C and 600 °C with a maximum at 300 °C indicated by DTG. This loss weight is attributed to the thermal decomposition of amorphous carbonate on the phosphor surface. As the BSEu phosphor is included in the membrane composition, a tendency of decreasing the loss weight is observed up to the PVDF:10BSEu sample (See Table 6.2).

Table 6.2 Loss weight in different temperature ranges obtained from TG and maximum decomposition temperature (max.) of PVDF films.

Membrane	Loss weight / %			BO	PVDF max. / °C	
	25 - 300 /°C	300-405 / °C	405-501 /°C	max. /°C		
BO	1.55±0.01	98.00±0.01	-	390.1±0.1	-	-
PVDF	3.28±0.01	1.72±0.01	62.7±0.01	-	-	437.0±0.1
PVDF:BO	2.26±0.01	14.07±0.01	53.29±0.01	383.4±0.1	426.9±0.1	442.4±0.1
PVDF:2BSEu	1.80±0.01	16.23±0.01	51.58±0.01	375.1±0.1	-	445.6±0.1
PVDF:5BSEu	1.42±0.01	16.78±0.01	50.56±0.01	372.8±0.1	-	448.1±0.1
PVDF:10BSEu	1.28±0.01	14.23±0.01	48.80±0.01	374.6±0.1	-	450.2±0.1

Source: Reproduced from Bispo-Jr.[11]

The decomposition temperature slightly increases as the BSEu amount increases (see Figure 6.6 (b) and Table 6.2), indicating that the attraction forces among PVDF and BSEu improve the thermal stability of the composite. Similar results were also observed by F. S. Al-Hazmi et al. for Cu_2O particles in PVDF films.[21] The improvement of the thermal stability due to the BSEu particles incorporation in the PVDF is related to the packing of the polar crystalline α-phase by the ionic phosphor particles.[22] This occurs because silicate materials obtained from the sol-gel synthesis usually display a polar behavior on the particle surface due to the presence of Si-O groups.

The DSC analysis gives further insight into the thermal behavior of the films, as illustrated in Figure 6.7.

Figure 6.7 (a) DSC scans of the PVDF:BSEu films. (b) Magnification of the DSC scans in the region between -67.5 ºC and -15 ºC. Assignments: (1) BO phase transition, (2) PVDF melting point, (3) Carbonate on BS4Eu surface, (4) BO decomposition, (5) PVDF decomposition. The glass transition is shown between the dashed lines in Figure 6 (b).

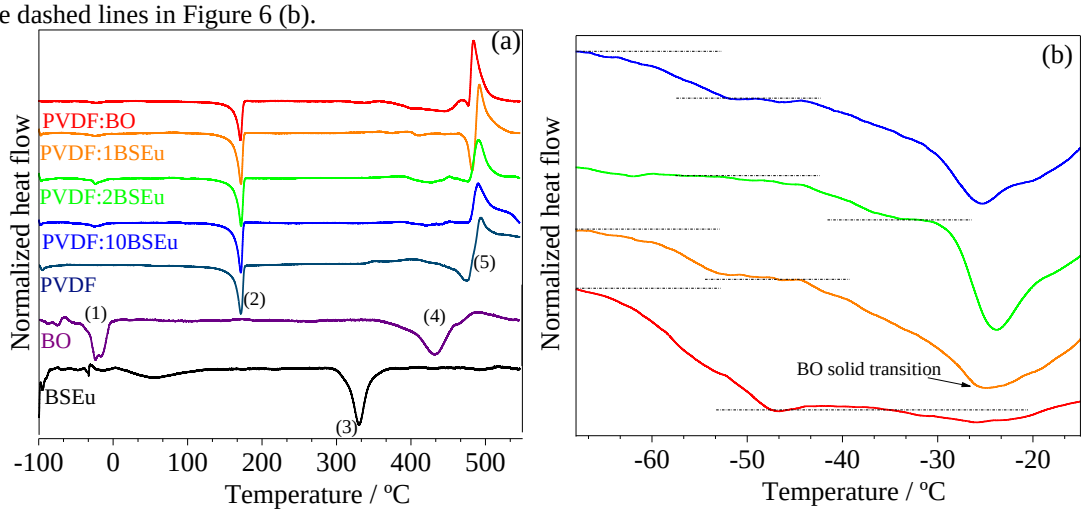

Source: Reproduced from Bispo-Jr.[11]

For pure BO, the DSC scan exhibits two endothermic events, the first around -17 °C (ΔH = 43.9 J.g^{-1}) associated with a solid phase transition of the oil,[23,24] and

the second is a broad peak at 433.2 ºC related to the BO decomposition, as it was previously shown by the TG measurement, Figure 6.6.

For the PVDF films, two events are also observed; an exothermic peak at 480 ºC attributed to the PVDF decomposition, and an endothermic peak around 170 ºC attributed to the PVDF melting point (T_m) characteristic of the PVDF α- phase.[25]

From the PVDF melting point, it is possible to estimate the polymer crystallinity degree (χ) by the following Equation 6.1,[26] in which ΔH_m is the experimental heat of fusion, W is the PVDF content (wt.%) in the PVDF membranes and $\Delta H_m°$ is the heat of fusion of PVDF considering a crystallinity degree of 100 % (90.4 J.g^{-1}).[27] Also, as the melting temperature is constant in the melting process, it is possible to estimate the entropy variation (ΔS_m) for the melting process by Equation 6.2.

$$\chi = \frac{\Delta H_m}{W.\Delta H_m^o}\ x\ 100\ (\%)\ (6.1), \qquad T_m = \frac{\Delta H_m}{\Delta S_m}\quad (6.2)$$

The polymer crystallinity is shown in Table 6.3. The BSEu addition in PVDF membranes decreases the PVDF crystallinity, as it was indicated by XRD before.

Table 6.3 Glass transition temperature (T_g), melting temperature (T_m), beginning of the melting process (T_{onset}), heat of fusion (ΔH_m), entropy variation in the melting process (ΔS_m) and crystallinity degree (χ).

Membrane	**T_g / ± 0.1 ºC**	**T_m / ± 0.1 °C**	**T_{onset} / ± 0.1 °C**	**ΔH_m / ±0.2 J g^{-1}**	**ΔS_m / x10^{-5} J g^{-1}K^{-1}**	**χ(%)**
PVDF	-35.9	171.6	161.1	32.3	0.07±0.001	35.(7)
PVDF:BO	-58.2	171.0	162.5	26.1	5.878±0.001	28.(9)
PVDF:2BSEu	-59.4	171.9	161.6	25.2	5.889±0.001	28.(4)
PVDF:5BSEu	-42.4	171.9	163.8	24.9	5.597±0.001	29.(0)
PVDF:10BSEu	-59.1	171.3	163.3	23.1	5.199±0.001	28.(4)

Source: Reproduced from Bispo-Jr.[11]

A glass transition with characteristic temperature (T_g) was observed in the DSC scans, Figure 6.7 (b) with values also listed in Table 6.3. The glass transition for the pure PVDF film occurs at -35.5 °C, matching with the literature.[28] The PVDF T_g values shown in Table 6.3 slightly varies with the BSEu addition in the films, except for the PVDF:5BSEu film.

6.3.4 Photoluminescence

The excitation and emission spectra (300 K) of the PVDF:10BSEu films are shown in Figure 6.8. The other PVDF films do not display luminescence. For the PVDF:10BSEu, the excitation transitions related to the phosphor are detected in the

excitation spectrum, Figure 6.8 (a). In this context, the emission spectrum monitored at 250 nm of the PVDF:10BSEu, Figure 6.8 (b) is dominated by narrow bands related to the $^5D_0 \rightarrow {}^7F_J$ (J = 1, 2 and 4) Eu^{3+} transitions, mainly in the red spectral region. The CIE color coordinates were determined as (0.684;0.314) for the PVDF:10BSEu, with 100% of color purity, which guarantee a pure red color for the membrane.

Figure 6.8 (a) Excitation spectra (300 K, 610 nm) and (b) emission spectra (300 K, 250 nm) of PVDF:10BSEu compared to BS4Eu.

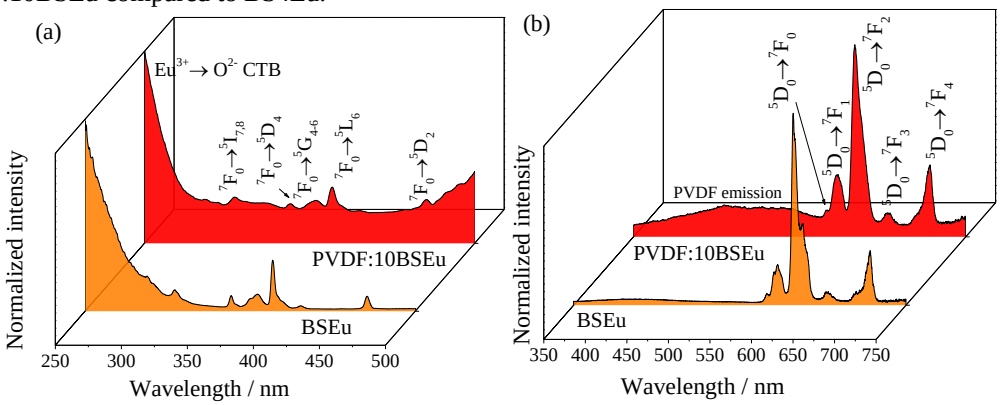

Source: Reproduced from Bispo-Jr.[11]

Finally, in this section, we introduced the synthesis of films based on $Ba_2SiO_4:Eu^{3+}$ dispersed in PVDF. However, the dispersion of the phosphor in PVDF is low, being 10 wt.% the maximum limit for homogenous dispersion. Therefore, aiming to improve the phosphor homogeneity in a polymeric film, PMMA:BSEu films were synthesized, as represented in the next section. As BO does not influence the Eu^{3+} emission, we choose to do not use it in the next studies even that it improves the mechanical and thermal properties of the PVDF films.[11]

6.4 Characterization of the PMMA-based films

The PMMA/$Ba_2SiO_4:Eu^{3+}$ films were fabricated by changing the amount of phosphor in order to control the thickness. The Eu-2h (BS4Eu calcined for 2 hours) was selected to optimize the deposition since it is easier to process due to its lower calcination time (lower energetic outlay than that of Eu-10h). Then, the best condition (1PMMA:2Eu-2h) was applied to fabricate the PMMA/2Eu-10h film.

To optimize the UV absorbance, the PMMA:Eu-2h film growth was monitored by UV–Vis absorption spectroscopy, Figure 6.9. The intense band in the deep-UV region near to 225 nm, Figure 6.9 (a) is attributed to the PMMA absorption[29] whereas the band

around 265 nm is related to the charge transfer band (CTB) of Eu^{3+}, confirming that the phosphor particles are incorporated in the membrane.

Figure 6.9 (a) UV–Vis absorption spectra of the PMMA:MEu-2h films. (b) Absorbance values at 600 nm for the PMMA:MEu-2h films; the red line is a visual guide. CTB 1 comes from Eu inserted in Ba sites.

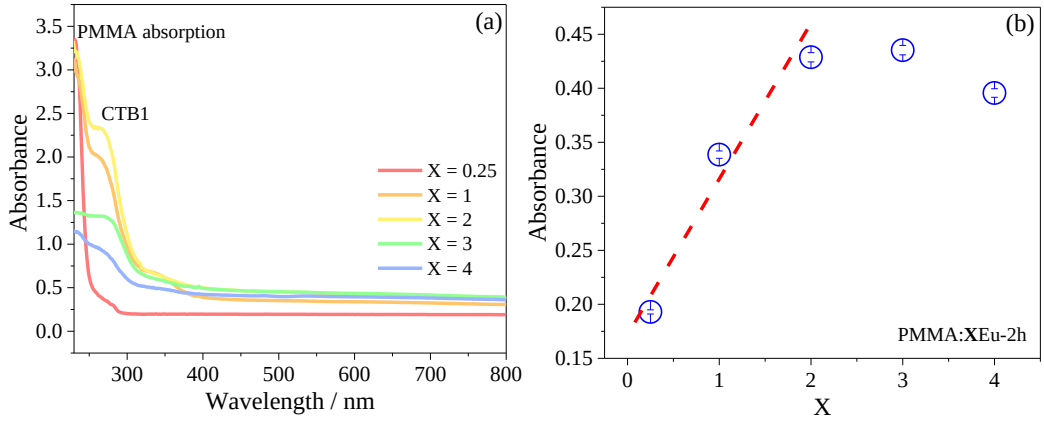

Source: Own authorship.

The UV absorption spectra were also used to evaluate the optical features as the composite films grow by monitoring the film absorption in a region (600 nm) that neither the phosphor nor the polymer absorbs, Figure 6.9 (b), thus, the absorption increase is related to light scattering by the phosphor particles.[30,31] The film absorbance at 600 nm reveals a linear increase up to the PMMA:2Eu-2h film, and then, the absorbance tends to a saturation regime, evidencing a minor decrease at larger phosphor content.

Based on these data, we conclude that the phosphor incorporation is homogeneous until the PMMA:2Eu-2h film. As the phosphor particles are micro-sized, it is expected that the precursor suspension becomes unstable as the phosphor amount increases, leading to a non-homogeneous deposition of the particles. Also, considering that the phosphor particle surface is partially ionic, weak interactions like Van der Waals forces are the main driving force that maintains the suspension stable, being strongly influenced by the particle concentration, leading to particle coalescence at high concentration.[30,32]

The film thickness was measured by optical microscopy, Table 6.4, where it is noticed a tendency of decreasing the film thickness as the phosphor amount increases from the proportion of PMMA:1Eu2-h. This tendency is correlated with the decrease of the PMMA content in the film composition.

Table 6.4 Film thickness (Thick.) and luminous flux (Φ) compared to the powder phosphors.

Sample	Thick. / μm	Φ / $\times 10^{-4}$ lm	Sample	Thick. / μm	Φ / $\times 10^{-4}$ lm
PMMA:0.25Eu-2h	26±2	0	PMMA:4Eu-2h	17±2	2.5±0.1
PMMA:1Eu-2h	88±4	3.8±0.1	PMMA:2Eu-10h	68±2	7.9±0.3
PMMA:2Eu-2h	72±3	5.9±0.2	Eu-2h	Powder	4.5±0.2
PMMA:3Eu-2h	55±6	4.3±0.2	Eu-10h	Powder	5.4±0.2

Source: Own authorship.

The excitation spectra, Figure 6.10, are dominated by the $Eu^{3+} \rightarrow O^{2-}$ CTB and *f-f* Eu^{3+} transition in accordance with the data reported for the Eu-2h, Figure 4.8.

Figure 6.10 Excitation spectra (300 K) monitored at 610.14 nm for the PMMA films.

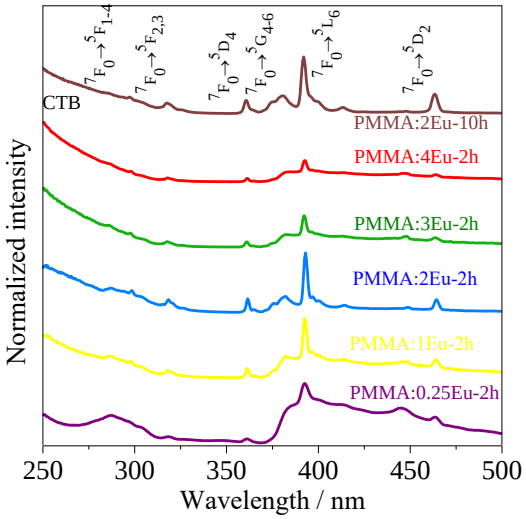

Source: Own authorship.

Under UV radiation exposition (255 nm), the PMMA:2Eu-10h films exhibit bright red luminescence at naked eyes, Figure 6.11 (a) in the next page, confirming the successful incorporation of the Eu-10h phosphor in the polymeric matrix.

The emission spectra (300 K), Figure 6.11 (c), resemble those measured for the isolated powder samples, Figure 4.9. All films emit red light upon 255 nm radiation exposition, Figure 6.11 (c), but there is a deviation of the color purity to lower values when the phosphor particles are dispersed in PMMA, as represented in the CIE chromaticity diagram, Figure 6.11 (d). This deviation is associated with the intrinsic PMMA emission (Figure 6.12) in the blue spectral region that has high contribution in the emission pattern as the phosphor content decreases.

Finally, the emission quantum yield of the PMMA:2Eu-10h film, Figure 6.11 (b), is statistically the same compared to the Eu-10h phosphor, Figure 4.9, confirming that the dispersion of the phosphor does not quench the Eu^{3+} emission.

Figure 6.11 (a) Photo of the PMMA:2Eu-10h film under UV radiation (255 nm) exposition. (b) Emission spectra (300 K, 255 nm) of the films. (c) CIE chromaticity diagram of the films (255 nm). (d) Absolute emission quantum yield (*q*) for the PMMA:2Eu-10h film compared to its excitation spectrum.

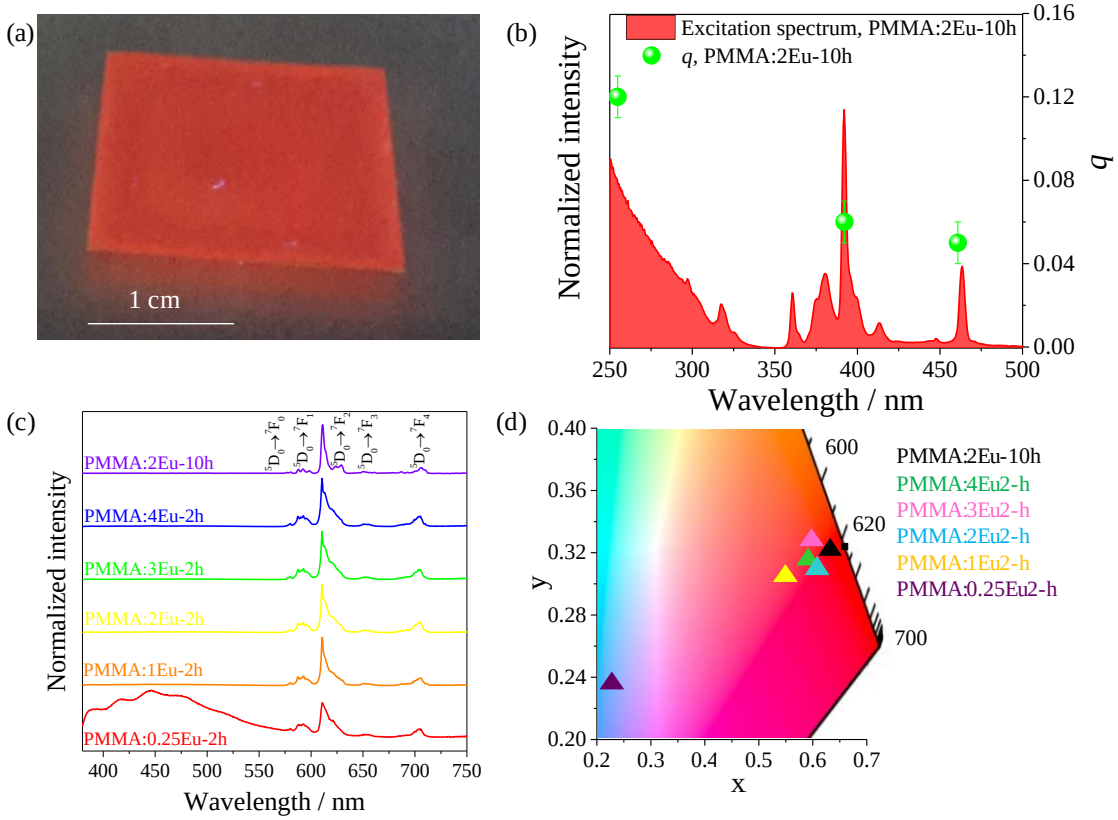

Source: Own authorship.

Figure 6.12 (a) Excitation spectrum (300 K, 450 nm) and (b) emission spectrum (300 K, 255 nm) of the undoped PMMA film.

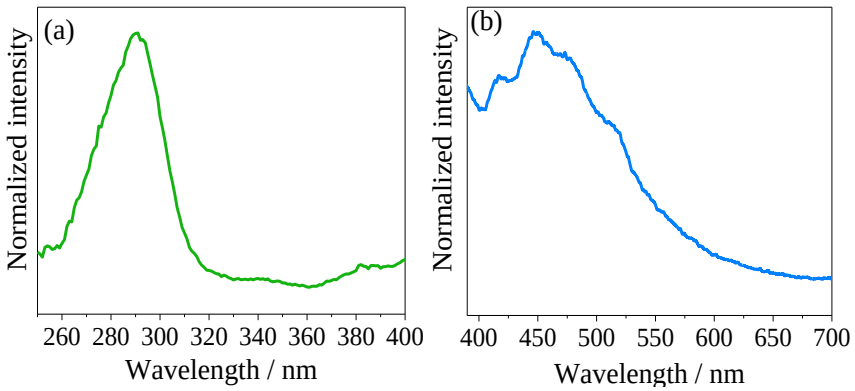

Source: Own authorship.

The luminous flux of the PMMA films enhances as the phosphor amount increases up to the proportion of PMMA:2Eu-2h and then the value decreases, Table 6.4. This tendency is directly correlated with the above-mentioned film coalescence as the phosphor amount increases. The PMMA:2Eu-10h film showed the best luminous flux in

all the film series, confirming that this is the ideal condition to achieve the best Eu^{3+} emission.

The luminous flux values of both PMMA:2Eu-2h and PMMA:2Eu-10h films are higher than the values found for the powder phosphors, Table 6.5, suggesting that the phosphor dispersion in PMMA leads to smooth structural changes in the Ba_2SiO_4 network. As the BS4Eu particles are micro-sized, it is expected that the PMMA polymer does not penetrate inside the particles, changing only their surface.

To understand the changes in the Ba_2SiO_4 structure after the phosphor dispersion in PMMA, the PMMA:2Eu-10h film was chosen as a representative sample. The high-resolution excitation and emission spectra of the PMMA:2Eu-10h film, Figure 6.13, are similar to those ones related to the Eu-10h sample, except in the relative intensity of some $^5D_0 \rightarrow {}^7F_0$ transitions, Figure 6.14, in the next page.

Figure 6.13 (a) Excitation spectra (14 K) of the PMMA:2Eu-10 h film monitored at distinct wavelengths around the $^5D_0 \rightarrow {}^7F_0$ transitions. (b) Emission spectra (14 K) of the PMMA:2Eu-10h film monitoring different excitation wavelength. CTB 1 comes from Eu inserted in Ba sites and CTB 2 arises from Eu^{3+}-O^{2-} associates.

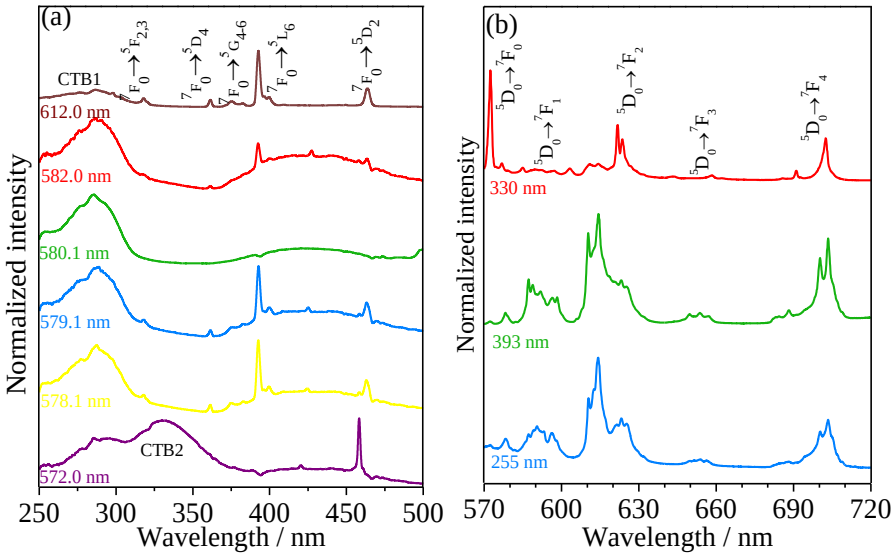

Source: Own authorship.

For the PMMA:2Eu-10h film, only five components for the $^5D_0 \rightarrow {}^7F_0$ transition at 572.6 (Eu_{A1}), 578.2 (Eu_1), 579.6 (Eu_2), 580.1 (Eu_3) and 582.3 nm (Eu_{D3}) are noticed, Figure 6.14. The excitation spectra monitored around those components, Figure 6.13 (a), features the same energy of those ones acquired for Eu-10h, Figure 4.12, confirming that the PMMA incorporation did not affect those Eu^{3+} local sites. The $^5D_0 \rightarrow {}^7F_0$ transitions at 580.2 (Eu_{D1}), 581.6 (Eu_{D2}), and 582.3 (Eu_{D3}) reveal a decrease in their relative intensity after the dispersion in PMMA, when compared to the component at 578.2 nm (Eu_1),

Figure 6.14, suggesting that the dispersion is filling the lacking oxy ion position, undoing the defects probably located on the surface of particles.

Figure 6.14 High-resolution emission spectra (14 K) monitored at 393 nm of the PMMA:2Eu-10h film in the $^5D_0 \rightarrow {}^7F_0$ transition region compared to the Eu-2h and Eu-10h samples.

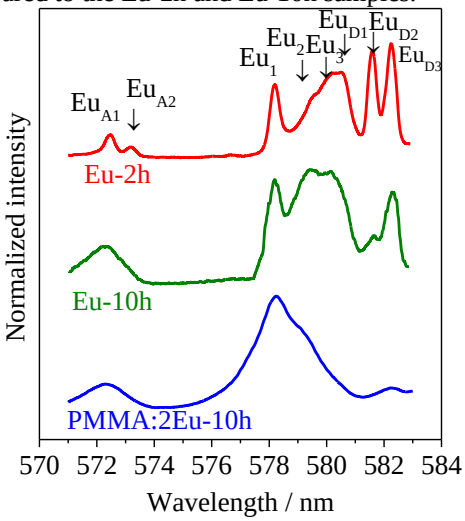

Source: Own authorship.

Selective emission decay curves (Figure 6.15) for the PMMA:2Eu-10h sample were monitored around each one of the five $^5D_0 \rightarrow {}^7F_0$ components at 14 K and the calculated $^5D_0$ lifetime values are also included in Table 6.5.

Figure 6.15 Emission decay curves (14 K) excited at 393 nm and monitored at distinct wavelengths around the $^5D_0 \rightarrow {}^7F_0$ transitions for the PMMA:2Eu-10h film. The solid lines correspond to the data best fit (R^2>0.9), using a single exponential function. The insert in the figures represents residual plots.

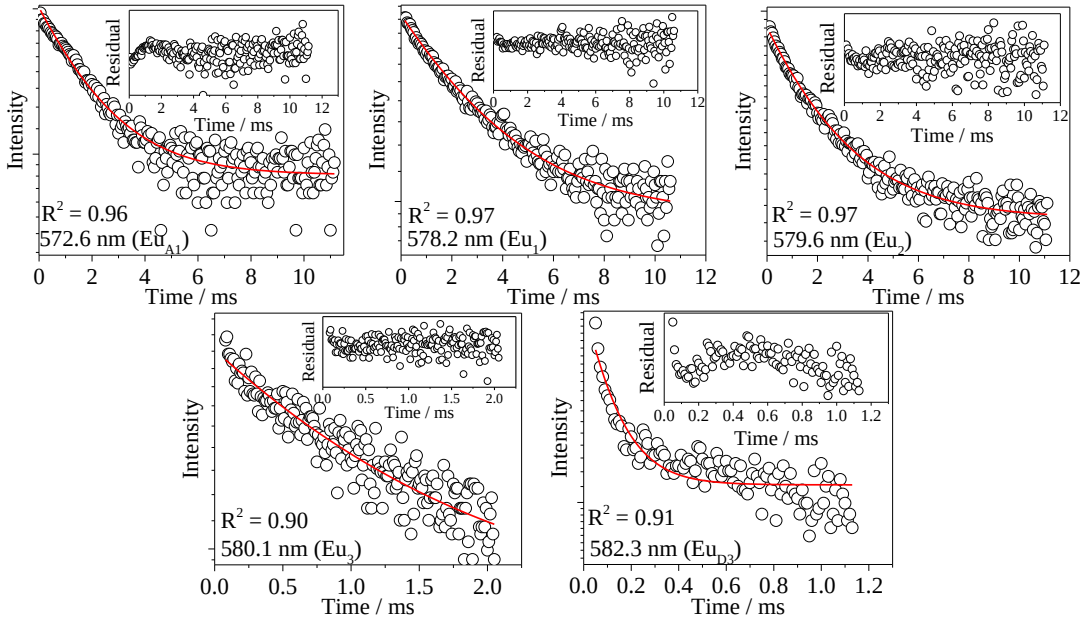

Source: Own authorship.

The $^5D_0$ lifetime values of the components at 580.2 (Eu_{D1}) and 582.3 nm (Eu_{D3}) decrease after the phosphor dispersion, Table 6.5, confirming that the concentration of these defects decreases, in accordance with the above-cited structural changes.

Table 6.5 Energy (cm^{-1}) and $^5D_0$ lifetime (τ) values of the components for the $^5D_0 \rightarrow {}^7F_0$ transitions of the PMMA:Eu-10h sample. The excitation wavelength was placed at 393 nm (14 K).

Notation for Eu ions	Wavelength / ±0.08 nm	Energy / ±3 cm^{-1}	PMMA:Eu-10h
Eu_1	578.22	17,295	0.903±0.015
Eu_2	579.56	17,256	0.846±0.014
Eu_3	580.12	17,238	0.495±0.032
Eu_{D1}	-	-	-
Eu_{D2}	-	-	-
Eu_{D3}	582.35	17,173	0.016±0.001
Eu_{A1}	572.64	17,464	0.628±0.009
Eu_{A2}	-	-	-

Source: Own authorship.

Multifunctional UV and red-emitting LEDs were tentatively built by coating a UV-emitting LED (255 nm) with the prepared PMMA:2Eu-10h film. However, we could not detect the red-light-emission of this prototype since the output optical power of the UV LED is too low (EQE = 0.1 %), limiting the film absorption and conversion. Yet, this effect is caused by the bare LED efficiency and not due to the phosphor,since the bright emission of the film was confirmed by Figure 6.11 (a). In this context, the main challenge to accomplish this device fabrication is improving the EQE of deep-UV LEDs, to which it is an open challenge in the literature.

Finally, the finds reported here confirm that by dispersing $Ba_2SiO_4:Eu^{3+}$ red-emitting phosphors in PMMA, high-brightness deep-UV-to-red downshifting converter films were fabricated, with potential to be applied in the future in UV/red-emitting multifunctional LEDs for indoor farms.

6.5 Conclusions

Herein, deep-UV-to-red downshifting converter films were synthesized by dispersing $Ba_2SiO_4:Eu^{3+}$ in PMMA or PVDF polymers. Both films emit light in the red spectral region characteristic of Eu^{3+} into the Ba_2SiO_4 network. Yet, the dispersion of the phosphor particles in PVDF is too low (10 wt.%). On the other hand, the phosphor incorporation in the PMMA matrix does not quench the Eu^{3+} emission, making homogeneous films until the proportion of 66 wt.%; PMMA also undoes Eu^{3+} defect sites

on the surface of the Ba_2SiO_4 particles. Therefore, the $Ba_2SiO_4:Eu^{3+}$/PMMA films display potential to be used as coatings of UV-emitting LEDs (250 nm), making devices that combine both UV and red-emission to be used in indoor farms.

6.6 References

This chapter was written according to a paper published by the authors in Materials Chemistry and Physics (2018)[11] and a paper submitted in ECS Journal of Solid State Science and Technology (2019).[33]

---

[1] PATTISON, P. M. et al. LEDs for photons, physiology and food, Nature, 2018, v. 563, n. 0, p. 493-500.

[2] YEH, N. DING, T. J.; YEH, P. Light-emitting diodes' light qualities and their corresponding scientific applications, Renewable and Sustainable Energy Reviews, 2015, v. 51, n. 0, p. 55–61.

[3] SCHULZE, P. S. C. et al. Light emitting diodes (LEDs) applied to microalgal production, Trends in Biotechnology, 2014, v. 32, n. 8, p. 422-430.

[4] DEMOTES-MAINARDA, S. et al. Plant responses to red and far-red lights, applications in horticulture, Environmental and Experimental Botany, 2016, v. 121, n. 0, p. 4–21.

[5] BOWKER, C., et al. Microbial UV fluence-response assessment using a novel UV-LED collimated beam system, Water Research, 2011, v. 45, n. 5, p. 2011–9.

[6] MORI. M. et al. Development of a new water sterilization device with a 365 nm UV-LED, Medical & Biological Engineering & Computing, 2007, v. 45, n. 12, p. 1237–41.

[7] CHEVREMONT, A. C. et al. Multivariate optimization of fecal bioindicator inactivation by coupling UV-A and UV-C LEDs, Desalination, 2012, v. 285, n. 0, p. 219–25.

[8] LI, Y. et al. High-power deep UV-LEDs for analytical optical instrumentation, Sensors and Actuators B, 2018, v. 255, n. 2, p. 1238–1243.

[9] PARK, J. et al. Review—Group III-Nitride-Based Ultraviolet Light-Emitting Diodes:Ways of Increasing External Quantum Efficiency, ECS Journal of Solid State Science and Technology, 2017, v. 6, n. 4, p. Q42-Q52.

[10] GU, M. H. et al. Formation of poly(vinylidene fluoride) (PVDF) membranes via thermally induced phase separation, Desalination, 2006, v. 192, n. 1-3, p. 160-167.

[11] BISPO-JR, A. G. et al. Red-light-emitting polymer composite based on PVDF membranes and Europium phosphor using Buriti Oil as plasticizer, Materials Chemistry and Physics, 2018, v. 217, n. 0, p. 160–167

[12] FRIAS, A. R. et al. Transparent Luminescent Solar Concentrators Using Ln3+-Based Ionosilicas Towards Photovoltaic Windows, Energies, 2019, v. 12, n. 3, p. 451-11.

[13] LOVINGER, A. J.; BASSET, D.C. Development in Crystalline Polymers-1, Chapter 5, 1982, Applied Science Publishers.

[14] SONG, J. et al. The effect of lanthanum oxide (La_2O_3) on the structure and crystallization of poly(vinylidene fluoride), Polymer international, 2010, v. 59, n. 7, p. 954-960.

[15] SHI, F. et al. Effect of quenching temperatures on the morphological and crystalline properties of PVDF and PVDF–TiO2 hybrid membranes, Journal of the Taiwan Institute of Chemical Engineers, 2012, v. 43, n. 6, p. 980-988.

[16] CRIST, B. SCHULTZ, J. M. Polymer spherulites: A critical review, Progress in Polymer Science, 2016, v. 56, n. 0, p. 1-63.

[17] DURAES, J. A. et al. Thermal and structural behavior of Buriti oil/poly(methyl methacrylate) and Buriti oil/polystyrene materials, Journal of Thermal Analysis and Calorimetry, 2008, v. 92, n. 2, p. 529-534.

[18] DURAES, J. A, et al. Preparation and characterization of blends of recycled polystyrene with cassava starch, Journal of Materials Science, 2007, v. 42, n. 17, p. 7530–7536

[19] ZULFIQAR, S. Study of the thermal degradation of polychlorotrifluoroethylene, poly(vinylidene fluoride) and copolymers of chlorotrifluoroethylene and vinylidene fluoride, Polymer Degradation and Stability, 1994, v. 43, n. 3, p. 423-430.

[20] MALMONGE, L. F.; MATTOSO, L. H. C. Thermal analysis of conductive blends of PVDF and poly(o-methoxyaniline), Polymer,2000, v. 41, n. 23, 8387-8391.

[21] AL-HAZMI, F. S et al. Synthesis and characterization of novel Cu_2O/PVDF nanocomposites for flexible ferroelectric organic electronic memory devices, Current Applied Physics, 2017, v. 17, n. 9, p. 1181-1188.

[22] MAHMOUD, W. E. Et al. Butadiene acrylonitrile rubber loaded fast extrusion furnace black as a compressive strain and pressure sensors, Sensors and Actuators A: Physical, 2007, v. 136, n. 1, p. 229-233.

[23] CEDEO, F. O. et al. Measurements of temperature and melting heat of some pure fatty acids and their binary and ternary mixtures by differential scanning calorimetry, Thermochimica Acta, 2001, v. 369, n. 1-2, p.39.

[24] GARCIA-QUIROZ, A. et al. Physical and Chemical Analysis of Dielectric Properties and Differential Scanning Calorimetry Techniques on Buriti Oil, Instrumentation Science & Technology, 2003, v. 31, n. 1, p. 93-101.

[25] SENCADAS, V.; LANCEROS-MÉNDEZ, S.; MANO, J. F. Characterization of poled and non-poled β-PVDF films using thermal analysis techniques, Thermochimica Acta,2004, v. 424, n. 1-2, 201-207.

[26] LIU, Z.; MARECHAL, P.; JEROME, R. d.m.a. and d.s.c. investigations of the β transition of poly(vinylidene fluoride), Polymer,1997, v. 38, n. 19, p. 4925-4929.

[27] CAMPOS, J. S.C.; RIBEIRO, A. A.; CARDOSO, C. X. Preparation and characterization of PVDF/$CaCO_3$ composites, Materials Science and Engineering: B, 2007, v. 136, n. 2-3, p. 123-128.

[28] INDERHERBERGH, J. Polyvinylidene Fluoride (PVDF) Appearance, General Properties and Processing, Ferroelectrics,1991, v. 115, n. 4, 295-302.

[29] BISEN, R. et al. Optical behaviour of coumarin dye in PVA and PMMA film matrices, Vacuum, 2018, v. 152, n. 0, p. 65-69.

[30] CAMACHO, S. A. et al. Nanostructured hybrid films containing nanophosphor: Fabrication and electronic spectral properties, Journal of Alloys and Compounds, 2012, v. 541, n. 0, p. 365–371.

[31] YAN-BAO, G. et al. Investigation of tribological behavior of lanthanum hybrid polyelectrolyte molecular deposition films, Surface & Coatings Technology, 2011, v. 205, n. 8, p. 2924–2930.

[32] MOYA, S.E. et al. Assembly of Polyelectrolytes on CNTs by Van der Waals Interactions and Fabrication of LBL Polyelectrolyte/CNT Composites, Macromolecular Chemistry and Physics, 2007, v. 208, n. 6, p. 603-608.

[33] BISPO-JR, A. G.; et al. Red-emitting coatings for multifunctional UV/red emitting LEDs applied in plant circadian rhythm control, ECS Journal of Solid State Science and Technology, 2019. ID number: JSSP-19-2763.

CHAPTER 7 - GREEN-EMITTING LEDs BASED ON $Ba_2SiO_4:Eu^{2+}$ AND NEAR-UV-EMITTING LEDs

7.1 Introduction

The revolution in lighting performed by WLEDs opened up new and exciting frontiers in solid-state lighting featuring distinct applications related to the control of the circadian rhythm of humans, animals and plants. [1,2] In this field, LEDs able to produce pure and monochromatic emission are essential; in particular, green light (~520 nm) plays a special role in the human circadian rhythm regulation due to the maximum sensitivity of the eye photopic response to this spectral region,[3] suppressing melatonin production, being, therefore, helpful to reset body clock, correct hyperpigmentation and eliminate skin spots.[4] Moreover, other applications in architecture, traffic signals and backlighting for displays are envisaged.[5]

The need for novel green-emitting LEDs is also favored by the so-called "green gap" that arises from the lack of high-efficient electroluminescent green-emitting LEDs.[6] One way to cope with this issue is through the development of near-UV downshifting phosphors able to convert the UV-emission from LED chips into green light. This strategy has successfully emerged in the last years due to the huge enhancement of the wall-plug efficiency achieved by commercial near-UV-emitting LEDs.[7]

Although a couple of UV-to-green downshifting converter phosphors are available in the market, namely $(Ba,Sr)SiO_4:Eu^{2+}$ and $Lu_3Al_5O_{12}:Ce^{3+}$, some withdraw related to the high annealing temperature (1,200 – 1,000 ºC) and the emission dependence on the device working temperature still need to be addressed.[8] Among the different green-emitting phosphors, the $Ba_2SiO_4:Eu^{2+}$, designated as B2S, presents several advantages previously pointed out in Chapter 1.[9,10,11] Concerning the phosphor processing as coating of near-UV-emitting LEDs, we introduce the $Ba_2SiO_4:Eu^{2+}$ dispersion in PMMA by applying the methodology optimized in section 6.4.

Therefore, inspired in the possibility of fabricating high-efficient green-emitting LEDs for a broad range of applications (Figure 7.1), this chapter focuses on the manufacture and optical characterization of high-efficient and photostable prototypes based on the combination of B2S/PMMA films and commercial near-UV-emitting LEDs (365 nm).

Figure 7.1 Architecture of the near-UV-emitting LED coated with green-emitting phosphors and applications as traffic signals, displays and regulation of human circadian rhythm.

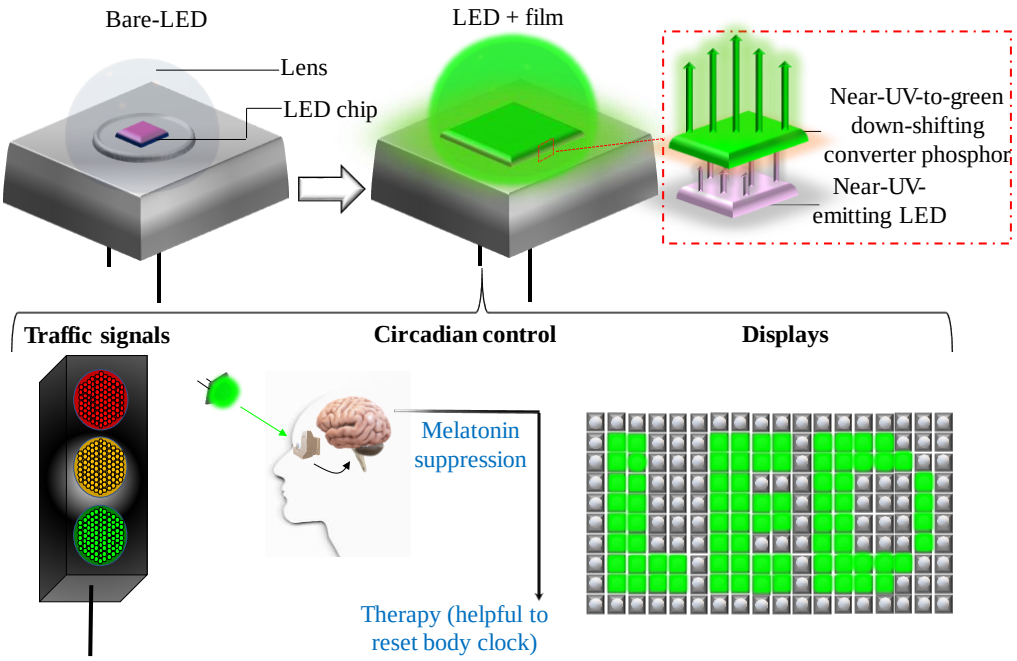

Source: Own authorship.

7.2 Experimental procedure

7.2.1 $Ba_2SiO_4:Eu^{2+}$ synthesis and processing

The Eu(1.5 at.%)-doped Ba_2SiO_4 ($Ba_{1.97}Eu_{0.03}SiO_4$) phosphor was synthesized from an adapted sol-gel route,[12] using CH_3COOH (acetic acid, Sigma-Aldrich, 97%), $C_8H_{20}O_4Si$, (TEOS, Sigma-Aldrich, 99.9%), $Ba(CH_3COO)_2$ (barium acetate, Sigma-Aldrich, 99.9%), Eu_2O_3 (Europium oxide, Sigma-Aldrich, 99.99%) and C_3H_7OH (isopropyl alcohol, CHEM-LAB, 99.8 %) as starting reactants or solvents.

The $Ba(CH_3COO)_2$ (1.3825 g) and Eu_2O_3 (0.0144 g) were mixed with CH_3COOH (10 mL) at 70 ºC; after total dissolution, 10 mL of TEOS in isopropyl alcohol solution (0.056 g/mL) was added and the solution was kept under stirring for 4 hours at 70 ºC until the formation of the gel phase.

The gel was dried at 100 ºC for 2 hours and the resulting SiO_2:Ba,Eu xerogel precursor was calcined at 450 ºC for 2 hours followed by 2 hours at 1,000 ºC (heating ramps of 5 ºC/min, air atmosphere), and at 1,100 ºC for 10 hours (5 ºC/min, 10 % H_2 / 90 % N_2 atmosphere). The chosen concentration of Eu^{2+} (1.5 at.%) was based on a previous study reported by M. Zhang et al.[13] and the sample will be labeled as B2S.

7.2.2 PMMA-based film

The PMMA based films were deposited by drop casting using a proportion of 66 wt.% of the phosphor previously optimized in section 6.4 for $Ba_2SiO_4:Eu^{3+}$. The thickness of the film was tuned by changing the total weight of PMMA and phosphor, as follows: 0.2082 g (film-A), 0.3123 g (film-B) and 0.3644 g (film-C).

For each film, stoichiometric amounts of PMMA (synthesis procedure previously shown in section 6.2.2.) were dissolved in CH_2Cl_2 in order to get a solution with concentration of 0.061 g/mL, followed by the addition of stoichiometric amount of B2S (66 wt.%). Finally, the suspension was transferred to a 2.2×2.2 cm^2 glass that was dried at 300 K for 24 hours.

7.2.3 Green-emitting LED prototype fabrication

The performance of the PMMA/B2S composites as green-emitting LEDs was evaluated through the combination of their films with commercial near-UV-emitting LEDs chips (365±10 nm, Shenzhen chang long Technology Co., ltd, SMD type). The PMMA/B2S films with size of 0.3×0.3 cm^2 were used to coat the surface of the UV-chips by using a cyanoacrylate glue (Permabond Cyanoacrylate 105), Figure 7.2 (a). The LED prototypes will be hereafter designated as 365-Y LED, where Y=A, B or C, depending on the film thickness (Table 7.1).

Figure 7.2 (a) 365-B LED prototype under white light exposition. (b) Emission spectra of the 365-A LED, 365-B LED and 365-C LED prototypes operating at 3.2 V.

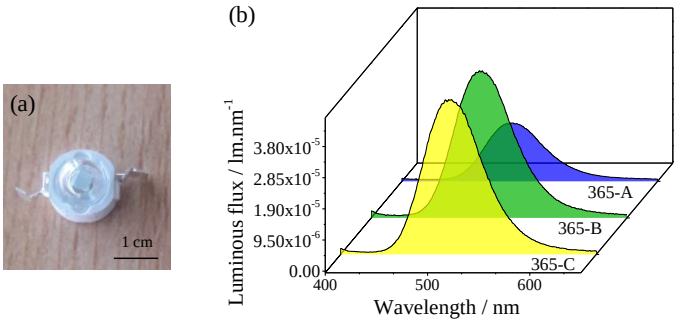

Source: Own authorship.

Table 7.1 Thickness (μm) of the films and luminous flux (ϕ_V, lm), luminous efficacy (LE, $lm.W^{-1}$), and input electric power (P_{el}, W) of the 365-A, 365-B and 365-C LED prototypes operating at 3.2 V.

Sample	Thickness	ϕ_V	P_{el}	LE
Film-A	301±8	0.47±0.01	0.101±0.001	4.65±0.01
Film-B	252±9	1.27±0.01	0.178±0.001	7.13±0.01
Film-C	77±3	1.21±0.01	0.178±0.002	6.80±0.01

Source: Own authorship.

In order to elect the best prototype to be further characterized, the luminous flux of them was measured, Figure 7.2 (b), and the 365-B LED prototype displayed the best luminous efficacy among all the fabricated prototypes (Table 7.1), and for this reason, it was elected to be further characterized.

The fabrication reproducibility of the 365-B LED was confirmed by fabricating five different LED prototypes, Figure 7.3. Operating at 3.2 V, the luminous flux of all prototypes is the same, indicating that the films are homogeneous, and the LED emission can be reproduced.

Figure 7.3 Emission spectra dependence on the operating voltage for 5 different prototypes of the 365-B LED.

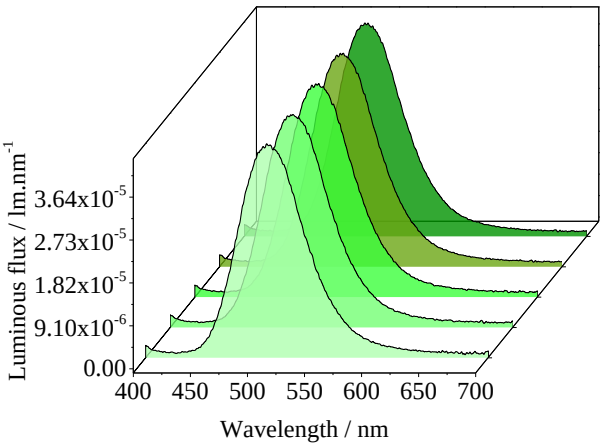

Source: Own authorship.

7.2.4. Structural and optical characterizations

X-ray diffraction (XRD).

The diffractogram of B2S was acquired in the same equipment described in section 4.2.2.

Optical microscopy.

The thickness of the films was estimated through optical microscopy using the same equipment described in section 4.2.2.

Photoluminescence Spectroscopy.

Photoluminescence spectra were recorded at 14 K and at 300 K in the same equipment described in section 4.2.2. The emission decay curves were acquired with the same instrumentation coupled to a TBX-04 photomultiplier tube module (950 V). The

exciting source was a Horiba Scientific pulsed diode light source (SpectraLED-355, peak at 356 nm).

Absolute Emission Quantum Yield.

The absolute emission quantum yields (*q*) were measured at 300 K by using the same equipment described in section 4.2.2.

Luminous flux

The luminous flux of the LED prototypes was measured by using the same equipment described in section 4.2.2.

7.3 Characterization of the B2S and B2S/PMMA phosphors

7.3.1. Structural characterization

The XRD pattern of B2S phosphor is consistent with the JCPDS standard card (no. 26-1403) relative to the orthorhombic Ba_2SiO_4 phase (number 62, P_{nma} space group), Figure 7.4. Once again, regarding the concentration limit of detection of the XRD technique, no impure phases are observed, indicating that the doping does not influence the crystalline structure formation of the matrix. Due to the similar ionic radius of Eu^{2+} (144 pm, CN = 9 and 149 pm, CN = 10) and Ba^{2+} (161 pm, CN = 9 and 166 pm, CN = 10), we will assume that Eu^{2+} replaces Ba^{2+} in the two different sites with CN 9 and 10.[14]

Figure 7.4 Powder XRD of B2S; the vertical green lines indicate the position and relative intensity of the data from JCPDS-26-1403 Ba_2SiO_4 pattern (Ba_2SiO_4 orthorhombic phase, number 62, P_{nma} space group).

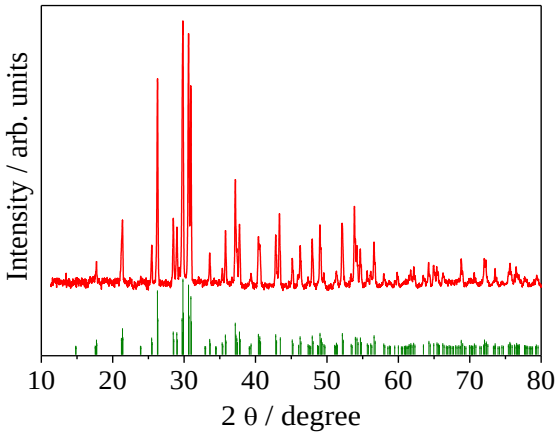

Source: Own authorship.

7.3.2 Steady-state photoluminescence

The room-temperature excitation spectra of the PMMA-based films is dominated by a broad absorption band centered around 366 nm, revealing additional components around 275 nm, 331 nm, and 410 nm, Figure 7.5 (a), resembling that also detected for the B2S phosphor prior to incorporation.

Figure 7.5 (a) Excitation and (b) emission spectra monitored at 505 nm and excited at 366 nm (300 K), respectively. In (a), the emission quantum yield is also plotted. Pictures of (c) B2S and (d) film-B under UV radiation (350 nm) exposition. (e) CIE color coordinate diagram.

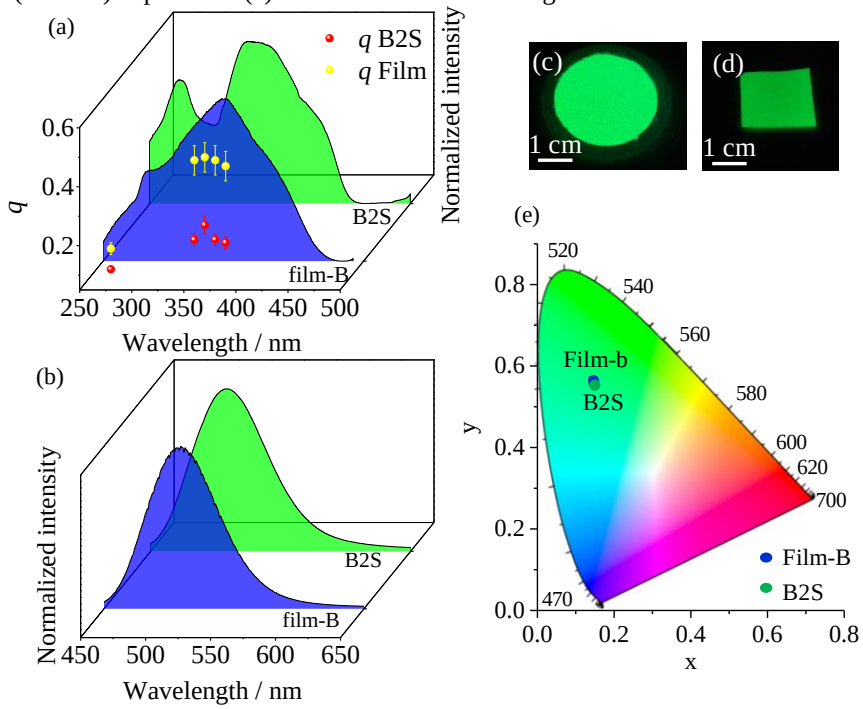

Source: Own authorship.

Under UV excitation, Figure 7.5 (b), the emission spectra display a broadband centered at 505 nm attributed to the $4f^6 5d \rightarrow 4f^7$ Eu^{2+} transition that arises from the strong coupling of the Eu^{2+} 5*d* electrons with the Ba_2SiO_4 matrix.[15] The intense light emission of the samples under UV radiation exposition is noticed also at the naked eye in Figure 7.5 (c) and (d). The green emission was quantified by the (*x*,*y*) CIE color coordinates, Figure 7.5 (e), being (0.143;0.568) for B2S and film.

The effect of the B2S phosphor incorporation into the PMMA films was also analyzed through the measurement of the absolute emission quantum yield (*q*) acquired at distinct excitation wavelength (280-390 nm), Figure 7.5 (a). The maximum *q* values are attained at 370 nm and an intriguing increase from 0.27±0.03 to 0.50±0.05 is observed after the B2S dispersion in PMMA.

The *q* value found for the film is among the best within the state-of-the-art of B2S phosphors, Table 7.2, evidencing that the decrease of the calcination temperature of the sol-gel synthesis and a simple dispersion of the phosphor in PMMA is a good strategy towards the enhancement of Eu^{2+} photoluminescent features.

Table 7.2 Figure of merit of the emission quantum yield (*q*, %) for the B2S phosphor. The excitation wavelength (λ_{exc}, nm) and the calcination temperature ($T_{calc.}$, ºC) to get the phase is also indicated.

Sample	$T_{calc.}$	λ_{exc}	q	[ref]
B2S	1,100	365	27±3	This study
Film-B	1,100	365	50±5	This study
$Ba_2SiO_4:Eu^{2+}$	1,200	450	53	[16]
$Ba_2SiO_4:Eu^{2+}$	1,300	370	47.4	[8]

Source: Own authorship.

7.3.3 Time-resolved photoluminescence

The emission decay curves monitored at 505 nm (14 K and 300 K), Figure 7.6, reveal a biexponential behavior, in line with the presence of more than one local coordination site in both B2S and film-B.

Figure 7.6 Emission decay curves (14 K or 300 K) excited at 355 nm and monitored at 508 nm for the B2S (left) and film-B (right). The solid lines correspond to the data best fit (R^2>0.9), using a biexponential function. The insert in the figures represents residual plots.

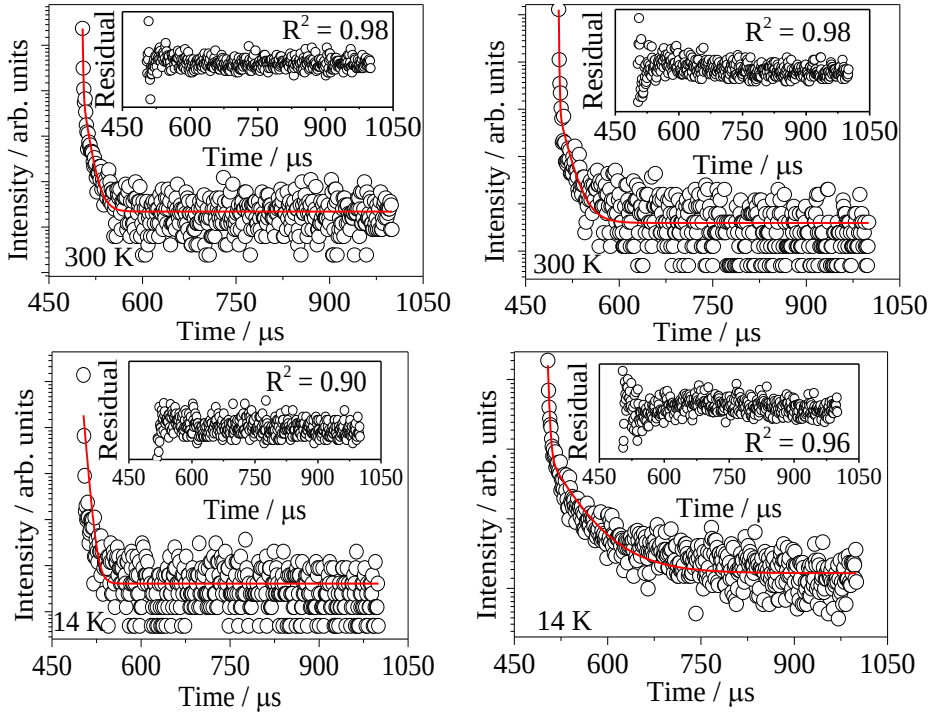

Source: Own authorship.

From the data best fit to a bi-exponential function, Figure 7.6, two different $4f^6 5d$ state lifetime values were found at 14 K and 300 K for both samples, Table 7.3. The long lifetime values (1-10×10^{-6} s) reinforces that the broad emission band arises from the presence of optically active Eu^{2+}, rather than from defect-related states whose lifetime values are typically faster (in the order of 10^{-9} s).

Table 7.3. Eu^{2+} $4f^6 5d$ state lifetime (×10^{-6} s) values measured at 14 and 300 K. The assignments of the shortest and the longest-lived lifetimes were done based on time-resolved spectroscopy.

Temperature	**300 K**		**14 K**	
	Eu_{10}	**Eu9**	**Eu_{10}**	**Eu_9**
B2S	10.10±0.04	0.80±0.02	36±1	1.65±0.01
Film-B	15.8±0.4	0.83±0.02	54±2	2.6±0.1

Source: Own authorship.

Further arguments supporting the origin of the green emission were found by time-resolved emission spectra monitored at 14 K (Figure 7.7). Despite a transition narrowing (detailed below), the energy of the emission band is independent of the starting delay (0 ≤ SD ≤ 4×10^{-5} s) value and resembles that acquired in the steady-state, as expected for the $4f^6 5d \rightarrow 4f^7$ Eu^{2+} transition and contrary to that found in defect-related components, whose emission displacement with the SD (starting delay) is typically observed.[17]

Figure 7.7 Time-resolved emission spectra (14 K) monitored at 366 nm at different starting delay values (0≤SD≤0.04 ×10^{-3} s) for B2S.

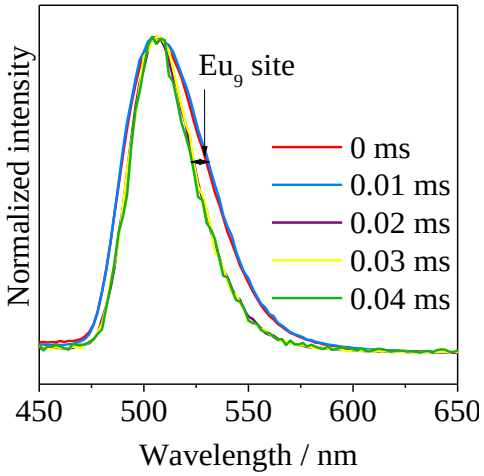

Source: Own authorship.

The two lifetime values found for both samples at 14 and 300 K confirms the presence of two optically active and non-equivalent Eu^{2+} local sites as a result of the replacement of Ba^{2+} sites with coordination number of CN = 9 (Eu_9) or CN = 10 (Eu_{10}),

being the emission band arising from Eu_{10} sites the one with the highest emission energy according to the literature and Equation 2.17.[18]

Time-resolved spectroscopy was also used to discern the lifetime values of the excited states ascribed to Eu_9 and Eu_{10} local coordination sites, Figure 7.7. For starting delay values larger than 10^{-5} s, the intensity of the high-wavelength region (~520 nm) of the emission spectra decreases, pointing out the presence of a short-lived low-energy component, ascribed to the Eu_9 site, that is characterized by a short lifetime value compared with that of the Eu_{10} site.[18]

The $4f^6 5d$ state lifetime values increase for both samples as the temperature decreases from 300 K to 14 K, Table 7.3 suggesting the presence of competing thermally activated nonradiative mechanisms. This aspect may be rationalized since at 300 K, $\tau^{-1} = k_r + k_{nr}$, where k_r and k_{nr} represent the nonradiative and radiative transition probabilities, respectively, and at 14 K, $\tau^{-1} \sim k_r$.

The $4f^6 5d$ state lifetime values are longer than those found for analogous Eu^{2+}-doped Ba_2SiO_4 phosphors ($6\text{-}11\times10^{-7}$ s)[11,19]. Moreover, we also notice that the $4f^6 5d$ state lifetime values at 14 K and 300 K increase after the phosphor dispersion in PMMA, Table 7.3, suggesting that k_r is favored.

The role played by PMMA in the $4f^6 5d$ state lifetime is correlated with the surface defects previously found in the Ba_2SiO_4 (section 6.4) responsible for an increase of k_{nr}. However, after the phosphor dispersion in PMMA, we proposed that the PMMA matrix decreases the concentration of the as-mentioned defects, decreasing the nonradiative transitions from the emitting state of the activator, enhancing the lifetime values. This model also explains the enhancement of the emission quantum yield after the B2S dispersion in PMMA, Figure 7.5 (a).

7.3.4 Temperature-dependent emission spectra

To discuss the mechanisms behind the green emission, temperature (14 - 450 K) dependent photoluminescence was carried out for the B2S phosphor, Figure 7.8, in the next page. As the temperature increases, the emission intensity decreases and the emission bandwidth increases, indicating thermal quenching whose mechanism is illustrated at the configurational coordinate diagram (Figure 7.9).[19]

Figure 7.8 Temperature-dependent (a) absolute and (b) normalized emission spectra excited at 366 nm for B2S.

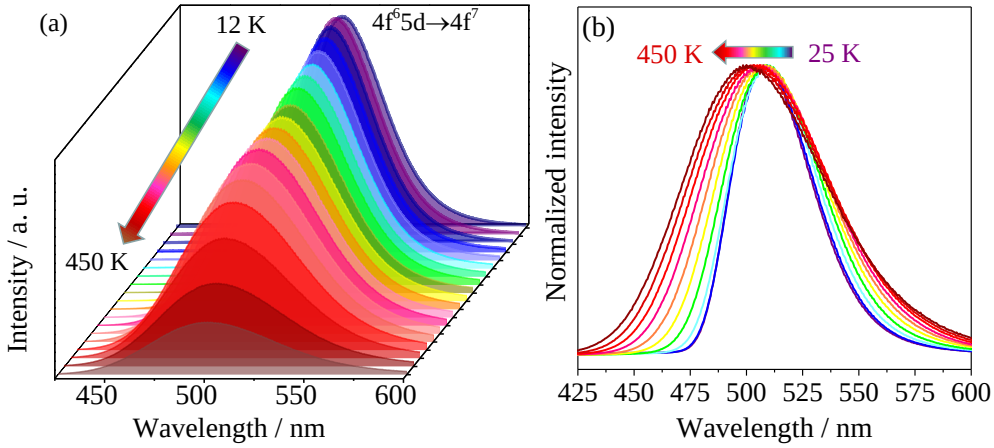

Source: Own authorship.

Figure 7.9 Configurational coordinate diagram for B2S, representing the two Eu^{2+} levels that arise from the Eu_9 and Eu_{10} sites; ΔE_1=3.76±0.01 $\times 10^{-2}$ eV represents the energy barrier for the energy transfer from the Eu_{10} to the Eu_9 site; ΔE_2=4.58±0.01 $\times 10^{-2}$ eV. Both values were estimated from the emission spectrum (14 K).

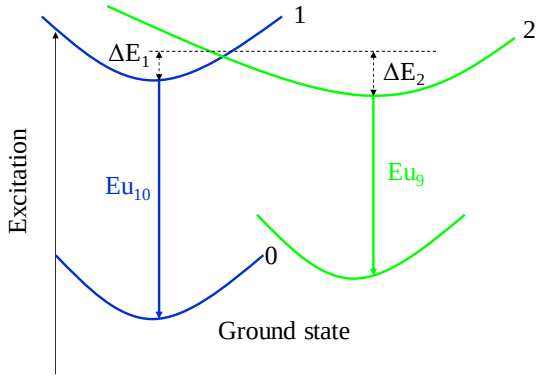

Source: Adapted from Kim et al.[19]

As the temperature is raised above 250 K, the emission energy is also blueshift, Figure 7.8 (b). The temperature-dependence of the emission energy is usually explained by the Varshini model for temperature dependence in semiconductors, given by Equation 7.1, where E_0 is the energy gap at T = 0 K, E(T) is the energy gap at a given temperature and *a* and *b* are constants. The Varshini model suggests that the emission band should display a red shift as the temperature increases.

$$E(T) = E_0 - \frac{aT^2}{T+b} \quad (7.1)$$

However, the deviation from this classical model suggests the presence of energy transfer between the two Eu^{2+} local sites in the matrix (Eu_9 and Eu_{10}), as thermally-activate phonon-assisted tunneling from the lowest excited state of the Eu_9 site to the higher-energy excited state of the Eu_{10} may occur, Figure 7.9. At 14 K, the low energy

difference between the minimum of the conduction band of the Eu_{10} site (ΔE_1= (3.76±0.01)×10^{-2} eV) and the intersection crossing with the Eu_9-related band is thermally activated, whereas as the higher energy difference (ΔE_2= (4.58±0.01)×10^{-2} eV) associated to the minimum of the conduction band in Eu_9 will be dominant at higher temperature values, through thermally-assisted energy back-transfer. In this case, the Eu_{10} emission is dominant over the Eu_9-related one, leading to the blueshift of the overall emission spectrum, Figure 7.8 (b).

The thermal dependence of the emission integrated intensity is well described by the Arrhenius model for a thermal quenching process, Equation 7.2, where I_0 is the emission intensity at 300 K, I_T is the intensity at a given temperature T, k is the Boltzmann constant, C is a constant and ΔE is the energetic difference between two coupled states (thermal activation energy). The emission spectra (Eu_9 site) was modeled applying a gaussian deconvolution, Figure 7.10.

$$I_T = I_0\left[1 + C exp\left(-\frac{\Delta E}{kT}\right)\right]^{-1} \quad (7.2)$$

Figure 7.10 Temperature-dependent emission spectra (300 – 450 K) excited at 366 nm for B2S sample. The Jacobin transformation, F(E) = F(λ)/E^2, was applied to converter the intensity of the emission spectra. The two-gaussian best fit (shadow curves) are also shown (R^2>0.9).

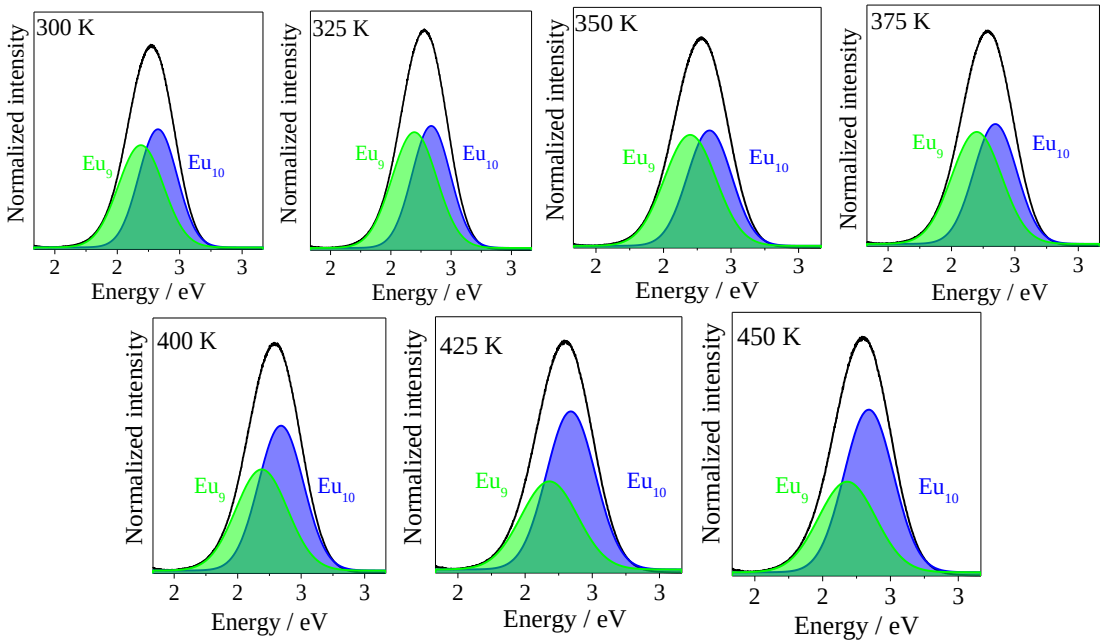

Source: Own authorship.

The thermal dependence of the emission intensity was fitted to equation 7.2, yielding ΔE = 0.46±0.04 eV, Figure 7.11, in good agreement with the presence of

thermally activated energy transfer between the excited levels of the two Eu^{2+}-local sites. This value is higher than those already found for thermal-quenching processes in Eu^{2+}-doped inorganic matrices applied in PC-LEDs (e.g. 0.38 eV for $(Ba,Sr)_2SiO_4:Eu^{2+}$,[8] 0.19 eV for $BaBeSiO_4:Eu^{2+}$,[20] and 0.31 eV for $Ba_2SiO_4:Eu^{2+}$ [8]) promptly indicating that the thermally-activated process is less efficient in the B2S phosphor.

Figure 7.11 (a) Temperature-dependent emission intensity of the Eu_9 site excited at 366 nm for B2S. (b) Plot of $\ln(I_0\text{-}I_T/I_T)$ vs. 1/T; the solid line represents the data best linear fit (R^2>0.99, slope = $-(5.4\pm0.1)\times10^2$ K^{-1}, intercept = 4.0±0.2).

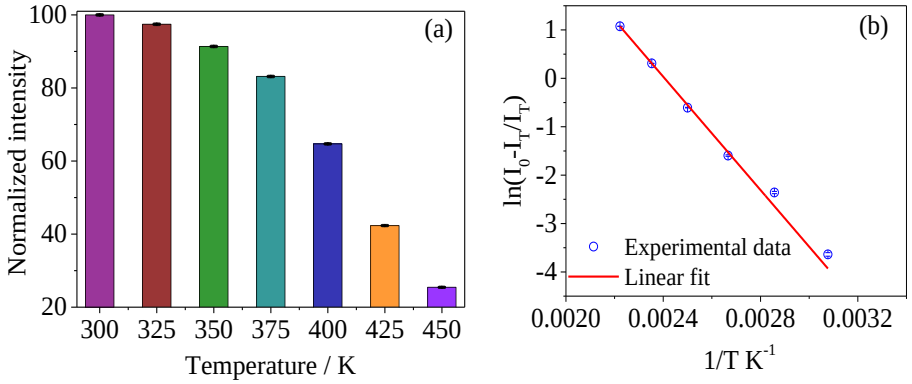

Source: Own authorship.

The temperature at which the integrated emission intensity is half of that at 14 K ($T_{1/2}$) and the ratio between the intensities at a given temperature T and at 300 K (I_T/I_{300K}) are meaningful parameters to be considered taking into account applications in PC-LEDs,[21] being I_T/I_{300K} equal to 72 % at 450 K, similar to that found in other classic phosphors applied in LEDs, Table 7.4, confirming that B2S meets the thermal standards for LED applications.

Table 7.4 Comparison of the thermal stability between the B2S sample and other Ln-based phosphors. $T_{1/2}$ (K) is the temperature to which the integrated emission intensity is half of that at 14 K and I_T/I_{300K} (%) is the ratio between the intensities at a temperature T and at 300 K. λ_{em} (nm) is the LED emission wavelength.

Phosphor	λ_{em}	$T_{1/2}$	I_T/I_{300K}	T	[ref]
B2S	505	440	72;	450	This work
$Sr_3SiO_5:Eu^{2+}$	568	400	-	-	[22]
$Sr_2BaAlO_4F:Ce^{3+}$	502	-	50;	500	[23]
$BaSi_2O_2N_2:Eu^{2+}$	494	440	-	-	[24]
$BaYSi_4N_7:Eu^{2+}$	520	-	15;	475	[25]
$SrYSi_4N_7:Eu^{2+}$	534	-	30;	475	25
$Y_3Al_5O_{12}:Ce^{3+}$	536	700	95;	450	[26]

Source: Own authorship.

7.4 Green-emitting LED prototype characterization

A photo of the 365-B LED operating at 3.2 V is shown in Figure 7.12 (a), and the emission spectra of the prototype, Figure 7.12 (b), reveal a broad emission band in the green spectral region assigned to the B2S phosphor, analogous to that found for the B2S film, Figure 7.5 (b).

Figure 7.12 (a) Photo and (b) emission spectra dependence on the operating voltage of the 365-B LED. (c) (x,y) 1,931 CIE coordinate-dependence on the operating voltage compared to the region required for traffic signals (black square) and automotive device (blue square) application.

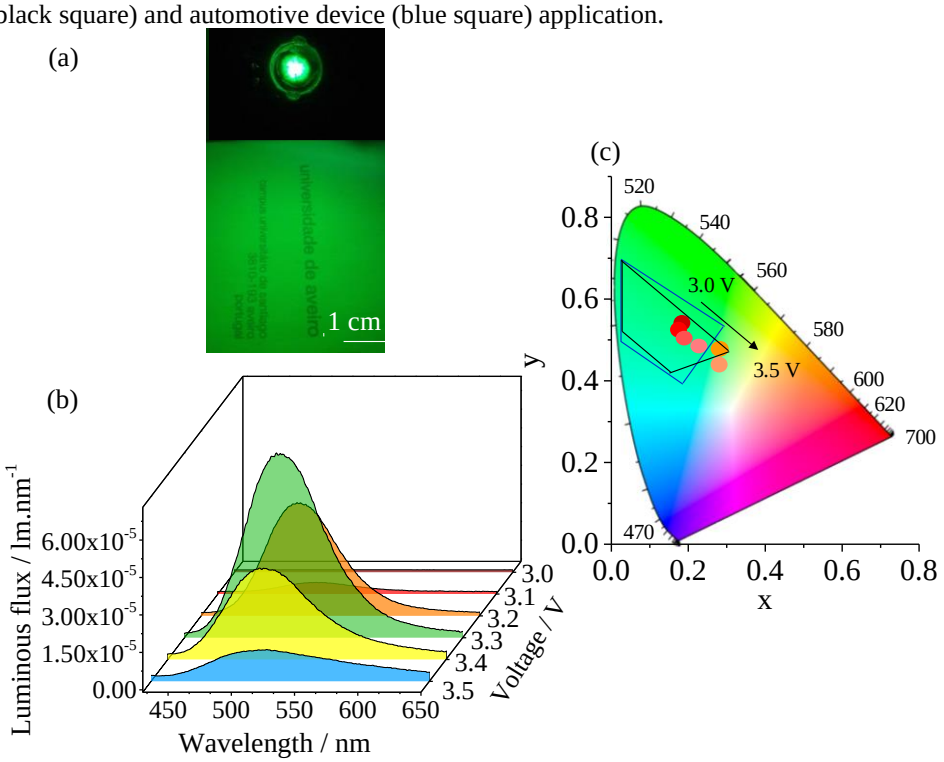

Source: Own authorship.

The luminous efficacy of the optimized prototype (365-B LED) is 7.20±0.01 lm.W^{-1}. We note, however, that a comparison of this value with others must be taken with caution since they depend on the wall-plug efficiency (WPE) of the UV-LED chip and the device geometry. As commercial near-UV-emitting LEDs usually have WPE near to 100 %, the LED prototype efficiency is limited by the phosphor efficiency (η_p), that was represented by Equation 2.7,† chapter 2. In the 365-B LED case, $\eta_{yield} = q =$

† $\eta_{PC-LED} = \eta_{yield} x \eta_{ex} x \eta_{stoke} x \eta_{SA}$, where η_{yield} the phosphor quantum efficiency, η_{stokes} the ratio between the energy of the excitation and emission photons, η_{SA} the self-absorption efficiency and η_{ext} the extraction efficiency

0.50, η_{stokes} = 0.72 and η_{SA} = 1, yielding η_p = 0.36. Therefore, a hypothetical WPE near to 36 % may be achieved for the 365-B LED device.

The experimental WPE measured for the 365-B LED device was 2 %. Thus, by comparing the experimental LE (7.20±0.01 lm.W^{-1}) and WPE (2 %) with the theoretical WPE (36 %), a theoretical LE near to 130 lm/W may be achieved for the 365-B LED.

By comparing the state-of-the-art of green-emitting LEDs using the theoretical LE (130 lm/W) as figure of merit, Table 7.5, the 365-B LED displays the best LE among the devices fabricated by using near-UV-emitting LEDs and different kind of phosphors as carbon dots (CDs),[27] quantum dots (QDs),[28,29,30] inorganic materials[31,32,33] or Ln^{3+}-based complexes[34,35]. Higher values of LE were only reported for (Ba,Sr)SiO_4:Eu^{2+}-based green-emitting LED excited by a blue-light emitting LED (445 nm),[36] Table 7.5, but calcinated at temperatures higher than 1,250 ºC.

Table 7.5 Figure of merit of luminous efficacy (LE, lm.W^{-1}) for the state-of-the-art of green-emitting PC-LEDs comparing temperature of synthesis of the phosphor (T_{synt}, ºC.), bare LED emission wavelength (λ_{exc}, nm), emission wavelength of the prototype (λ_{em}, nm), (x;y) 1931 CIE color coordinates, input current (I, mA) and voltage (V, V).

Material	$T_{synt.}$	λ_{exc}[a]	λ_{em}	(*x;y*)	V/I	LE	[ref]
365-B LED	1 100	365	508	(0.182;0.533)	3.2/57	7.2 (~130)	This work
Organosilane-CDs	160	460	524	(0.335;0.565)	[b]/50	60.96	27
CSSO:Ce^{3+},Tb^{3+}	1 450	460	500	(0.292;0.494)	[b]/20	12.9	37
CSO:Ce^{3+}	1 350	460	500	(0.273;0.457)	[b]/20	27.84	38
CSO:1%Ce^{3+},0.5%Tb^{3+}	1 250	460	500	(0.389;0.269)	[b]/20	7.12	38
$CaSc_2O_4$:Ce^{3+}	1 450	455	517	(0.2646;0.3576)	[b]/350	[b]	31
CdSe-based quantum dots	200	452	544	(0.437, 0.502)	3.2/[b]	62.4	28
$CsPbBr_3$/PMMA	RT	445	535	(0.23;0.75)	[b]	[b]	29
(Ba,Sr)$_2SiO_4$:Eu^{2+}	>1 250	445	513	[b]	[b]/60	143	36
(Sr,Ba)$_2SiO_4$:Eu^{2+}	1 250	445	520	(0.240;0.600)	[b]/60	134	33
(Sr,Ca)Ga_2S_4:Eu^{2+}	[b]	440	538	(0.30;0.66)	[b]/100	82.7	39
$CsPbBr_3$ quantum dots	150	435	533	(0.203, 0.757)	[b]/10	31.92	30
$Ba_5SiO_4(F_3Cl_3)$:0.05Eu^{2+}	1 500	370	503	(0.1833;0.4808)	[b]/20	2.2	32
Tb(3Cl-acac)$_3$(H_2O)$_2$	RT	370	544	(0.320;0.610)	3.8/20	0.8	35
$Ba_5SiO_4(F_3Cl_3)$:0.05Eu^{2+}	900	370	510	(0.183;0.481)	[b]/20	2.2	40
$(Ba_{0.46}Sr_{0.46}Eu_{0.08})_3BP_3O_{12}$	950	370	510	(0.250;0.270)	[b]/350	5.2	41
$Ba_{1.98}SiO_{4-\delta}N_{2/3\delta}$:$Eu_{0.02}$	1 200	375	503	(0.167;0.531)	[b]/60	[b]	42
Tb(p-BBA)$_3$UA	55	365	550	(0.298;0.617)	3.6/350	17.3	34
$NaCaPO_4$:Tb^{3+}	[b]	365	550	[b]	3.6/350	16.7	34

[a] Emission wavelength of the LED chip applied as excitation source for the downshifting converter material. [b] No value is reported. CDs = carbon dots, p-BBA = 4-benzoylbenzoic acid, CSO = $CaSc_2O_4$; CSSO = $Ca_3Sc_2Si_3O_{12}$; 3Cl-acac = 3-chloro-2,4-pentaedionate, UA = undecylenic acid, RT = room temperature,

The luminous flux dependence on the operating voltage of the 365-B LED was measured, Figure 7.12 (b), being observed that it is maximized at 3.3 V. The (*x;y*) color coordinates features a blueshift on the operating voltage due to the increase of the blue

emission component from the LED chip, and the phosphor emission quenching at high operating voltage, as better viewed in Figure 7.13.

Figure 7.13 Normalized emission spectra dependence on the operating voltage for the 365-B LED prototype. The black arrow represents the component of the bare LED emission in the blue spectral region.

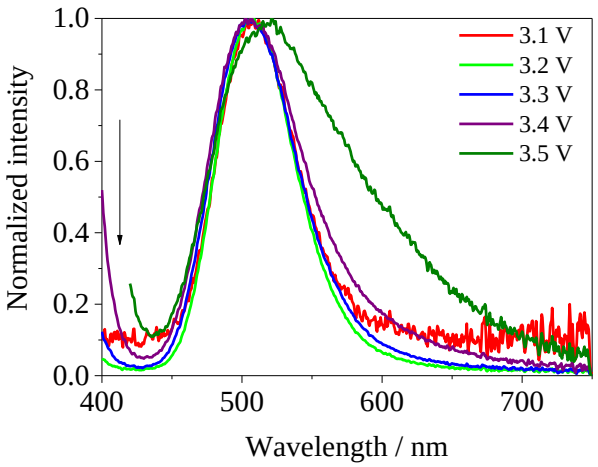

Source: Own authorship.

Attending to the emission blueshift and the relative contribution of the UV-chip-related emission, the emission color of the green-emitting prototype may be tuned by selecting the applied voltage, Figure 7.12 (c). Yet, in the range of 3.0 – 3.3 V, the CIE coordinates meet the criteria required for application in traffic signals or in automotive displays.[13]

At higher operating voltage values, the phosphor luminous flux is probably quenched due to an increase of the operating temperature of the LED and to the larger excitation photon flux that yield absorption saturation.[43] This last aspect is well evidenced in Figure 7.13, that reveals at lower wavelength, the contribution of the UV-LED chip emission that increases its relative intensity as the applied voltage is also increased.

As the electrical power is augmented, the excitation photon flux is also increased and due to the absorption saturation of the B2S phosphor, part of the excitation energy is not absorbed. We note that, however, the mechanism for Eu^{2+}-based phosphor luminescent quenching is still an open question in the literature, being reported another hypothesis. In particular, for Mn^{2+}-based phosphors, the emission quenching has been assigned to the Mn-Mn energy transfer followed by Mn ground-state depletion.[43]

Finally, the radiant flux stability of the 365-B LED was monitored over 180 hours under continuous operation, Figure 7.14. After an initial decrease of 16 % in the 20 first hours, the intensity maintains constant after 100 hours, with a decrease of 43 % of the

initial radiant flux. However, this decrease of the luminous flux comes from the bare-LED, Figure 7.14, confirming the high photostability of the B2S phosphor.

Figure 7.14 State-of-the-art for radiant flux stability of downshifting phosphor-converted green-light emitting LEDs.

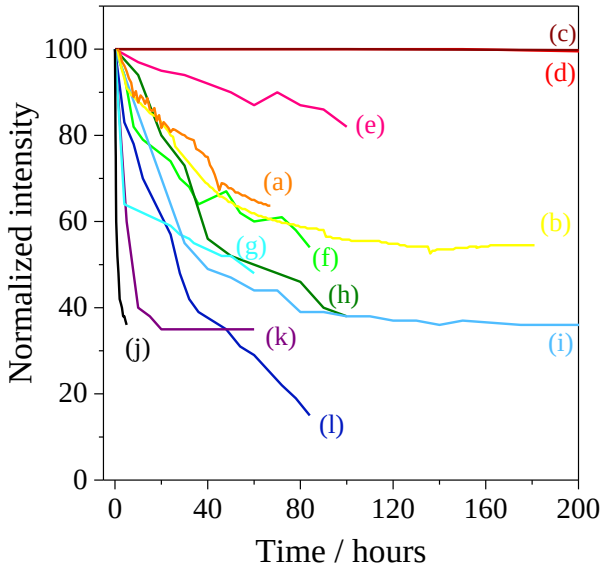

Source: Own authorship.

Table 7.6 Assignments of the curves represented in Figure 7.14. Abbreviations: Hpba = 4-(2-pyridyl)benzaldehyde. 3Cl-acac = 3-chloro-2,4-pentanedionate. The assignments of each curve are represented in Table 7.6.

	Material	**λ_{exc} / nm**	**λ_{em} / nm**	**Degradation / % (time)**	**[ref]**
(a)	Bare UV LED	-	365	33 (66 hours)	This study
(b)	365-B LED	365	508	45 (180 hours)	This study
(c)	$LuAl_3O_{12}:Ce^{3+}$	460	515	56 (40 000 hours)	[44]
(d)	$Sr_{1-x}Ba_xSi_2O_2N_2:Eu^{2+}$	450	532	8 (800 hours)	[45]
(e)	$CsPbBr_3$ NCs	460	525	20 (100 hours)	[46]
(f)	CaF_2-$CsPbBr_3$	460	525	45 (80 hours)	[47]
(g)	CdSe/CdS/ZnS QDs	360	530	52 (60 hours)	[48]
(h)	$CsPbBr_3$ NCs/SiO_2	460	525	65 (60 hours)	[30]
(i)	$Ca_3Sc_2Si_3O_{12}:Ce^{3+},Tb^{3+}$	460	500	75 (250 hours)	[49]
(j)	$[Tb(3Cl\text{-}acac)_3(H_2O)_2]$	370	550	75 (5 hours)	[35]
(k)	Ir-pba@SiO_2	380	535	^{6}5 (60 hours)	[50]
(l)	$CsPbBr_3$	460	525	85 (80 hours)	[46]

Source: Own authorship.

There is also no color shift after 180 hours of operation, evidencing the high color stability of the prototype. It is worth pointing out that by comparing the B2S radiant flux stability with other PC-green-emitting LEDs based on QDs,[30,48] Ln^{3+}-complexes[34,35] or inorganic materials, [45,38] Figure 7.14, the stability displayed by the S2S film is among the best, confirming its potential for commercialization.

Therefore, the findings reported here confirm that by dispersing the B2S phosphor in the PMMA polymer, it is possible to achieve the best emission quantum yield of the material, and its use as a coating of near-UV emitting LEDs enables getting high-efficient and photostable green-emitting LEDs for applications in traffic light, displays, and human circadian rhythm regulation.

7.5 Conclusions

In this chapter, we fabricated green-emitting LED prototypes by coating near-UV-emitting LEDs (365 nm) with films of $Ba_2SiO_4:Eu^{2+}$ dispersed in PMMA. After the $Ba_2SiO_4:Eu^{2+}$ dispersion in PMMA, the emission spectrum revealed a broad emission band centered at about 509 nm with intriguing absolute emission quantum yield values up to 0.50±0.05. The emission of the LED prototype lies within the green spectral region with luminous efficacy of 7.2±0.1 lm/W that may be increased up to 130 lm/W, among the best values in the literature. The emitted color is also independent on the operating voltage within the 3.0 – 3.3 V range. Finally, the radiant flux of the prototype was overseen for 180 hours, evidencing high color stability. Therefore, the findings reported here confirm that the fabricated LED matches desirable features to be applied as commercial green-emitting LEDs for traffic light, displays or control of human circadian rhythm.

7.6 References

[1] JACOBY, M. Tuning phosphors for better white light Advances in the inorganic powders boost the efficiency and appeal of LED bulbs, Chemical and engineering news, 2018, v. 96, n. 0, p. 28-33.

[2] PATTISON, P. M.; HANSEN, M.; TSAO, J. Y. LED lighting efficacy: Status and directions, Comptes Rendus Physique, 2018, v. 19, n. 3, p. 134-145.

[3] GATES, T. A.; FERNANDEZ, D. C.; HATTAR, S. Light as a central modulator of circadian rhythms, sleep and affect, Nature Reviews Neuroscience 2015, v. 15, n. 7, p. 443–454.

[4] KHAN, A. Laser diodes go green, Nature photonics, 2009, v. 3, n. 0, p. 432-434.

[5] DING, B. Improving radiative recombination efficiency of green light-emitting diodes, Materials science and technology, 2018, v. 34, n. 14, p. 1615–1630

[6] ROLLES, M.; HYOT, B.; MISKA, P. New Architecture of $ZnGeN_2/In_{0.16}Ga_{0.84}N$ Type-II Quantum Well-Based Green Emitting LED, Physics Status Solidi RRL, 2018, v. 12, n.8, p. 1800173-4.

[7] MATAFONOVA, G.; BATOEV, V. Recent advances in application of UV light-emitting diodes for degrading organic pollutants in water through advanced oxidation processes: A review, Water Research, 2018, v. 132, n. 0, p.177-189.

[8] PAVITRA, E. et al. $(BaSr)_2SiO_4:Eu^{2+}$ nanorods with enhanced luminescence properties as green-emitting phosphors for white LED applications, Dyes and Pigments, 2017, v. 142, n. 0, p. 447-456.

[9] VENKATARAVANAPPA, M. et al; Facile ultrasound route for the fabrication of green emitting Ba_2SiO_4: Eu^{2+} nanophosphors for display and dosimetric applications, Materials Research Bulletin, 2018, v. 97, n. 0, p. 281–292.

[10] Pires, A. M.; Davolos, M. R. Luminescence of Europium(III) and Manganese(II) in Barium and Zinc Orthosilicate, Chemistry of Materials, 2001, v. 13, n. 1, p. 21-27.

[11] Han, J. K. et al. Europium-activated barium/strontium silicates for near-UV light emitting diode applications, Journal of Luminescence, 2013, v. 133, n. 0, p. 184–187.

[12] RAYMUNDO-PEREIRA, P. A. et al. Study on the structural and electrocatalytic properties of Ba^{2+}- and Eu^{3+}-doped silica xerogels as sensory platforms, RSC Advances, 2016, v. 6, n. 106, p. 104529- 104536.

[13] ZHANG, M. et al. Optical properties of Ba_2SiO_4:Eu^{2+} phosphor for green light-emitting diode (LED), Materials Research Bulletin, 2007, v. 42, n. 1, p. 33–39.

[14] BARSOUM, M. W.; Fundamentals of Ceramics, 2002, CRC Press

[15] MIAO, S. et al. Increased Eu^{2+} Content and Codoping Mn^{2+} Induced Tunable Full- Color Emitting Phosphor $Ba_{1.55}Ca_{0.45}SiO_4$:Eu^{2+},Mn^{2+}, Inorganic Chemistry, 2014, v. 53, n. 19, p. 10386−10393.

[16] SATO, Y. et al. Large redshifts in emission and excitation from Eu^{2+} activated Sr_2SiO_4 and Ba_2SiO_4 phosphors induced by controlling Eu^{2+} occupancy on the basis on crystal-site engineering, Optics Photonics Journal, 2015, v. 5, n. 11, p. 326-333.

[17] HAN, N. S. et al. Defect states of ZnO nanoparticles: Discrimination by time-resolved photoluminescence spectroscopy, Journal of applied physics, 2010, v. 107, n. 8, p. 084306-7.

[18] BIRKEL, A. et al. Eu^{2+}-doped M_2SiO_4 (M = Ca, Ba) phosphors prepared by a rapid microwave-assisted solegel method: Phase formation and optical properties, Solid State Sciences, 2013v. 19, n. 0, p. 51-57.

[19] KIM, J. S. et al. Temperature-dependent emission spectra of M_2SiO_4:Eu^{2+} (M = Ca, Sr, Ba) phosphors for green and greenish white LEDs, Materials Research Bulletin, 2007, v. 42, n. 7, p. 33–39.

[20] YEH, K. Y. et al. Novel blue-emitting phosphors-$BaBeSiO_4$: Eu^{2+}: luminescence properties and its application for UV-light emitting diodes, Optics Material Express, 2016, v. 6, n. 2, p. 416-28.

[21] YE, S. F. et al. Phosphors in phosphor-converted white light-emitting diodes: Recent advances in materials, techniques and properties, Materials Science and Engineering, 2010, v. 71, n. 1, p. 1–34.

[22] DORENBOS, P. Thermal quenching of Eu^{2+} 5d–4f luminescence in inorganic compounds, Journal of Physics-Condensed Matter, 2005, v. 17, n. 50, p. 8103-8111.

[23] IM, W. B. et al. $Sr_{2.975-x}Ba_xCe_{0.025}AlO_4F$: a Highly Efficient Green-Emitting Oxyfluoride Phosphor for Solid State White Lighting, Chemistry of Materials, 2010, v. 22, n. 9, p. 2842-2849.

[24] BACHMANN, V. et al. Color Point Tuning for (Sr,Ca,Ba)$Si_2O_2N_2$:Eu^{2+} for White Light LEDs, Chemistry of Materials, 2009, v. 21, n. 2, p. 316-325.

[25] KURUSHIMA, T. et al. Synthesis of Eu^{2+}-Activated $MYSi_4N_7$ (M = Ca , Sr , Ba) and $SrYSi_{4-x}Al_xN_{7-x}O_x$ (x = 0 – 1) Green Phosphors by Carbothermal Reduction and Nitridation, Journal of the Electrochemical Society, 2010, v. 157, n. 3, p. J64-J68.

[26] BACHMANN, V.; RONDA, C.; MEIJERINK, A. Temperature Quenching of Yellow Ce^{3+} Luminescence in YAG:Ce, Chemistry of Materials, 2009, v. 21, n. 10, p. 2077-2084.

[27] WANG, K.; YIN, Z.; DU, F. Green light–emitting diodes with high efficiency organosilane-functionalized carbon dots, Integrated ferroelectrics, 2017, v.181, n. 14, p. 170-177.

[28] LIU, W. et al. ZnCuInS/ZnSe/ZnS Quantum Dot-Based Downconversion Light-Emitting Diodes and Their Thermal Effect, Journal of Nanomaterials, 2015, v. 2015, n. 0, 1-10.

[29] LANA J. et al. One pot gram-scale synthesis of $CsPbBr_3$ nanocrystals and their application in green LED, Journal of Luminescence, v. 210, n. 0, p. 464-471.

[30] LI, C. et al. Highly pure green light emission of perovskite $CsPbBr_3$ quantum dots and their application for green light-emitting diodes, Optics express, 2016, v. 24, n. 13, p. 15072-15078.

[31] ZHANG, Q. et al. Thermal Quenching Behavior of the Green Emitting $CaSc_2O_4$:Ce^{3+} Phosphor for LED Application, ECS Journal of Solid-State Science and Technology, 2016, v. 5, n. 3, p. R34-R36.

[32] ZHANG, X. et al. Near UV-based LED fabricated with $Ba_5SiO_4(F,Cl)_6:Eu^{2+}$ as blue- and green-emitting phosphor, Optical Materials, 2009, v. 32, n. 1, p. 75–78

[33] OH, J. H. et al. Improved color coordinates of green monochromatic pc-LED capped with a band-pass filter, Optics Express, 2013, v. 21, n. 4, p. 4539-4550.

[34] SUN, N. et al. Synthesis, characteristics and luminescent properties of a new Tb(III)ternary complex applied in near UV-based LED, Optical Materials. 2015, v. 49, n. 0, p. 39-45

[35] NOLASCO, M. M. et al. A green-emitting α-substituted β-diketonate Tb3+ phosphor for ultraviolet LED-based solid-state lighting, Journal of Coordination Chemistry, 2014, v. 67, n. 23-24, p. 4076-4089.

[36] OH, J. H. et al. Highly-efficient, tunable green, phosphor-converted LEDs using a long-pass dichroic filter and a series of orthosilicate phosphors for tri-color white LEDs, Optics Express, 2012, v. 20, n. S1, p. A1-A11.

[37] CHEN, Y. CHEAH, K. W. GONG, M. Low thermal quenching and high-efficiency Ce^{3+}, Tb^{3+}-co-doped $Ca_3Sc_2Si_3O_{12}$ green phosphor for white light-emitting diodes, Journal of Luminescence, 2011, v. 131, n. 8, p. 1589–1593

[38] CHEN, Y.; GONG, M.; CHEAH, K. W. Effects of fluxes on the synthesis of $Ca_3Sc_2Si_3O_{12}:Ce^{3+}$ green phosphors for white light-emitting diodes, Materials Science and Engineering B, 2010, v. 166, n. 1, p. 24–27

[39] OH, J. R. et al. The realization of a whole palette of colors in a green gap by monochromatic phosphor converted light-emitting diodes, Optics Express, 2011, v. 19, n. 5, p. 4188-4198.

[40] ZHANG, X. G. et al. Near UV-based LED fabricated with $Ba_5SiO_4(F,Cl)_6:Eu^{2+}$ as blue- and green-emitting phosphor, Optical Material, 2009, v. 32, n. 1, p. 75-78.

[41] KUO, T. W. et al. Emission color variation of (Ba,Sr)3BP3O12:Eu2+ phosphors for white light LEDs, Optics Express, 2010, v. 18, n. 3, p. 1888-1897.

[42] WANG, S. et al. Enhancement of the photoluminescence properties of $Ba_{1.98}SiO_{4-\delta}N_{2/3\delta}$:Eu0.02 phosphors and their application to green LEDs, Journal of Material Science in Material Electronic, 2016, v. 27, n. 3, p. 2809–2815

[43] SETLUR, A. A.; SHIANG, J. J.; HAPPEK U. Eu^{2+} - Mn^{2+} phosphor saturation in 5 mm light emitting diode lamps, Applied physics letters, 2008, v. 92, n. 8, p. 081104-3.

[44] RAHMAN, F.; GEORGE, A. F.; DRINKARD, R. Short- and Long-Term Reliability Studies of Broadband Phosphor-Converted Red, Green, and White Light-Emitting Diodes, IEEE Transactions on Device and Materials Reliability, 2016, v. 16, n. 1, p. 1-8.

[45] CHO, I. H. et al. On the stability and reliability of $Sr_{1-x}Ba_xSi_2O_2N_2:Eu^{2+}$ phosphors for white LED applications, Optical Materials Express, 2012, v. 2, n. 9, p. 1292-1305.

[46] X. DI, et al. Efficient white LEDs with bright green-emitting $CsPbBr_3$ perovskite nanocrystal in mesoporous silica nanoparticles, Journal of Alloys and Compounds, 2017, v. 729, n. 0, p. 526-532.

[47] WEI, Y. et al. Highly Luminescent Lead Halide Perovskite Quantum Dots in Hierarchical CaF_2 Matrices with Enhanced Stability as Phosphors for White Light-Emitting Diodes, Advanced Optical Materials, 2018, v. 6, n. 11, p. 1701343.

[48] JUN, S.; LEE, J.; JANG, E. Highly Luminescent and Photostable Quantum Dot Silica Monolith and Its Application to Light-Emitting Diodes, ACS Nano, 2013, v. 7, n. 2, p. 1472–1477.

[49] CHEN, Y.; CHEAH, K. W.; GONG, M. Low thermal quenching and high-efficiency Ce^{3+}, Tb^{3+}-co-doped $Ca_3Sc_2Si_3O_{12}$ green phosphor for white light-emitting diodes, Journal of Luminescence, 2011, v. 131, n. 8, p. 1589–1593

[50] KIM, O. et al. Excellent Photostability of Phosphorescent Nanoparticles and Their Application as a Color Converter in Light Emitting Diodes, ACS nano, 2010, v. 4, n. 6, p. 3397–3405.

CHAPTER 8 - WHITE-EMITTING LEDs BASED ON Eu^{2+}-DOPED SILICATE

8.1 Introduction

White-light-emitting diodes (WLEDs) are the main white light source for indoor and outdoor lighting as well as backlighting of displays. The research on solid-state lighting (SSL) is now focused not only on the luminous efficacy (LE) enhancement, but also on the improvement of the color qualities, mainly CCT (correlated color temperature) and CRI (color rendering index) since high values of CCT (>5,500 K) disturb the human circadian rhythm, alertness, and neuroendocrine and neurobehavioral physiology,[1] motivating researchers to come up with new devices featuring better color qualities than the commercially-available WLEDs for new and exciting therapeutic and lighting applications, as previously highlighted in Table 2.3, section 2.2.4.[2]

Currently, there is a limitation on tuning CCT and CRI values since the main commercially-available WLED (GaN blue-emitting semiconductor coated with YAG:Ce^{3+} yellow-emitting phosphor) features a cool-white color (CCT > 6,500 K).[3] Thus, another approach to improve the CCT and CRI has emerged in the last years and is based on the combination of near-UV-to-visible downshifting converter phosphors and near-UV-emitting LED chips (known as PC-WLEDs), allowing broader color tunability than in the YAG-based LED.[4]

In special, the combination of blue and yellow-emitting phosphors as coatings of near-UV-emitting LEDs is a desirable approach in what concerns a tangible balance among the human eye response due to the lack of red-emitting component. However, this approach still challenges the SSL due to the difficulty of matching desirable CCT (~ 4,000 K) and CRI (> 90 %) values for daylight application. For this approach, the blue-emitting $BaMgAl_{10}O_{17}:Eu^{2+}$ (BAM) phosphor excels due to the high emission quantum yield (70 %) and thermally-stable luminescence.[4] However, although yellow-emitting phosphors such as $Sr_9MgK(PO_4)_7:Eu^{2+}$ [5] or $RE_4Ba_2[Si_{12}O_2N_{16}C_3]:Eu^{2+}$ (RE = Lu, Y)[6] are found, some properties as high annealing temperature (1,300 ºC – 1,600 ºC) and low emission quantum yield (40 %) still need to be addressed.

Therefore, inspired in the possibility of fabricating high-efficient and stable PC-WLEDs for indoor and outdoor lighting, in this study, we coated commercial near-UV-emitting LEDs (395 nm) with films based on BAM blue-emitting phosphor and $Sr_2SiO_4:Eu^{2+}$ (S2S) yellow-emitting phosphor dispersed in PMMA, Figure 8.1.

Figure 8.1 Architecture of WLEDs built by coating near-UV-emitting LEDs with PMMA/BAM/S2S films and applications in indoor and outdoor lighting and circadian rhythm control.

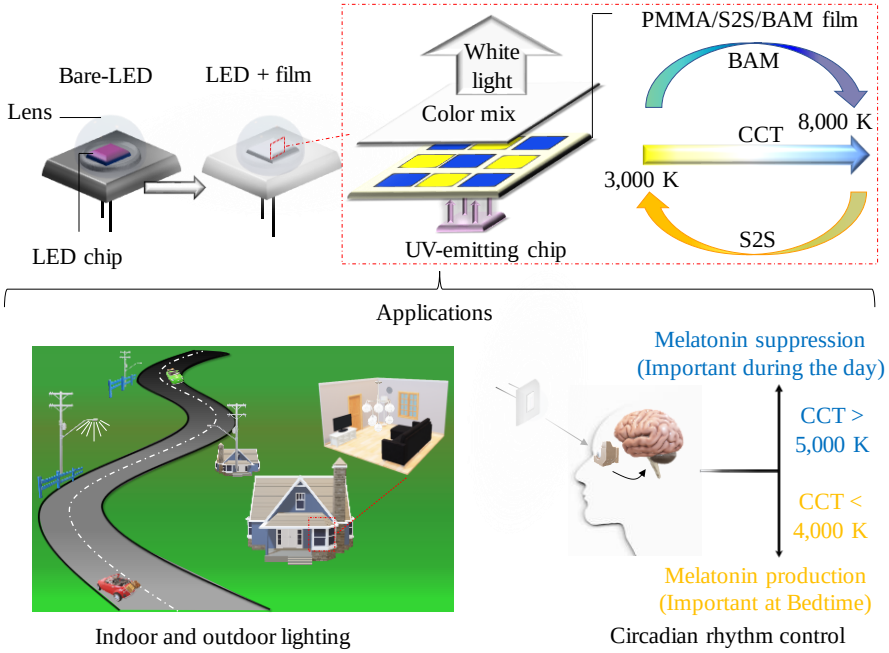

Source: Own authorship.

8.2 Experimental procedure

8.2.1 S2S synthesis and processing

$Sr_2SiO_4:Eu^{2+}$ (3 at.%), $Sr_{1.94}Eu_{0.06}SiO_4$, sample was synthesized from an adapted sol-route previously reported for $Ba_2SiO_4:Eu^{3+}$ [7] by using $Sr(CH_3COO)_2$ (Strontium acetate, Sigma, 99.9 %), Eu_2O_3 (Europium oxide, Sigma, 99.99 %), $C_8H_{20}O_4Si$, (TEOS, Sigma, 99.9 %), C_3H_8O (isopropyl alcohol, Sigma, 99 %) and CH_3COOH (Acetic acid, Sigma, 97 %) as starting reactants without any further purification.

$Sr(CH_3COO)_2$ (2.9427 g) and Eu_2O_3 (0.1557 g) were dissolved in 10 mL of acetic acid at 70 ºC and then, 10 mL of TEOS in isopropyl alcohol solution (0.73 g/mL) was added. The solution was kept under stirring for 4 hours at 70 ºC until the formation of the gel phase that was dried at 120 ºC for two hours until the formation of the SiO_2:Sr,Eu xerogel precursor. The precursor was calcined at 1,000 ºC for 2 hours with a heating ramp of 5 ºC/min (air atmosphere), and 1,200 ºC for 10 hours with a heating ramp of 5 ºC/min (10 % H_2 / 90 % N_2 atmosphere). The chosen concentration of Eu^{2+} and the calcination temperature were based on a previous study reported by J. K Han et. at.[8] and the sample will be hereafter designated as S2S.

8.2.2 PMMA-based film synthesis

The PMMA/S2S films were deposited by the drop casting method using a proportion of 66 wt.% of the phosphor and for that, PMMA (0.1041 g) was dissolved in dichloromethane (2.00 mL) at 25 ºC and then, S2S (0.2082 g) was added in the system. Finally, the suspension was transferred to a glass subtract with dimension of 2.2×2.2 cm^2 and it was dried at 25 ºC for 24 hours. The PMMA-based films containing BAM and S2S were also fabricated by changing the amount of BAM in 20, 40, 60, 80 and 100 wt.% in relation to the S2S weight. The samples will be hereafter designated as S2S(X)BAM(Y), where X and Y are weight percentage in relation to the S2S and BAM phosphors, respectively. The thickness of the films is shown in Table 8.1.

Table 8.1 Thickness of the S2S/BAM films measured by optical microscopy.

Film	Thickness	Film	Thickness
S2S(100)/BAM(0)	84±2	S2S(40)/BAM(60)	146±5
S2S(80)/BAM(20)	97±3	S2S(20)/BAM(80)	72±4
S2S(60)/BAM(40)	133±4	S2S(0)/BAM(100)	67±4

Source: Own authorship.

Pictures of the S2S/BAM powder and film under UV radiation exposition are provided in Figure 8.2.

Figure 8.2 Pictures of the S2S/BAM powder and film under UV radiation (350 nm) exposition.

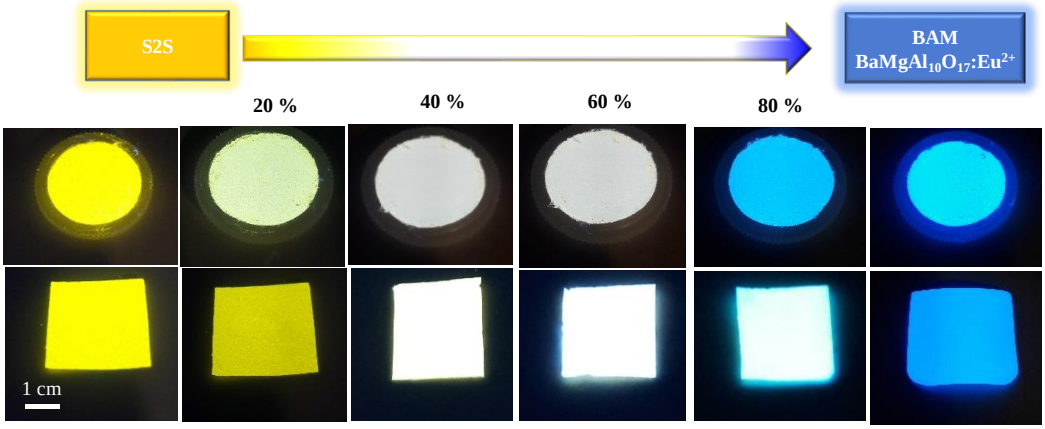

Source: Own authorship.

8.2.3 Fabrication of the WLED prototypes

The performance of the S2S(X)BAM(Y) films was evaluated through the combination with commercial near-UV-emitting LEDs (395±10 nm, Shenzhen chang long Technology Co., ltd, SMD type). For this, a small piece of the S2S(X)/BAM(Y) film with dimension of 0.3x0.3 cm^2 was fixed on the LED chip top by using cyanoacrylate

glue (Permabond Cyanoacrylate 105). The LED prototypes will be hereafter designated as S2S(X)/BAM(Y)-LED. The LED fabrication reproducibility was confirmed by fabricating five different LED prototypes of S2S(60)BAM(40)-LED and S2S(40)BAM(60)-LED, Figure 8.3.

Figure 8.3 Emission spectra of five different (a) S2S(60)BAM(40)-LED and (b) S2S(40)BAM(60)-LED prototypes operating at 3.1 V.

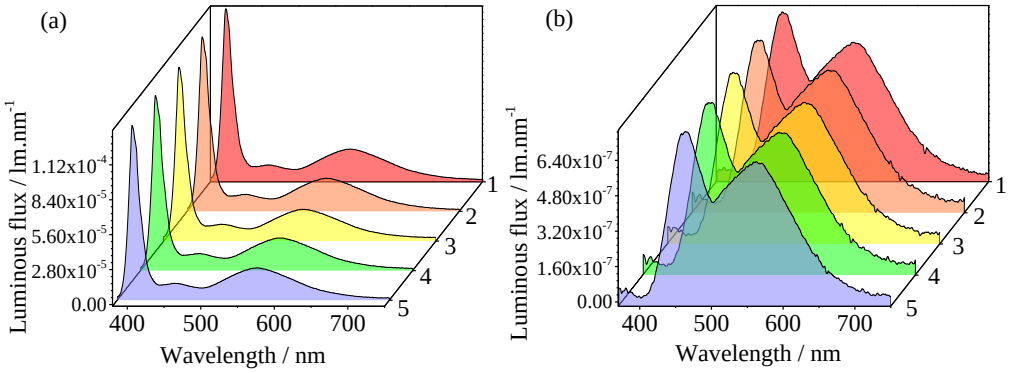

Source: Own authorship.

8.2.4. Structural and optical characterizations

X-ray diffraction (XRD)

The diffractogram of the S2S powder sample was acquired in the same equipment described in section 4.2.2.

Photoluminescence Spectroscopy

The photoluminescence spectra of the S2S and S2S(100)BAM(0) samples were recorded at 14 K and 300 K in the same equipment described in section 4.2.2.

Luminous flux.

The luminous flux of the LED prototypes was measured using in the same equipment described in section 4.2.2.

Absolute Emission Quantum Yield

The absolute emission quantum yields were measured at room temperature in the same equipment described in section 4.2.2.

8.3 S2S and S2S(100)/BAM(0) characterization

8.3.1. Structure and phase composition of S2S

Powder XRD was performed for the S2S sample, Figure 8.4, and the XRD pattern is best-indexed to the orthorhombic α-Sr_2SiO_4 phase (04-013-5411 ICDD database code, number 62, P_{nma} space group) as being the major phase (64.5 wt.%) and to the monoclinic β-Sr_2SiO_4 (00-038-0271 ICDD database code, number 14, $P12_1/c1$ space group) (16.7 wt.%), α-$SrSiO_3$ (04-009-8356 ICDD database code, number 5, $C121$ space group) (13.4 wt.%), $Sr(OH)_2(H_2O)$ (04-009-0743 ICDD database code, number 26, $Pmc2_1$ space group) (3.2 wt.%) and $SrCO_3$ (04-013-9700 ICDD database code, number 62, P_{nma} space group) (2.3 wt.%) spurious phases.

Figure 8.4 Powder XRD of the S2S sample.

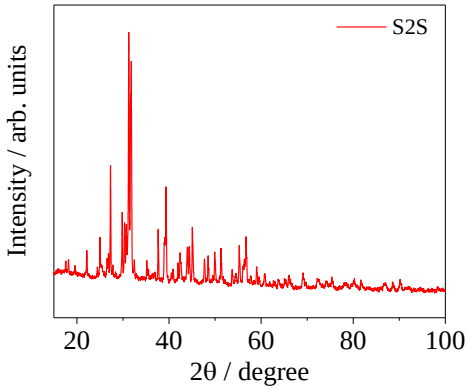

Source: Own authorship.

Both α and β-Sr_2SiO_4 phases coexist at 300 K since a short-range rearrangement of the atoms without any broken bond is enough to convert them, leading to a low phase transition temperature (~358 K).[9] The $SrCO_3$ formation occurs due to the strong reductive atmosphere during the calcination step, that avoids the total decomposition of the organic matter coming from TEOS. Moreover, alkaline earth ions have a high tendency to form carbonates due to the similar ionic radii of CO_3^{2-} and Sr^{2+}. The $Sr(OH)_2(H_2O)$ and α-$SrSiO_3$ phases were also observed in other wet syntheses of S2S[10,11] due to the reaction of SrO with hydroxides in the air atmosphere.

The standardized crystallographic data for the α and β-Sr_2SiO_4 phases are represented in Table 8.2 and they are in accordance with other data previously reported.[12] As previously pointed out in section 2.4, in both α and β-Sr_2SiO_4 phases, Sr^{2+} occupies two non-equivalent local sites with CN 10 (Sr_{10}) or CN 9 (Sr_9), and we will assume that

Eu^{2+} replaces both Sr local sites. The photoluminescence technique will be helpful to assign the optically active Eu^{2+} sites in the sample structure.

Table 8.2 Refinement parameters obtained from the XRD measurement. The refinement factors converge to R_p = 2.10 %, R_{wp} = 2.74 %, and χ^2 =1.55.

Phase	α-Sr_2SiO_4	β-Sr_2SiO_4	α-$SrSiO_3$	$Sr(OH)_2(H_2O)$	$SrCO_3$
ICDD code	04-013-5411	00-038-0271	04-009-8356	04-009-0743	04-013-9700
Wt.%	64.5	16.7	13.4	3.2	2.3
Space group	*Pnma*	*P12₁/c1*	*C121*	*Pmc2₁*	P_{nma}
Lattice parameters / Å	a = 7.0735 b = 5.6640 c = 9.7425	a = 5.6603 b = 7.0757 c = 11.052	a = 12.353 b = 7.1394 c = 10.910	a = 3.6470 b = 6.1980 c = 6.7180	a = 5.9970 b = 5.0220 c = 8.5660
Angle / °	α = β = γ = 90	α = γ = 90, β = 118	α = γ = 90, β = 118	α = β = γ = 90	α = β = γ = 90
V/ 10^6 pm^3	390.34	390.24	892.86	151.85	257.98

Source: Own authorship.

8.3.2 Steady-state photoluminescence

The excitation spectra of the S2S phosphor and the S2S(100)BAM(0) film monitored at 556 nm (300 K) are a set of broadbands with maximum at about 277, 314, 366 and 424 nm assigned to the Eu^{2+} excitation, Figure 8.5 (a).

Figure 8.5 (a) Excitation spectra (300 K, 550 nm) compared to the absolute emission quantum yield (*q*), (b) emission spectra (300 K, 365 nm), (c) CIE color coordinate diagram (300 K) of S2S and film.

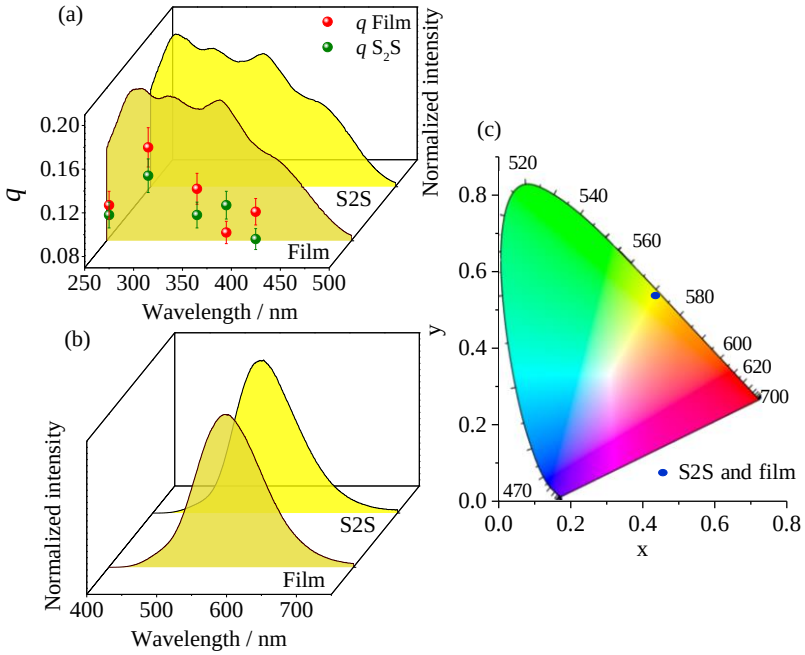

Source: Own authorship.

The emission spectra of the samples monitored at 365 nm (300 K), Figure 8.5 (b), is a broadband with maximum at around 556 nm assigned to the $4f^6 5d \rightarrow 4f^7$ Eu^{2+} transition

allowed by Laporte's rule. The yellow emission quantified by the calculation of the 1,931 *Commission Internationale d´Eclairage* (CIE) color coordinate diagram are (0.14;0.56) for the S2S and S2S(100)BAM(0) samples, Figure 8.5 (c).

The absolute emission quantum yield (*q*) values of S2S and S2S(100)/BAM(0) samples were monitored at 275 nm, 315 nm, 365 nm, 395 nm, and 425 nm, Figure 8.5 (a). The *q* values have maximum at 315 nm and they are statistically the same for both S2S (0.15±0.01) and S2S(100)/BAM(0) (0.18±0.02) samples, confirming that the S2S dispersion in PMMA does not quench the Eu^{2+} emission. The achieved *q* values for the film-B is lower than the values found within the state-of-the-art of S2S, Table 8.3, and it may be correlated to the spurious phases observed through XRD.

Table 8.3 Figure of merit of absolute emission quantum yield for the S2S phosphor comparing excitation wavelength (λ_{exc}) and calcination temperature (T_{calc}).

	λ_{exc} / nm	**$T_{calc.}$ / ºC**	**q**	**[ref]**
S2S	315	1,200	0.15±0.01	-
S2S(100)/BAM(0)	315	1,200	0.18±0.02	-
$Sr_2SiO_4:Eu^{2+}$	400	1,200	0.6	[13]
$Li_2SrSiO_4:Eu^{2+}$	325	900	0.62	[14]

Source: Own authorship.

8.3.3 Selective excitation and emission spectra

To further examine the nature of the Eu^{2+} emission in the S2S phosphor, selective excitation and emission spectra (300 K) were monitored for the S2S sample, Figure 8.6, in the next page.

The intensity of the four bands at about 277, 314, 366 and 424 nm in the excitation spectra, Figure 8.6 (a), is dependent on the emission wavelength, suggesting that the emission band comes from different emitting centers. In the emission spectra monitored by selective excitation, the emission band is redshifted as the excitation wavelength increases from 425 nm to 475 nm, Figure 8.6 (b), in good agreement with Eu^{2+} replacing Sr^{2+} in both α and β-Sr_2SiO_4 phases since J. K. Han et al. previously shown that the Eu^{2+} emission in the β-Sr_2SiO_4 phase has larger energy than in the α-one, confirming that the excitation band at 424 nm is assigned only to the excitation of Eu^{2+} in the α-Sr_2SiO_4 phase.

Moreover, as the Eu^{2+} emission in $SrSiO_3$ phase would occur at 400 nm according to Z. Lu et al.[15], and no emission band is noticed in this range, Figures 8.6 (a) and 8.6 (c), it is feasible to assume that there is no optically active Eu^{2+} center in the $SrSiO_3$ phase and Eu^{2+} replaces only Sr^{2+} local sites in both α and β-Sr_2SiO_4 phases.

Figure 8.6 Selective (a) excitation (300 K), (b) emission (300 K), (c) excitation (14 K) and (d) emission (14 K) spectra monitored at different wavelengths for the S2S sample.

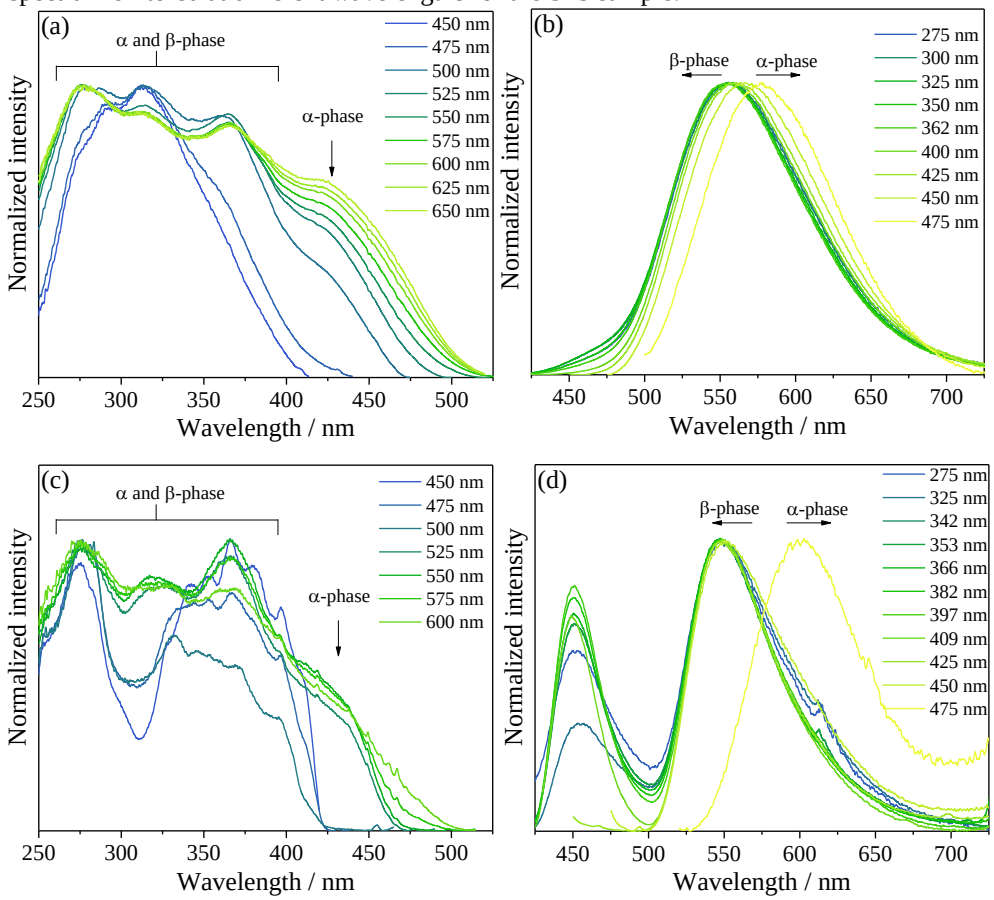

Source: Own authorship.

To infer on the Eu^{2+} local site occupancy in both α and β-Sr_2SiO_4 phases, selective excitation and emission spectra of the S2S sample were also carried out at 14 K, Figure 8.6. The emission spectra monitored at 14 K, Figure 8.6 (d), is quite different from those ones obtained at 300 K, Figure 8.6 (b), and two emission bands at 450 and 550 nm are noticed; the position of the component at 450 nm has no dependence on the excitation wavelength but the second one has the same redshift reported at 300 K, Figure 8.6 (b). The emission bands at 450 and 550 nm are assigned to Eu^{2+} replacing both Sr_{10} and Sr_9 local sites, respectively, according to A. Birkel et al.[16].

The excitation spectra (14 K) of the S2S sample, Figure 8.6 (c), are also dependent on the monitored emission wavelength, yet, the excitation bands are more split than at 300 K, especially when the excitation spectrum was monitored near to 450 nm, Figure 8.7.

Figure 8.7 High resolution excitation spectrum (14 K) monitored at 450 nm of the S2S sample. The Jacobin transformation, $F(E) = F(\lambda)/E^2$, was applied to converter the intensity of the spectrum.

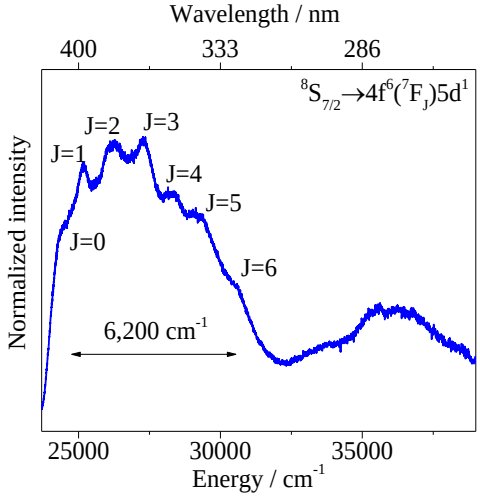

Source: Own authorship.

In this case, 7 well-defined components are noticed (Figure 8.7), and the energy difference between the first and the last components is 6,200 cm^{-1}, close to the energy difference between the $^7F_0$ and $^7F_6$ levels of Eu^{3+}, Table 8.4. This behavior was previously reported for other Eu^{2+}-based phosphors as $MgF_2{:}Eu^{2+}$,[17] $CaF_2{:}Eu^{2+}$, $SrF_2{:}Eu^{2+}$, $BaF_2{:}Eu^{2+}$,[18] and $LuPO_4{:}Eu^{2+}$[19] and it has been assigned to a set of narrow zero-phonon lines (ZPLs) related to transitions from the $^8S_{7/2}$ ground state of Eu^{2+} to the ^7F_J Stark levels of the $4f^6(^7F_J)5d^1$ configuration. The ZPLs are followed by vibrionic components, to which justify the relatively high width observed for the transitions compared to the usual Eu^{3+} emission spectrum in inorganic matrices.[20]

Table 8.4 Positions of ZPLs observed in the 14 K high-resolution excitation spectrum and energy difference between the $4f^6(^7F_0)5d^1\rightarrow{}^8S_{7/2}$ and $4f^6(^7F_J)5d^1\rightarrow{}^8S_{7/2}$ transition of the S2S sample compared to the Eu^{3+} ^7F_J (J = 0- 6) energy level energies.

Transition	Emission spectral position		ΔE (^7F_J-$^7F_0$)	Eu^{3+} level energy
	λ / ±0.03 nm	E / cm^{-1}	/ cm^{-1}	cm^{-1} *
$4f^6(^7F_0)^5d^1\rightarrow{}^8S_{7/2}$	409.93	24,315±5	0	0
$4f^6(^7F_1)^5d^1\rightarrow{}^8S_{7/2}$	397.29	25,037±5	722	379
$4f^6(^7F_2)^5d^1\rightarrow{}^8S_{7/2}$	380.63	26,138±9	1,823	1,043
$4f^6(^7F_3)^5d^1\rightarrow{}^8S_{7/2}$	366.33	27,355±7	3,040	1,896
$4f^6(^7F_4)^5d^1\rightarrow{}^8S_{7/2}$	352.48	28,273±8	3,958	2,869
$4f^6(^7F_5)^5d^1\rightarrow{}^8S_{7/2}$	341.08	29,243±18	4,928	3,912
$4f^6(^7F_6)^5d^1\rightarrow{}^8S_{7/2}$	326.43	30,593±8	6,278	4,992

* Theoretical values for the Eu^{3+} free ion. [20]

Source: Own authorship.

8.3.4 Time-resolved spectroscopy

Selective emission decay curves were monitored for the emission bands coming from the Eu_{10} (450 nm, measured at 14 K) and Eu_9 (550 nm, measured at 14 and 300 K)

local sites, and they were best-fitted through a biexponential adjustment, Figure 8.8, to get the $4f^{6}5d$ state lifetime values.

Figure 8.8 Emission decay curves (14 K or 300 K) of S2S and S2S(100)/BAM(0) excited at 355 nm and monitored at different emission wavelength. The solid lines correspond to the data best fit (R^2>0.9), using a biexponential function. The insert in the figures represents the residual plots.

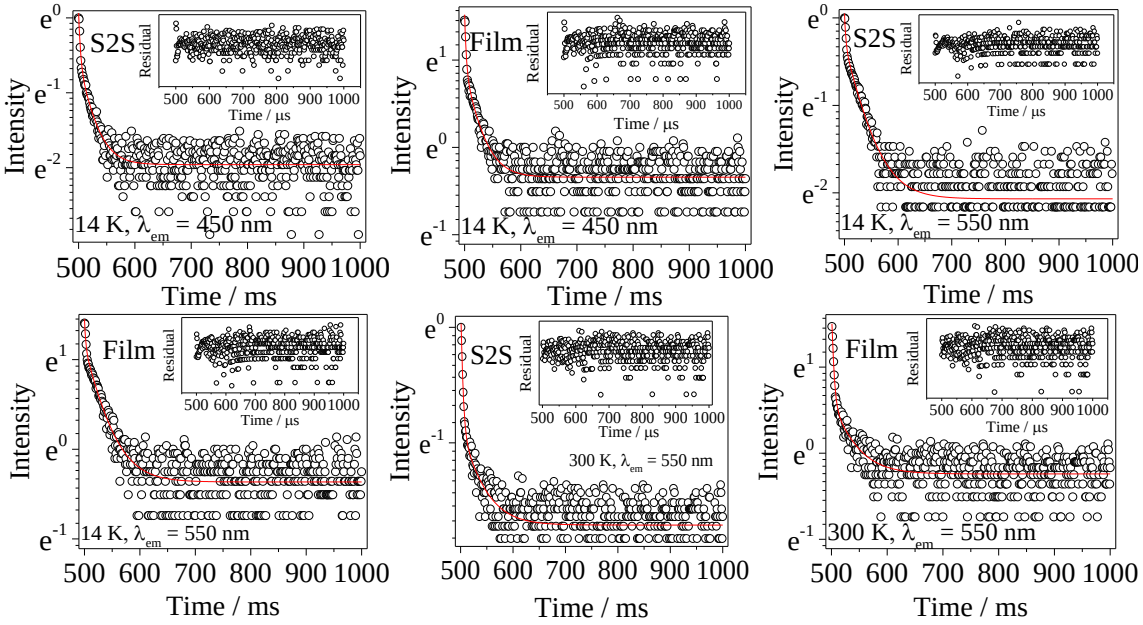

Source: Own authorship.

The long $4f^{6}5d$ state lifetime values (1-40×10^{-6} s), Table 8.5, reinforces the presence of optically active Eu^{2+} ions, rather than the presence of a defect-related component whose lifetime values are typically in the order of 10^{-9} s. Two lifetime values were found for both Eu_{10} and Eu_{9} sites, Table 8.5, because of Eu^{2+} replaces Sr_{9} and Sr_{10} local sites in the α and β-Sr_2SiO_4 phases. For both Eu_{10} and Eu_{9} local sites, one $4f^{6}5d$ state lifetime value is quite shorter than the other one, and the values are statistically the same regardless of the temperature and phosphor processing, confirming that the S2S dispersion in PMMA does not quench the Eu^{2+} luminescence.

Table 8.5 Eu^{2+} $4f^{6}5d$ state lifetime values (μs) for the Eu_{9} (14 and 300 K) and Eu_{10} (14 K) local sites of the S2S and S2S(100)/BAM(0) samples. The assignments of the lifetime values were done based on the time-resolved emission spectra.

T / K	**300 K**		**14 K**		**14 K**	
Eu site	**Eu_{10}**		**Eu_{9}**		**Eu_{10}**	
	β-Sr_2SiO_4	**α-Sr_2SiO_4**	**β-Sr_2SiO_4**	**α-Sr_2SiO_4**	**β-Sr_2SiO_4**	**α-Sr_2SiO_4**
S2S	31.3±0.4	2.6±0.2	25.2±0.4	2.3±0.2	31.9±0.4	2.6±0.1
S_2S(100)/BAM(0)	32.0±0.6	3.2±0.2	25.8±0.5	2.3±0.2	32.1±0.6	2.0±0.2

Source: Own authorship.

To assign the different $4f^6 5d$ lifetime values to the α and β-Sr_2SiO_4 phases, time-resolved emission spectra monitored at 14 K were collected for the S2S sample, Figure 8.9, revealing no displacement in the steady-state emission band maximum, as the starting delay (SD) time changes from 0.00 to 0.04 ms. This observation is in good agreement with the $4f^6 5d \rightarrow 4f^7$ Eu^{2+} transition attribution instead of defect-related emission.[21]

Figure 8.9 Time-resolved emission spectra (14 K) monitored at 366 nm by changing the starting-delay (SD) for the S2S sample.

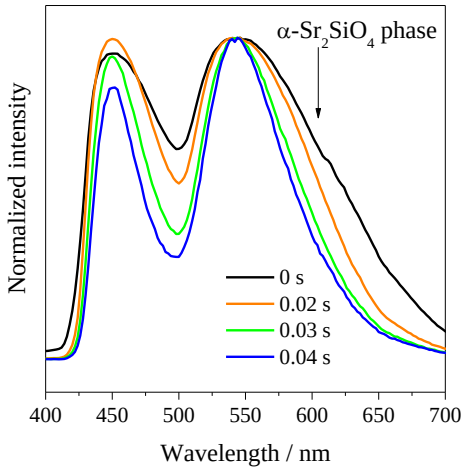

Source: Own authorship.

However, the emission band shape changes after a starting delay of 0.02 s, confirming that the emission comes from more than one non-equivalent Eu^{2+} local site. Clearly, near to 480 and 600 nm, there is an abrupt decrease of the intensity in the emission band, Figure 8.10, suggesting that those components have shorter lifetime values. Therefore, as the emission coming from Eu^{2+} local sites in the α-phase has lower energy than in the β one, it is feasible to assign the components with the shortest lifetimes at 480 and 600 nm to Eu^{2+} local sites in the α-phase, Table 8.5.

8.3.5 Temperature-dependent emission spectra

Temperature-dependent emission spectra were monitored from 14 K to 450 K for the S2S sample, Figure 8.10 (a), showing that the emission intensity decreases as the temperature enhances, due to the ionization of the Eu^{2+} *5d* level to the conduction band of the Sr_2SiO_4 matrix by thermal stimulation.[14] Moreover, as the temperature increases, the emission at 450 nm (Eu_{10} site) disappears due to thermally-activated energy transfer to the Eu_9 site (550 nm), as previously highlighted in Figure 7.9, chapter 7.

Figure 8.10 Temperature-dependent (a) absolute and (b) normalized emission spectra monitored at 366 nm of the S2S sample.

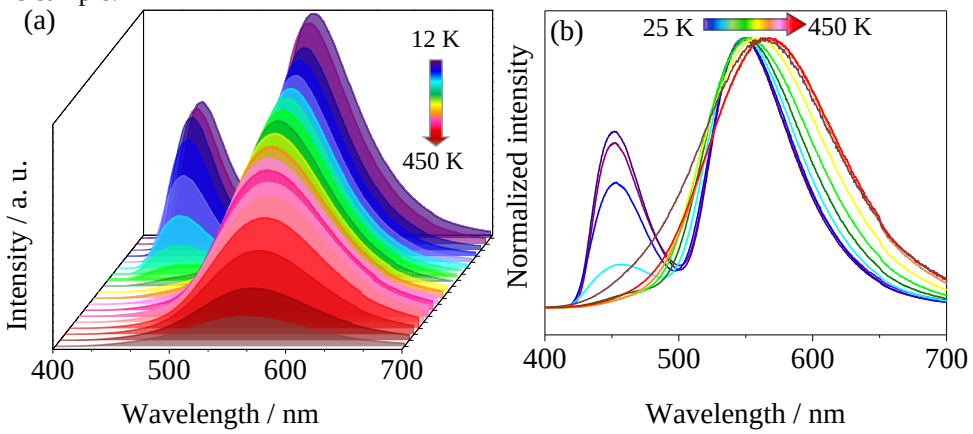

Source: Own authorship.

The $T_{1/2}$ (temperature at which the integrated emission intensity is half of that at 14 K) for the S2S sample is 400 K, and the I/I_{300K} (the ratio between the intensities at a temperature T and at 300 K) is 80 % at 450 K, in good agreement with other classic phosphors applied in PC-LEDs, Table 7.4 in chapter 7, confirming the thermally-stable emission of the phosphor. It is also observed a redshift of the emission band at 550 nm as the temperature increases after 250 K, Figure 8.10 (b), and this is explained by the Varshini model for temperature dependence (Equation 7.1, chapter 7).

8.4 Characterization of the WLED prototypes

Photos of the LED prototypes operating at 3.1 V are shown in Figure 8.11 (a), in the next page. Three bands are noticed in the emission spectra of the devices operating at 3.1 V, Figure 8.11 (b), the first in the lower-wavelength region is assigned to the emission of the near-UV LED (395 nm), the second at 450 nm is the BAM emission and the third at 550 nm is the S2S emission.

The CIE color coordinate dislocates from the yellow toward the blue spectral region, crossing the white-emission region as the amount of BAM increases in the film composition, Figure 8.11 (c).

Considering the white-emitting LED prototypes, the CCT values increases from 3,346 K to 8,406 K as the amount of BAM increases, Figure 8.11 (a), showing that, by varying the proportion of phosphors, it is possible to get warm white light desirable for night light application in bedrooms and dining areas (S2S(60)BAM(40)-LED prototype) and cool white light expected for daylight applications in office space, shops or hospitals (S2S(40)BAM(60)-LED prototype).

Figure 8.11 (a) Photos, (b) emission spectra and (c) CIE color coordinate diagram of the LED prototypes operating at 3.1 V

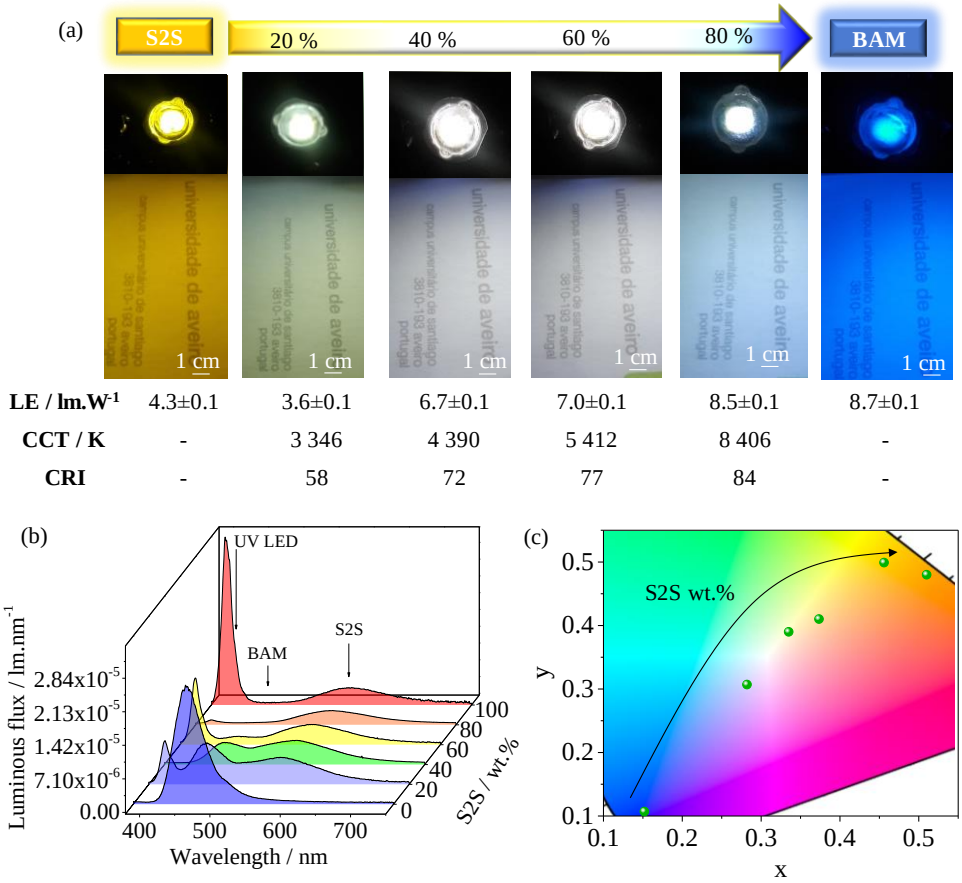

LE / lm.W^{-1}	4.3±0.1	3.6±0.1	6.7±0.1	7.0±0.1	8.5±0.1	8.7±0.1
CCT / K	-	3 346	4 390	5 412	8 406	-
CRI	-	58	72	77	84	-

Source: Own authorship.

From the comparison between the CCT value of the S2S(60)BAM(40)-LED and the state-of-the-art of WLEDs, Table 1.2 in chapter 1, the CCT reported by us is among the best taking into account desirable CCT value (~4,000K) for night light applications. Already the CRI value is lower than those highlighted in the state-of-the-art, Table 1.2, however, it is comparable to the value of the YAG:Ce^{3+}-based WLED (Figure 8.12), and it enhances as the amount of BAM increases in the phosphor mix.

Figure 8.12 CRI of the fabricated WLED prototypes compared to the YAG:Ce^{3+}-based commercial LED.

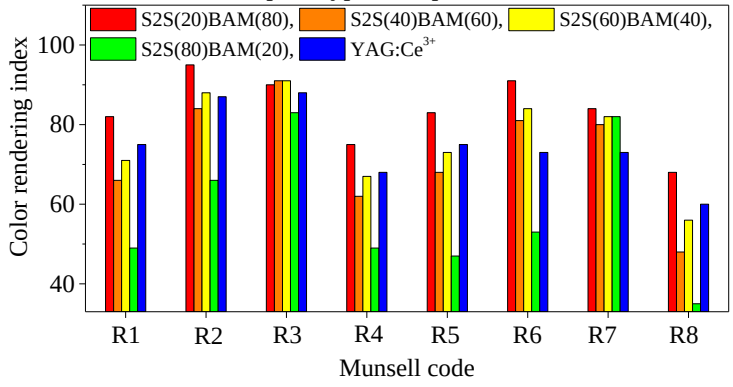

Source: Own authorship.

As the S2S(60)BAM(40)-LED and S2S(40)BAM(60)-LED prototypes displayed desirable CCT and CRI values for lighting, the emission dependence on the operating voltage was evaluated, Figure 8.13.

Figure 8.13 Operating voltage-dependent emission spectra of S2S(40)BAM(60)-LED and S2S(60)BAM(40)-LED prototypes.

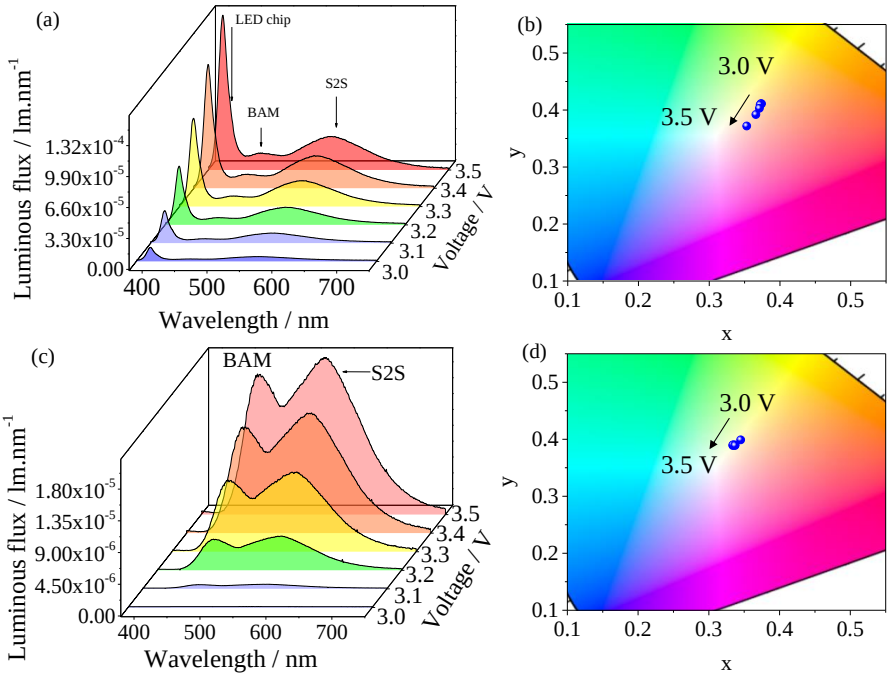

Source: Own authorship.

The best luminous efficacy (LE) was achieved at 3.1 V, Table 8.6, and from then on, it decreases, suggesting that quenching of the phosphor luminescence takes place, which has been ascribed to the increased temperature and/or the large excitation photon flux, saturating the emitter centers.[22]

Table 8.6 Luminous efficacy (LE, $lm.W^{-1}$), correlated color temperature (CCT, K) and color rendering index (CRI) dependence on the operating voltage (V) for the S2S(40)BAM(60)-LED and S2S(60)BAM(60)-LED prototypes.

V / V	S2S(60)BAM(40)-LED			S2S(40)BAM(60)-LED		
	LE	CCT	CRI	LE	CCT	CRI
3.0	6.7±0.3	4,365±2x10^3	72±4	6.7±0.3	5,127±3x10^3	72±4
3.1	6.7±0.3	4,390±2x10^3	72±4	7.0±0.3	5,412±3x10^3	72±4
3.2	6.4±0.3	4,428±2x10^3	72±4	6.6±0.3	5,448±3x10^3	73±4
3.3	5.8±0.3	4,412±2x10^3	72±4	5.3±0.3	5,448±3x10^3	73±4
3.4	5.0±0.3	4,482±2x10^3	72±4	4.7±0.2	5,347±3x10^3	73±4
3.5	3.9±0.2	4,779±2x10^3	72±4	3.8±0.2	5,337±3x10^3	74±4

Source: Own authorship.

However, in our case, as there is no redshift characteristic of the temperature increase in the emission spectra of the devices as the voltage increases, Figure 8.13, the saturation of the emitter centers must be the main cause for the emission quenching. It is worth pointing out that there is almost no change in the (*x;y*) CIE coordinate (Figure 8.13), CCT and CRI values (Table 8.6) of the WLEDs as the operating voltage increases, especially in the interval between 3.0 and 3.3 V, which is not the case of the YAG:Ce^{3+}-based WLED.[23]

The LE of the prototypes enhances from 4.3±0.1 lm/W to 8.7 lm/W as the amount of BAM increases, Figure 11 (a). Furthermore, the LE of the S2S(100)/BAM(0)-LED (4.3±0.1 $lm.W^{-1}$) is higher than the only value reported so far for a $Sr_2SiO_4:Eu^{2+}$-based LED (3.8 $lm.W^{-1}$, $\lambda_{UV\ LED}$ = 400 nm),[24] confirming that the sol-gel synthesis and the dispersion of the S2S phosphor in PMMA is useful to improve the phosphor optical features for application in SSL. However, we highlight again that a comparison of these values must be taken with caution.

Thus, a hypothetical phosphor efficiency was determined (Table 8.7) by applying Equation 2.7,‡ chapter 2, and from a comparison of these values with the experimental WPE also shown in Table 8.7, we carried out an estimative of the LE considering a situation in which the devices are built by using near-UV-emitting LEDs with WPE values of 100 %, meaning that a luminous efficacy value near to 120 lm/W could be achieved for the S2S(60)BAM(40)-LED and S2S(40)BAM(60)-LED prototypes.

Table 8.7 Phosphor quantum yield (η_{yield}), ratio between the energy of the excitation and emission photons (η_{stokes}), self-absorption efficiency (η_{SA}), extraction efficiency (η_{ext}), phosphor efficiency (η_p), experimental wall-plug efficiency (WPE) and theoretical luminous efficacy (LE) of all the fabricated LED prototypes. The η_{SA} of the phosphors was determined from their excitation and emission spectra, Figure 8.14.

LED prototype	η_{yield}	η_{stokes}	η_{SA}	η_{ext}	η_p	WPE / %	LE / $lm.W^{-1}$
S2S(100)BAM(0)	0.12±0.01	0.7	1	1	0.08	1	40
S2S(80)BAM(20)	0.13±0.01	0.7	1	1	0.09	1	40
S2S(60)BAM(40)	0.20±0.02	0.9	1	1	0.18	1	120
S2S(40)BAM(60)	0.20±0.02	0.9	1	1	0.18	1	120
S2S(20)BAM(80)	0.28±0.03	0.9	1	1	0.25	2	110
S2S(0)BAM(100)	0.64±0.06	0.9	1	1	0.58	2	200

Source: Own authorship.

‡ $\eta_{PC-LED} = \eta_{yield} x \eta_{ex} x \eta_{stoke} x \eta_{SA}$, where η_{yield} the phosphor quantum efficiency, η_{stokes} the ratio between the energy of the excitation and emission photons, η_{SA} the self-absorption efficiency and η_{ext} the extraction efficiency

Figure 8.14 Excitation and emission spectra of the (a) S2S/BAM powder mix and (b) S2S/BAM immobilized in the PMMA.

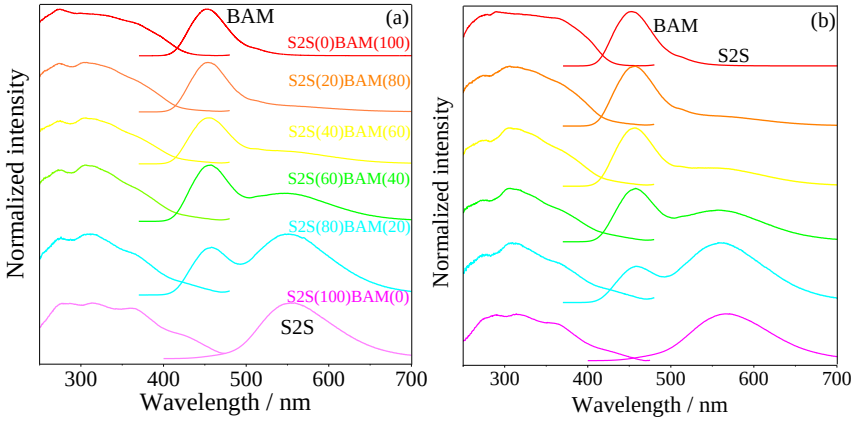

Source: Own authorship.

By comparing the state-of-the-art of WLEDs using the hypothetical LE as figure of merit, Table 1.2, the LE reported by us is among the best values considering devices fabricated by using near-UV-emitting LEDs and different kind of phosphors as carbon dots (CDs), quantum dots (QDs), inorganic materials or Ln^{3+}-complexes. Only one WLED prototype based one near-UV LEDs and CdZnSeS/ZnS QDs displays higher LE than our prototypes,[25] Table 1.2, however, this prototype features poor radiant stability since the QDs are not stable under high excitation photon flux.

Finally, the radiant flux stability of all WLEDs were monitored over 100 hours under continuous operation, Figure 8.15, in the next page, and surprisingly, the intensity maintains constant after it, with no color shift, evidencing the high color stability of the prototype, which is quite unusual considering PC-LEDs built by using phosphors with different thermally-dependent luminescence and structural stability. Moreover, the radiant stability displayed by the prototypes is the same of WLEDs based on classic phosphors as YAG,[26] $CaS:Eu^{2+}$ and $Lu_3Al_5O_{12}:Ce^{3+}$ [27] and it is the best among WLEDs fabricated by coating near-UV-emitting LEDs with phosphors, Table 8.8.

Therefore, the findings reported here confirm that the dispersion of the S2S/BAM phosphor in PMMA does not quench the Eu^{2+} emission, and the use of the films as coatings of near-UV emitting LEDs enables getting efficient and photostable WLED prototypes with tunable CCT values by changing the phosphor mix proportion for night and daylight applications. These prototypes display desirable characteristics as luminous efficacy and radiant stability to be used in indoor or outdoor lighting as well as backlighting of displays or in phototherapy, by regulating the human circadian rhythm.

Figure 8.15 State-of-the-art of PC-WLEDs comparing the radiant flux stability (%) over 100 hours of operation. The assignments of each curve are shown in Table 8.8, above.

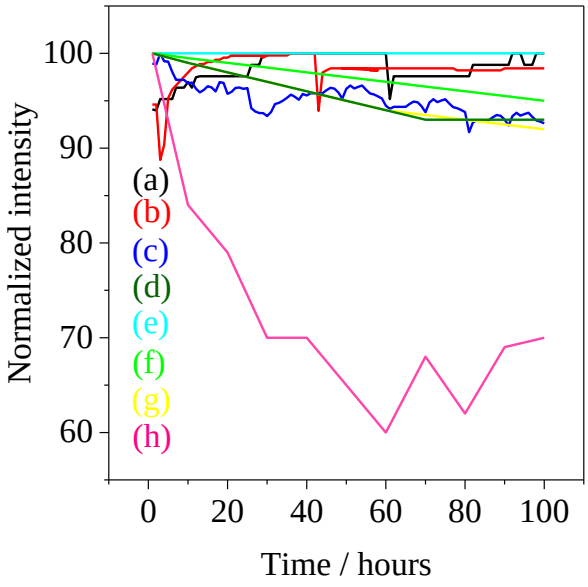

Source: Own authorship.

Table 8.8 Assignments of the curves represented Figure 8.15

	Material	LED chip / nm	Radiant flux stability / %	[ref]
(a)	S2S(40)BAM(60)-LED	395	2	This study
(b)	S2S(60)BAM(40)-LED	395	2	This study
(c)	Bare UV LED	395	6	This study
(d)	$CaS:Eu^{2+}$, $Lu_3Al_5O_{12}:Ce^{3+}$, $(Y,Gd)_3Al_5O_{12}:Ce^{3+}$	455	1	[27]
(e)	YAG	450	0	[26]
(f)	$Sr_{1-x}Ba_xSi_2O_2N_2:Eu^{2+}$	450	10	[26]
(g)	Multi-color phosphor-in-glass	385	5	[28]
(h)	Boehmite hybrid phosphors	360	40	[29]

Source: Own authorship.

8.5 Conclusions

Herein, high-efficient and photostable WLED prototypes were fabricated by coating commercial near-UV-emitting LEDs (395 nm) with $Sr_2SiO_4:Eu^{2+}$ and BAM phosphors dispersed in PMMA. By changing the phosphor mix proportion, the CCT of the prototypes was tuned from cool (6,500 K) toward warm (4,000 K) white light desirable for daylight and night light application, respectively, with CRI comparable to the commercial YAG-based WLED. All the WLED prototypes also display luminous efficacy and photostability among the best values reported for WLEDs built by using near-UV-emitting LEDs, with no changes in CCT and CRI over the time of use, which is not the case of the commercial WLEDs. Therefore, the finds reported in this study showed

that the WLED prototypes appeal as attractive alternatives to be applied in lighting, traffic signs, displays as well as phototherapy.

8.6 References

[1] PATTISON, P. M. et a. LEDs for photons, physiology and food, Nature, 2018, v. 563. n. 0, p. 493 – 500.

[2] OH, J. H.; YANG, S. J.; DO, Y. R. Healthy, natural, efficient and tunable lighting: four-package white LEDs for optimizing the circadian effect, color quality and vision performance, Light: Science & Applications, 2014, v. 3, n. 0, p. e141.

[3] YOO, H. C. et al. Circadian-tunable Perovskite Quantum Dot-based Down-Converted Multi-Package White LED with a Color Fidelity Index over 90, Nature, 2017, v. 7, n. 0, p. 2808-11.

[4] KIM, D. et al. Wide range yellow emission $Sr_8MgLa(PO_4)_7$: Eu^{2+}, Mn^{2+},Tb^{3+} phosphors for near ultraviolet white LEDs, Materials Research Bulletin, 2018, v. 107, n. 0, p. 280–285.

[5] YU, L. et al. Cation vacancy repair for the enhancement of orange-yellow luminescence in $Sr_9Mg_{1.5\_x}K_x(PO_4)_7$:$Eu^{2+}$ phosphors, Journal of Materials Chemistry C, 2018, v. 6, n. 40, p. 10723-10729.

[6] ARTINI, C. et al. Rare-Earth-Doped Ceria Systems and Their Performance as Solid Electrolytes: A Puzzling Tangle of Structural Issues at the Average and Local Scale, Inorganic Chemistry, 2018, v. 57, n. 21, p. 13840−13846.

[7] RAYMUNDO-PEREIRA, P. A. et. Al. Study on the structural and electrocatalytic properties of Ba^{2+}- and Eu^{3+}-doped silica xerogels as sensory platforms, RSC Advances, 2016, v. 6, n. 106, p. 104529-104536.

[8] HAN, J. K. et al. Structure dependent luminescence characterization of green–yellow emitting Sr_2SiO_4:Eu^{2+} phosphors for near UV LEDs, Journal of Luminescence, 2012, v. 132, n. 1, p. 106–109.

[9] CATTI, M. GAZZONI, G. The β -α' phase transition of Sr_2SiO_4. II. X-ray and optical study, and ferroelasticity of the β form, Acta Crystallography B, 1983, v. 39, n. 39, p. 679-684.

[10] PARK, J. H.; AHN, W.; KIM Y. J. Phase formation and luminescence of Sr_2SiO_4:Eu^{2+} nanopowders prepared by a hybrid process, Ceramics International, 2015, v. 41, n. 1, p. S734–S739.

[11] LEE, J. S.; Kim, Y. J. Synthesis and Luminescent characterization of Sr_2SiO_4:Eu^{2+} nanopowders, J. Nanoscience and Nanotechnology, 2012, v. 12, n. 11, p. 8630–8634.

[12] XIE, R. et al. A Simple, Efficient Synthetic Route to $Sr_2Si_5N_8$:Eu^{2+}-Based Red Phosphors for White Light-Emitting Diodes, Chemistry of Materials, 2006, v. 18, n. 23, p. 5578-5583.

[13] HAN, J. K. et al. Structure dependent luminescence characterization of green–yellow emitting Sr_2SiO_4:Eu^{2+} phosphors for near UV LEDs, Journal of Luminescence, 2012, v. 132, n. 1, p. 106–109.

[14] Nasir, S. S. B. et Al. Luminescence properties of Li_2SrSiO_4:Eu^{2+} silicate yellow phosphors with high thermal stability for high-power efficiency white LED application, Journal of Luminescence, 2019, v. 207, n. 0, p. 22–28.

[15] LU, Z. et al. Hydrothermal synthesis, morphology and photoluminescence of hexagonal $SrSiO_3$:Eu^{2+} micro-octahedrons and prism-like hollow microstructures, Materials Chemistry and Physics, 2012, v. 132, n. 2-3, p. 800– 807.

[16] BIRKEL, A. et al. Eu^{2+}-doped M_2SiO_4 (M = Ca, Ba) phosphors prepared by a rapid microwave-assisted sol-gel method: Phase formation and optical properties, Solid State Sciences, 2013, v. 19, n. 0, p. 51-57.

[17] LIZZO, S. et al. The luminescence of Eu^{2+} in magnesium fluoride crystals, Journal of Luminescence, 1995, v. 65, n. 6, p. 303–311.

[18] CHASE, L. L. et al. Microwave-optical double resonance of the metastable $4f^65d$ level of Eu^{2+} in the fluorite lattices, Physics Review B, 1970, v. 2, n. 7, p. 2308–2318.

[19] ZELER, J. et al. Fine structure in high resolution $4f^7$–$4f^65d$ excitation and emission spectra of X-ray induced Eu^{2+} centers in $LuPO_4$:Eu sintered ceramics, Journal of Luminescence, 2019, v. 207, n. 0, p. 435–442.

[20] BINNEMANS, K. Interpretation of Europium(III) spectra, Coordination Chemistry Reviews, 2015, v. 295, n. 0, p. 1–45.

[21] HAN, N. S. et al. Defect states of ZnO nanoparticles: Discrimination by time-resolved photoluminescence spectroscopy, Journal of applied physics, 2010, v. 107, n. 8, p. 084306-7.

[22] SETLUR, A. A.; SHIANG, J. J.; HAPPEK U. Eu^{2+} - Mn^{2+} phosphor saturation in 5 mm light emitting diode lamps, Applied physics letters, 2008, v. 92, n. 8, p. 081104-3.

[23] GEORGE, N. C.; DENAULT, K. A.; SESHADRI, R. Phosphors for solid-state white lighting. Annual Review of Materials Research, 2013, v. 43, n. 0, p. 481–501.

[24] PARK, J. K. et al. White light-emitting diodes of GaN-based Sr_2SiO_4:Eu and the luminescent properties, Applied Physics Letters, 2003, v. 82, n. ,8 p. 683-685.

[25] LE, T. et al. Highly Luminescent Quantum Dots in Remote-Type Liquid-Phase Color Converters for White Light-Emitting Diodes, Advanced Materials Technology, 2018, v. 3, n. 11, p. 1800235.

[26] CHO, I. H. et al. On the stability and reliability of $Sr_{1-x}Ba_xSi_2O_2N_2:Eu^{2+}$ phosphors for white LED applications, Optical Materials Express, 2012, v. 2, n. 9, p. 1294-1305.

[27] RAHMAN, F. et al. Short- and Long-Term Reliability Studies of Broadband Phosphor-Converted Red, Green, and White Light-Emitting Diodes, IEEE transactions on device and materials reliability, 2016, v. 16, n. 1, p. 1-8.

[28] JIANG, P. et al. Thermally stable multi-color phosphor-in-glass bonded on flip-chip UV-LEDs for chromaticitytunable WLEDs, Applied Optics, 2017, v. 56, n. 28, p. 7921-7926.

[29] BAI, X. et al. Efficient and tuneable photoluminescent boehmite hybrid nanoplates lacking metal activator centres for single-phase white LEDs, Nature communications, 2014, v. 5, n. 5702, p. 1-8.

CHAPTER 9 – FINAL REMARKS

9.1 Conclusions

In this study, UV-to-blue ($Ba_2SiO_4:Tb^{3+}$), green ($Ba_2SiO_4:Tb^{3+}$ and $Ba_2SiO_4:Eu^{2+}$), yellow ($Sr_2SiO_4:Eu^{2+}$) and red ($Ba_2SiO_4:Eu^{3+}$) downshifting converter phosphors were synthesized by the sol-gel route and dispersed in polymeric matrices (PVDF or PMMA), making films that were used as coatings of UV LEDs, fabricating green, yellow, and white-emitting LED prototypes.

All phosphors were synthesized in softer calcination conditions (1,100 ºC-1,200 ºC) than the tradition solid-state route (> 1,200 ºC) and their dispersion in the PMMA polymer seems to be an alluring alternative to enhance the luminescent features of the films since PMMA undo superficial defects in the phosphor network, enhancing the emission quantum yield. Yet, although the phosphor dispersion in PVDF may enhance the phosphor emission, the low amount dispersed in the polymer (10 wt.%) is a remarkable drawback compared to PMMA.

$Ba_2SiO_4:Tb^{3+}$ was synthesized as monophasic phase and as the Tb^{3+} amount increases from 0.1 % to 5 %, the overall emitted color dislocates from the blue toward the green spectral region due to a cross-relaxation energy transfer by a dipole-dipole mechanism. We also introduced a simple approach to calculate the $^5D_3$ state quantum efficiency from the emission spectrum, and these values decrease as the Tb^{3+} amount increases in the lattice.

Already the $Ba_2SiO_4:Eu^{3+}$ phosphor displays the usual Eu^{3+} emission in the red spectral region. Eu^{3+} is inserted in 8 non-equivalent local sites, 2 from the replacement of Ba^{2+} in the Ba_2SiO_4 lattice, 1 in the $BaSiO_3$ spurious phase (trace), 2 in Eu^{3+}-O^{2-} associates and 3 defect-related sites. It is worth pointing out that Tb^{3+} may act as a sensitizer for the Eu^{3+} luminescence in the case that the Tb^{3+} content is much lower than the Eu^{3+} one.

Considering the $Ba_2SiO_4:Eu^{3+}$ features for applications in multifunctional LEDs for indoor farm application, its emission quantum yield (11 %) is among the best considering silicate-based phosphors, but it is lower than the classical red-emitting phosphors. Finally, the PMMA/$Ba_2SiO_4:Eu^{3+}$ films were tentatively applied as coatings of deep-UV emitting LEDs (250 nm), but the low external quantum efficiency of the UV LED limits the real use of the prototype.

The $Ba_2SiO_4:Eu^{2+}$ green-emitting phosphor features a thermally stable broad emission band in the green spectral region and its emission quantum yield increases from

0.27±0.03 up to 0.50±0.05 after the dispersion in PMMA. The PMMA/$Ba_2SiO_4:Eu^{2+}$ films were used as coatings of near-UV emitting LEDs (365 nm), making green-emitting LED prototypes with luminous efficacy and reliability among the best already reported, thus, being an alternative to work around the "green gap" and be used as traffic light, backlight of displays and mainly in phototherapy.

$Sr_2SiO_4:Eu^{2+}$ yellow emitting phosphor was combined to the commercial BAM blue-emitting phosphors, making tunable white-light-emitting films, to which were used to coat near-UV-emitting LEDs (395 nm). By changing the phosphor mix in the WLED prototypes, the CCT values dislocate from 5,412 K (ideal for daylight application) toward 3,346 K (ideal for nigh light application), being that all the prototypes feature luminous efficacy and reliability among the best already reported. Therefore, these prototypes match the required characteristics to be used in lighting, backlight of displays and in phototherapy, by regulating the human circadian rhythm, following the sunlight changes over the day.

Finally, the main contributions of this thesis to the solid-state lighting field are summarized by the following three points. (1) Although the "green-gap" is still a challenge considering green-emitting LEDs fabricated by semiconductors, this study evidences that it is possible to fabricate efficient and photostable green-emitting LEDs by coating UV LEDs with green-emitting phosphors, and these prototypes appeal as an alternative to replace the commercial LEDs, to which features high power consumption and low luminous efficacy. (2) The phosphor processing as coatings of LEDs is an important step considering the optimization of the luminous efficacy, and homogenous films based in PMMA containing the phosphor particles now are an alluring protocol for that. (3) The use of PC-WLEDs may achieve the luminous efficacy displayed by the YAG-based WLED.

9.2 Perspectives for futures investigations

After the end of this study, there are some points that may be further investigated in future studies in the LLuMes research group, and we highlight some of them:

1) To investigate other approaches for the charge-balancing in the $Ba_2SiO_4:Eu^{3+}$ and $Ba_2SiO_4:Tb^{3+}$ phosphors, for instance, by using alkaline ions as Li^+, Na^+ and K^+, or Al^{3+} to replace Si^{4+}.

2) To synthesize nanoparticles of all the systems by other methods as co-precipitation or hydrothermal route in order to improve the phosphor dispersion in the polymeric matrices and to decrease the light scattering.

3) To fabricate monophasic $Sr_2SiO_4:Eu^{2+}$ phosphor, enhancing its emission quantum yield.

4) To combine to the $Sr_2SiO_4:Eu^{2+}$ and BAM phosphors, a near-UV-to-red downshifting converter phosphor in order to improve the CRI of the WLEDs.

9.3 Papers published by the authors during the Ph.D.

Published papers

BISPO-JR A. G.; LIMA, S. A. M.; LANFREDI, S.; PRAXEDES, F. R.; PIRES, A. M. Tunable blue-green emission and energy transfer properties in $Ba_2SiO_4:Tb^{3+}$ obtained from sol-gel method, Journal of Luminescence, 2019, v. 214, n. 0, p. 116604-8.

LEITE-SILVA, C. M.; **BISPO-JR, A. G.**, LIMA, S. A. M.; PIRES, A. M. Eu^{3+} complex/polymer films for light-emitting diode applications, Optical materials, 2019, v. 96, n. 0, p. 109323-7.

LEITE-SILVA, C. M.; **BISPO-JR, A. G.**, CANISARES, F. S. M.; Castilho, S. A.; Lima, S. A. M.; Pires, A. M. Eu^{3+}-Tetrakis β-diketonate complexes for solid-state lighting application, 2019, v. X, n. X, p. 1-10

BISPO-JR, A. G.; PIRES, A. M.; LIMA, S. A. M.; CARDOSO, C. X. Evaluation of cryo-treatment in the luminescent properties of PVDF/Eu_2O_3 composite obtained by using buriti oil as additive. Solid State Sciences, v. 92, n.0, p. 24-30, 2019.

BISPO-JR, A. G.; SHINOHARA, G. M. M.; PIRES, A. M.; CARDOSO, C. Red phosphor based on Eu^{3+}-doped $Y_2(MoO_4)_3$ incorporated with Au NPs synthesized via Pechini's method. Optical Materials, v. 84, n. 0, p. 137-145, 2018.

BISPO-JR, A. G.; OLIVEIRA, N. A.; CARDOSO, C. X.; LIMA, S. A. M.; JOB, A. E.; OSORIO-ROMÁN, I. O.; DANNA, C. S.; PIRES, A. M. Red-light-emitting polymer composite based on PVDF membranes and Europium phosphor using Buriti Oil as plasticizer. Materials Chemistry and Physics, v. 217, n. 0, p. 160-167, 2018.

BISPO-JR, A. G.; LIMA, S. A. M.; PIRES, A. M. Energy transfer between terbium and europium ions in barium orthosilicate phosphors obtained from sol-gel route. Journal of Luminescence, v. 199, n. 0, p. 372-378, 2018.

BISPO-JR, A.G.; CECCATO, D. A.; LIMA, S.A. M.; PIRES, A. M. Red phosphor based on Eu^{3+}-isoelectronically doped Ba_2SiO_4 obtained via sol-gel route for solid state lightning. RSC Advances, v. 7, n. 85, p. 53752-53762, 2017.

RAYMUNDO-PEREIRA, P. A.; CECCATO, D. A.; **BISPO-JR, A. G.**; TEIXEIRA, M. F. S.; LIMA, S. A. M.; PIRES, A. M. Study on the structural and electrocatalytic properties of Ba^{2+}- and Eu^{3+}-doped silica xerogels as sensory platforms. RSC Advances, v. 6, n. 106, p. 104529-104536, 2016.

SANTOS, D. C.; **BISPO-JR, A. G.**; MACHINIA, W. B. S.; PIRES, A. M.; TEIXEIRA, M. F. S. Estudo do comportamento espectroscópico do ligante base de schiff N,N-,N-,N-Tetrasaliciideno- 1,2,4,5-tetraaminobenzoato e seus complexos com cobre(II). Colloquium Exactarum, v. 6, n. 3, p. 97-104, 2014.

Submitted papers

FANG, M.; **BISPO-JR, A. G.**; FU, L.; FERREIRA, R. A. S.; CARLOS, L. D. Green-emitting coating phosphors for near-UV excited light-emitting diodes, ACS Applied Materials & Interfaces, 2019, am-2019-10701v.

Accepted papers

BISPO-JR; A. G.; LIMA, S. A. M.; CARLOS, L. D.; FERREIRA, R. A. S., PIRES, A. M. Red-emitting coatings for multifunctional UV/red emitting LEDs applied in plant circadian rhythm control, ECS Journal of Solid State Science and Technology, 2019, JSSP-19-2763.

UNIVERSIDADE ESTADUAL PAULISTA
"JÚLIO DE MESQUITA FILHO"
Campus de São José do Rio Preto

TERMO DE REPRODUÇÃO XEROGRÁFICA

Autorizo a reprodução xerográfica do presente Trabalho de Conclusão, na íntegra ou em partes, para fins de pesquisa.

São José do Rio Preto, 10/09/2019

_____

Airton Germano Bispo Junior